Tenebrescent minerals by in silico modelling

Pauline Colinet

N° National de Thèse : 2022LYSEN002

THÈSE de DOCTORAT de L'UNIVERSITÉ DE LYON

opérée par

l' École Normale Supérieure de Lyon

École Doctorale n°206

École Doctorale de Chimie (Chimie, Procédés, Environnement)

Spécialité : **Chimie Théorique**

Discipline : **Chimie**

Présentée et soutenue publiquement le 27 janvier 2022
par **Pauline COLINET**

Tenebrescent minerals by *in silico* modelling

Modélisation des propriétés spectroscopiques de matériaux ténébrescents

---

Devant le jury composé de :

Ilaria Ciofini	Directrice de Recherche, *Chimie Paristech*	Rapporteure
Denis Jacquemin	Professeur des Universités, *Université de Nantes*	Rapporteur
Mariachiara Pastore	Chargée de Recherche, *Université de Lorraine*	Examinatrice
Mika Lastusaari	Professeur Adjoint, *Université de Turku (Finlande)*	Examinateur
Elise Dumont	Professeure des Universités, *ENS de Lyon*	Examinatrice
Tangui Le Bahers	Maître de Conférences, *Université de Lyon*	Directeur de thèse

Laboratoire de Chimie ENS de Lyon
46 allée d'Italie
69364 LYON CEDEX 07
FRANCE

École doctorale 206
7 avenue Jean Capelle
69621 Villeurbanne
FRANCE

N° National de Thèse : 2022LYSEN002

THÈSE de DOCTORAT de L'UNIVERSITÉ DE LYON

opérée par

l' École Normale Supérieure de Lyon

École Doctorale n°206

École Doctorale de Chimie (Chimie, Procédés, Environnement)

Spécialité : **Chimie Théorique**

Discipline : **Chimie**

Présentée et soutenue publiquement le 27 janvier 2022
par **Pauline COLINET**

Tenebrescent minerals by *in silico* modelling

Modélisation des propriétés spectroscopiques de matériaux ténébrescents

---

Devant le jury composé de :

Ilaria Ciofini	Directrice de recherche, *Chimie Paristech*	Rapporteure
Denis Jacquemin	Professeur des universités, *Université de Nantes*	Rapporteur
Mariachiara Pastore	Chargée de Recherche, *Université de Lorraine*	Examinatrice
Mika Lastusaari	Professeur Adjoint, *Université de Turku (Finlande)*	Examinateur
Elise Dumont	Professeure des universités, *ENS de Lyon*	Examinatrice
Tangui Le Bahers	Maître de Conférences, *Université de Lyon*	Directeur de thèse

Remerciements

Faute d'être originale je serai sincère, et remercierai tout d'abord mon directeur de thèse, Tangui, qui m'a permis de participer à cette aventure scientifique au pays des matériaux ténébrescents. Au delà des connaissances scientifiques acquises tout au long des ces années de thèse j'ai en effet beaucoup appris sous ta supervision et espère avoir acquis un peu des tes compétences humaines (générosité, humour, patience ...), pédagogiques et bien sûr scientifiques. Merci de m'avoir aidée à progresser, de m'avoir appris tant de choses et d'avoir été patient face à mes erreurs ou errances.

Ce travail de thèse n'aurait pas été possible sans cette superbe collaboration avec l'équipe de Mika Lastusaari que je voudrais remercier pleinement. J'aimerais donc remercier Mika, mais aussi Hannah et Sami qui de par leur engouement et dynamisme m'ont presque donné envie de faire de l'expérimentale ! Rassurez-vous, rien de cela n'est prévu pour le moment, je vais rester sagement derrière mon écran mais compte bien garder contact avec le monde expérimental.

J'aimerais aussi remercier le jury de thèse que je n'ai pu malheureusment rencontrer en raison des conditions sanitaires que l'on connait. J'aurais aimé pouvoir échanger plus facilement sur ce sujet de recherche qui m'a bien occcupée pendant ces trois ans et que j'ai trouvé plus qu'intéressant. Merci aux rapporteurs, Ilaria Ciofini et Denis Jacquemin pour leurs commentaires et remarques constructifs ainsi que leurs questions lors de la soutenance qui m'ont permi d'approfondir encore un peu plus mon sujet. Merci aussi aux examinateurs Mariachiara Pastore, Elise Dumont et Mika Lastusaari qui ont complété et poussé la discussion encore un peu plus loin dans des domaines qui je l'espère me deviendront plus familers avec l'expérience.

Il est maintenant temps de remercier le laboratoire de chimie de l'ENS de Lyon, tous les collègues permanents et non permanents avec lesquels j'ai pu échanger lors de réunions, autour d'un repas, d'un café ou juste au détour d'un couloir... Ce furent de belles discussions scientifiques bien sûr, mais aussi littéraires, footbalistiques (désolée Thibault pour cette année difficle.. XD), politiques (coucou Maxime, Martin et Vincent !) ou simplement absurdes (bon bah Vincent c'est à toi que je pense en premier pour celles-ci ha ha...). Merci à tous pour ces beaux moments qui se sont souvent prolongés hors du labo: Thibault, Vincent, Martin, Lilian, Margaux, Alix, Madleen, Loïc, Emma, Jean, Caroline, Adriaan, Léa, Marine, Antonio, Pablo, Rafaël, Chiara, Sylvain, Maxime, Geof-

frey, Vivien, Guillaume, Isis, Bénédicte, Lucille... Un merci particulier à mes différents co-bureaux qui me donnaient envie de venir au laboratoire: Antton, Massoud, Sachini, Maxime (merci de m'avoir nourrie pendant un an aussi, j'aime bien les pains au chocolat finalement, ça ressemble pas mal aux chocolatines), Agustin et "last but not least" Quentin (meilleur stagiare du jeudi, on n'oublie pas !). Merci profondément à l'équipe de chimie théorique pour les discussions scientifiques (mais pas que) : Ruben, Sarah, Paul, Maxime (encore!), Laleh, Kateryna, Nawras, Toyese, Akif, Sylvain, Rémi, Adrian, Tangui (of course !), Natacha, Jérôme, Carine, Stephan, Tao, Elise, Agilio, Pascal, David... Merci à mon deuxième bureau/salle de pause: Maëlle, Vincent, Thibault, Martin, Marine; et désolée de vous avoir tant dérangés (c'était ma stratégie pour que vous ne m'oubliez pas pour aller manger... en y réfléchissant j'ai peur que ça ait été contre productif...)
Merci à Yann pour les chouettes collaborations qui m'ont permis de conserver un semblant de ma formation en chimie organique, et surtout merci pour ton humour piquant qui permet de bien se réveiller à la pause café ! Pause café qui ne serait pas la même sans JC, Laure, Delphine, ... et Christian; mais Christian je dois surtout te remercier pour tout ton temps, ton aide et ton attention (tes cabanes en carton et tes conseils en vin !). J'espère croiser des collègues aussi gentils que toi dans le futur.

La vie au labo c'est vraiment sympa mais sans toutes ces personnes que je connais en dehors ça ne serait pas aussi bien. Et oui, encore une longue liste de belles personnes en perspectives. Je voudrais commencer par Shanis mon ami le plus cher qui m'a apporté tellement de belles choses (au sens figuré mais aussi littéral !) et Thomas (aka ThomaM, aka pcdb, aka bruce...) qui ... je ne saurais par où commencer, mais sache que mes sentiments envers toi sont univoques ! Merci à(aux) l'équipe(s) de foot: Matthieu (meilleur entraîneur ever), Claire, Lise, Emma, Adrienne, Armelle, Laure, Clara, Marie, Amélie, et toute les petites nouvelles. Le foot m'a beaucoup appris, savoir jouer en équipe mais surout savoir perdre en équipe (12-0 ça peut faire mal mais en fait ça rapporche...si si). Un immense merci (un chacun) à Gilles, Sabine, Ophélie, Paul, Pegah, Laureline, Pauline, Octavie, Mélie, Quentin, Lozéa, Coco, Chris...Les moments en votre compagnie ont toujours été superbes bien que trop courts.

Et puis la familia bien sûr (ça ne s'arrête jamais...): merci donc aux parents (même lorsqu'ils partent au pôle nord à un moment incongru) pour leur soutien ainsi que leur accueil sans limite lors de mes squats chroniques à Bordeaux, on forme une sacrée belle équipe (et merci pour toutes ces bonnes pommes de l'amap quand même !) ; merci à ma soeur pour tout son soutien et tout son amour mais aussi sa pensée très fine (tu es une personne extraordinaire, à un point tel que l'on ne peut l'imaginer et qu' il faut te rencontrer pour le comprendre) ; à mon frère que j'admire énormément, pour son esprit, sa présence subtile et son humour (parfois maladroit) ; merci aux "pièces rapportées" qui enrichissent la famille (Lisa et Adri <3) et à mes petites nièces qui m'ont déjà apporté plein de belles joies: Jeanne, Camille et la petite dernière : Marilou.

Enfin, un merci tout particulier à Myriam et Noémie qui ne liront certainement jamais ces mots mais qui ont été d'un soutien incommensurable. Ainsi qu'à Victor et sa famille.

J'aurais forcément oublié des personnes... j'espère avoir eu l'opportunité de vous remercier avant. Au cas où: merci à vous ! (en plus ça rime...)

Contents

Acronyms

BSE Bethe Salpeter Equation.

BVK Born-von Karman.

CAM Coulomb Attenuated Method.

CAS Complete Active Space.

CASSCF Complete Active Space Self Consistent Field.

CB Conduction Band.

CC Coupled Cluster.

CCSD Coupled Cluster Single Double.

CI Configuration Interaction.

CIE Commision Internationale de l'Eclairage (Internartional Comission on Illumination).

CIS Configuration Interaction Single.

CISD Configuration Interaction Single Double.

CPU Central Process Unit.

CT Charge Transfer.

DFT Density Functional Theory.

DOS Density Of States.

ECM Embedded Cluster Model.

EES Electronic Excited State.

ES Excited State.

FC Franck-Condon.

FWHM Full Width Half Maximum.

GGA Generalized Gradient Approximation.

GS Ground State.

HF Hartree-Fock.

HK Hohenberg and Kohn.

HOMO Highest Occupied Molecular Orbital.

IBZ Irreducible Brillouin Zone.

IR Irreducible Representation.

IVCT Inter Valence Charge Transfer.

KS Kohn Sham.

LC Long-range Corrected.

LDA Local Density Approximation.

LR-TD-DFT Linear Response Time Dependant Density Functional Theory.

LUMO Lowest Unoccupied Molecular Orbital.

MAE Mean Average Error.

MCM Molecular Cluster Model.

MM Molecular Mechanics.

MSE Mean Signed Error.

NVM Normal Vibration Mode.

PBC Periodic Boundary Conditions.

PC Photochromism.

PCM Polarizable Continuum Model.

PDOS Projected Density Of States.

PeL Persistent Luminescence.

PES Potential Energy Surface.

QM Quantum Mechanics.

RSH Range Separated Hybrid.

SAC Symmetry Adapted Cluster.

SCF Self Consistent Field.

SCM Supercell Model.

TD-DFT Time Dependant Density Functional Theory.

TDA Tamm-Dancoff Approximation.

TMO Transition Metal Oxide.

UV Ultra Violet.

VB Valence Band.

XANES X-ray Absorption Near Edge Spectroscopy.

XPS X-ray Photoelectron Spectroscopy.

XRD X-Ray Diffraction.

XRF X-Ray Fluorescence.

ZPE Zero Point Energy.

List of Figures

List of Tables

CHAPTER I

Introduction: Tenebrescent minerals

Come forth into the light of things, let
Nature be your teacher

William Wordsworth.

Nature is truly an inspiration in many research fields, and many great inventions come from a thorough observation of it. There exists a long list of such examples of biomimetism, however Nature still retains much of its mystery, and one can not even imagine the vastness of it.

In this PhD project we are more precisely interested in processes involving light-matter interactions, that is photophysics or photochemistry.[1] Since the main source of energy on Earth comes from the sun light, many animal and vegetal species have developped, during the course of their evolution, processes to harvest and transform light into other forms of energy. Here, the photosynthesis comes in mind as a beautiful illustration of complexicity and efficiency in light harvesting. One can also think about the retinal/rhodopsin photoswitch at the basis of the vision process.[2] A priori less known but no less important, the properties of minerals with regard to light are subjects of investigation, both for the knowledge itself and for the new applications that would, hopefully, arise from this knowledge. In this project we are particularly interested in some natural minerals that show **tenebrescence**.

This chapter is devoted to the introduction of the tenebrescence phenomenon, which to summarize is the "ability" for a mineral to change colour under certain conditions, that is photochromism (PC). A brief introduction on the origin of colour in minerals (I.1) will be given before introducing in more details the notion of tenebrescence (I.2). In

that section a subsection is specifically devoted to inorganic photochromic compounds to which belong the tenebrescent minerals (I.2.2). Finally, a section presents the special case of photochromism in the most studied tenebrescent mineral: sodalite (I.3), followed by a new section aiming at introducing other naturally tenebrescent minerals: tugtupite and marialite (I.4). After this contextual introduction of the project, the last part of this chapter will give the organisation of the manuscript and present the overall aim of the project (I.5).

I.1. Colour in minerals

The colour of a mineral is one of the first, if not the first, physical characteristic we see by looking at it. There is a wide variety of minerals that present different colours. In Figure I.1 are presented some examples of natural minerals such as fluorite (CaF_2, Figure I.1b), franckeite ($Pb_5FeSn_3Sb_2S_{14}$, Figure I.1d), or opal ($SiO_2 \cdot nH_2O$, Figure I.1i).

(a) Amethyst (b) Fluorite (c) Blue diamond

(d) Franckeite (e) Pyrite (f) Iron oxide

(g) Moonstone (h) Chalcopyrite (i) Opal

Figure I.1: Examples of colours in minerals.

The origin of the colour in these compounds is not unique. We can then classify them in three main groups:

1. Band-gap absorption of the pristine bulk in the visible range (*e.g.* semi-conductors such as franckeite, pyrite, or iron oxide);

2. Presence of impurities (*e.g.* point defects in crystals such as amethyst, fluorite or blue diamond);

3. Physical explanation: scattering (*e.g.* moonstone), diffraction or interference (*e.g.* chalcopyrite, opal).

For most of them (groups 1 and 2) it is due to an absorption process in the visible range but related to their nature as solids.[3]
In the first groups, the colour is explained by the band structure of solids. The electronic states of a solid are indeed described by the band theory (cf. section II.1.2.2.d for more details). Semi-conductors, such as iron oxide Fe_2O_3 that has a band gap around 2.2 eV ($\approx$ 564 nm), will absorb in the visible range giving the colour to the material, here reddish.

However, in this work we are interested in some natural minerals, crystals, that are insulators so that the energy required to send an electron from the valence band (VB) to the conduction band (CB) is not in the range of energy covered by visible light (1.8-3.2 eV *e.g.* 390-700 nm). In that case, group 2, the colour is explained by some defects (*e.g.* vacancy) in their structure, and/or presence of substitutional or interstitial impurities.[4] This will obviously modify the electronic structure of the material, with the apparition of new electronic states in the band gap, hence its interaction with light.

(a) ruby

(b) emerald

Figure I.2: Different colours due to the same impurity, a Cr^{3+} ion, in a different environment. The ion is located in an octahedral crystal field in both cases, but the lattice parameters are not the same.

Impurities in the crystallographic structure can directly absorb in the visible range due to their electronic configuration. It is the case of a trapped electron in a vacancy, called F-center (cf. section I.2.2), and the reason why, when a mineral is naturally or artificially doped with metal ions dispersed in its structure, it often presents a nice colour. One can think of ruby, a corundum (Al_2O_3) mineral doped with trivalent chromium ions (Cr^{3+}) (cf. Figure I.2a).[5] Here crystal field theory, represented in Figure I.3, allows us to understand the removing of degeneracy of defect's electronic levels of energy in a

h!]

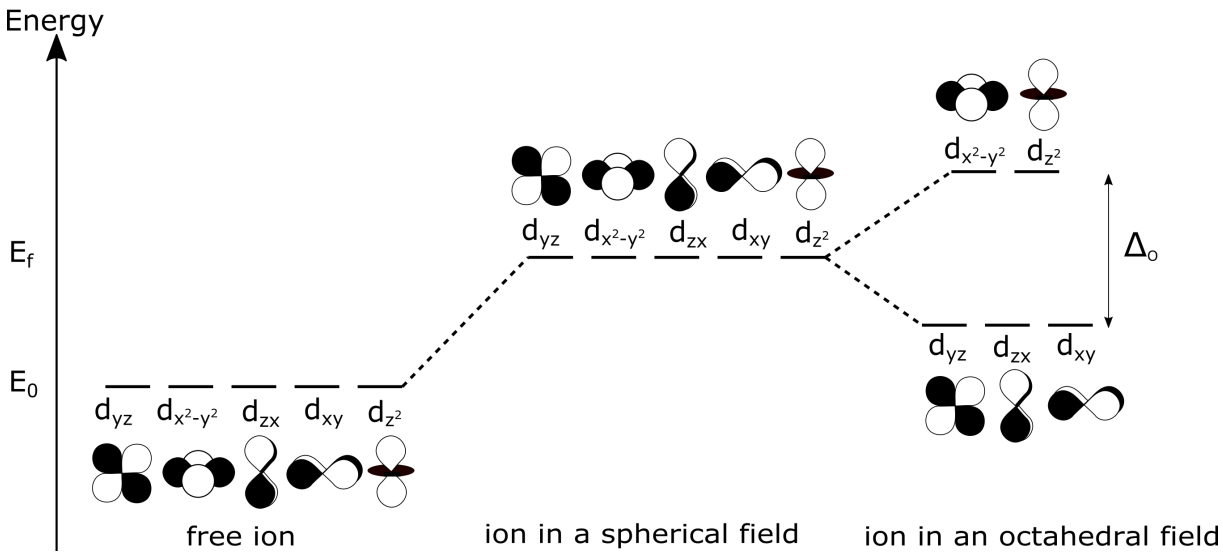

Figure I.3: Illustration of the effect of crystal field in an octahedral environment

particular octahedral environment, as is the case for Cr^{3+} in ruby. The possibility of absorption in the visible range depends then on the orbitals occupancy and their difference in energy Δ_O. The existence of such particular environments in these minerals is made possible by another property of crystals we have to introduce, although apparent: their crystallographic structure. Indeed, they present an ordered arrangement of their atoms that is periodically repeated in space. This confers them some properties of symmetry, from which we can classify them in different space groups. Apart from the symmetry, the nature of the environment (i.e. type of atoms, distance to the neighbouring atoms, lattice parameters) surrounding the metal ion will impact on the strength of the field felt by the ion, and so on Δ_O. This explains the difference of colour between ruby and emerald (cf. Figure I.2) in which the same ion, Cr^{3+}, in a similar octahedral environment, will absorb at a different wavelength.

There can also be phenomena of interaction between different impurities leading among others to the formation of the aforementioned F-centers. Also mentionable is charge transfer transition between two impurities differing only by their valence, leading to the specific intervalence charge transfer, as it is the case for cordierite (cf. VII). Here, a colour will appear if the process requires an energy in between 1.8 and 3.2 eV.

However, even for well-known materials, such as amethyst, the origin of the colour is still controversial.[6] That is also the case for naturally tenebrescent minerals, such as sodalite, that not only present a nice colour but can experience a change of their colour!

I.2. Photochromism/Tenebrescence

The variety of colours in minerals is captivating, but even more would be minerals changing colour: tenebrescent minerals.

I.2.1. Presentation of the phenomenon

I.2.1.1. A brief history

The word tenebrescence is a contraction of two words: tenebrae (darkness) and luminescence. This geological term refers to the luminescence phenomenon of reversible colour change in some materials. In other words, it is equivalent to the concept of reversible photochromism (more frequently used in chemistry). The way to get to a clear definition of photochromism was, if not rough, not straightforward either.
The term photochromism first appeared in 1867 in M. Fritsche work on tetracene molecules who observed a change in their colour under visible light, and a return back to the first colour after heating .[7] At the end of the XIXth century, Phipson observed what he called a "curious actinic phenomenon" on painting containing zinc turning black under visible light to the great hardship of the painting manufacturer[8, 9]. Later, Marckwald, who was investigating the behaviour of some naphthyridine and naphthalenone in light, called the same observed phenomenon "phototropy".[10, 11] Following his work, this "phototropy" was reported for different systems, organic and inorganic ones.[9, 12, 13] Hirshbeg, in 1950, gave a partial definition of the phenomenon and called it photochromism (from the greek words: $\phi\omega\zeta$ = light and $\chi\rho\omega\mu\alpha$ = colour).[14, 15] The word phototropy was still used after that work even if "photochromism" progressively replaced it.

I.2.1.2. Definition and examples of photochromic compounds

Nowadays, it is admitted that photochromism is a transformation of a single chemical species between two isomers (A and B) having different distinguishable absorption spectra, induced in one or both direction by an electromagnetic radiation (cf. Equation I.1).[16] If the process is reversible we qualify it at reversible photochromism, even if it is often omitted.

$$A(\lambda_1) \underset{h\nu_2}{\overset{h\nu_1}{\rightleftharpoons}} B(\lambda_2) \tag{I.1}$$

In order to illustrate the phenomenon of photochromism with a simple example, let us consider the 4-butyl-4'-methoxyazobenzene molecule (cf. Figure I.4), which can undergo a trans-cis isomerisation under UV light. The two isomers have different absorption spectra (cf. Figure I.4b), which gives them different colours. The mechanism is reversible (cf. Figure I.4a); by heating the cis isomer with enough energy, it can go back to its more

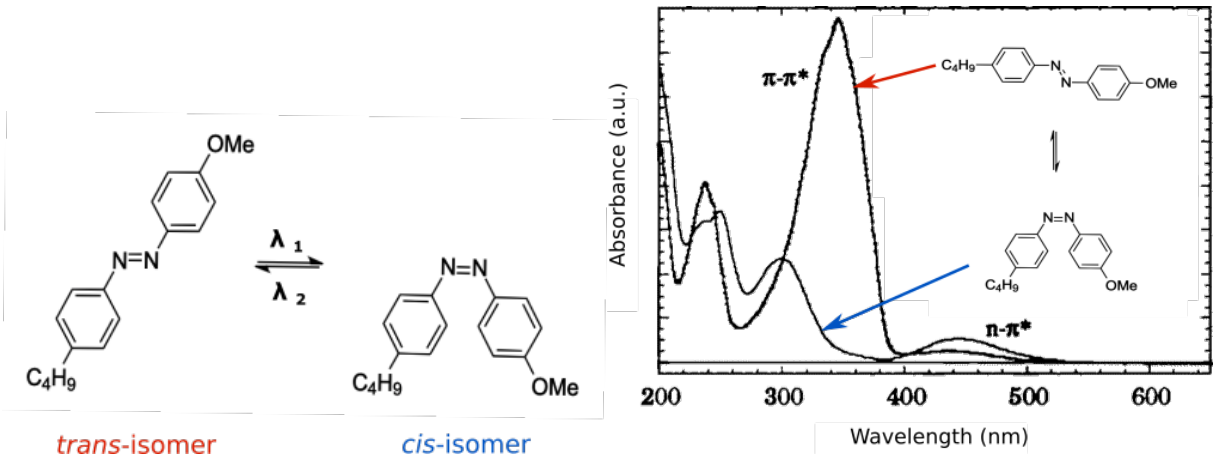

(a) (b)

Figure I.4: (a) *trans-cis* isomerization of the 4-butyl-4'-methoxyazobenzene, (b) Absorpion spectra of the two species.[17]

stable trans-configuration. The cis-configuration is metastable.

I.2.1.3. Prevalence of organic photochromsim

Contrary to inorganic photochromism (cf. section I.2.2), organic one has rapidly become a very attractive line of research from the 1960's along with the development of analytical methods.

The family of azobenzene molecules for instance, such as 4-butyl-4'-methoxyazobenzene (cf. section I.2.1.2), has been studied a lot for their property of reversible photo-switches, and their are innumerable references on the subject.[18–20] Interestingly, the change of colour is not always the primordial characteristic. Much depends on the application (cf. section I.2.3), and not only the absorption spectra but also other physicochemical properties change, such as in the dielectric constant, the oxidation/reduction potential, the conductivity or the geometrical structure can be particularly interesting. [21–23]

The main investigated families of organic compounds include: spyropyrans, spyrooxazines, diarylethene (especially dithienylethene), and azobenzene (cf. Figure I.5). The "easy" adaptation of the absorption properties by addition of functional groups on the molecule during synthesis make them indeed very attractive. Both experimental and theoretical (computational) studies have been conducted. Hence, there exist significant literature on the subject and we will cite just a few, even if for each family of molecule the amount of information gathered by the scientific community is remarkable.[14, 24–29]

However, as we will see in I.2.1.4, there exist important characteristics for a photochromic compound to possess. Most of organic compounds are often presented with having the major drawback of being unstable with respect to change in temperature or humidity,[30]

which can drastically hinder the applications. In the next subsection we will actually see important parameters to be fulfilled by photochromic compounds.

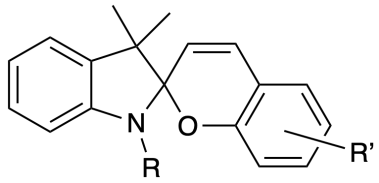

(a) spyropyran

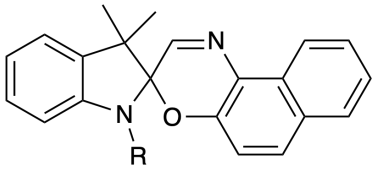

(b) spyrooxazines

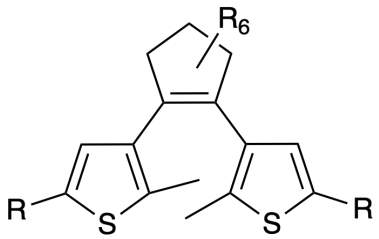

(c) dithienylethene

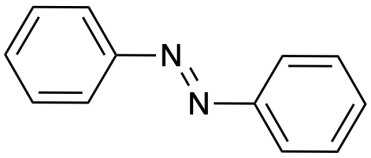

(d) azobenzene

Figure I.5: Examples of organic photochromic compounds.

I.2.1.4. Important parameters of photochromism

We have previously assert the fact that organic photochromic compounds present some limitations, this allows us to introduce important criteria photochromic compounds should met in order to be effective. First of all they should be resistant, able to perform multiple cycles between their different forms. This is the notion of reversibility or fatigue of the material. A schematic illustration of the notion of fatigue is represented in Figure I.6b. We can imagine that after some cycles, one of the isomer will experience some degradation, changing its interaction with light. The resistance must take place on different levels: temperature changes, humidity (presence of water molecules), possible oxidation (*e.g.* by air contact), side-reactions...[16]. Resistant photochromic compounds overcome more than 10^5 photochemical cycles without damage. Lots of work is done to improve the resistance, with strategies depending on the nature of the compounds.

If the material is resistant, we have then to check the relative stability of the two forms, especially the lifetime of the metastable one; that is thermodynamic aspects. Moreover, the change between the two forms should possess a high quantum yield for a good selectivity and display a rapid and effective response; that is kinetic aspects.
Depending on its spectral region of absorption (*i.e.* the energy necessary for the activation of photochromism) and the one related to the backward process the applications will not be identical. Actually, in most cases the colourless form A absorbs in the near UV or visible region, while the coloured form B absorbs in the range 450-600 nm. Then the

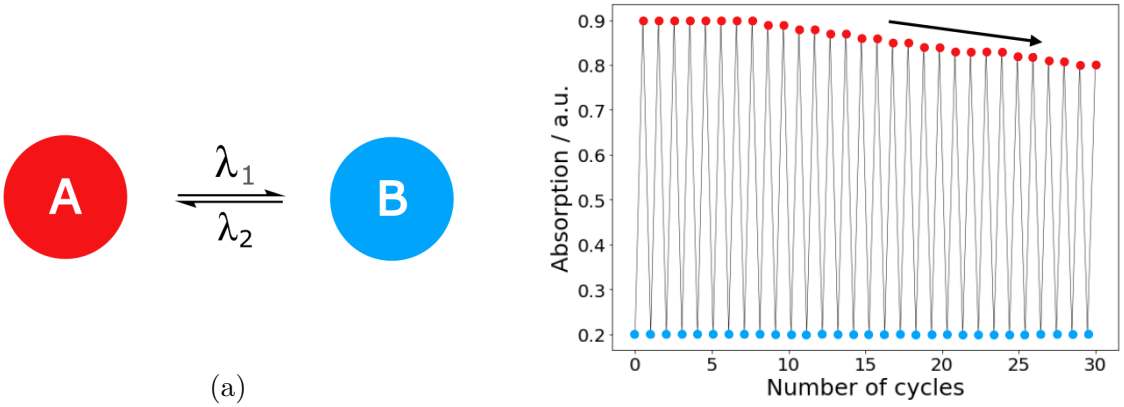

(a) (b)

Figure I.6: Illustration of the notion of fatigue. (a) Isomerization of the photochromic compound from A to B with the characteristic activation (λ_1) and bleaching (λ_2) wavelengths. (b) Schematic representation of the notion of cycles. One cycle is composed by measure of B's absorption (one blue bullet), isomerization and measure of A's absorption (one red bullet). The absorption is measured at λ_1, where compound A absorbs the most. Fatigue experienced by the photochomic system is highlighted by the black arrow which shows change in absorption properties of the second isomer.

form A is colourless and the process to regenerate it is called bleaching. If the activation energy is higher than the bleaching one we qualify the photochromism phenomenon as normal; if not it is an inverse photochromism.
Finally, the type of reaction occurring during photochromism will make possible design of smart devices in various forms: films, gels, solutions,... There exists a classification of photochromic systems according to the reaction at stake.[26, 27]

I.2.2. Photochromism in inorganic materials

I.2.2.1. Different families of inorganic photochromic compounds

Although less studied inorganic photochromism are no less interesting. The phenomenon has been observed since the XIXth century[8, 9, 31] (cf. section I.2.1.1) but most of the explanations about their mechanism came later.
In solids, PC is often attributed to the presence of F-centers (F stands for the German word "farbe" meaning colour) in the material,[32] that is a trapped electron in a vacancy that absorbs in the visible range (giving the colour to the material). Indeed, in the second half of the XXth century, observation of photochromic properties in alkali halides and alkali earth halides (*e.g.* KCl, KI, MgF_2, CaF_2) due to the formation of F-centers under light irradiation were reported. [33–35] The mechanism proposed involved the excitation of the constitutive anions followed by their de-excitation and dissociation by losing an electron. This results in the formation of vacancies in which electrons can be trapped,

forming F-centers. Investigations of the influence of the crystallographic structure, such as: cell parameters, nature of atomic composition, symmetry; provided explanations on the different parameters governing the photochromism (colouration, kinetics, etc ...)[36] An important inorganic photochromic compound is silver halide crystal. Indeed, the discovery of its properties might be the one that most speaks to people: photochromic glass lenses based on silver halides crystals in 1964 by Armistead and Stookey (it is important to note that it is not anymore the main technology used in photochromic lenses). [37] In that case the photochromism is attributed to the formation of small aggregates of silver in the material due to the presence of photo-excited electrons under light irradiation (cf. Equation I.2). These aggregates form spherical colloids that absorb widely in the visible range, making the glass darkening. It is equivalent to silver halide photography process, but in a reversible form thanks to the presence of copper that will help the re-oxidation of silver atoms (cf. Equation I.3).[38, 39]

$$\mathrm{Ag^{I}} + e^{*} \rightarrow \mathrm{Ag^{0}} \tag{I.2}$$

$$\mathrm{Ag^{0}} + \mathrm{Cu^{II}} \underset{h\nu}{\overset{\text{dark}}{\rightleftharpoons}} \mathrm{Ag^{I}} + \mathrm{Cu^{I}} \tag{I.3}$$

Then come the transition metal oxides (TMO) and their doped version: WO_3 tungsten trioxide, MoO_3 molybdenum oxide, ZnO zinc oxide, TiO_2 titanium oxide, VO_2 vanadium oxides[40]... In this family, photochromism is ascribed to the formation of colour centers (F-centers or transition metal in the appropriate oxidation state) or to oxido-reduction reactions that can lead to intervalence charge transfer (IVCT), sometimes the two models coexist.[41–43]

Let's take the example of vanadium doped TiO_2. Under light irradiation photo-generated electron-hole pairs are produced. Then, the metal ion dopant acts both as an electron and as a hole trap within the band gap of the material. The electron in the CB, will reduce the vanadium ion according to the following equation:

$$e^{-} + \mathrm{V^{5+}} \rightarrow \mathrm{V^{4+}} \quad \text{(electron trapped)} \tag{I.4}$$

Then appears a brownish violet colour which is not due to a trapped electron in a vacancy but an electron trapped by the reduce vanadium. This *d*-electron can absorbs in the visible light by populating higher in energy and empty *d* orbitals of the metal ion. The change of colour is visible in Figure I.7, adapted from the work of Songara *et al.*[43] When removing the light source, the trapped particles will slowly be released leading to the oxidation of the reduced vanadium ions. The material is bleached and take back its original colour. Here we can see that the colour is guided by the nature of the dopant

while the kinetics of bleaching is related to its relative redox potentials. Finally, the activation energy of the photochromism process is dictated by the band gap of the material.

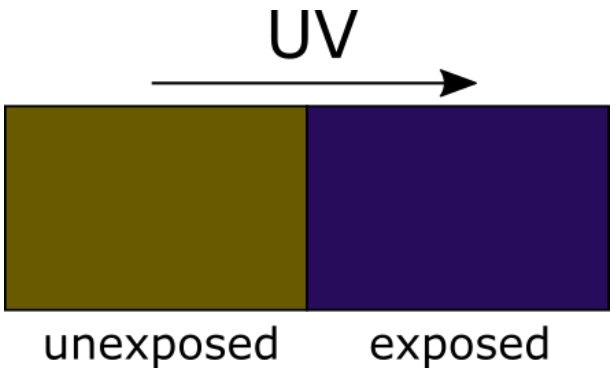

Figure I.7: Photochromism of titanium oxide doped with vanadium. On the left part the beige colour is the one observed before UV irradiation, while the right part shows the brownish violet colour the material takes after irradiation. Adapted from ref. [43]

In MoO_3, similarly photo-generated hole-electron pairs will react with adsorbed water molecules and lead to the formation of an hydrogen molybdenum bronze of formula: $H_xMo^6_{1-x}Mo^5_xO_3$. Then IVCT can occur between Mo^{5+} and Mo^{6+} leading to a blue colouration. The bleaching of the material is due to the oxidation of the bronze thanks to atmospheric oxygen.

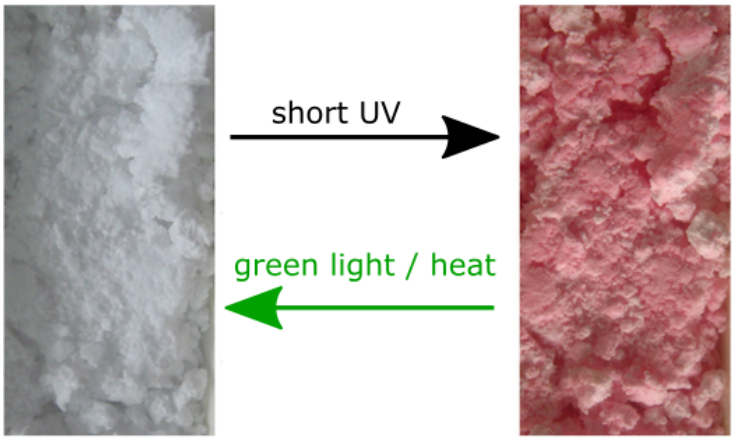

Figure I.8: Photochromism of rare-earth doped materials $Ba_5(PO_4)_3Cl:Eu^{2+}$. Under short UV irradiation the grey material becomes pink. It can goes back to its grey colour by heating or irradiating it with green light. Picture adapted from ref.[44]

We can also touch upon polyoxometalates[45, 46] and rare-earth doped minerals[44, 47, 48] which have also been reported for their photochromic properties. The mechanisms involve again the formation of trapped electrons. In the case of rare-earth doped materials such

as $Ba_5(PO_4)_3Cl:Eu^{2+}$ for instance, an electron from the $4f$ orbital of the Eu^{2+} ion is send to the empty $5d$ orbitals under UV irradiation. Since the $5d$ orbitals energy is close enough to the energy of the CB (if not at the same level), a substantial probability exists for the electron to get into it. Electrons in the CB can eventually be trapped in lattice defects and absorb in the visible light (cf. pink colouration in Figure I.8 taken from ref. [44]).

The naturally tenebrescent minerals are a last class of inorganic photochromic materials, which include sodalite[38, 49]. A section is devoted to their description (cf. section I.3).

I.2.2.2. Pro and cons of inorganic materials

Inorganic compounds offer different advantage already mentioned such as good thermal stability, good resistance to humidity changes, low fatigability, ease of synthesis... Moreover and very importantly they can easily be shaped into films, coatings,..., making their use easier.[40, 45]

However, inorganic species mentioned previously have some drawbacks. For instance MoO_3 photochromism is hampered by the presence of H_2 in the environment, making the colouration irreversible. But more generally, inorganic compounds are reported to exhibit a poor reversibility and a slow response time.[45] It is also not easy to slightly tune their parameters. In the case of rare-earth doped materials they obviously are expensive. That is why many efforts have been conducted and have generated tangible advancements in inorganic photochromism.[50–52] A solution to overcome the current difficulties faced by both type of materials is to make the best of both world by combining the two: developing hybrid organic-inorganic materials.[53, 54] Combination of single inorganic species into inorganic-inorganic hybrid materials compounds have also provided good enhancement of the photochromic properties compared with their isolated constituents.[45] The amount of possibilities meets the expectations in that field but we will not develop this topic in the present work.

I.2.3. Most current applications and future challenges

Previously, we have seen a variety of chemical compounds having photochromic properties. Depending on their inherent properties, these systems can lead to different applications. Indeed, the applications very often not only involve the change in the absorption properties of the materials, even if this characteristic in itself can lead to the development of smart devices. Along with the change of colour, the materials can experience changes in vibrational spectra, luminescence properties, conductivity, dipole moment, polarizability, refractive index...[55] Hence the number of possible applications currently known and in-

vestigated is wide, and the amount of future possibilities even wider! Here we will not be exhaustive but will try to illustrate the diversity.

Similar to the already mentioned and famous photochromic lenses exist the concept of smart windows. In our developped temperate areas, a great part of the energy consumption is related to air conditioning. Photochromic TMO glasses (or smart windows), behaving as pass-band filters can help saving energy by absorbing part or all of UV light.[53, 56] Illustration of the device is shown in Figure I.9 adapted from the work of Pardo *et al.*[53]

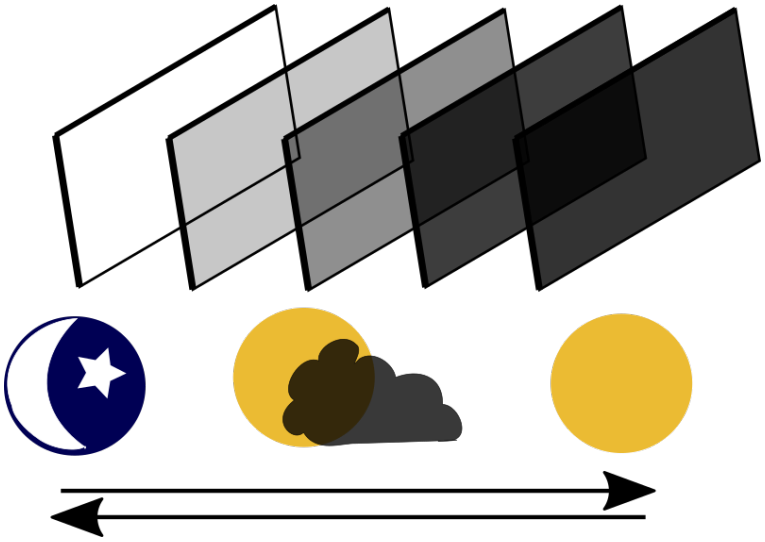

Figure I.9: Illustration of photochromic smart windows. They darken under UV light and can go back to their initial hue when the light intensity decreases.

Another challenge in our societies is health, in particular the growing amount of cancers. Being able to deliver medicines in some specific areas in order to kill only the cancer cells is crucial both for efficiency and care of the patients. In combination with technical advances allowing high precision, photochromic compounds that can be switch on with light and fix to a specific site "on demand" would elegantly tackle this challenge. Here the change of colour is not useful but different fluorescence properties of the two isomers could help imaging the process for more efficiency. Some work remain to be done to tune the activation energy in order not to be too high or be absorb by the biological tissues. The compounds should not be toxic too. An illustration of this concept based on the isomerization of an N-N moiety can be seen in Figure I.10.

Photochromic compounds can also be used for the control and measurement of specific radiation intensity (*e.g.* the ones that take part in the change between two isomers). On the same topic, this is particularly useful when the device is selective towards UVC light

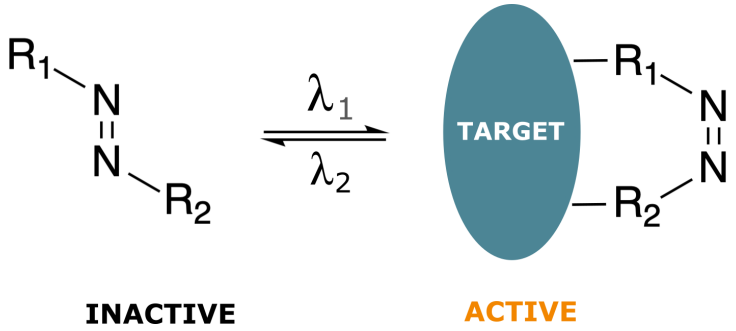

Figure I.10: Illustration of the concept of photoswitchable drugs. When irradiated with λ_1 wavelength, isomerization towards the less stable form occurs leading to interaction with target sites in the cell. The compound can be turned "off" thanks to irradiation with λ_1 wavelength.

(*e.g.* short wavelength: 100 to 280 nm), since these radiations are known to cause skin cancers.[40] In Figure I.11 you can see photochromic sodalite used as efficient solar UV index. Being able to tune the range of energy the material will respond to will allow to develop UV sensors. Industrial development for accessible portable use has not been fulfilled yet.

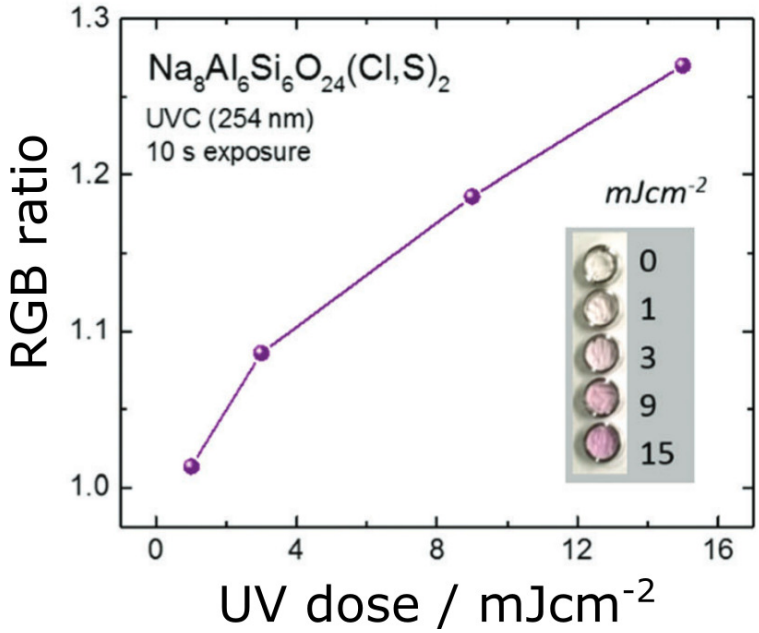

Figure I.11: UVC dose detected with sodalite minerals .The RGB ratios were obtained from the photos shown in the inset[57]

Apart from this famous application, photochromic compounds have been reported as optical sensors[58], chemical sensors[59], solar energy converters[21, 60], information imaging and storage devices[61], holographic devices[55, 62], catalytic devices, self cleaning and antifogging surfaces[63], optical memories[64, 65], photo-switchable drugs[66, 67], molec-

ular machines[51, 61], bio-imaging and other medical devices[67],...

More generally knowing the mechanism of photochromism at stake and the characteristic of the material, is paramount for future applications. If the characteristics do not meet the expectations, being able to tune some of the fundamentals parameters of the material can also prove very useful. A lot of work has already been done but much remains or is currently ongoing.

I.3. The tenebrescence in sodalite material

We have previously introduced the concepts of tenebrescence and photochromism, and the challenges and applications arising therefrom. Finally, particular attention shall be drawn onto naturally-photochromic inorganic compounds such as sodalite, which are easy to synthesize, stable, affordable and present a very good reversibility. This gives cause for the investigation of their photochromic properties. This section focus on the photochromism of the particularly fascinating sodalite material.

I.3.1. Presentation of sodalite

The sodalite mineral was first discovered in the Ilímaussaq Alkaline Complex, a famous place in Greenland in the geological community. The discoverer, Karl Ludwig Giesecke, a mineral dealer of that time, managed to bring it to the continent after several incidents due to Napoleonic war as the backdrop.[68] This mineral eventually ended up in Thomas Thomson's hands, a chemist who is the first one to identify it as a new mineral. He named it sodalite on the grounds of it high sodium content.[69] Greenland is not the only part of the world where one can find sodalite, well-developped crystals can be found in Canada, Brazil and Afghanistan.[70–72]

The first official record was found in 1834[73], and almost one century later the crystal structure was determined by Frans Maurits Jaeger. [74, 75]. Sodalite, of general formula $Na_8(SiAlO_4)_6Cl_2$, is an aluminosilicate that crystallizes in the cubic space group $P\bar{4}3n$. Its structure can be seen as a Russian doll with a β-cage, surrounding a sodium tetrahedron (yellow in Figure I.12) in which is included a chloride anion (Cl^-, green in Figure I.12). The β-cage is typical of sodalite mineral and has a cubo-octahedral structure made by the connection of four-membered and six-membered rings of corner-shared tetrahedra of alternating[76] SiO_4 and AlO_4. In Figure I.12, the β-cage appears blue with navy blue tetrahedra corresponding to SiO_4, and cyan ones corresponding to AlO_4. The repetition of this characteristic β-cage in all three directions of space (cf. Figure I.13b) makes the

crystallographic structure of the material. The unit cell axis length is usually referred to be 8.85 Å, as measured on a natural mineral from Canada.[77]

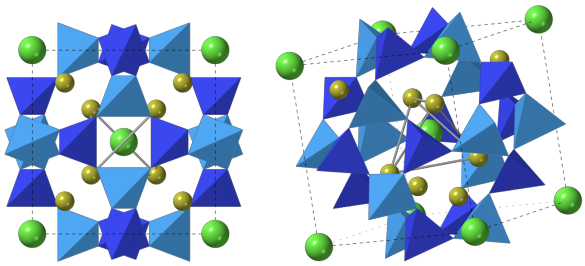

Figure I.12: Two different views of the primitive cell of sodalite mineral. Chloride anion are represented in green and sodium cation in yellow. The blue and cyan tetrahedra represent SiO_4 and AlO_4 respectively, and form the β-cage structure. Oxygen atoms are not explicitly represented.

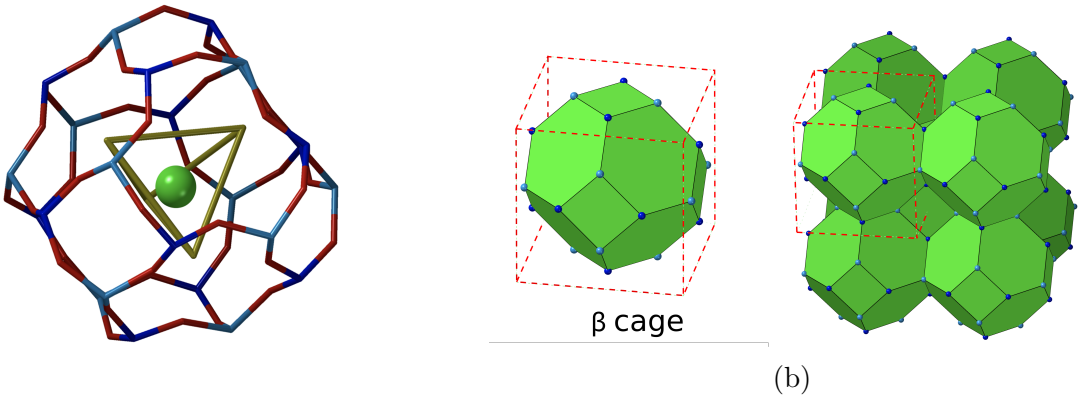

(a) (b)

Figure I.13: (a) Skeleton of the sodalite typical structure with the β-cage made of Si (blue), Al (cyan) and O (red) atoms, surrounding the sodium tetrahedron (yellow) in which lies a Cl^- anion (green). (b) Representation of the periodic structure of the material made by the repetition of β-cages (green cubo octahedral structure) in all three direction. Red dotted lines define the unit cell of the structure.

The potential of substitution is quite high[78] which is why there are several members of the sodalite group, of which the main ones are: sodalite, nosean ($Na_8Al_6Si_6O_{24}(SO_4)$), haüyne ($Na_6Ca_2Al_6Si_6O_{24}(SO_4)_2$), lazurite ($(Na,Ca)_8(AlSiO_4)_6(SO_4,S,Cl,OH)_2$), or tugtupite ($Na_8Al_2Be_2Si_8O_{24}Cl_2$). Only sodalite and tugtupite (cf. I.4.1) are known to be tenebrescent.

Actually, these minerals can be prepared in a lab[79], with the possibility to tune the composition. In Chapter IV we will show some results related to atomic substitution in the structure, but we can already highlight here the works done in the 2000's in particular by Weller and co-workers. They investigated the effects of chemical modification in the β-cage framework[80] or in the tetrahedron of sodium[81]. With the complementary work

of Zahoransky,[82] these studies confirm the impact of the composition on the spectroscopic properties of this family of minerals, especially the possibility to tune the colour the material will get under irradiation.

I.3.2. The mechanism of tenebrescence in sodalite

As previously mentioned, sodalite can undergo a change of colour under light irradiation, going from colourless to purple (cf. Figure I.14). To be more precise, the process requires energy in the UV range. This tenebrescent property leads to some publications from the 1950's to the 1970's[83–85]. At this time, the material was named hackmanite (after a Finnish geologist, Victor Hackman) and qualified as tenebrescent sodalite. Even if the term "hackmanite" is not considered as a relevant designation anymore since sodalite and hackmanite are the same mineral, it is still used to characterized the tenebrescent variety of sodalite.

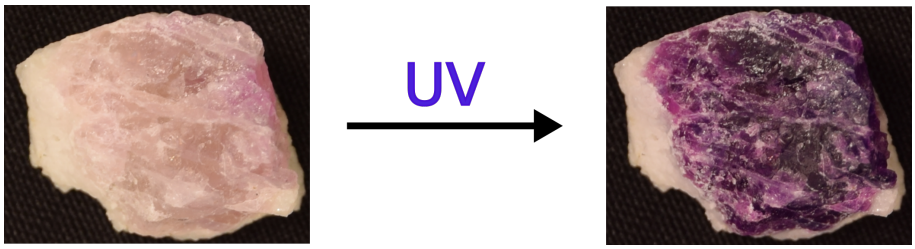

Figure I.14: Colouration of tenebrescent sodalite under UV light irradiation. It goes from colourless (left) to purple (right).

In 1967, Hodgson *et al.*[86], through electron spin resonance investigations, have shown that the center responsible for the colouration of the material was a trapped electron. In this study they also offered the hypothesis of the origin of the electron being a sulfur anion: the disulfide anion S_2^{2-}; hypothesis also supported by Mark Weller's team[87]. Actually the precise nature of the impurity was, until recently, a discussion topic.[88] Anyway, the presence of sulfur impurities in the mineral composition was nonetheless shown to be necessary in order to observe photochromism[89]. Nowadays, thanks to both experimental and computational studies[57, 90], the mechanism has been unravelled and S_2^{2-} has been confirmed to be the activator species of photochromism.

During the formation of the mineral, in a sulfur rich environment, S_2^{2-} impurity will substitute a chloride anion in a β-cage. Since, it has a charge of -2, another chloride anion in a nearby β-cage will not be incorporated, keeping the overall electroneutrality of the material. This is represented in Figure I.15, with in the end two modified β-cages: one containing S_2^{2-} instead of Cl^-, the other one presenting a vacancy noted V_{Cl} (*e.g.* its tetrahedron of sodium being empty).

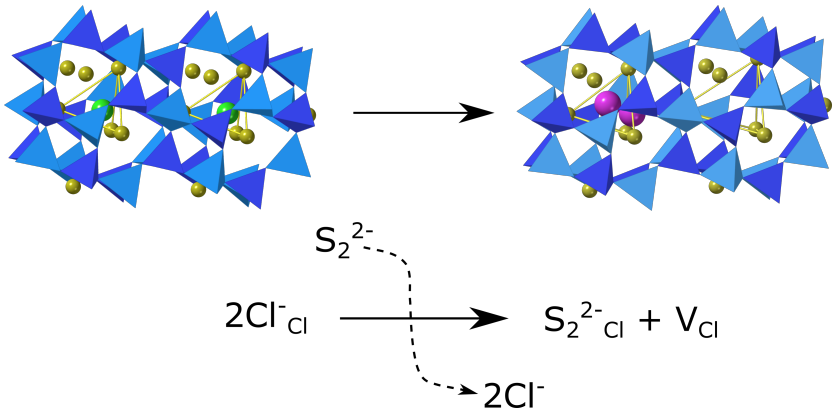

Figure I.15: Defect formation in sodalite responsible for the photochromism. (top) representation of two β-cages before and after substitution of two chloride anions (green) by the sulfur impurity (S_2^{2-}, purple). (bottom) Equation of the reaction at stake. The overall electroneutrality of the crystal is kept during the process, and a chloride vacancy V_{Cl} is created.

The different defects described will now take part in the photochromism phenomenon. The process can be divided into three steps for a better understanding:

1. Activation.
   The activation consists in a direct through space electron transfer from a disulfide anion, S_2^{2-}, towards a chloride vacancy, V_{Cl}, leading to the trapping of an electron (cf. Equation IV.1). This is the step requiring UV light.

$$S_2^{2-} + V_{Cl} \rightarrow S_2^{-} + V_{Cl}^{-} \tag{I.5}$$

2. Absorption.
   This electron, called F-center, is trapped in the tetrahedral box made by the sodium atoms which gives it quantified level of energy allowing an absorption in the visible range. This absorption explains the nice purple colour of the material (cf. Figure I.14).

3. Bleaching (or deactivation).
   Even if there was some relaxation of geometry after the charge transfer, the trapped electron is in a metastable state, but stable enough so that we can observe the colour up to few hours. By absorbing light in the visible range or under heating, it will reversibly go back onto the sulfur species, and the material will bleach (*i.e.* loss of colour).

The overall mechanism, summarized in Figure I.16, has a very good reversibility with no fatigue reported unless the material was exposed to very high frequency irradiations or

temperatures.
An important aspect of the tenebrescent process is the structural change happening inside the material on which we will discuss in more details in Chapter V. These changes were partially highlighted for the first time thanks to neutron diffraction.[87]

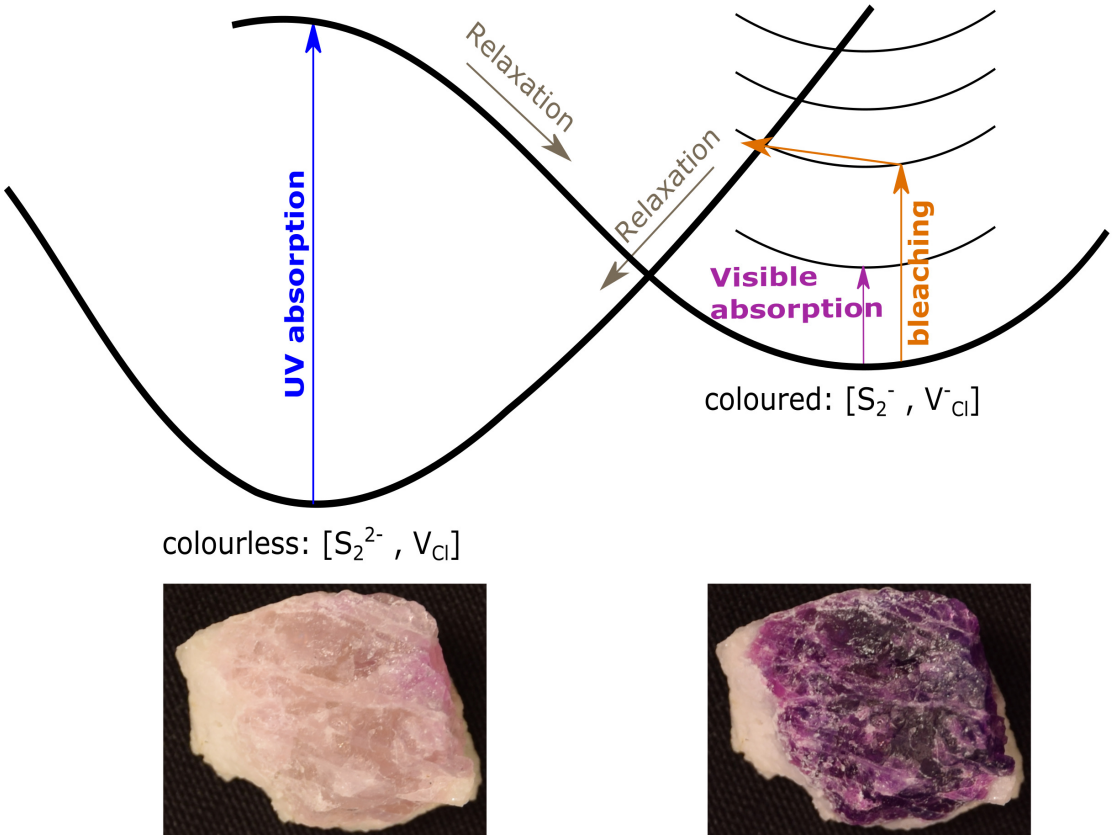

Figure I.16: Mechanism of tenebrescence in sodalite. Under UV absorption (blue arrow), an electron from the sulfur impurity is excited and send to a nearby vacancy. After relaxation this state with the trapped electron becomes metastable. The trapped electron has quantified levels of energy and can absorb light in the visible range giving the colour to the purple colour material. The system can go back to its initial state (bleaching, orange arrow) under visible light irradiation or by heating the material.

I.3.3. Other luminescence properties of sodalite

It is interesting to note that sodalite type minerals have more to show than tenebrescence in terms of spectroscopic properties.
Known for a long time[78, 83] is the fluorescence property of tenebrescent sodalites under UV excitation (365nm). The typical orange fluorescence is characteristic of the S_2^- emission (cf. Figure I.17b).[91] Blue, reddish and yellow luminescence were also reported and attributed to some defects in the composition of the material.[68, 92]

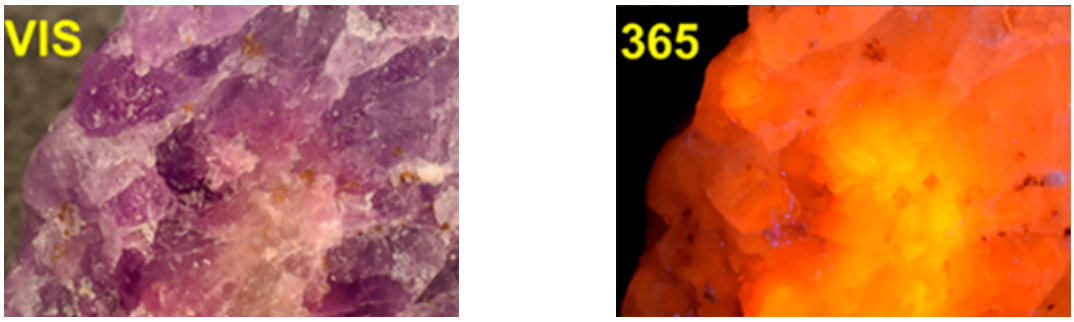

(a) (b)

Figure I.17: (a) Coloured form of a tenebrescent sodalite mineral. (b) Orange fluorescence of the same mineral after UV irradiation (365 nm).[93]

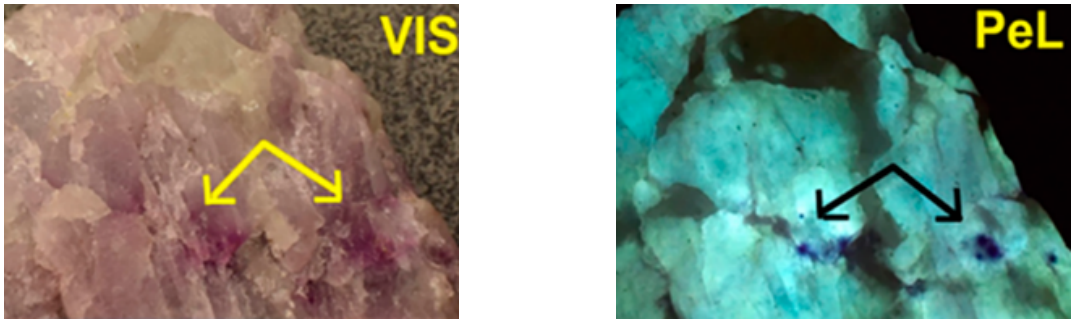

(a) (b)

Figure I.18: (a) Coloured form of a tenebrescent sodalite mineral. (b) Persistent luminescence of the same mineral after UV irradiation (275 nm).[93]

Another property of sodalite mineral is persistent luminescence (PeL), that is the natural "glow-in-the-dark" phenomenon you can observe on many self-lit emergency exit signs[93]. It happens after UV exposition of the material and give this teal glow one can see in Figure I.18b. The phenomenon is related to the presence of other type of defects in the material: titanium impurities (Ti^{3+}) and oxygen vacancies (V_O). The black arrows, in Figure I.18b indicate spots where the PeL is weak and similar yellow arrows indicate a strong PC in Figure I.18a. This suggests an apparent competition between the two phenomena. Some explanation about it can be found in section VI.2.3.3, along with the detailed PeL mechanism occuring in sodalite.

I.4. Other naturally tenebrescent aluminosilicate materials

I.4.1. Tugtupite

Alike sodalite, tugtupite is an aluminosilicate of formula $Na_8Al_2Be_2Si_8O_{24}Cl_2$.[68] It was discovered in 1957 in Tugtup Agatakorfia region in Greenland where it is far from scarce, hence its name.

Tugtupite is one of the variation of the sodalite structure with the substitution of some aluminium atoms by beryllium or silicon ones. This entails a drop of symmetry in comparison with sodalite, with tugtupite belonging to the tetragonal space group $I\bar{4}$ (space group number 82). The unit cell is presented in Figure I.19 with two different views. Beryllium are surrounded by oxygen atoms (not shown) forming (pale green) tetrahedra. The colour for the other atoms are similar to the ones used for sodalite unit cell (cf. Figure I.12).

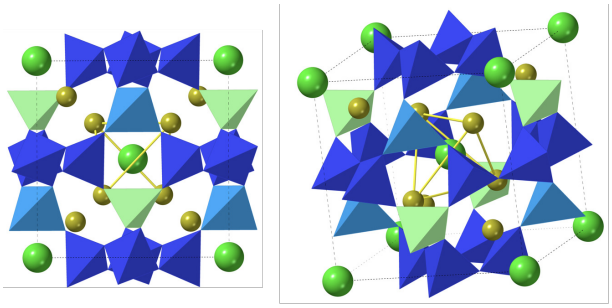

Figure I.19: Two different views of the primitive cell of tugtupite mineral. Chloride anion are represented in green and sodium cation in yellow. The blue, pale green and cyan tetrahedra represent SiO_4, BeO_4 and AlO_4 respectively, and form the β-cage structure. Oxygen atoms are not explicitly represented.

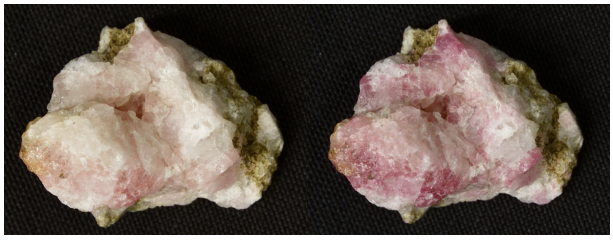

Figure I.20: Colouration of tenebrescent tugtupite under UV light irradiation. It goes from colourless (left) to red (right).

This mineral although less studied, is also naturally tenebrescent, presenting a reddish

coloured form. In Figure I.20; one can see on the left part the mineral before UV irradiation and on the right one the mineral after UV irradiation.

I.4.2. Marialite

Marialite is one of the end-members of the solid solution series of scapolite,[94] identified in 1866 by G. von Rath who named it marialite after the name of its wife Maria Rosa. It is an aluminosilicate with formula being $Na_4(Al_3Si_9O_{24})Cl$ and space group number 87 (I4/m). The main difference with sodalite mineral, along with the proportionally higher amount of oxygen and the different Al/Si ratio, is the change in the 3D structure. Indeed, the chloride anion, is located inside a square of sodium and no longer a tetrahedron. Moreover, the β-cage has an ellipsoid shape (cf. Figure I.21) and is flattened in comparison with the cubo-octahedral one of sodalite.

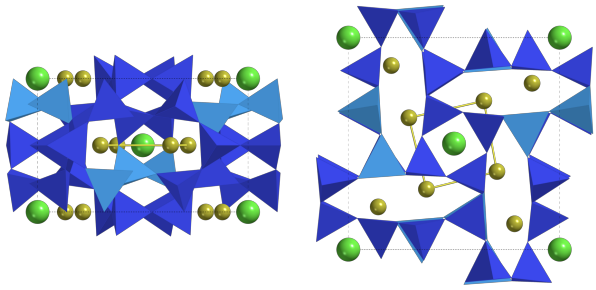

Figure I.21: Two different views of the primitive cell of marialite mineral. Chloride anion are represented in green and sodium cation in yellow. The blue and cyan tetrahedra represent SiO_4 and AlO_4 respectively, and form the flatten β-cage structure. Oxygen atoms are not explicitely represented.

The mineral is tenebrescent. In Figure I.22, one can see the mineral before UV irradiation on the left part and after on the right part. It has a nice lapis blue coloured form and the difference of colour compared with sodalite is attributed to the change of geometry (cf. Chapter V).

Figure I.22: Colouration of tenebrescent marialite under UV light irradiation. It goes from colourless (left) to blue (right).

I.5. Organisation of the manuscript and aim of the project

Along the chapter we have put in evidence the advantages of naturally-photochromic inorganic compounds such as sodalite. They show promise due to the fact that they are easy to synthesize, stable, affordable and present a very good reversibility. Understanding the mechanism of photochromism at stake and the degrees of freedom one can play on is necessary to be able to develop new photochromic devices based on sodalite's structure.

The aim of the project is to develop a computational protocol, based on existing methodologies, to investigate the mechanism of photochromism in these tenebrescent mineral. In order to meet this challenge, we will use computational chemistry tools, but will also be provided with valuable experimental data thanks to a collaboration with Prof. Mika Lastusaari from Turku University.
The computational protocol should meet the following expectations:

- confirm current knowledge on the overall mechanism or update it;
- simulate the absorption spectrum of the colour center (F-center);
- simulate the colour of the material;
- provide an estimation of the activation and bleaching energies;
- provide an explanation of the metastability of the colour form.

Arising from that challenge is the possibility to predict photochromic properties of other materials among which never synthesized ones. Hence, qualitative and consistent results (when changing the composition and/or structure of the material) should be obtained with that protocol, hopefully at a reasonable computational cost. Definitely, the more precise will be the protocol on the estimation of the different energies, the better.

To tackle the challenge, knowledge acquired by the scientific community in theoretical and computational chemistry as well as in spectroscopy and crystallography have been used. The following chapter, Chapter II, aims at providing the mains concepts and methodologies employed along the project with their possibilities and limitations.
The study resulted in the elaboration of a methodology that will be presented in details in Chapter IV. This main chapter provides the reader with the results obtained while developing the methodology on sodalite material, along with the refinement obtained by testing it on artificial materials. It eventually brings an affordable protocol able to simulate the absorption of the F-center along with the colour of the material. Moreover, activation and

bleaching energies can be estimated. Computational details used throughout the project are all gathered in Chapter III for convenience and easier reading.
A comparative study on the three natural materials: sodalite, tugtupite and scapolite is presented in Chapter V. That hand in hand computational and experimental study allows us to study the origin of the metastabilty of the coloured forms of these minerals.
Finally, the relative simplicity of the protocol that comes with its robustness enables to simulate other luminescence properties of sodalite. This is presented in Chapter VI. The possibilities offered by the methodology are further highlighted in the Conclusion and Perspectives section, when introducing the first results of the study currently led on polychromic minerals.

References Chapter I.

[1] J. Delaire, J. Piard, R. Méallet-Renault, and G. Clavier, *Photophysique et photochimie.* edp sciences ed., **2016**.

[2] G. Wald *Nature*, vol. 219, pp. 800–807, **1968**.

[3] E. Fritsch and G. R. Rossman *Gems & Gemology*, vol. 24, no. 2, pp. 81–102, **1988**.

[4] E. Fritsch and G. R. Rossman *Gems & Gemology*, vol. 24, no. 1, pp. 3–15, **1988**.

[5] E. Fritsch, G. R. Rossman, *et al. Gems & gemology*, vol. 23, no. 3, pp. 126–139, **1987**.

[6] O. Michael, *Gems : their sources, descriptions and identification.* Butterworth-Heinemann Elsevier, 6th ed., **2006**.

[7] J. Fritsche *Comptes Rendus de l'Académie des Sciences*, vol. 69, p. 1035, **1867**.

[8] T. Phipson *Scientific American*, vol. 12, pp. 4677–4677, **1881**.

[9] L. Chalkley *Chemical Reviews*, vol. 6, no. 2, pp. 217–280, **1929**.

[10] W. Marckwald *Zeitschrift für Physikalische Chemie*, vol. 30, no. 1, pp. 140–145, **1899**.

[11] G. Scheibe and F. Feichtmayr *The Journal of Physical Chemistry*, vol. 66, no. 12, pp. 2449–2455, **1962**.

[12] A. Senier and F. G. Shepheard *Journal of the Chemical Society, Transactions*, vol. 95, pp. 1943–1955, **1909**.

[13] V. de Gaouck and R. J. W. Le Fèvre *Journal of the Chemical Society, Transactions*, pp. 1457–1465, **1939**.

[14] H. Bouas-Laurent and H. Dürr, *Photochromism : Molecules and systems.* Elsevier B.V., 2nd ed., **2003**.

[15] Y. Hirshberg *Comptes Rendus de l'Académie des Sciences*, vol. 231, no. 18, pp. 903–904, **1950**.

[16] H. Bouas-Laurent and H. Dürr *Pure and Applied Chemistry*, vol. 73, no. 4, pp. 639–665, **2001**.

[17] N. Tamai and H. Miyasaka *Chemical Reviews*, vol. 100, no. 5, pp. 1875–1890, **2000**.

[18] O. Sadovski, A. Beharry, F. Zhang, and G. Woolley *Angewandte Chemie International Edition*, vol. 48, no. 8, pp. 1484–1486, **2009**.

[19] M. Böckmann, N. L. Doltsinis, and D. Marx *Physical Review E*, vol. 78, no. 3, **2008**.

[20] A. A. Beharry and G. A. Woolley *Chemical Society Reviews*, vol. 40, no. 8, p. 4422, **2011**.

[21] L. Dong, Y. Feng, L. Wang, and W. Feng *Chemical Society Reviews*, vol. 47, no. 19, pp. 7339–7368, **2018**.

[22] Y.-B. Wei, Q. Tang, C. B. Gong, and M. H. W. Lam *Analytica Chimica Acta*, vol. 900, pp. 10–20, **2015**.

[23] M. Poutanen, O. Ikkala, and A. Priimagi *Macromolecules*, vol. 49, no. 11, pp. 4095–4101, **2016**.

[24] M. Irie *Chemical Reviews*, vol. 100, no. 5, pp. 1683–1684, **2000**.

[25] S. Kobatake and M. Irie *Annual Reports on the Progress of Chemistry - Section C*, vol. 99, no. 8, pp. 277–313, **2003**.

[26] H. Dürr *Angewandte Chemie International Edition in English*, vol. 28, no. 4, pp. 413–431, **1989**.

[27] S. Nešpůrek *International Journal of Electronics*, vol. 76, no. 5, pp. 777–786, **1994**.

[28] A. Perrier and D. Jacquemin *Tetrahedron*, vol. 73, no. 33, p. 4936–4949, **2017**.

[29] L. N. Lameijer, S. Budzak, N. A. Simeth, M. J. Hansen, B. L. Feringa, D. Jacquemin, and W. Szymanski *Angewandte Chemie*, vol. 132, no. 48, p. 21847–21854, **2020**.

[30] G. Sevez, J. Gan, S. Delbaere, G. Vermeersch, L. Sanguinet, E. Levillain, and J. L. Pozzo *Photochemical and Photobiological Sciences*, vol. 9, no. 2, pp. 131–135, **2010**.

[31] E. L. Rao, K. Varahalu, and M. V. Narasimhaswami *Nature*, vol. 124, no. 3121, p. 303–303, **1929**.

[32] D. Medved *American Mineralogist*, vol. 39, pp. 615–629, **1954**.

[33] H. N. Hersh *Physical Review*, vol. 148, no. 2, pp. 928–932, **1966**.

[34] W. A. Sibley and O. E. Facey *Physical Review*, vol. 174, no. 3, p. 1076–1082, **1968**.

[35] C. Catlow *Journal of Physics C: Solid State Physics*, vol. 12, no. 6, p. 969, **1979**.

[36] W. D. Compton *Journal de Physique Colloques*, vol. 28, no. C4, pp. 10–22, **1967**.

[37] W. H. Armistead and S. D. Stookey *Science*, vol. 144, no. 3615, pp. 150–154, **1964**.

[38] G. P. Smith *Journal of Materials Science*, vol. 2, no. 2, p. 139–152, **1967**.

[39] M. Kang, Y. Deng, O. Oderinde, F. Su, W. Ma, F. Yao, G. Fu, and Z. Zhang *Chemical Engineering Journal*, vol. 375, p. 121994, **2019**.

[40] A. B. A. Kayani, S. Kuriakose, M. Monshipouri, F. A. Khalid, S. Walia, S. Sriram, and M. Bhaskaran *Small*, vol. 2100621, pp. 1–31, **2021**.

[41] T. He and J. Yao *Journal of Photochemistry and Photobiology C: Photochemistry Reviews*, vol. 4, no. 2, p. 125–143, **2003**.

[42] T. He and J. Yao *Journal of Materials Chemistry*, vol. 17, no. 43, pp. 4547–4557, **2007**.

[43] S. Songara, M. Patra, M. Manoth, L. Saini, V. Gupta, G. Gowd, S. Vadera, and N. Kumar *Journal of Photochemistry and Photobiology A: Chemistry*, vol. 209, no. 1, p. 68–73, **2010**.

[44] G. Ju, Y. Hu, L. Chen, and X. Wang *Journal of Photochemistry and Photobiology A: Chemistry*, vol. 251, p. 100–105, **2013**.

[45] T. He and J. Yao *Progress in Materials Science*, vol. 51, no. 6, pp. 810–879, **2006**.

[46] W. Wardzynski, T. Łukasiewicz, and J. Żmija *Optics Communications*, vol. 30, no. 2, p. 203–205, **1979**.

[47] S. Cornelius, G. Colombi, F. Nafezarefi, H. Schreuders, R. Heller, F. Munnik, and B. Dam *The Journal of Physical Chemistry Letters*, vol. 10, no. 6, p. 1342–1348, **2019**.

[48] Z. Yang, J. Du, L. I. D. J. Martin, D. Van Der Heggen, and D. Poelman *Laser & Photonics Reviews*, vol. 15, no. 4, p. 2000525, **2021**.

[49] J. Armstrong and M. Weller *Dalton Transactions*, pp. 2998–3005, **2006**.

[50] J. Zhang, Q. Zou, and H. Tian *Advanced Materials*, vol. 25, no. 3, pp. 378–399, **2013**.

[51] L. Wang and Q. Li *Chemical Society Reviews*, vol. 47, no. 3, pp. 1044–1097, **2018**.

[52] W. Zou, M. Sastry, J. J. Gooding, R. Ramanathan, and V. Bansal *Advanced Materials Technologies*, vol. 5, no. 4, **2020**.

[53] R. Pardo, M. Zayat, and D. Levy *Chemical Society Reviews*, vol. 40, no. 2, p. 672, **2011**.

[54] A. Parrot, A. Bernard, A. Jacquart, S. A. Serapian, C. Bo, E. Derat, O. Oms, A. Dolbecq, A. Proust, R. Métivier, P. Mialane, and G. Izzet *Angewandte Chemie*, vol. 129, no. 17, pp. 4950–4954, **2017**.

[55] A. Bianco, S. Perissinotto, M. Garbugli, G. Lanzani, and C. Bertarelli *Laser and Photonics Reviews*, vol. 5, no. 6, pp. 711–736, **2011**.

[56] S. S. Kanu and R. Binions *Proceedings of the Royal Society A: Mathematical, Physical and Engineering Sciences*, vol. 466, no. 2113, pp. 19–44, **2010**.

[57] I. Norrbo, A. Curutchet, A. Kuusisto, J. Mäkelä, P. Laukkanen, P. Paturi, T. Laihinen, J. Sinkkonen, E. Wetterskog, F. Mamedov, *et al. Materials Horizons*, vol. 5, no. 3, pp. 569–576, **2018**.

[58] M. Qin, Y. Huang, F. Li, and Y. Song *Journal of Materials Chemistry C*, vol. 3, no. 36, pp. 9265–9275, **2015**.

[59] H. Xia, J. Li, G. Zou, Q. Zhang, and C. Jia *Journal of Materials Chemistry A*, vol. 1, no. 36, pp. 10713–10719, **2013**.

[60] M. Cacciarini, A. B. Skov, M. Jevric, A. S. Hansen, J. Elm, H. G. Kjaergaard, K. V. Mikkelsen, and M. Brøndsted Nielsen *Chemistry–A European Journal*, vol. 21, no. 20, pp. 7454–7461, **2015**.

[61] H. Nie, J. L. Self, A. S. Kuenstler, R. C. Hayward, and J. Read de Alaniz *Advanced Optical Materials*, vol. 7, no. 16, p. 1900224, **2019**.

[62] K. D. Belfield, Y. Liu, R. A. Negres, M. Fan, G. Pan, D. J. Hagan, and F. E. Hernandez *Chemistry of Materials*, vol. 14, no. 9, p. 3663–3667, **2002**.

[63] T. He and J. Yao *Journal of Materials Chemistry*, vol. 17, no. 43, pp. 4547–4557, **2007**.

[64] M. Irie *Chemical Reviews*, vol. 100, no. 5, p. 1685–1716, **2000**.

[65] L. Frolova, A. Rezvanova, B. Lukyanov, N. Sanina, P. Troshin, and S. Aldoshin *Journal of Materials Chemistry C*, vol. 3, no. 44, pp. 11675–11680, **2015**.

[66] H. Cheng, J. Yoon, and H. Tian *Coordination Chemistry Reviews*, vol. 372, p. 66–84, **2018**.

[67] Z. L. Pianowski *Chemistry–A European Journal*, vol. 25, no. 20, pp. 5128–5144, **2019**.

[68] H. Friis *Geology Today*, vol. 27, no. 5, pp. 194–198, **2011**.

[69] T. Thomson *Earth and Environmental Science Transactions of the Royal Society of Edinburgh*, vol. 6, p. 387–395, **1812**.

[70] D. Kondo and D. Beaton *Gems & Gemology*, vol. 45, no. 1, pp. 38–43, **2009**.

[71] M. Graft, G. Panczer, L. Nagli, and H. Yeates *Physics and Chemistry of Minerals*, vol. 36, no. November 1918, pp. 127–141, **2009**.

[72] A. Sidike, A. Sawuti, X. M. Wang, H. J. Zhu, S. Kobayashi, I. Kusachi, and N. Yamashita *Physics and Chemistry of Minerals*, vol. 34, no. 7, pp. 477–484, **2007**.

[73] R. Allan, *Modern Luminescence Spectroscopy of Minerals and Materials*. **1834**.

[74] F. M. Jaeger *Transactions of the Faraday Society*, vol. 25, pp. 320–345, **1929**.

[75] W. H. Baur and R. X. Fischer *Microporous and Mesoporous Materials*, vol. 116, no. 1, pp. 1 – 3, **2008**.

[76] W. Loewenstein *American Mineralogist*, vol. 39, pp. 92–96, **02 1954**.

[77] I. Hassan, S. M. Antao, and J. B. Parise *American Mineralogist*, vol. 89, no. 2-3, pp. 359–364, **2004**.

[78] M. Gaft, R. Reisfeld, and G. Panczer, *Modern luminescence spectroscopy of minerals and materials*. Springer, **2015**.

[79] J. M. Carvalho, I. Norrbo, R. A. Ando, H. F. Brito, M. C. A. Fantini, and M. Lastusaari *Chemical Communications*, vol. 54, no. 53, p. 7326–7329, **2018**.

[80] E. R. Williams, A. Simmonds, J. A. Armstrong, and M. T. Weller *Journal of Materials Chemistry*, vol. 20, no. 48, p. 10883, **2010**.

[81] G. Johnson, P. Mead, and M. Weller *Physical Chemistry Chemical Physics*, vol. 1, no. 15, pp. 3709–3714, **1999**.

[82] T. Zahoransky, H. Friis, and M. A. Marks *Physics and Chemistry of Minerals*, vol. 43, no. 7, pp. 459–480, **2016**.

[83] R. D. Kirk *American Mineralogist: Journal of Earth and Planetary Materials*, vol. 40, no. 1-2, pp. 22–31, **1955**.

[84] O. I. Lee *American Mineralogist: Journal of Earth and Planetary Materials*, vol. 21, no. 12, pp. 764–776, **1936**.

[85] H. D. Miser and J. J. Glass *American Mineralogist: Journal of Earth and Planetary Materials*, vol. 26, no. 7, pp. 437–445, **1941**.

[86] W. G. Hodgson, J. S. Brinen, and E. F. Williams *The Journal of Chemical Physics*, vol. 47, no. 10, pp. 3719–3723, **1967**.

[87] J. A. Armstrong and M. T. Weller *Chemical communications*, no. 10, pp. 1094–1096, **2006**.

[88] T. E. Warner and J. H. Andersen *Physics and Chemistry of Minerals*, vol. 39, no. 2, pp. 163–168, **2012**.

[89] I. Norrbo, P. Gluchowski, P. Paturi, J. Sinkkonen, and M. Lastusaari *Inorganic chemistry*, vol. 54, no. 16, pp. 7717–7724, **2015**.

[90] I. Norrbo, P. Gluchowski, I. Hyppanen, T. Laihinen, P. Laukkanen, J. Makela, F. Mamedov, H. S. Santos, J. Sinkkonen, M. Tuomisto, A. Viinikanoja, and M. Lastusaari *ACS Applied Materials & Interfaces*, vol. 8, no. 18, pp. 11592–11602, **2016**.

[91] A. Sidike, I. Kusachi, S. Kobayashi, K. Atobe, and N. Yamashita *Physics and Chemistry of Minerals*, vol. 35, no. 3, p. 137–145, **2008**.

[92] I. Norrbo, *Synthetic hackmanites and their optical properties - From theory to applications.* PhD thesis, University of Turku, **2019**.

[93] C. Agamah, S. Vuori, P. Colinet, I. Norrbo, J. M. de Carvalho, L. K. Okada Nakamura, J. Lindblom, L. van Goethem, A. Emmermann, T. Saarinen, T. Laihinen, E. Laakkonen, J. Lindén, J. Konu, H. Vrielinck, D. Van der Heggen, P. F. Smet, T. Le Bahers, and M. Lastusaari *Chemistry of Materials*, vol. 32, no. 20, pp. 8895–8905, **2020**.

[94] D. M. Shaw *Journal of Petrology*, vol. 1, no. 2, pp. 218–260, **1960**.

CHAPTER II

Modelling methods for spectroscopic properties of extended systems

I learned very early the difference between knowing the name of something and knowing something.

Richard P. Feynman.

This chapters aims at giving some basic insights into the theoretical concepts used in this research project. All the systems were studied in a quantum chemistry approach in which systems' states are described in terms of wavefunctions. A wavefunction $\psi(t)$, is a probability amplitude function which satisfies the normalisation condition when integrated over the entire space. By applying an operator (*e.g.* energy operator - Hamiltonian) on it, it becomes possible to derive system's properties (observables). Schrödinger's equation (cf. Equation II.1) provides a relation between a wavefunction (ψ), the Hamiltonian ($\hat{H}$) and energy (E) of a system:

$$\hat{H}\psi = E\psi \tag{II.1}$$

In the following, the Born-Oppenheimer approximation is applied so that the electrons are moving in a potential created by motionless nuclei. For the sake of simplicity the atomic units will be used (*i.e.* $\hbar = m_e = \frac{e^2}{4\pi\epsilon_0} = 1$).

Schrödinger's equation (cf. Equation II.1) exists in its time dependent and time independent forms. The chapter begins with the resolution of the latter which allows one to access stationary states of a system, hence its ground state (GS). The first section (cf.

II.1) starts with the presentation of the Hartree-Fock (HF) approximation, cornerstone of quantum chemistry, before introducing the Density Functional Theory (DFT). In the same section, a special attention will be given to DFT methods in the case of extended systems. The following section (cf. II.2) will focus on the excited states methods with a closer look on the Time Dependent Density Functional Theory (TD-DFT) used throughout this project. A third section (cf. II.3) is actually dedicated to some limitations of the latter when modelling charge transfer processes. Finally, in section II.4 we will present the model used for Embedded Cluster Model (ECM) calculations.

II.1. Ground state methods

Different methods exist to solve the famous Schrödinger's equation in its time independent form. Among *ab initio* methods many start within the Hartee-Fock approximation.

II.1.1. Hartree-Fock approximation

II.1.1.1. Hartree-Fock Hamiltonian

Let's start by writing down the expression of the time independent non-relativistic Hamiltonian $\hat{H}_0$ for a system containing N electrons (with positions $\boldsymbol{r_i}$) and N_0 nuclei (with positions $\boldsymbol{R_a}$):

$$\begin{aligned}\hat{H}_0(\boldsymbol{r_1},...,\boldsymbol{r_N}) = & \overbrace{-\frac{1}{2}\sum_{i=1}^{N}\Delta_{\boldsymbol{r_i}}}^{\text{electrons' kinetic energy}} - \underbrace{\sum_{i=1}^{N}\sum_{a=1}^{N_0}\frac{Z_a}{|\boldsymbol{R_a}-\boldsymbol{r_i}|}}_{\text{nuclei-electrons attraction}} + \overbrace{\sum_{i=1}^{N}\sum_{j=1}^{i-1}\frac{1}{|\boldsymbol{r_i}-\boldsymbol{r_j}|}}^{\text{electrons-electrons repulsion}} + \underbrace{\sum_{a=1}^{N_0}\sum_{b=1}^{a-1}\frac{Z_aZ_b}{|\boldsymbol{R_a}-\boldsymbol{R_b}|}}_{\text{nuclei-nuclei repulsion}} \\ = & \hat{T}_e + \hat{V}_{Ne} + \hat{V}_{ee} + \hat{V}_{NN}\end{aligned} \tag{II.2}$$

In this expression, the electrons' kinetic energy ($\hat{T}_e$) and the nuclei-electrons attraction ($\hat{V}_{Ne}$) are sums of mono-electronic terms, each term depending on one electron only. The nuclei-nuclei repulsion ($\hat{V}_{NN}$) that does not depend on any electron's position is a constant operator for the system. Finally, the electrons-electrons repulsion operator ($\hat{V}_{ee}$) depends on the simultaneous position of two electrons which makes the overall equation unsolvable analytically for systems with more than one electron. The Hartree-Fock (HF) approximation allows to overcome this issue by considering that each electron sees the mean-field created by all the other electrons, converting the electrons-electrons repulsion term into a mono-electronic operator and the Hamiltonian into a sum of mono-electronic

hamiltonians ($\hat{H}_0 \rightarrow \hat{\tilde{H}}_0$):

$$\hat{\tilde{H}}_0(\boldsymbol{r_1}, ..., \boldsymbol{r_N}) = \sum_{i=1}^{N} \hat{F}(\boldsymbol{r_i}) + \sum_{a=1}^{N_0} \sum_{b=1}^{a-1} \frac{Z_a Z_b}{|\boldsymbol{R_a} - \boldsymbol{R_b}|} \tag{II.3}$$

In the following, the exponent *elec* will characterized electronic Hamiltonian H^{elec} for which only electron interactions are considered and not the nuclei-nuclei repulsion term.

II.1.1.2. Fock operator

$\hat{F}(\boldsymbol{r_i})$ in Equation II.3 is called the Fock operator and is a function of its own solution; it is a self consistent problem. Let's suppose we know the exact solutions, we can introduce its eigenvectors $\chi_i(\boldsymbol{r})$, and the respective eigenvalues ϵ_i through the following equation:

$$\hat{F}(\boldsymbol{r_i})\chi_i(\boldsymbol{r}) = \epsilon_i \chi_i(\boldsymbol{r}) \tag{II.4}$$

To take into account the spin of the electron, the mono-electronic functions χ_i, called orbitals, are coupled with spin function $\zeta_s(\sigma)$ leading to the construction of spin-orbital functions $\phi_{i,s}$:

$$\phi_{i,s}(\boldsymbol{r}, \sigma) = \phi_{i,s}(\boldsymbol{x}) = \chi_i(\boldsymbol{r})\zeta_s(\sigma) \tag{II.5}$$

Then the eigenvectors of $\hat{\tilde{H}}_0$ are Slater determinants, that is products of the mono-electronic functions $\phi_{i,s}$ that satisfy anti-symmetry requirements: $|\psi_I\rangle = |\prod_{i,s} \phi_{i,s}\rangle$.

Fock operator can be decomposed into three components:

$$\hat{F} = \hat{h} + \sum_k (\hat{J}_k - \hat{K}_k) \tag{II.6}$$

$\hat{h}$ operator includes the kinetic energy and the nuclear attraction, $\hat{J}_k$ is a Coulomb operator to take into account the repulsion between one electron and the mean-field created by the other ones (cf. Equation II.8), and $\hat{K}_k$ is the exchange operator (cf. Equation II.9). The latter translates a quantum mechanical effect with no classical analog, due to the wave-like properties of electrons. The energy associated with one orbital of Fock operator can then be expressed as:

$$\epsilon_i = h_i + \sum_{k=1}^{N} J_{ik} - K_{ik} \tag{II.7}$$

with

$$\begin{cases} J_{ik} = \langle \phi_{i,s_i} | \, \hat{J}_k \, | \phi_{i,s_i} \rangle & \text{(II.8a)} \\ \langle \phi_{i,s_i} | \, \hat{J}_k \, | \phi_{j,s_j} \rangle = \int\int \dfrac{\chi_i^*(\boldsymbol{r})\chi_k^*(\boldsymbol{r'})\chi_j(\boldsymbol{r})\chi_k(\boldsymbol{r'})}{|\boldsymbol{r} - \boldsymbol{r'}|} d\boldsymbol{r} d\boldsymbol{r'} \delta_{s_i = s_j} & \text{(II.8b)} \end{cases}$$

and

$$\begin{cases} K_{ik} = \langle \phi_{i,s_i} | \hat{K}_k | \phi_{i,s_i} \rangle & \text{(II.9a)} \\ \langle \phi_{i,s_i} | \hat{K}_k | \phi_{j,s_j} \rangle = \int\int \frac{\chi_i^*(\boldsymbol{r})\chi_k^*(\boldsymbol{r'})\chi_k(\boldsymbol{r})\chi_j(\boldsymbol{r'})}{|\boldsymbol{r}-\boldsymbol{r'}|} d\boldsymbol{r}d\boldsymbol{r'}\delta_{s_i=s_j=s_k} & \text{(II.9b)} \end{cases}$$

The Ground-State (GS) $|\psi_0\rangle$ of the mean field Hamiltonian is constructed by filling the orbitals in ascending order of energy (two electrons for each, since one orbital is associated with two spin-orbitals). The energy of the GS, is the sum of the nuclei-nuclei repulsion energy and the energies ϵ_i of all occupied orbitals from which the electron-electron energy term has been substracted to avoid double counting. The variational principle ensures that the solution found self consistently is the one of minimum energy.

Variational principle: for any trial N-electron wavefunction $|\psi\rangle$ satisfying the normalization condition, the expectation value E of the Hamiltonian over this wavefunction is higher than the ground-state energy E_0,

$$E = \langle \psi | \bar{H} | \psi \rangle \geq \langle \psi_0 | \bar{H} | \psi_0 \rangle = E_0 \qquad \text{(II.10)}$$

II.1.1.3. The missing electronic correlation

While the HF formulation is nice and quite intuitive, it lacks the description of what is called electron correlation. The correlation energy is defined as the difference between the exact (non-relativistic) energy of the system, and its HF energy (calculated with a complete basis):

$$E_{\text{corr}} = E_{\text{exact}} - E_{\text{HF}} \qquad \text{(II.11)}$$

This error can be divided into what is called dynamic correlation related to the fact that each electron should instantaneously interact with every other electron and not with a mean field; and static (or non-dynamic) correlation that can be recovered by describing the electronic state with a linear combination of more than one Slater determinant. There exist different post Hartree-Fock methods aiming at recovering the correlation energy, some do a good job on the static part (*e.g.* CASSCF), other on the dynamic part (*e.g.* CCSD) while high level couple cluster methods (CCSDT(Q)) combine the best of both world (at this level of theory, the distinction between static and dynamic correlation actually breaks down). These methods, that we will briefly introduce in section II.2.4 do have limitations regarding the size of the system studied.

II.1.2. Density Functional Theory for extended systems

A popular alternative to HF is density functional theory (DFT) in which the multielectronic wavefunctions are replaced by the electron density for deriving system's properties. The computational time is equivalent to an Hartree-Fock calculation, and part of the correlation energy is recovered.

II.1.2.1. Background on DFT

In 1927[1], Thomas and Fermi introduced a mono-electronic function called electron density, a less complicated object than the wavefunction from which it is derived. The square modulus of a normalized wavefunction $|\psi(\boldsymbol{x_1}, \boldsymbol{x_2}, ..., \boldsymbol{x_N})|^2 d\boldsymbol{x_1} d\boldsymbol{x_2} ... d\boldsymbol{x_N}$ is the probability of finding simultaneously electron 1 in the volume element $d\boldsymbol{x_1}$ around $\boldsymbol{x_1}$, electron 2 in $d\boldsymbol{x_2}$ around $\boldsymbol{x_2}$, etc. The electron density is obtained by integrating $|\psi(\boldsymbol{x_1}, \boldsymbol{x_2}, ..., \boldsymbol{x_N})|$ over all variables but one (the electrons are indistinguishable):

$$n(\boldsymbol{r}) = N \int |\psi(\boldsymbol{x_1}, \boldsymbol{x_2}, ..., \boldsymbol{x_N})|^2 d\sigma d\boldsymbol{x_2} ... d\boldsymbol{x_N} \tag{II.12}$$

From this definition comes that $n(\boldsymbol{r})d\boldsymbol{r}$ is the average number of electrons in the volume $d\boldsymbol{r}$ around $\boldsymbol{r}$ and $\int n(\boldsymbol{r})d\boldsymbol{r} = N$. It is an observable related to the density operator $\hat{n}$.

II.1.2.1.a Hohenberg-Konh theorems

Density functional theory inherits deeply from the Thomas–Fermi model for the electronic structure of materials. Later, in 1965, Hohenberg and Kohn provided a strong formalism of the theory through two famous theorems.[2] First, Hohenberg and Kohn stated that for any system of interacting particles "the external potential, and hence the total energy is a unique functional of the electron density". Indeed, the density contains all the information needed to construct the electron-nuclei potential. From that follows that any property, in particular the ground-state energy, is a functional of the density.

H.K. I Theorem: Each N-electron density is the ground-state density of at most one Hamiltonian $\hat{H}[v_{ext}, N]$ where the external potential v_{ext} is determined up to an additive constant c

$$n(\boldsymbol{r}) = n'(\boldsymbol{r}) \rightarrow v_{ext}(\boldsymbol{r}) = v'_{ext}(\boldsymbol{r}) + c \tag{II.13}$$

Hence, there exists a unique functional, $F_{\mathrm{HK}}[n]$, of the density that allows to access GS's

properties.

$$\begin{aligned}\hat{H}_0^{elec}[n] &= \hat{T}_e + \hat{V}_{ee} + \hat{V}_{Ne} \\ &= F_{HK}[n] + \int v_{Ne}(\boldsymbol{r})n(\boldsymbol{r})d\boldsymbol{r}\end{aligned} \tag{II.14}$$

The second theorem brings the proof that the variatonal principle holds for this universal functional. Although we know that $F_{HK}[n]$ is unique and exists, its mathematical formulation is unfortunately unknown.

H.K. II Theorem: For any positive integer N and potential v, it exists a density functional $F_{HK}[n]$ such that $F_{HK}[n] + \int v(\boldsymbol{r})n(\boldsymbol{r})dr$ reaches its minimal value at the ground-state density of a system composed of N electrons in the potential $v(\boldsymbol{r})$. This minimum is then the ground-state energy of this system $E[v]$.

The theorems were latter generalized and extended by Levy and Lieb to the formalism currently used.[3]

II.1.2.1.b Konh-Sham method

As introduced previously, the difficulty of finding a solution to the Schrödinger's equation (cf. Equation II.2) comes from the electron-electron interactions. Based on the second Hohenberg-Kohn theorem which states that the ground-state of a system is the global minimum value of this functional, Kohn and Sham provided a way to solve the multiparticles equation.[4] The idea is to replace the system by a fictitious one of non-interacting particles through a set of orthonormal orbitals $\{\alpha_i\}$. The non-interacting kinetic functional $T_S[n]$ can be calculated exactly:

$$T_S[n] = -\frac{1}{2}\sum_i \langle\alpha_i|\,\Delta\,|\alpha_i\rangle \tag{II.15}$$

The fictitious electrons move in a modified potential such that it has the same ground state density as the real system. The overall functional is generated by adding the Hartree energy functional ($E_H[n]$), which describes the classical Coulomb interaction, and the exchange-correlation energy functional ($E_{xc}[n]$) of unknown expression to the Konh-Sham functional in the equation. Eventually, this functional $F[n]$ can be expressed as:

$$F[n] = T_S[n] + E_H[n] + E_{xc}[n] \tag{II.16}$$

And the related KS potential as:

$$v_{KS}(\boldsymbol{r}) = v_{Ne}(\boldsymbol{r}) + v_H(\boldsymbol{r}) + v_{xc}(\boldsymbol{r}) \tag{II.17}$$

The density n is obtained in the set of KS orbitals ($n(\boldsymbol{r}) = \sum_i |\alpha_i|^2$) and the ground state energy correspond to

$$\begin{aligned} E_0 &= \min_{\{\alpha_i\}} \left\{ F[n] + \int n(\boldsymbol{r}) v_{\mathrm{Ne}}(\boldsymbol{r}) d\boldsymbol{r} \right\} \\ &= \min_{\{\alpha_i\}} \left\{ T_S[n] + E_{\mathrm{H}}[n] + E_{\mathrm{xc}}[n] + \int n(\boldsymbol{r}) v_{\mathrm{Ne}}(\boldsymbol{r}) d\boldsymbol{r} \right\} \end{aligned} \tag{II.18}$$

At last, the one-electron Kohn-Sham (KS) equations (cf. Equation II.19) are solved self consistently by varying the total energy expression with respect to the orbitals.

$$\left[-\frac{1}{2}\Delta + v_{\mathrm{KS}}(\boldsymbol{r}) \right] \alpha_i(\boldsymbol{r}) = \epsilon_i^{\alpha} \alpha_i(\boldsymbol{r}) \tag{II.19}$$

ϵ_i^{α} are the energies associated with the KS orbitals. The difficulty of the method lies eventually in the determination of E_{xc} functional. Numerous approximations to the exchange-correlation energy as a functional of the spin-density have been developed and tested in order to get access to the best description possible of the interactions.

II.1.2.1.c Presentation of different families of functionals

The exact universal functional should provide a good description of any studied system, let it be a molecule, a solid, or whatever can be studied... Unfortunately, this functional is not known so that we only have approximations of it based on physical construction (*ab initio*) and/or fitted experimentally (they are classified according to it on Jacob's ladder cf. Figure II.1 [5]). Their reliability will depend on the system at stake.

The first rung of Jacob's ladder corresponds to the Local Density Approximation (LDA), for which the exchange correlation functional depends only on the electronic density:

$$E_{\mathrm{xc}}^{\mathrm{LDA}}[n(\boldsymbol{r})] = \int d\boldsymbol{r} n(\boldsymbol{r}) \varepsilon_{\mathrm{xc}}(n(\boldsymbol{r})) \tag{II.20}$$

We do not use LDA functionals (local functionals) in this work but more sophisticated ones, following the Generalized Gradient Approximation (GGA) in which the gradient of the density is considered in order to account for the non-homogeneity of the electron density:

$$E_{\mathrm{xc}}^{\mathrm{GGA}}[n(\boldsymbol{r})] = \int d\boldsymbol{r} n(\boldsymbol{r}) \varepsilon_{\mathrm{xc}}(n(\boldsymbol{r}), \nabla n(\boldsymbol{r})) \tag{II.21}$$

In this family of semi-local functionals, one can find among others, the famous PBE functional but also BP86, PW91, or else B97D functionals.
Going further, the exchange-correlation functional can be designed to take into account also the derivative of the density gradient, and a non-interacting kinetic energy density

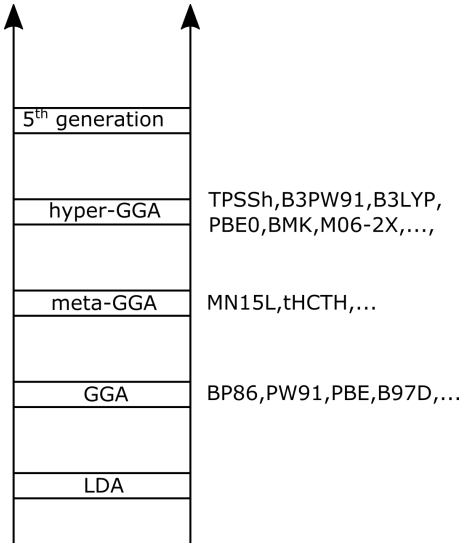

Figure II.1: Jacob's ladder with its five first rungs leading towards the theoretical universal functional. Functionals from the 2nd, 3rd and 4th generations were used in this project.

term (τ). This leads to the so called meta-GGA functionals such as tHCTH, or M06L.

$$E_{\mathrm{xc}}^{\text{meta-GGA}}[n(\boldsymbol{r})] = \int d\boldsymbol{r} n(\boldsymbol{r}) \varepsilon_{\mathrm{xc}}(n(\boldsymbol{r}), \nabla n(\boldsymbol{r}), \nabla^2 n(\boldsymbol{r}), \tau(\boldsymbol{r})) \tag{II.22}$$

A last class of functionals used in this project are the hyper-GGA, which are hybrid-GGA or hybrid meta-GGA. Indeed, if the Hartree-Fock method lacks the description of the correlation energy, it provides an exact description of the exchange energy. Hybrid functionals have been developed to make the best of both worlds, incorporating a portion of exact exchange from HF theory and completing it with either an empirical or an *ab initio* density functional. One famous example of it is the PBE0 functional that incorporates 25% of exact exchange with the remaining 75% described by the GGA PBE:

$$E_{\mathrm{xc}}^{\mathrm{PBE0}} = \frac{1}{4} E_{\mathrm{x}}^{\mathrm{HF}} + \frac{3}{4} E_{\mathrm{x}}^{\mathrm{PBE}} + E_{\mathrm{c}}^{\mathrm{PBE}} \tag{II.23}$$

During the course of this work we also used the famous semi-empirical hybrid B3LYP functional whose expression is:

$$E_{\mathrm{xc}}^{\mathrm{B3LYP}} = (1-a) E_{\mathrm{x}}^{\mathrm{VWN1}} + a E_{\mathrm{x}}^{\mathrm{HF}} + b \mathrm{B88}_{\mathrm{x}} + (1-c) E_{\mathrm{c}}^{\mathrm{VWN1}} + c E_{\mathrm{c}}^{\mathrm{LYP}} \tag{II.24}$$

with VWN1 an LDA funtional, B88 and LYP GGA functionals, and $a = 0.20$, $b = 0.72$ and $c = 0.81$ fitted parameters.

The 5th generation, in which one can find double-hybrid functionals or the generalized Random Phase Approximation, is beyond the scope of this project and will not be developped here.

II.1.2.2. The case of extended systems

For the moment we have given very general idea on DFT, but when it comes to study solids for which one cubic milimetre contains more than 10^{20} atoms, some mathematical cunning has to be used.

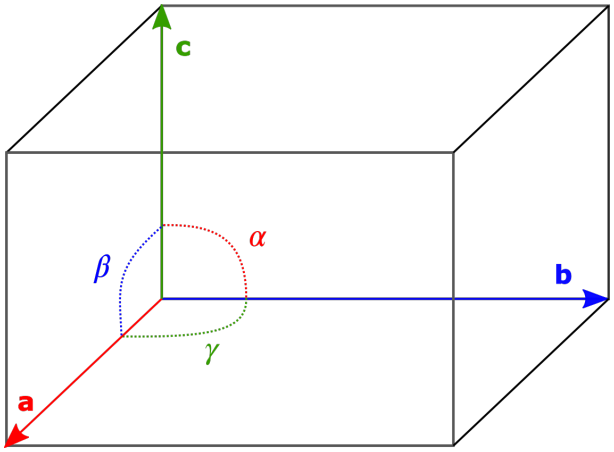

Figure II.2: Representation of a unit cell defined by its cell parameters: the three basis vectors $\boldsymbol{a}$, $\boldsymbol{b}$ and $\boldsymbol{c}$ and the asssociated angles they form two by two, α, β and γ.

In this project we are interested in crystal solids that have properties of symmetry and periodicity. Some notions specific to crystallography will be used. For instance a lattice is a collection of points repeated at intervals of length a, b and c along three non-coplanar directions. a, b and c are the lattice parameters and $\boldsymbol{a}$, $\boldsymbol{b}$ and $\boldsymbol{c}$ the associated basis vectors. The latter compose with the angles they form two by two (α, β and γ), the cell parameters that are represented in Figure II.2. The repetition of a cell in all dimensions of space, makes the crystallographic structure of a material. The minimum cell that can be used to form the structure of the material is called the primitive cell and depends on space group (symmetry) of the crystal and the type and positions of the atoms. The unit cell will be the minimal cell used for a calculation and can be equivalent to the primitive cell of the material, or an integer multiple of it for practical reasons.

II.1.2.2.a Bloch's equations

Since we are not interested in the surface effects of the materials, but their bulk properties, we can consider the solid as a perfect infinite and translational invariant crystal in which the ions are arranged in a regular periodic array (the unit cell). The problem to solve becomes the one of independent electrons in an effective periodic potential. The potential has the same periodicity as the lattice. If $\boldsymbol{a}$, $\boldsymbol{b}$ and $\boldsymbol{c}$ are the basis vectors of the unit cell

we have every lattice vector, $\boldsymbol{g}$, that is equal to:

$$\boldsymbol{g} = n_1\boldsymbol{a} + n_2\boldsymbol{b} + n_3\boldsymbol{c} \quad \text{with } \{n_1, n_2, n_3\} \in \mathbb{N} \tag{II.25}$$

and the potential has the following property:

$$v(\boldsymbol{r} - \boldsymbol{g}) = v(\boldsymbol{r}) \tag{II.26}$$

This property of the potential passes to the Hamiltonian. Bloch showed that good eigenvectors, ϕ, of the respective Schrödinger's equation must obey Bloch's theorem, that is:

$$\phi(\boldsymbol{r} + \boldsymbol{g}; \boldsymbol{k}) = \mathrm{e}^{i\boldsymbol{k}\boldsymbol{g}}\phi(\boldsymbol{r}; \boldsymbol{k}) \tag{II.27}$$

This actually implies that the wavefunctions can be chosen to have the form of a plane wave times a function (u) with the periodicity of the lattice:

$$\phi(\boldsymbol{r}; \boldsymbol{k}) = \mathrm{e}^{i\boldsymbol{k}\boldsymbol{r}}u(\boldsymbol{r}) \tag{II.28}$$

ϕ is a function of position $\boldsymbol{r}$ and wave vector $\boldsymbol{k}$, the latter labelling the different solution of Schrödinger's equation. Since ϕ verifies Bloch's theorem, it is called a Bloch function.

II.1.2.2.b Periodic Boundary Conditions and k-points

An important aspect of *in silico* studies is the necessary amount of computational time which corresponds to the central processing unit (CPU) time calculated by the computer in order to obtain the final solution. Regardless of the methodology used, as you increase the number of particles in your system, you increase the computational time in turn. Hence, you have to find the balance between the time required for your computation and the accuracy of your description. In order to consider our crystal as infinite we need a great amount of atoms, so that the surface can appropriately be neglected. However, this would be computationally expensive and still present border effects, so that another strategy is used instead: Periodic Boundary Conditions (PBC) within Born-von Karman (BVK) framework. The idea is to apply the periodicity of the material to the wavefunctions and to remove the borders of the system by connecting them mathematically. If we have a number N of unit cell in our lattice, they will form a cyclic cluster so that there is no physical effects of the boundaries and no discontinuities in the functions and:

$$\phi(x + L_a, y, z; \boldsymbol{k}) = \phi(x, y + L_b, z; \boldsymbol{k}) = \phi(x, y, z + L_c; \boldsymbol{k}) = \phi(x, y, z; \boldsymbol{k}) \tag{II.29}$$

with L_a, L_b and L_c lengths along the three basis vectors defining a supercell containing N unit cells of the crystal. If the functions verify Boch's theorem, this entails discretization of the wave vectors $\boldsymbol{k}$.

$$\begin{aligned} &e^{ik_xL_a} = e^{ik_yL_b} = e^{ik_zL_c} = 1 \\ &\boldsymbol{k} = \frac{2\pi}{L_a}n_1\boldsymbol{k_1} + \frac{2\pi}{L_b}n_2\boldsymbol{k_2} + \frac{2\pi}{L_c}n_3\boldsymbol{k_3} \;\; \forall n_i \in \mathbb{Z} \end{aligned} \tag{II.30}$$

Then, $\boldsymbol{k}$ vectors form a periodic lattice, called reciprocal lattice, that is a useful mathematical abstraction to solve KS equations. The basis vectors of the reciprocal latttice are $\boldsymbol{k_1}$, $\boldsymbol{k_2}$, and $\boldsymbol{k_3}$. In this set of reciprocal vectors, the direction of each vector coincides with the direction of normal planes in the real space, so that the properties of symmetry of the crystal are included in this imaginary space. The smallest lattice containing all the information necessary to build the whole space by periodicity is called the Irreducible Brillouin Zone (IBZ) and the 1^{st} irreducible Brillouin zone is the one closer to the origin ($\boldsymbol{\Gamma} = (0,0,0)$) than to any integer multiple of the reciprocal lattice vectors. The vectors in the 1^{st} IBZ connect the origin of the grid to points (k-points) that define the K-space. In theory, K-space is a continuum but in practice, a finite number of k-points is used to sample the IBZ. This is in order that the calculation remains finite, and is justified so long as the crystalline orbitals vary smoothly along $\boldsymbol{k}$. The sampling is done in a regular grid of points spaced evenly throughout IBZ, called a Monkhorst-Pack grid. The larger the dimensions of the grid, the finer and more accurate will be the calculations.[6] Actually, the relation between real and reciprocal space is such that doubling the input (real) unit cell in one direction will divide the necessary k-points by two.

II.1.2.2.c Localized basis-set

In this work we used localized basis sets. This allows us to define ghost atoms and control the position of a trapped electron in our crystalline cell. We assumed that the electronic states of the trapped electrons are well localized within a relatively small spatial region around the defect.

The local functions $\phi_\mu(\boldsymbol{r})$ are linear combination of a certain number of gaussian type functions. From these functions, Bloch functions $\Phi_\mu(\boldsymbol{r}, \boldsymbol{k})$ are built according to:

$$\Phi_\mu(\boldsymbol{r}, \boldsymbol{k}) = \sum_g \phi_\mu(\boldsymbol{r} - \boldsymbol{A_\mu} - g)e^{i\boldsymbol{k}g} \tag{II.31}$$

$\boldsymbol{A_\mu}$ refers to the coordinates of the nucleus in the reference cell (primitive cell), and g is a lattice vector. Finally, crystalline orbitals wavefunctions ψ_i are built by linear combination

of the Bloch functions:

$$\psi_j(\boldsymbol{r}, \boldsymbol{k}) = \sum_{\mu} a_{\mu j}(\boldsymbol{k}) \Phi_{\mu}(\boldsymbol{r}_j, \boldsymbol{k}) \tag{II.32}$$

For more details CRYSTAL 17 manual should prove useful.[7]

II.1.2.2.d Band theory and density of states

In solid-state physics, the electronic structure of system is described by its band structure. An isolated atom has quantified levels of energy, and the formation of bonds with others leads to the creation of new states from the starting atomic orbitals, called crystalline orbitals for a crystal. These new states have discrete energies in a molecule, but become a continuum in the case of a solid. This leads to what is called the band structure of the material, with the bonding levels forming the valence band (VB), and the anti-bonding ones the conduction band (CB). The space between this two bands is called the band gap and is associated with the energy E_{gap} that is the difference in energy between the first unoccupied state (in the CB) and the last occupied one (in the VB).

For efficient and practical reason, the calculation of the electronic structure is done in K-space (*i.e.* resolution of KS equations for each value of $\boldsymbol{k}$). Indeed, the energy of the different states is a function of $\boldsymbol{k}$ as can easily be shown for a one-dimensional system of free particles with no potential. In that case we can express the Schrödinger's equation as:

$$\frac{-\hbar^2}{2m}\frac{d^2\psi(x)}{dx^2} = E\psi(x) \quad \text{with} \quad \psi(x) = C\mathrm{e}^{i\boldsymbol{k}x} \tag{II.33}$$

C being a constant. This leads to:

$$E = \frac{\hbar^2}{2m}\boldsymbol{k}^2 \tag{II.34}$$

and can be generalized for three-dimensional system with potential. The energy landscape obtained, $E(\boldsymbol{k})$, is a three-dimensional function that is usually represented in two-dimensional plot by following a specific path of k-points in the IBZ corresponding to the highest symmetry points. Low symmetry crystals will require more extensive paths to capture the electronic structure than high symmetry crystals. Moreover, the larger the initial unit cell, the lower the necessary number of k-points, which in some extent, can justify calculations done only at the $\boldsymbol{\Gamma}$ point. This will allow a good description of the intra-cell interactions and a reduction of the CPU time at the price of treating inter-cell interactions in a less rigorous way.

Since the energy of the system is a continuum over k-space, the concept of density of state has been introduced. The density of state (DOS), $g(E) = n(E)dE$, is the number of

states in between energy E and energy $E + dE$, with $n(E)$ the distribution of the probability density function specific of the system. This density of states can be projected on some orbitals in order to see their contribution to the DOS, this is called projected density of states (PDOS).

II.1.2.2.e Treatment of defect: the supercell model

Thermodynamic laws ensure a certain disorder such that defects are intrinsic features of materials, which can actually provide them with fascinating properties (cf. section I.1). The introduction of a defect in a PBC calculation, using the supercell model (SCM), has some limitations and should be done carefully.[8] Indeed, the intrinsic periodicity of the lattice means that the defect introduced in the unit cell will have a similar artificial periodicity which does not correspond to reality where defects actually tend to gather in a same location in the crystal. Moreover, the defect in the unit cell will be able to interact with its periodic image if the cell is not large enough which can be problematic in some cases. If not, the size of the unit cell still has to be consistent with the natural "dilution" of the considered defect in the material. If 10% of some specific atomic positions are occupied by an impurity, the unit cell should contain at least 10 of these positions with one containing the impurity.
Introduction of a defect can also entail a drop of symmetry which increases the size of the IBZ and makes the calculation computationally more demanding. This can be balanced by the size of the unit cell chosen. In most cases this type of calculations are done at the $\mathbf{\Gamma}$ point only for the sake of computational time saving.

Other model exists called the cyclic cluster model (CCM)[9] that avoid defect-defect interaction by considering only one unit cell mathematically folded on itself. This methods has also the advantage to allow in principle the application of sophisticated post HF methods but is unfortunately difficult to implement and not available in the most famous quantum-chemistry packages for solid state calculations.[10]

II.2. Excited States methods: localized transitions

There exist different theories to describe light-matter interaction in quantum chemistry. They allow to access the (or some specific) transition energies, and electronic excited states' (EES) properties. In this section, we will introduce different methods used throughout the project, in order to highlight their strengths but also their limitations.

II.2.1. ΔSCF

ΔSCF-DFT method can be considered as an extension of DFT.[11] It consists in controlling the choice of the electronic state to converge. Indeed, DFT give the GS energy of the system, that is the energy of the irreducible representation lowest in energy. However, if there are several IRs related to group space symmetry or to spin multiplicity, it is possible to obtain their energy by constraining the KS states along the self-consistent procedure. Hence, this method is justified if the EES described by this occupation corresponds to the lowest state of a given (space or spin) symmetry. For instance, the difference in energy between the GS of a system and its first triplet EES can be obtained through two GS-like simple calculations. The first one being the classical DFT calculation providing the energy $E(\text{DFT})$, the second being identical with the exception of constraining the spin of the overall system to a triplet state. This excited state population will have an energy $E(\Delta\text{SCF})$. The transition energy, ΔE, between the two states is eventually computed following:

$$\Delta E = E(\Delta\text{SCF}) - E(\text{DFT}) \tag{II.35}$$

Theoretically, the exchange-correlation functional used should be adapted but in practise the same as for the GS calculation is kept. Some studies showed that ΔSCF and TD-DFT procedures provide qualitatively similar solutions, with ΔSCF being numerically undemanding.[12, 13] However, in practice they are often limited to calculation of triplet state's energy as in the example presented above.

II.2.2. Excited states with PBC calculations

There exist method to calculate the excited states' properties of periodic systems such as semi-empirical approaches[14], the periodic electrostatic embedding cluster method [15] implemented only in TURBOMOLE, or else the most famous Bethe-Salpeter Equation formalism along with the *GW* approximation. [16]
Even if the last one is comparable to TD-DFT in terms of accuracy,[17] we preferred instead the use of molecular approaches (TD-DFT + embedding methods, cf. sections II.2.3, II.4) that are less computationally demanding and workable on large systems containing more than 150 atoms.

II.2.3. TD-DFT

Time Dependent Density Functional theory (TD-DFT) is the most widely used theoretical approach when it comes to study EES. Compared with the situation in II.1.2, the system now evolves in a time dependent electromagnetic field (due to a light source), hence the

necessity to go for the time dependent version of the Schrödinger's equation:

$$i\hbar\frac{\partial}{\partial}|\psi(t)\rangle = \hat{H}|\psi(t)\rangle \tag{II.36}$$

with the introduction of a time dependent Hamiltonian ($\hat{H}$) which can be decomposed into a time independent part $\hat{H}_0$ and a time dependent one describing the external potential, $\hat{v}_{ext}$.

$$\hat{H}(t) = \hat{H}_0 + \hat{v}_{ext}(t) \tag{II.37}$$

$v_{ext}(t)$ is considered to be steady until a perturbation is "switched on" (*i.e.* an external field), at a time t, conventionally set to 0. Then we can express the external potential with the following formula:

$$\hat{v}_{ext}(\boldsymbol{r},t) = \hat{v}_{ext,0}(\boldsymbol{r}) + \delta\hat{v}_{ext}(\boldsymbol{r},t) \tag{II.38}$$

with $v_{ext,0}(\boldsymbol{r})$ the field free unperturbed external potential and,

$$\delta\hat{v}_{ext}(\boldsymbol{r},t) = 0 \quad for \;\; t \leqslant 0 \tag{II.39}$$

When the time dependency of the Hamiltonian is introduced by a weak perturbation, the response of the system to this perturbation can be accessed through time dependent density functional theory (TD-DFT) by solving the time dependent Schrödinger's equation within the linear response scope.

II.2.3.1. Runge Gross Theorem

Introduced by Runge and Gross in 1984,[18] this theorem can be seen as a prolongation of the HK theorems for a time dependent potential. It proves the existence of a one-to-one mapping between the potential in which the system evolves and the density of this system, making time dependent density functional theory formally exact.

R.G. Theorem: For a system of N interacting electrons, the densitities $n(\mathbf{r},t)$ and $n'(\mathbf{r},t)$ evolving from a common initial state $\psi(t_0)$ under the influence of two external time dependent potentials $v(\mathbf{r},t)$ and $v'(\mathbf{r},t)$, are always different provided that the potentials differ by more than an additive spatially constant time dependent function $c(t)$.

If the initial wavefunction is the ground state one, that is $\psi(t_0) = \psi_0$, the first HK theorem tells us the dependance on the initial state is already taken into account into the density

functional so that:

$$\hat{v}_{ext}(\boldsymbol{r},t) = \hat{v}_{ext}[n,\psi_0](\boldsymbol{r},t) = \hat{v}_{ext}[n](\boldsymbol{r},t) \tag{II.40}$$

and it is possible to write the Hamiltonian as a density functional.

II.2.3.2. Linear response theory

In linear response time dependent density functional theory (LR-TD-DFT), the response of the system to a change in the external field, $\delta\hat{v}_{ext}(\boldsymbol{r},t)$, is described by the variation of the electron density, $n(\boldsymbol{r},t)$, at the first order. To do so, the electron density is developed into its Taylor series at $t = 0$:

$$n(\boldsymbol{r},t) = n_0(\boldsymbol{r}) + n_1(\boldsymbol{r},t) + n_2(\boldsymbol{r},t) + n_3(\boldsymbol{r},t) + ... \tag{II.41}$$

with

$$n_x(\boldsymbol{r},t) = \frac{n^{(x)}}{x\,!}(t-0) = \frac{n^{(x)}}{x\,!}(t) \qquad \forall x \in \mathbb{N} \tag{II.42}$$

The blue part of Equation II.41 corresponds to the terms taken into account in the linear response theory: zeroth and first orders only. Indeed, the perturbation being small, only the first order dominates. $n_0(\boldsymbol{r})$ is actually the density of the ground state before the perturbation ($n_0(\boldsymbol{r}) = |\Psi_0|^2$), and $n_1(\boldsymbol{r},t)$ can be expressed by introducing the density-density linear response function χ:

$$n_1(\boldsymbol{r},t) = \int_0^t dt' \int d\boldsymbol{r'}\chi(\boldsymbol{r}t,\boldsymbol{r'}t')\ \delta v_{ext}(\boldsymbol{r},t) \tag{II.43}$$

with

$$\chi(\boldsymbol{r}t,\boldsymbol{r'}t') = \frac{\delta n(\boldsymbol{r},t)}{\delta v_{ext}(\boldsymbol{r'},t')}\bigg|_{v_{ext},0} \tag{II.44}$$

This response function is obtained after a little math. We recommend the book *Fundamentals of Time dependent Density Functional Theory*[19] for more mathematical details. However, important steps have to be highlighted. The perturbation operator expressed by a series truncated at the first order term, (cf. linear response theory) is applied onto the ground state of the system, $|\Psi_0\rangle$, through the *adiabatic approximation*:

$$|\Psi(t)\rangle = |\Psi_0\rangle - i\int_{-\infty}^{t} dt' v_{ext}(\boldsymbol{r'},t')\,|\Psi_0\rangle \tag{II.45}$$

In this approximation, the perturbation is turned on infinitely long ago, mimicking a very slow change of the external field so that the ground state wavefunction can handle the perturbation. This means that in LR-TD-DFT one has to be careful if dealing with strong fields.

Finally, the density-density linear response can be reached trough the following formula:

$$\chi(\boldsymbol{r}t, \boldsymbol{r'}t') = \lim_{\eta \to 0} \; -i\theta(t-t') \left\langle \Psi_0 \right| \left[\hat{n}(\boldsymbol{r}, t), \hat{v}_{ext}(\boldsymbol{r'}, t') \right] \left| \Psi_0 \right\rangle \mathrm{e}^{\eta(t-t')} \tag{II.46}$$

$\hat{n}$ is the density operator. The Heaviside function ($\theta(t-t')$) ensures that the system is responding only when the perturbation is turned on (allowing an easier integration from $-\infty$ to ∞). Here, it is interesting to note that the response function depends only on the ground state wavefunction which avoids explicit calculation of the excited states ones.

II.2.3.3. Spectral decomposition

Conventionally, we work not in the time domain but in the frequency one. Using Fourier transform and convolution theorem we obtain the equivalent frequency dependent equations among which the expression of the first order response of the density to the perturbation:

$$n_1(\boldsymbol{r}, \omega) = \int d^3r' \chi(\boldsymbol{r}, \boldsymbol{r'}, \omega) \; \delta v_{ext}(\boldsymbol{r'}, \omega) \tag{II.47}$$

with,

$$\chi(\boldsymbol{r}t, \boldsymbol{r'}\omega) = \left. \frac{\delta n(\boldsymbol{r}, \omega)}{\delta v_{ext}(\boldsymbol{r'}, \omega)} \right|_{v_{ext}[n_0]} \tag{II.48}$$

$\chi(\boldsymbol{r}, \boldsymbol{r'}, \omega)$ is the corresponding linear response function in the frequency domain. When a perturbation's frequency allows a transition from the GS towards an EES, it produces a change in the density of the system making $\chi(\boldsymbol{r}, \boldsymbol{r'}, \omega)$ diverging at this specific ω value Actually its inverse function, $\chi^{-1}(\boldsymbol{r}t, \boldsymbol{r'}\omega)$ (cf. Equation II.49), is the cornerstone of LR-TD-DFT, with the basic idea of finding its zeros which correspond to frequencies (ω) of the perturbation matching excitation energies.

$$\chi^{-1}(\boldsymbol{r}, \boldsymbol{r'}\omega) = \left. \frac{\delta v_{ext}(\boldsymbol{r'}, \omega)}{\delta n(\boldsymbol{r}, \omega)} \right|_{n_0} \tag{II.49}$$

II.2.3.4. Reformulation in matrix form: Casida's equation

Finding the zeros of $\chi^{-1}(\boldsymbol{r}t, \boldsymbol{r'}\omega)$ (*i.e.* the excitation energies), can be done through a reformulation in a matrix form. The equations to find the resulting eigenvalues are known as Casida's equations.

An important point in this reformulation is the expression of the perturbed state vectors $|\psi(t)\rangle$ in the complete basis set of unperturbed states ($\sum_n |k_n\rangle \langle k_n| = 1$) and the fact that the system is initially in its ground state $|\Psi_0\rangle = |k_0\rangle = |0\rangle$, with:

$$\hat{H}_0 \left| k_n \right\rangle = \epsilon_n \left| k_n \right\rangle \quad \forall n \in \mathbb{N} \tag{II.50}$$

The expression of the linear response function becomes:

$$\chi(\boldsymbol{r},\boldsymbol{r'},\omega) = \lim_{\eta\to 0}\sum_{k\neq 0}\left[\frac{\langle 0|\,\hat{n}(\boldsymbol{r})\,|k\rangle\,\langle k|\,\hat{n}(\boldsymbol{r})\,|0\rangle}{\omega-(\epsilon_k-\epsilon_0)+i\eta} - \frac{\langle 0|\,\hat{n}(\boldsymbol{r'})\,|k\rangle\,\langle k|\,\hat{n}(\boldsymbol{r'})\,|0\rangle}{\omega+(\epsilon_k-\epsilon_0)+i\eta}\right] \tag{II.51}$$

and one can see its asymptotic behaviours when $\omega \to (\epsilon_k - \epsilon_0)$ (excitation), or when $\omega \to (\epsilon_0 - \epsilon_k)$ (deexcitation).
Then, it is possible to express the linear response function, or its inverse, in Kohn-Sham (KS) formalism (cf. II.1.2.1.b), by dividing it into the response of non-interacting electrons and an Hartree exchange-correlation kernel:

$$\chi^{-1}(\boldsymbol{r},\boldsymbol{r'}\omega) = \chi_{\mathrm{KS}}^{-1}(\boldsymbol{r},\boldsymbol{r'}\omega) - f_{\mathrm{Hxc}}(\boldsymbol{r},\boldsymbol{r'}\omega) \tag{II.52}$$

In order to find the zeros of χ^{-1}, in most algorithms currently used, this expression is actually reformulated in another complete basis set made of Kohn-Sham spin-orbitals (ϕ) products, such as:

$$g_{ia}(\boldsymbol{r},\boldsymbol{r'}) = \phi_i^*(\boldsymbol{r'})\phi_a(\boldsymbol{r}) \tag{II.53}$$

$$g_{ai}(\boldsymbol{r},\boldsymbol{r'}) = \phi_a^*(\boldsymbol{r'})\phi_i(\boldsymbol{r}) \tag{II.54}$$

with a an occupied orbital of energy ϵ_a and i an empty one of energy ϵ_i. Then, g_{ia} corresponds to excitation of an electron from ϕ_a to ϕ_i, and g_{ai} to the deexcitation process. This gives the following formula for Kohn-Sham linear response function:

$$\chi^{\mathrm{KS}}(\boldsymbol{r},\boldsymbol{r'},\omega) = \lim_{\eta\to 0}\sum_{i,a}\left[\frac{g_{ia}(\boldsymbol{r},\boldsymbol{r})g_{ia}^*(\boldsymbol{r'},\boldsymbol{r'})}{\omega-(\epsilon_a-\epsilon_i)+i\eta} - \frac{g_{ai}(\boldsymbol{r},\boldsymbol{r})g_{ai}^*(\boldsymbol{r'},\boldsymbol{r'})}{\omega-(\epsilon_a-\epsilon_i)+i\eta}\right] \tag{II.55}$$

Concerning f_{Hxc} kernel, it is taken into account by the introduction of the coupling matrix K which mathematical expression is:

$$K_{ia,jb}(\omega) = \int\int \phi_i^*(\boldsymbol{r_1})\phi_a(\boldsymbol{r_1})f_{\mathrm{Hxc}}(\boldsymbol{r_1},\boldsymbol{r_2},\omega)\phi_j(\boldsymbol{r_2})\phi_b^*(\boldsymbol{r_2}) \tag{II.56}$$

In the end, by taking the inverse functions of χ^{KS} and f_{Hxc} we obtain an expression for χ^{-1} in a matrix form:

$$\chi^{-1}(\omega) = -\left[\begin{pmatrix} A(\omega) & B(\omega) \\ B(-\omega)^* & A(-\omega)^* \end{pmatrix} - \omega\begin{pmatrix} 1 & 0 \\ 0 & -1 \end{pmatrix}\right] \tag{II.57}$$

with

$$A_{ia,jb}(\omega) = (\epsilon_a - \epsilon_i)\delta_{ij}\delta_{ab} + K_{ia,jb}(\omega) \tag{II.58}$$

and

$$B_{ia,jb}(\omega) = K_{ia,jb}(\omega) \tag{II.59}$$

Finally the response of the system to an individual frequencies $\chi^{-1}(\omega_i)$ of light, only for mono-electronic transitions, is obtained by solving:

$$\begin{pmatrix} A(\omega) & B(\omega) \\ B(-\omega)^* & A(-\omega)^* \end{pmatrix} \begin{pmatrix} X(\omega) \\ Y(\omega) \end{pmatrix} = \omega_i \begin{pmatrix} 1 & 0 \\ 0 & -1 \end{pmatrix} \begin{pmatrix} X(\omega) \\ Y(\omega) \end{pmatrix} \tag{II.60}$$

with $A(\omega) = A(-\omega)^*$ and $B(\omega) = B(-\omega)^*$ for real orbitals. Solving the linear system provides the excitation energy ω_n associated with the eigenvector $(\boldsymbol{X}_n, \boldsymbol{Y}_n)$. B matrices hold the coupling between excitation and de-excitation and are neglected in the Tamm-Dancoff approximation (TDA). More details can be found in the very comprehensive and pleasant work of Elisa Rebolini.[20]

II.2.3.5. Oscillator's strength calculation with LR-TD-DFT

We have just seen how to access the transition energies with LR-TD-DFT. Each transition is characterized by its energy but also by its probability, called oscillator strength. Indeed, all transitions are not equally allowed, some are even forbidden by what are called selection rules. We access the oscillator strengths, f_n, of the different transitions by looking at the mean dynamic dipole polarizability ($\bar{\alpha}(\omega)$ cf. Equation II.61) which is a tensor connecting the dipole moment induced by the external field and the strength of the latter.

$$\bar{\alpha}(\omega) = \sum_{n \neq 0} \frac{f_n}{\omega_n^2 - \omega^2} \tag{II.61}$$

f_n is the oscillator strength associated with the excited state $|\psi_n\rangle$ of energy ω_n. And,

$$\bar{\alpha}(\omega) = \frac{1}{3}(\alpha_{xx}(\omega) + \alpha_{yy}(\omega) + \alpha_{zz}(\omega)) \tag{II.62}$$

with

$$\alpha_{qq}(\omega) = -\int \chi(\boldsymbol{r}, \boldsymbol{r'}, \omega) r_q r'_q d\boldsymbol{r}\boldsymbol{r'} \quad \forall q \in \{x, y, z\} \tag{II.63}$$

Using the spectral decomposition of χ provided in the previous section, we eventually obtain the following expression for the oscillator strength, with $\hat{q}$ the position operator along one direction:

$$f_n = \frac{2}{3} \sum_q \left(\sum_{ia} \langle \phi_i | \hat{q} | \phi_a \rangle (\boldsymbol{X}_n + \boldsymbol{Y}_n)_{ia} \right)^2 \omega_n \tag{II.64}$$

For more physical understanding, the oscillator strength can be written as a function of the transition dipole moment between the GS and a state n: $\mu_{q,0\to n} = \langle \psi_0 | \hat{q} | \psi_n \rangle$. It

corresponds to the expression between parenthesis in Equation II.64 and leads to:

$$f_n = \frac{2}{3} \sum_q |\langle \psi_0 | \hat{q} | \psi_n \rangle|^2 \omega_n \tag{II.65}$$

II.2.4. Brief overview of some Post Hartree-Fock methods

We have mentioned the reintroduction of the missing correlation energies thanks to what are called post-HF methods. In this work, these methods were used for some calculations of vertical transition energies between the GS and different EES, that is why they are introduced now. Post-Hartree Fock methods, for most of them, have the advantage of providing more reliability than TD-DFT but at an important computational cost, which explain why TD-DFT is a more widely used theoretical approach. Indeed, it is difficult to do calculations with more than 100 atoms and taking account of an embedding is not always straightforward. However, they can be used from time to time in order to provide precious reference values of specific calculations, for instance transitions energies of some types of systems.

All post Hartree-Fock methods are based on the expansion of the many-electron wavefunction in a linear combination of "excited" Slater determinants, which allows a good description of both the GS of a system and its EES (at least the first ones). In the following, only three main families of post-HF methods are succinctly presented, from which different extensions have been developed so far.

II.2.4.1. Configuration Interaction methods

Configuration Interaction (CI) methods consist in adding to the Slater (Φ_0) determinant describing the GS of a system of N electrons other Slater determinants one can build by exciting one, two, ... N electrons. If

$$\Phi_0 = |\phi_{i1} ... \phi_{iN}\rangle \tag{II.66}$$

then the mono-excitation determinants are built by placing one electron from occupied orbital $\phi_j \ \forall j \leq \frac{N}{2}$ to unoccupied orbital $\phi_k^* \ \forall k > \frac{N}{2}$, keeping the same spin for the electron. Similarly, the double-excitations determinants are build by moving two electrons from two occupied orbitals to two unoccupied orbitals of Φ_0, ... one can repeat the same process until the N-excitations determinants.

The final wavefuntion of the systems is then a linear combination of the different determinants, so that both the coefficients of these combinations and the ones of each specific Slater determinants have to be optimized self-consistently which is computationally expensive.

If only the determinant of mono-excitation are taken into account, the method is called Configuration Interaction Single (CIS). When one adds the double-excitation determinants the method becomes Configuration Interaction Single Double (CISD)... until all possible determinants are included and the method is then referred to as Full-CI. The more type of excitation you add, the more computationally expensive. Except for the Full-CI all CI methods lack size-consistency.

II.2.4.2. Complete Active Space methods

Complete Active Space (CAS) methods have been developed on the idea that the important orbitals in terms of chemical properties are the one around the Fermi level, that is close to the HOMO and LUMO. Based on it, the orbitals obtained from a previous calculation (HF, DFT...) are divided among three groups:

1. $Nocc$ doubly occupied orbitals: $\phi_{i_{occ}} = \chi_{i_{occ}}\bar{\chi}_{i_{occ}}$, with $\chi_{i_{occ}}$ orbital containing spin-up electron and $\bar{\chi}_{i_{occ}}$ orbital containing spin-down electron
2. $N - 2Nocc$ active orbitals: their occupancy can change
3. Virtual orbitals: unoccupied

The mean field approach is used for the electrons in the occupied orbitals, and the correlation is considered only for the active orbitals by applying CI method on this specific group of orbitals. The wavefunction can be expressed as a sum of functions called configuration state functions (CSF) following:

$$\Phi = \sum_I C_I \left| \left(\prod_{i_{occ}=1}^{N_{occ}} \chi_{i_{occ}}\bar{\chi}_{i_{occ}} \right) \prod_{j=1}^{N-2N_{occ}} \phi_{I,j} \right\rangle \tag{II.67}$$

Both the coefficients of the CSFs (C_I) and the occupation of the basis functions in the molecular orbitals are self-consistently opimized: we talk about CASSCF method. It is a size-consistent method.

II.2.4.3. Coupled Cluster methods

As for CI, the Coupled Cluster (CC) methods reintroduce the excitations successively in the final wavefunction starting from the initial mono-determinantal GS wavefunction, Φ_0. However, the process is size-consistent whatever the level of excitations considered. Indeed, in this method the wavefunction Φ_{CC} is constructed as an exponential ansatz of Φ_0 by applying the cluster operator $\hat{T}$ on it:

$$|\Phi_{CC}\rangle = \mathrm{e}^T |\Phi_0\rangle \tag{II.68}$$

with

$$\begin{aligned} \hat{T} &= \hat{T}_1 + \hat{T}_2 + ... + \hat{T}_N \\ \mathrm{e}^{T} &= \hat{1} + \hat{T}_1 + \frac{\hat{T}_2}{2!} + ... + \frac{\hat{T}_N}{N!} \end{aligned} \tag{II.69}$$

$\hat{T}_i$ being the operator of i$^{\text{th}}$ excitations (*i.e.* i electrons transferred from occupied spin-orbitals to unoccupied ones). These operators can be coupled to generate higher excitations levels which leads to the following formulation:

$$\mathrm{e}^{T} = \hat{1} + \hat{C}_1 + \hat{C}_2 + ... + \hat{C}_N \tag{II.70}$$

with for instance:

$$\begin{aligned} \hat{C}_1 &= \hat{T}_1 \\ \hat{C}_2 &= \hat{T}_2 + \frac{1}{2}\hat{T}_1^2 \\ \hat{C}_3 &= \hat{T}_3 + \hat{T}_1\hat{T}_2 + \frac{1}{6}\hat{T}_1^3 \\ &... \end{aligned} \tag{II.71}$$

Hence, in CC method, double excitations generated by the operator $\hat{C}_2$ correspond to two simultaneous single excitations ($\hat{T}_2$), or to two independent ones ($\hat{T}_1^2$). Moreover, when the cluster operator is truncated at the second order ($\hat{T} = \hat{T}_1 + \hat{T}_2$), single and double excitations are fully determined and higher excitations are partly included by products of single and double excitations, contrary to CISD for which the operator would be $\mathrm{e}^{T_{\text{CSID}}} = \hat{1} + \hat{C}_1 + \hat{C}_2$. This truncation is known as Couple Cluster Single Double (CCSD) method. When higher excitations are taken into account perturbatively they are indicated in round brackets. For instance CCSD(T) for which the triples contribution are calculated non-iteratively through perturbation theory.
Excited states energies and oscillator strengths can then be obtained through a response theory (similar to LR-TD-DFT) or the Equation-of-Motion framework.[21]
The SAC-CI method is drawn from CC theory with the CC operator replaced by a symmetry adapted cluster (SAC) one which aims at selecting only the configurations that satisfy the symmetry requirements for excitation.

II.2.5. Taking into account of the vibronic coupling

We have seen different quantum chemistry methods to calculate the transition energies of a system from its GS to its EESs. The energies obtained correspond to vertical transitions (cf. Figure II.3a). Yet, in spectroscopy measurements we usually record bands and not

peaks. This is to a large extent due to residual movement of the nuclei at the origin of vibronic levels of energy associated to every electronic level of energy of the system. An electronic absorption from the GS to an EES is thus a sum of transitions from the vibronic levels of energy of the GS to the one of the EES considered, and not a unique peak (cf. Figure II.3b). The same is true for the fluorescence process. This is called vibronic coupling. When we consider vibronic coupling, we are no more in the Born-Oppenheimer approximation since the nuclei have to move, but in Franck-Condon one. The latter states that due to the much faster rearrangement of the electrons than motion of the nuclei, the nuclear configuration does not change significantly during the energy absorption. In that approximation, one can consider absorption spectra made of several vertical excitation energies, after which they would be a rearrangement of the EES geometry.

All other things being equal, the higher the overlapping between two vibronic levels n and

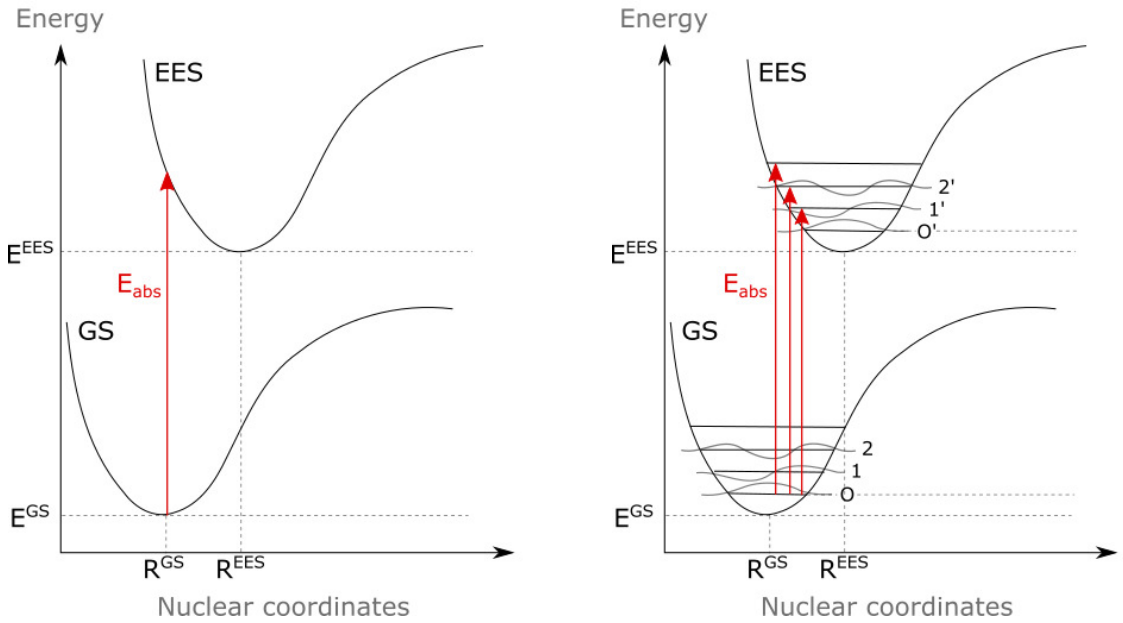

Figure II.3: Taking into account the vibronic coupling in the electronic transitions: (a) simple vertical transition of absorption (red arrow) between GS and one EES with respective energies and geometries E^{GS}, E^{EES} and $\mathbf{R}^{GS}$, $\mathbf{R}^{EES}$; (b) absorption transition made of several vertical transitions (FC approximation) between the vibronic levels of GS and one EES. The vibronic level of energy of each electronic state are represented up to the third one, the numbering starting at 0.

n' (*i.e.* $\langle n'|n\rangle$), the higher the probability of a vibrational transition between them.[22] Indeed, the transition dipole moment between the vibronic levels n and n' of initial and final states described by the wavefunctions ψ_i and ψ_f, is expressed as:

$$\mu_{if} = \langle\psi_i|\,\hat{V}\,|\psi_f\rangle = \langle n'|n\rangle\,\langle\phi_i|\,\hat{V}\,|\phi_f\rangle \tag{II.72}$$

with ϕ_i and ϕ_f the electronic space and spin components of the respective wavefunctions. $\langle n'|n\rangle$ is the Franck-Condon coefficient.

II.3. Limit of TD-DFT for charge transfer transitions

II.3.1. Origin of the error

The developed exchange correlation functionals lack some properties that must have the exact one. This is particularly problematic for the description of charge transfer transitions.[23, 24] Let's illustrate that with the classical example of a simple charge transfer from a donor towards an acceptor, the two moieties being separated by a distance R. In that context, the CT energy, E_{CT}, can be expressed by:

$$E_{\mathrm{CT}} \approx IP^{\mathrm{D}} - EA^{\mathrm{A}} - \frac{1}{R} \tag{II.73}$$

In LR-TD-DFT the energy of charge transfer from an occupied orbital ϕ_i (of energy ϵ_i) on the donor toward an unoccupied orbital ϕ_a (of energy ϵ_a) on the acceptor is given by Equation II.58. A first error comes from the non-overlapping of the donor and acceptor orbitals and the fact that the Hartree-exchange-correlation kernel f_{Hxc} provides only a (semi)-local description of the density leading to $\frac{1}{R}$ term going rapidly to 0 as the distance R increases (cf. Equation II.56). Hence, the asymptotic behaviour is not obtained. This can be corrected by adding non-local exact exchange in the functional.
Moreover, contrary to HF theory for which Koopman's theorem can be applied, in DFT the ionization potential and the electronic affinity can not be well approximated by the HOMO and LUMO energies. That is $\epsilon_a - \epsilon_i \neq IP^{\mathrm{D}} - EA^{\mathrm{A}}$. This can be explained by the fact that the energy of the LUMO is calculated for the GS system containing N electrons, while it should be evaluated for the $N+1$ electron system (as in HF theory). This explains the underbounding of this orbital and the underestimation of the $\epsilon_a - \epsilon_i$ term. This is the reason why Janak's theorem,[25] that aims at offering an analogue to Koopman's theorem for DFT, has been reported as flawed.[26, 27]
Dreuw and Head-Gordon[24] interestingly showed that the bad description of the CT in TD-DFT can be seen as an overall self-interaction error.

II.3.2. Range-separated hybrid functional

A solution to the bad description of CT is to reintroduce the long-range exchange interaction. This is done through the so-called rang-separated hybrid (RSH) functionals for which the overall Hartree-exchange-correlation functional is split between a short-range

term and a long-range term, following:

$$f_{\text{Hxc}}^{\mu} = f_{\text{Hxc}}^{sr,\mu} + f_{\text{Hxc}}^{lr,\mu} \tag{II.74}$$

The parameter, $\mu \in \mathbb{R}+$, characterizing the switch between the two is called the range-separation parameter. This parameter should be designed to depend locally on the density but is not for the sake of simplicity. Instead a compromise is found, and its value depends on the functional one will use. There exist standard values of this parameter according to the functionals used for the exchange or correlation part, but it is also possible to tune it, which is beyond the scope of this project.[28]
In the case where only the exchange part of the functional is range-separated (long-range corrected functionals (LC)), the Coulomb interaction is split into two parts, with f often derived from the standard error function (erf):

$$\begin{aligned} f_{\text{x}}^{\mu} &= f_{\text{x}}^{sr,\mu} + f_{\text{x}}^{lr,\mu} \\ &= \frac{1 - f_{\mu}(|\boldsymbol{r} - \boldsymbol{r'}|)}{|\boldsymbol{r} - \boldsymbol{r'}|} + \frac{f_{\mu}(|\boldsymbol{r} - \boldsymbol{r'}|)}{|\boldsymbol{r} - \boldsymbol{r'}|} \end{aligned} \tag{II.75}$$

LC-ωHPBE and ωB97X-D (even if its name does not suggest it) are LC functional used in this project.
Going further, it is possible to add some Hartree exchange also in the short-range. This is called Coulomb Attenuated Method (CAM), and needs two new parameters α and β to incorporate respectively HF or DFT exchange in the different terms:

$$f_{\text{x}}^{\mu,\alpha\beta} = \frac{1 - [\alpha + \beta f_{\mu}(|\boldsymbol{r} - \boldsymbol{r'}|)]}{|\boldsymbol{r} - \boldsymbol{r'}|} + \frac{\alpha + \beta f_{\mu}(|\boldsymbol{r} - \boldsymbol{r'}|)}{|\boldsymbol{r} - \boldsymbol{r'}|} \tag{II.76}$$

In the family of RSH functionals exist also an opposite approach to LC: the so-called screened-exchange hybrid functionals. The HSE06 functional belongs to this family in which a finite amount of HF exchange is used for the short-range part and none is incorporated in the long-range one. This functional has been developed for solid state calculation and fitted on TiO2's properties. See [29] for more details.
The parameters of the different functionals have been fitted on experimental data or derived from *ab initio*. As for its GS counterpart, in TD-DFT the choice of the functional is crucial. It depends on the system studied and the parameters one wants to access. There is no "best" functional thus far, but thorough benchmarks can help one to chose the relevant functional. [30, 31]

II.4. Embedded Cluster Model

The inclusion of the environment is even more important when dealing with excited states that are more sensitive to it than their ground state counterpart.
In this project, in which we used finite molecular approaches for the EES calculations (*e.g.* TD-DFT on clusters), account for the effect of the environment can be done through different methods. Here we will introduce the Embedded Cluster Model (ECM) one. In this approach a cutout of the material (cluster) is used to represent the local structure of the material around a particular atomic site, or a defect. This cluster that will be treated quantum computationally and referred to as the QM part, is embedded into an environment that can take different forms. Finally, it is similar to a QM-MM approach, and some cares have to be taken when introducing an artificial boundary between the QM part and its embedding. There exist as many ECM methods as possibilities of embedding.

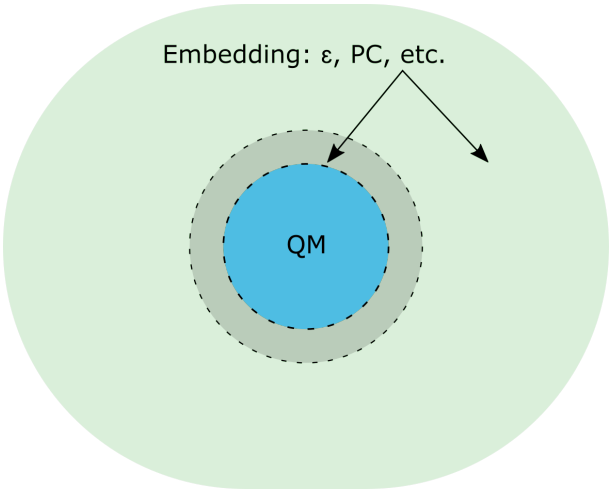

Figure II.4: Schematic picture of the Embedded Cluster Model approach. The cluster (QM) is surrounded by one or several layers (grey and green) that provide the system with long-range coulomb interactions, the isolated cluster would lack. The embedding layers can be of different nature.

This type of approaches allows to free oneself from the interaction of a defect with its images in periodic boundary conditions calculations. Moreover, this non periodic approach enables the use of standard molecular quantum chemical codes such as Gaussian 16[32] or Orca[33, 34]. However, there are some limitations for modelling excited states of extended crystalline systems due to the drop-out of their intrinsic periodicity.

II.4.1. MCM and PCM methods

The extracted cluster will obviously lack information, and above all suffer from the introduction of border effects such as dangling bonds.[35] This can cause artificial electronic artefacts in the calculation leading possibly to a bad description of the electronic density. This is specially true if the cluster is small. A solution would then to increase the size of the cluster and/or saturate the dangling bonds with pseudo-atoms (*e.g.* addition of hydrogen atoms to saturate oxygen pending bonds). In the last solution, called Molecular Cluster Model (MCM)[8], some atoms (at the edge) do not have the same environment as their equivalent within the cluster, and the system gets really close to a molecular system. This is particularly annoying in the case of an ionic system.
A similarly simple and well implemented in codes solution is to place the QM cluster inside a polarizable continuum model (PCM). This approach has several advantages among which its simplicity, low computational cost, and its wide implementation. Moreover, its popularity leads to great developments, such as the implementation of PCM depending on the excited state density (SS-PCM), and a good knowledge of its limitations (*e.g.* lack of specific interactions). This approach is particularly relevant when studying molecules in solvents. [31]
However, in this project we want to get closer to the crystal structure of the systems studied. In the next section, we will see that it is actually possible to keep the attractive aspect of the finite approach while also improving the embedding in order to keep as much as possible the properties of an extensive system.

II.4.2. Reproduction of the Madelung potential

To improve the embedding in the case of crystals, an existing solution consists in adding point charges of different values around the cluster. The point charges being place on atomic lattice sites with starting values equal to the oxidation state of the atom corresponding to this site. This allows to reproduce the periodicity and heterogeneity (in terms of atom type) of the real crystal structure around the QM part. Actually, the nature of the charges can vary according to the system studied (Bader, Mulliken, etc.), but in the case of ionic crystals choosing the oxidation state works well and is particularly easy to implement.[36]
The electrostatic interactions at the long range are included in the Madelung potential of the solid. The Madelung potential V_i corresponds to the electrostatic potential produced by all ions j with charge q_j of the lattice on the ion at position r_i.

$$V_i = \sum_{j \neq i} \frac{q_j}{r_{i,j}} \tag{II.77}$$

In order to reproduce the Madelung potential of the infinite solid in the extracted cluster, we have to add many shells of point charges. However, it has been proven mathematically that adding successive layers of charges around the cluster within a fixed distance will never make the potential calculated at a specific point in the cluster converge to the corresponding Madelung potential of the real solid.[37]
To overcome this issue, the solution followed in this project is the one offered by a group in Berkeley.[38] They developed a code that will produce an array of point charges around a given cluster (QM, containing N_1 atoms) that reproduces the Madelung potential at different sites k of the cluster corresponding to the ones calculated in the periodic system. These potentials, $V^{\mathrm{PBC}}(\boldsymbol{r_k})$, are calculated in the periodic system through Ewald summation method.

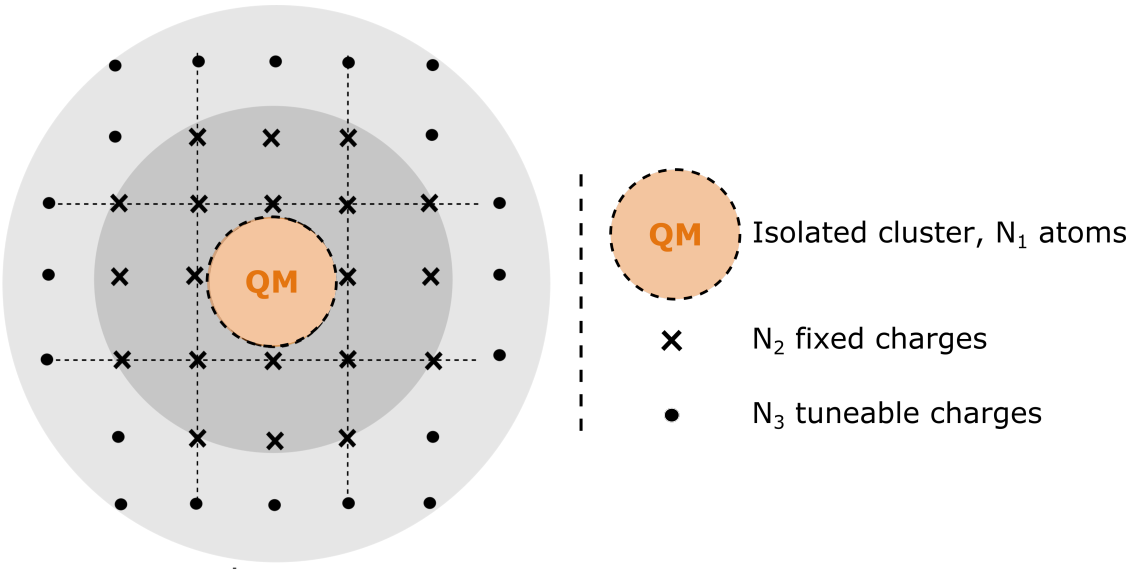

Figure II.5: Representation of the cluster (QM) surrounding by the point charges array that reproduces the Madelung potential.

To be more precise, the array of point charges surrounding the cluster is divided into two groups (cf. Figure II.5). The N_2 point charges in the first group (Z_2) are closer to the cluster and keep their charge value fixed (*e.g.* the oxidation state of the atomic site). The remaining N_3 ones, further away, can be tuned so that their value divert from the original oxidation state by a small amount Δq. By doing so, the close environment of the cluster is very similar to the one it would have in the infinite solid and the long range coulomb interactions are reproduced.
Mathematically, tuning the charges is made through the resolution of a linear system of $k = N_1 + N_2$ equations to reproduce the Madelung potential at the sites in QC and Z_2

(cf. Equation II.78).

$$\forall k \leq N_1 + N_2 : \quad \sum_{i \neq k}^{N} \frac{q_i + \Delta q_i}{r_{ik}} - V^{\mathrm{PBC}}(\boldsymbol{r_k}) = 0 \quad \text{with} \quad N = N_1 + N_2 + N_3 \quad \Delta q_i = 0 \quad \forall i \leq N_1 + N_2 \tag{II.78}$$

To that system of equations are added 4 equations in order to keep the charge neutrality and the dipole moments of the system equal to 0. Since $N_1 + N_2 + 4 < N_3$, there are more parameters than equations and the additional constraint of selecting the smallest possible variations of Δq is applied. The quality of the fit is eventually checked by choosing randomly $j \approx 1000$ points in the QM part for which $V^{\mathrm{PBC}}(\boldsymbol{r_j})$ has been calculated and is compared to the generated Madelung potential V_j.

Further improvement of the embedding can actually be achieved. Indeed, the point charges surrounding the cluster are classical particles that are interacting with a quantum cluster. The boundary between the cluster and its embedding is then a bit abrupt. On the basis of an approach developed in the 1990's, one can add a sphere of pseudopotentials in between the two in order to mitigate the border transition.[39–41] This approach consists in treating the first sphere of cations appearing beyond the QM part with pseudopotentials and no basis functions.

References Chapter II.

[1] E. Fermi *Rendiconti Accademia Nazionale Lincei*, vol. 6, no. 602-607, p. 5, **1927**.

[2] P. Hohenberg and W. Kohn *Physical Review*, vol. 136, no. 3B, p. 864–871, **1964**.

[3] L. D. Site *Journal of Physics A: Mathematical and Theoretical*, vol. 40, no. 11, p. 2787–2792, **2007**.

[4] W. Kohn and L. J. Sham *Physical Review*, vol. 140, no. 4A, p. 1133, **1965**.

[5] J. P. Perdew and K. Schmidt, "Jacob's ladder of density functional approximations for the exchange-correlation energy," in *AIP Conference Proceedings*, vol. 577, pp. 1–20, American Institute of Physics, **2001**.

[6] G. Makov, R. Shah, and M. C. Payne *Physical Review B*, vol. 53, no. 23, p. 15513–15517, **1996**.

[7] R. Dovesi, V. Saunders, C. Roetti, R. Orlando, C. Zicovich-Wilson, F. Pascale, B. Civalleri, K. Doll, N. Harrison, I. Bush, P. D'Arco, M. Llunell, M. Causà, Y. Noël, L. Maschio, A. Erba, M. Rerat, and S. Casassa **2017**.

[8] P. Deak *Physica Status Solidi (B)*, vol. 217, no. 1, pp. 9–21, **2000**.

[9] F. Janetzko, A. M. Köster, and D. R. Salahub *The Journal of Chemical Physics*, vol. 128, no. 2, p. 024102, **2008**.

[10] Y. F. Zhukovskii, E. A. Kotomin, R. A. Evarestov, and D. E. Ellis *International Journal of Quantum Chemistry*, vol. 107, no. 14, pp. 2956–2985, **2007**.

[11] J. Gavnholt, T. Olsen, M. Engelund, and J. Schiøtz *Physical Review B*, vol. 78, no. 7, **2008**.

[12] T. Kowalczyk, S. R. Yost, and T. V. Voorhis *The Journal of Chemical Physics*, vol. 134, no. 5, p. 054128, **2011**.

[13] R. J. Maurer and K. Reuter *The Journal of Chemical Physics*, vol. 135, no. 22, p. 224303, **2011**.

[14] I. Gadaczek, K. J. Hintze, and T. Bredow *Physical Chemistry Chemical Physics*, vol. 14, no. 2, p. 741–750, **2012**.

[15] A. M. Burow, M. Sierka, J. Döbler, and J. Sauer *The Journal of Chemical Physics*, vol. 130, no. 17, p. 174710, **2009**.

[16] X. Blase, I. Duchemin, D. Jacquemin, and P.-F. Loos *The Journal of Physical Chemistry Letters*, vol. 11, no. 17, pp. 7371–7382, **2020**.

[17] D. Jacquemin, I. Duchemin, and X. Blase *The Journal of Physical Chemistry Letters*, vol. 8, no. 7, p. 1524–1529, **2017**.

[18] E. Runge and E. K. Gross *Physical Review Letters*, vol. 52, no. 12, p. 997, **1984**.

[19] M. A. Marques, N. T. Maitra, F. M. Nogueira, E. K. Gross, and A. Rubio, *Fundamentals of time-dependent density functional theory*, vol. 837. Springer Science & Business Media, **2012**.

[20] E. Rebolini, *Range-separated density-functional theory for molecular excitation energies*. PhD thesis, Université Pierre et Marie Curie-Paris VI, **2014**.

[21] K. Sneskov and O. Christiansen *Wiley Interdisciplinary Reviews: Computational Molecular Science*, vol. 2, no. 4, pp. 566–584, **2012**.

[22] J. M. Hollas, *Modern Spectroscopy*, ch. 7. John Wiley & Sons, **2004**.

[23] J. Autschbach *ChemPhysChem*, vol. 10, no. 11, p. 1757–1760, **2009**.

[24] A. Dreuw and M. Head-Gordon *Journal of the American Chemical Society*, vol. 126, no. 12, p. 4007–4016, **2004**.

[25] J. F. Janak *Physical Review B*, vol. 18, no. 12, p. 7165, **1978**.

[26] X. Blase, "Introduction to density functional theory," **2019**.

[27] E. J. Baerends *Molecular Physics*, vol. 118, no. 5, p. e1612955, **2020**.

[28] H. Iikura, T. Tsuneda, T. Yanai, and K. Hirao *The Journal of Chemical Physics*, vol. 115, no. 8, pp. 3540–3544, **2001**.

[29] T. M. Henderson, A. F. Izmaylov, G. Scalmani, and G. E. Scuseria *The Journal of Chemical Physics*, vol. 131, no. 4, p. 044108, **2009**.

[30] D. Jacquemin, B. Moore, A. Planchat, C. Adamo, and J. Autschbach *Journal of Chemical Theory and Computation*, vol. 10, no. 4, pp. 1677–1685, **2014**.

[31] D. Jacquemin, B. Mennucci, and C. Adamo *Physical Chemistry Chemical Physics*, vol. 13, no. 38, p. 16987, **2011**.

[32] M. J. Frisch, G. W. Trucks, H. B. Schlegel, G. E. Scuseria, M. A. Robb, J. R. Cheeseman, G. Scalmani, V. Barone, G. A. Petersson, H. Nakatsuji, X. Li, M. Caricato, A. V. Marenich, J. Bloino, B. G. Janesko, R. Gomperts, B. Mennucci, H. P. Hratchian, J. V. Ortiz, A. F. Izmaylov, J. L. Sonnenberg, D. Williams-Young, F. Ding, F. Lipparini, F. Egidi, J. Goings, B. Peng, A. Petrone, T. Henderson, D. Ranasinghe, V. G. Zakrzewski, J. Gao, N. Rega, G. Zheng, W. Liang, M. Hada, M. Ehara, K. Toyota, R. Fukuda, J. Hasegawa, M. Ishida, T. Nakajima, Y. Honda, O. Kitao, H. Nakai, T. Vreven, K. Throssell, J. A. Montgomery Jr., J. E. Peralta, F. Ogliaro, M. J. Bearpark, J. J. Heyd, E. N. Brothers, K. N. Kudin, V. N. Staroverov, T. A. Keith, R. Kobayashi, J. Normand, K. Raghavachari, A. P. Rendell, J. C. Burant, S. S. Iyengar, J. Tomasi, M. Cossi, J. M. Millam, M. Klene, C. Adamo, R. Cammi, J. W. Ochterski, R. L. Martin, K. Morokuma, O. Farkas, J. B. Foresman, and D. J. Fox, "Gaussian 16 Revision C.01," **2016**.

[33] F. Neese *Wiley Interdisciplinary Reviews: Computational Molecular Science*, vol. 2, no. 1, pp. 73–78, **2012**.

[34] F. Neese *Wiley Interdisciplinary Reviews: Computational Molecular Science*, vol. 8, no. 1, pp. 4–9, **2018**.

[35] S. T. Pantelides *Review of Modern Physics*, vol. 50, pp. 797–858, **1978**.

[36] A. Curutchet and T. Le Bahers *Inorganic Chemistry*, vol. 56, no. 1, p. 414–423, **2017**.

[37] D. Borwein, J. M. Borwein, and K. F. Taylor *Journal of Mathematical Physics*, vol. 26, no. 11, pp. 2999–3009, **1985**.

[38] M. Klintenberg, S. E. Derenzo, and M. J. Weber *Computer Physics Communications*, vol. 131, no. 1, pp. 120–128, **2000**.

[39] P. J. Hay and W. R. Wadt *The Journal of Chemical Physics*, vol. 82, no. 1, pp. 299–310, **1985**.

[40] J. M. Vail, E. Emberly, T. Lu, M. Gu, and R. Pandey *Physical Review B*, vol. 57, no. 2, p. 764–772, **1998**.

[41] L. Kantorovich *Journal of Physics C: Solid State Physics*, vol. 21, no. 29, p. 5041, **1988**.

CHAPTER III

Technical aspects of the project

There are two objectionable types of believers: those who believe the incredible and those who believe that 'belief' must be discarded and replaced by the scientific method.

Max Born

This chapter is equivalent to a computational details section in an article. It aims at introducing all the parameters chosen for the different type of calculation in order to avoid repeating them in the different chapters devoted to results and discussion. The chapter is divided into two sections. The first and main one is devoted to computational aspects of this research project, while the second one will introduce experimental details of specific setups developed by collaborators to study tenebrescent minerals.

III.1. Computational details

III.1.1. Basis sets used for the study

Unless mentioned otherwise, the basis sets used in the different calculations (within periodic or molecular approaches) are the ones provided in the following paragraph.
All-electron double-ζ basis sets with polarization functions were used for Si ([4s3p1d]/(20s12p1d)), [1] Al ([4s3p1d]/(17s9p1d)),[2] O ([3s2p1d]/(10s4p1d)),[3] and Cl ([4s3p1d]/(16s10p1d)).[4]
For Se a modified version of Heyd's double-ζ basis sets was used ([5s4p2d]/(15s14p7d)).

[5]
All-electron triple-ζ basis sets with polarization functions were used for Na ([4s3p1d]/(15s7p1d),[6] K ([5s4p1d]/(21s13p3d)),[7] Ga ([6s5p4d]/(17s12p8d)),[8] Ge ([5s4p3d]/(26s17p7d)),[6] Te ([4s4p4d]/(9s8p9d)),[8] I ([4s4p4d]/(9s9p9d)), [9] and Br ([6s5p4d]/(17s13p8d)).[8]
For the S atom, the quadruple-ζ basis set ([6s5p2d]/(20s12p2d)) was used.[10]
For selenium, tellurium and iodine, pseudopotentials are used to exclude the atomic core electrons, while the respectively 14, 24 and 25 valence electrons are treated with the previously given basis set.

Basis set for the trapped electron

Gaussian basis sets for trapped electrons in different materials were optimized (cf. IV.2.1.1) They are of the form 111G(d) and their alpha exponents were successively optimized by minimizing the energy of the the $[Na_4V_{Cl}]^{3+}$ system in a gaussian calculation with PBE0 functional. The method was developed on sodalite material but the same approach was followed in the case of trapped electron in a Na_4 square (*i.e.* in marialite). The basis set for the trapped electron in a material was reoptimized when going from the coloured to the colorless form of the material since the geometry around the defect changes quite a lot. The optimized α exponent coefficients of the radial part of 111G(d) basis set for the coloured and colourless forms of the different materials studied are given in table III.1.

III.1.2. Periodic Boundary Conditions calculations

All PBC calculations, included frequency calculations, were performed within the density functional theory (DFT) framework with the global hybrid functional PBE0[11] along with the ab initio CRYSTAL17 code,[12] using localized (Gaussian) basis sets. HF and KS equations were solved self-consistently with convergence criterion for the SCF cycles fixed at 10^{-7} Ha per unit cell. Numerical derivatives were used to compute vibrational frequency.
The reciprocal space was sampled according to a sublattice with a 12x12x12 k-points mesh for the geometry optimization of the bulk system, while a single k point (the Γ point) was used for the geometry optimization of the supercells.

Density of States calculations

The different density of state calculations were performed with a k-points sampling of 4X4X1. 2500 uniformly spaced energy values were used for the calculation of the DOS and PDOS, from -0.4 to 0.3 Hartree. 15 Legendre polynomials were used to expand the densities of state following the suggested value of CRYSTAL package.[12]

Materials name / formula	colourless forms *sp* #1	*sp* #2	*sp* #3	*d* #4	coloured forms *sp* #1	*sp* #2	*sp* #3	*d* #4
Hackmanite / $Na_8(SiAlO_4)_6Cl_2$	0.065	0.034	0.128	0.050	0.050	0.025	0.232	0.055
SiAl**Br** / $Na_8(SiAlO_4)_6\mathbf{Br}_2$	0.031	0.016	0.057	0.044	0.047	0.024	0.367	0.055
SiAl**I** / $Na_8(SiAlO_4)_6\mathbf{I}_2$	0.027	0.014	0.029	0.039	0.043	0.022	0.324	0.053
GeAlCl / $(Na_8(\mathbf{Ge}AlO_4)_6Cl_2$	0.032	0.016	0.030	0.046	0.051	0.026	0.431	0.055
GeAl**Br** / $Na_8(\mathbf{Ge}AlO_4)_6\mathbf{Br}_2$	0.032	0.016	0.050	0.044	0.047	0.024	0.389	0.054
GeAl**I** / $Na_8(\mathbf{Ge}AlO_4)_6\mathbf{I}_2$	0.029	0.015	0.030	0.042	0.043	0.022	0.354	0.053
Si**Ga**Cl / $Na_8(Si\mathbf{Ga}AlO_4)_6Cl_2$	0.034	0.017	0.063	0.046	0.051	0.026	0.489	0.055
Si**GaBr** / $Na_8(Si\mathbf{Ga}AlO_4)_6\mathbf{Br}_2$	0.032	0.016	0.037	0.045	0.048	0.024	0.380	0.055
Si**GaI** / $Na_8(Si\mathbf{Ga}AlO_4)_6\mathbf{I}_2$	0.030	0.015	0.031	0.043	0.044	0.022	0.331	0.053
GeGaCl / $Na_8(\mathbf{GeGa}O_4)_6Cl_2$	0.033	0.017	0.047	0.046	0.051	0.026	0.483	0.055
GeGaBr / $Na_8(\mathbf{GeGa}O_4)_6\mathbf{Br}_2$	0.032	0.016	0.039	0.045	0.047	0.024	0.429	0.054
GeGaI / $Na_8(\mathbf{GeGa}O_4)_6\mathbf{I}_2$	0.030	0.015	0.032	0.043	0.044	0.022	0.340	0.053
Na_3K / $(Na_{0.984}\mathbf{K}_{0.016})_8(SiAlO_4)_6Cl_2$	0.069	0.035	0.133	0.069	0.050	0.025	0.212	0.062
Na_2K_2 / $(Na_{0.969}\mathbf{K}_{0.031})_8(SiAlO_4)_6Cl_2$	0.072	0.036	0.146	0.071	0.050	0.025	0.198	0.065
NaK_3 / $(Na_{0.953}\mathbf{K}_{0.047})_8(SiAlO_4)_6Cl_2$	0.076	0.038	0.150	0.075	0.050	0.025	0.175	0.063
Tugtupite / $Na_8Al_2Be_2Si_8O_{24}Cl_2$	0.034	0.017	0.069	0.047	0.051	0.026	0.241	0.063
Scapolite (Marialite) / $Na_4(Al_3Si_9O_{24})Cl$	0.035	0.018	0.077	0.048	0.045	0.230	0.056	0.060

Table III.1: Optimized α exponent coefficients of the radial part of 111G(d) basis set in $[Na_4V_X]^{3+}$ for the geometries of colourless and coloured forms of different materials. The purple, red and blue lines correspond respectively to hackmanite, tugtupite and marialite materials. The green block contains information about the so-called artificial hackmanites for which the atom(s) in bold substitute(s) the original one of hackmanite's composition. The yellow block provide the α exponent coefficients optimized in $[Na_xK_xV_X]^{3+}$ ($\forall x \in \{1,2,3\}$).

III.1.3. TD-DFT calculations

TD-DFT calculations were performed preferentially with Gaussian 16 package[13] on extracted clusters of the different systems studied. The cluster could be saturated by hydrogen atoms, embedded in a sphere of pseudo-potentials or in an array of point charges. The pseudopotentials used are D95 Stuttgart/Dresden when considering beryllium cations, and LANL2 (Los Alamos National Laboratory) when considering Si or Al cations. Different functionals have been used throughout the course of this work and are listed below:

- GGA functionals: BP86,[14, 15] PW91,[16] PBE,[17] B97D;[18]
- hybrid-GGA: TPSSh,[19] B3PW91,[14, 15, 17] B3LYP,[16, 20–23] PBE0,[11] BMK,[24] M06-2X;[25]
- pure meta-GGA functionals: MN15-L,[26] tHCTH;[27]
- RSH functionals: CAM-B3LYP,[28] ωB97X-D,[29] LC-ωHPBE,[30] HSE06.[31]

For triplet states calculations we switched to the TDA method.[32, 33]
Default UltraFine grid was kept for numerical integration.

III.1.4. Vibronic coupling

Normal vibration modes (NVM) of the GS and EES of interest were obtained from PBC frequency calculations and associated two by two using the hungarian algorithm (we implemented in python[34]). Vibronic coupling calculations were then performed within the Franck-Condon approximation using FCclasses code. [35] The adiabatic energy of a transition was defined as the average value between the absorption and emission energies related to that transition[36], obtained through TD-DFT calculations. For C_1 and C_2 class FC integrals, the maximum number of states considered was fixed respectively at 25 and 20. The temperature was set to 10 K, the accuracy parameter for the integral calculation set at 10^6 (as suggested for small displacements) and up to 7 NVMs could be coupled (C_7 class FC integrals).
Up to 500 points were used to generate the final curve. Validity of the FC approximation was systematically verified with FCT factors greater than 0.99.

III.1.5. Generation of the array of point charges

Point charges used to simulate the Madelung potential of the crystal were obtained through the Ewald package.[37–39] A 5X5X5 supercell was used to generate the point charges in order to embed the cluster in approximately 50000 charges. The fitting procedure leads to an RMS error lower than 1 µV on the Madelung potential.

III.1.6. Post Hartree Fock calculations

SAC-CI

Only few calculations were done in SAC-CI through Gaussian 16 package.[13] The recommended Direct algorithm[40] was used to access the 10 lowest excited singlet and triplet states of each irreducible representation, setting the selection parameter for the double excitation operator to its recommended highest value (LevelThree).

CISD

CISD calculations were performed with Orca[41, 42] with the def2-TZVP basis set, and RIJCOSX approximation was used in order to speed up the calculations.

CASSCF/CASPT2

CASSCF/CASPT2 calculations were performed using openMOLCAS package [43] with orbital optimisation for the average energy of 4 states with equal weight (CiRoot 4 4 1) and multistate perturbation correction on the same 4 states. Threshold for energy was set to 10^{-8} Ha.

III.1.7. Simulation of the colour

The energies of transition and the respective oscillator strengths were used as input in a code developed in our group to obtain the corresponding coordinates of transmittance. This data are the input for the script that simulates the colour. In the model we use, adopted in 1931 by the International Commission on Illumination (CIE), a colour is defined in a vectorial space by three components called the trichromatic components: X, Y and Z. These components result from the conversion of the absorption properties (or reflectance R) of a material combined with the spectral density (S) of the irradiating light into numbers according to the following formula:

$$X = K \int S(\lambda)\bar{x}(\lambda)R(\lambda)\,\mathrm{d}\lambda \tag{III.1}$$

$$Y = K \int S(\lambda)\bar{y}(\lambda)R(\lambda)\,\mathrm{d}\lambda \tag{III.2}$$

$$Z = K \int S(\lambda)\bar{z}(\lambda)R(\lambda)\,\mathrm{d}\lambda \tag{III.3}$$

K is a normalisation factor and $\bar{x}$, $\bar{y}$ and $\bar{z}$ are functions to take into account the relative sensibility of the observer. Tables containing the data for a standard observer and the spectral density of different light source exist, and were included in the code. Unless

otherwise specified, the spectral density of sunlight at 6504 K was used. Finally, linear equations allow to convert the X,Y and Z components into the more familiar R,G and B ones.

III.2. Analytical chemistry methods

All experimental results were provided by the group of Mika Lastusaari, our collaborators from Turku University (Finland). They developed specific analytical techniques for studying tenebrescent minerals that we will briefly introduce: tenebrescence excitation experiments and thermotenebrescence experiments.[44]

III.2.1. Classical analysis

Classical chemical analysis were performed on the natural samples used in this project, among which X-Ray diffraction (for structure analysis), X-Ray photoelectron spectroscopy (for compositional analysis), or reflectance UV-Vis spectroscopy. Details about the method and the different devices can be found in publications we will provide as soon as needed.

III.2.2. Tenebrescence excitation experiments

This method has been developed in order to extract the activation energy of photochromism in tenebrescent minerals and proceeds as follows:

- white samples are irradiated for one minute at a given wavelength with a Xenon lamp (Varian Cary Eclipse spectrometer equipped with a 150 W xenon lamp & Samsung A3 camera),
- at each wavelength, a photography of the sample is taken from which the color intensity is determined by the ratio of RGB values for the irradiated and non-irradiated parts using ImageJ program, [45]
- the color is bleached with white light between each point.

Tenebrescence excitation spectra were recorded from powder samples.
There is no convention for extracting activation energies from the tenebrescence excitation spectra obtained. Hence we combined the moment the colour can be seen with eyes, and changes in the shape of the curve.

III.2.3. Thermotenebrescence experiments

The discoloration of tenebrescent mineral can be followed thanks to a new method[46] called thermotenebrescence. The idea is to follow the discolouration of an initially fully

coloured sample as a function of temperature. In practise, the heating rate is of 3° C.s^{-1} and the discolouration is evaluated by measuring the reflectance of the material at several temperatures.
Some care has to be taken due to the fact that bleaching of the material can also be induced by light. Hence a second measurement is done where the material is not heated but simply illuminated by the lamp used in the spectrometer, and the resulting fading is removed from the thermotenebrescence curves.
Finally, the thermal bleaching energies can be obtained from these curves using the initial rise method. [47]

References Chapter III.

[1] R. Nada, J. B. Nicholas, M. I. McCarthy, and A. C. Hess *International Journal of Quantum Chemistry*, vol. 60, no. 4, pp. 809–820, **1996**.

[2] R. Demichelis, Y. Noel, B. Civalleri, C. Roetti, M. Ferrero, and R. Dovesi *The Journal of Physical Chemistry B*, vol. 111, no. 31, pp. 9337–9346, **2007**.

[3] M. Corno, C. Busco, B. Civalleri, and P. Ugliengo *Physical Chemistry Chemical Physics*, vol. 8, no. 21, pp. 2464–2472, **2006**.

[4] P. C. Hariharan and J. A. Pople *Theoretica Chimica Acta*, vol. 28, no. 3, pp. 213–222, **1973**.

[5] J. Heyd, J. E. Peralta, G. E. Scuseria, and R. L. Martin *The Journal of Chemical Physics*, vol. 123, no. 17, p. 174101, **2005**.

[6] G. Sophia, P. Baranek, C. Sarrazin, M. Rerat, and R. Dovesi, "www.crystal.unito.it/basis-sets.php," **2014**.

[7] B. Civalleri, A. M. Ferrari, M. Llunell, R. Orlando, M. Merawa, and P. Ugliengo *Chemistry of Materials*, vol. 15, no. 21, pp. 3996–4004, **2003**.

[8] M. F. Peintinger, D. V. Oliveira, and T. Bredow *Journal of Computational Chemistry*, vol. 34, no. 6, pp. 451–459, **2013**.

[9] J. Laun, D. Vilela Oliveira, and T. Bredow *Journal of Computational Chemistry*, vol. 39, no. 19, p. 1285–1290, **2018**.

[10] T. Bredow, P. Heitjans, and M. Wilkening *Physical Review B*, vol. 70, no. 11, **2004**.

[11] C. Adamo and V. Barone *The Journal of Chemical Physics*, vol. 110, no. 13, pp. 6158–6170, **1999**.

[12] R. Dovesi, V. Saunders, C. Roetti, R. Orlando, C. Zicovich-Wilson, F. Pascale, B. Civalleri, K. Doll, N. Harrison, I. Bush, P. D'Arco, M. Llunell, M. Causà, Y. Noël, L. Maschio, A. Erba, M. Rerat, and S. Casassa **2017**.

[13] M. J. Frisch, G. W. Trucks, H. B. Schlegel, G. E. Scuseria, M. A. Robb, J. R. Cheeseman, G. Scalmani, V. Barone, G. A. Petersson, H. Nakatsuji, X. Li, M. Caricato, A. V. Marenich, J. Bloino, B. G. Janesko, R. Gomperts, B. Mennucci, H. P. Hratchian, J. V. Ortiz, A. F. Izmaylov, J. L. Sonnenberg, D. Williams-Young, F. Ding, F. Lipparini, F. Egidi, J. Goings, B. Peng, A. Petrone, T. Henderson, D. Ranasinghe, V. G. Zakrzewski, J. Gao, N. Rega, G. Zheng, W. Liang, M. Hada, M. Ehara, K. Toyota, R. Fukuda, J. Hasegawa, M. Ishida, T. Nakajima, Y. Honda, O. Kitao, H. Nakai, T. Vreven, K. Throssell, J. A. Montgomery Jr., J. E. Peralta, F. Ogliaro, M. J. Bearpark, J. J. Heyd, E. N. Brothers, K. N. Kudin, V. N. Staroverov, T. A. Keith, R. Kobayashi, J. Normand, K. Raghavachari, A. P. Rendell, J. C. Burant, S. S. Iyengar, J. Tomasi, M. Cossi, J. M. Millam, M. Klene, C. Adamo, R. Cammi, J. W. Ochterski, R. L. Martin, K. Morokuma, O. Farkas, J. B. Foresman, and D. J. Fox, "Gaussian 16 Revision C.01," **2016**.

[14] A. D. Becke *Physical Review A*, vol. 38, no. 6, p. 3098, **1988**.

[15] J. P. Perdew *Physical Review B*, vol. 33, pp. 8822–8824, **1986**.

[16] J. P. Perdew, J. Chevary, S. Vosko, K. A. Jackson, M. R. Pederson, D. Singh, and C. Fiolhais *Physical Review B*, vol. 48, no. 7, p. 4978, **1993**.

[17] J. P. Perdew, K. Burke, and M. Ernzerhof *Physical Review Letters*, vol. 77, pp. 3865–3868, **1996**.

[18] S. Grimme *Journal of Computational Chemistry*, vol. 27, no. 15, pp. 1787–1799, **2006**.

[19] J. Tao, J. P. Perdew, V. N. Staroverov, and G. E. Scuseria *Physical Review Letters*, vol. 91, no. 14, p. 146401, **2003**.

[20] A. D. Becke *The Journal of Chemical Physics*, vol. 98, no. 2, pp. 1372–1377, **1993**.

[21] C. Lee, W. Yang, and R. G. Parr *Physical Review B*, vol. 37, no. 2, p. 785, **1988**.

[22] S. H. Vosko, L. Wilk, and M. Nusair *Canadian Journal of Physics*, vol. 58, no. 8, pp. 1200–1211, **1980**.

[23] P. J. Stephens, F. J. Devlin, C. F. Chabalowski, and M. J. Frisch *The Journal of Physical Chemistry*, vol. 98, no. 45, pp. 11623–11627, **1994**.

[24] A. D. Boese and J. M. L. Martin *The Journal of Chemical Physics*, vol. 121, no. 8, p. 3405–3416, **2004**.

[25] Y. Zhao and D. G. Truhlar *Theoretical Chemistry Accounts*, vol. 120, no. 1, pp. 215–241, **2008**.

[26] H. S. Yu, X. He, and D. G. Truhlar *Journal of Chemical Theory and Computation*, vol. 12, no. 3, pp. 1280–1293, **2016**.

[27] A. D. Boese and N. C. Handy *The Journal of Chemical Physics*, vol. 116, no. 22, p. 9559–9569, **2002**.

[28] T. Yanai, D. P. Tew, and N. C. Handy *Chemical Physics Letters*, vol. 393, no. 1-3, p. 51–57, **2004**.

[29] J.-D. Chai and M. Head-Gordon *Physical Chemistry Chemical Physics*, vol. 10, no. 44, p. 6615, **2008**.

[30] T. M. Henderson, A. F. Izmaylov, G. Scalmani, and G. E. Scuseria *The Journal of Chemical Physics*, vol. 131, no. 4, p. 044108, **2009**.

[31] A. V. Krukau, O. A. Vydrov, A. F. Izmaylov, and G. E. Scuseria *The Journal of Chemical Physics*, vol. 125, no. 22, p. 224106, **2006**.

[32] M. J. Peach, M. J. Williamson, and D. J. Tozer *Journal of Chemical Theory and Computation*, vol. 7, no. 11, pp. 3578–3585, **2011**.

[33] M. J. Peach, N. Warner, and D. J. Tozer *Molecular Physics*, vol. 111, no. 9-11, pp. 1271–1274, **2013**.

[34] Python Software Foundation. Python Language Reference, version 2.7., **http://www.python.org**.

[35] F. Santoro, R. Improta, A. Lami, J. Bloino, and V. Barone *The Journal of Chemical Physics*, vol. 126, no. 8, p. 084509, **2007**.

[36] D. Jacquemin, A. Planchat, C. Adamo, and B. Mennucci *Journal of Chemical Theory and Computation*, vol. 8, no. 7, pp. 2359–2372, **2012**.

[37] M. Klintenberg, S. E. Derenzo, and M. J. Weber *Computer Physics Communications*, vol. 131, no. 1, pp. 120–128, **2000**.

[38] S. E. Derenzo, M. K. Klintenberg, and M. J. Weber *The Journal of Chemical Physics*, vol. 112, no. 5, pp. 2074–2081, **2000**.

[39] D. Stueber, F. N. Guenneau, and D. M. Grant *The Journal of Chemical Physics*, vol. 114, no. 21, pp. 9236–9243, **2001**.

[40] M. Ehara, M. Ishida, K. Toyota, and H. Nakatsuji, "SAC-CI general-R method: theory and applications to the multi-electron processes," in *Reviews of Modern Quantum Chemistry: A Celebration of the Contributions of Robert G Parr (In 2 Volumes)*, pp. 293–319, World Scientific, **2002**.

[41] F. Neese *Wiley Interdisciplinary Reviews: Computational Molecular Science*, vol. 2, no. 1, pp. 73–78, **2012**.

[42] F. Neese *Wiley Interdisciplinary Reviews: Computational Molecular Science*, vol. 8, no. 1, pp. 4–9, **2018**.

[43] I. Fdez. Galván, M. Vacher, A. Alavi, C. Angeli, F. Aquilante, J. Autschbach, J. J. Bao, S. I. Bokarev, N. A. Bogdanov, R. K. Carlson, L. F. Chibotaru, J. Creutzberg, N. Dattani, M. G. Delcey, S. S. Dong, A. Dreuw, L. Freitag, L. M. Frutos, L. Gagliardi, F. Gendron, A. Giussani, L. González, G. Grell, M. Guo, C. E. Hoyer, M. Johansson, S. Keller, S. Knecht, G. Kovačević, E. Källman, G. Li Manni, M. Lundberg, Y. Ma, S. Mai, J. P. Malhado, P. Å. Malmqvist, P. Marquetand, S. A. Mewes, J. Norell, M. Olivucci, M. Oppel, Q. M. Phung, K. Pierloot, F. Plasser, M. Reiher, A. M. Sand, I. Schapiro, P. Sharma, C. J. Stein, L. K. Sørensen, D. G. Truhlar, M. Ugandi, L. Ungur, A. Valentini, S. Vancoillie, V. Veryazov, O. Weser, T. A. Wesołowski, P.-O. Widmark, S. Wouters, A. Zech, J. P. Zobel, , and R. Lindh *Journal of Chemical Theory and Computation*, vol. 15, no. 11, p. 5925–5964, **2019**.

[44] I. Norrbo, *Synthetic hackmanites and their optical properties - From theory to applications.* PhD thesis, University of Turku, **2019**.

[45] C. A. Schneider, W. S. Rasband, and K. W. Eliceiri *Nature Methods*, vol. 9, no. 7, pp. 671–675, **2012**.

[46] I. Norrbo, A. Curutchet, A. Kuusisto, J. Mäkelä, P. Laukkanen, P. Paturi, T. Laihinen, J. Sinkkonen, E. Wetterskog, F. Mamedov, T. Le Bahers, and M. Lastusaari *Materials Horizons*, vol. 5, no. 3, p. 569–576, **2018**.

[47] R. Chen and S. W. McKeever, *Theory of thermoluminescence and related phenomena*, pp. 101–110. World Scientific, **1997**.

CHAPTER IV

Modelling the photochromism of sodalite types minerals

Have no fear of perfection, you will never reach it.

Salvador Dali.

The interest in designing new photochromic material has been introduced in Chapter I with naturally-occurring photochromic mineral appearing as attractive for, among others, their high resistance towards humidity or temperature changes and possible compositional and structural tuning.[1]
Among naturally-occurring tenebrescent minerals, sodalite ($Na_8(SiAlO_4)_6Cl_2$) is the most studied one (cf. section I.3). Its photochromic properties have already been studied experimentally providing the scientific community with some insights into the phenomenon and paramount data.[1] In particular, the overall mechanism of photochromism in sodalite has been partly solved[2] and can be divided into three steps (cf. section I.3.2):

1. Activation (formation of the F-center)
2. F-center's absorption (colouration of the material)
3. Bleaching (annihilation of the F-center)

It has been shown that presence of sulfur impurities (assumed to be S_2^{2-} in this chapter) and chloride vacancies (V_{Cl}) in the structure during mineral's formation are necessary conditions for F-centers' formation (cf. I.3.2). Indeed, energy supplied by light in the UV range activates the transfer of one electron from the sulfur impurity, called **activator**, towards a nearby vacancy, leading to the formation of the F-center. The energy required

to form the F-center is called **activation energy**, while the reverse process needs an energy referred to as **bleaching energy**. This last energy can be obtained thermally or by light exposure.

$$S_2^{2-} + V_{Cl} \underset{\text{bleaching energy}}{\overset{\text{activation energy}}{\rightleftharpoons}} S_2^{-} + V_{Cl}^{-} \tag{IV.1}$$

In Equation IV.1, V_{Cl}^{-} represents the F-center (*i.e.* electron trapped in a vacancy) responsible for the colouration of the material, S_2^{2-} is the sulfur impurity. Actually the precise nature of the sulfur impurity is still open to discussion (cf. Chapter V and discussion in Section IV.3), but unless otherwise specified the activator is assumed to be the disulfide anion S_2^{2-}.

Hence, the mineral can reversibly go from the colourless to the coloured form through a charge transfer. The relative geometries of the two forms correspond respectively to the stable structure with an empty vacancy and the stable structure with a vacancy containing an electron (F-center). The lowest in energy electronic configurations of the two geometries differ by occupations of the HOMO orbital located on the activator (*e.g.* π^*) and the LUMO orbital located in the vacancy (a_1) as represented in Figure IV.1. $^1[S_2^{2-}, V_{Cl}]$ is the most stable electronic configuration in the geometry of the colourless form. In the case of the coloured form the triplet state ($^3[S_2^{-}, V_{Cl}^{-}]$ electronic configuration) is more stable than the singlet one ($^1[S_2^{-}, V_{Cl}^{-}]$ electronic configuration).

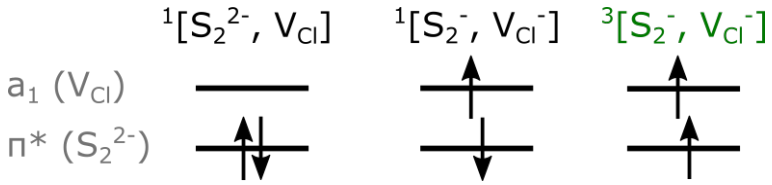

Figure IV.1: Orbital description of different electronic states. π^* is the HOMO located on the sulfur impurity, a_1 the LUMO located in the vacancy.

To summarize the overall process, these different states are energetically classified onto the Jablonski diagram representing the electron transfers at stake in sodalite's photochromism (cf. Figure IV.2). After the electron transfer from S_2^{2-} to V_{Cl} (*i.e.* $^1[S_2^{2-}, V_{Cl}] \rightarrow^1 [S_2^{-}, V_{Cl}^{-}]$) there is a geometry relaxation leading to an inversion of stability between the different states, followed by a spin relaxation. This is in agreement with the experimental metastability of the coloured form. Conventionally, bleaching energy is negative, the reference electronic state being $^1[S_2^{2-}, V_{Cl}]$. On the same Figure is also represented the configurations and respective energies of the GS ($^3[S_2^{-}, V_{Cl}^{-}] =^3 [S_2^{-}, V_{Cl}^{-}(a_1)]$) and first ES ($^3[S_2^{-}, V_{Cl}^{-}(t_2)]$) of the trapped electron that are involved in the absorption process leading to the colouration of the material.

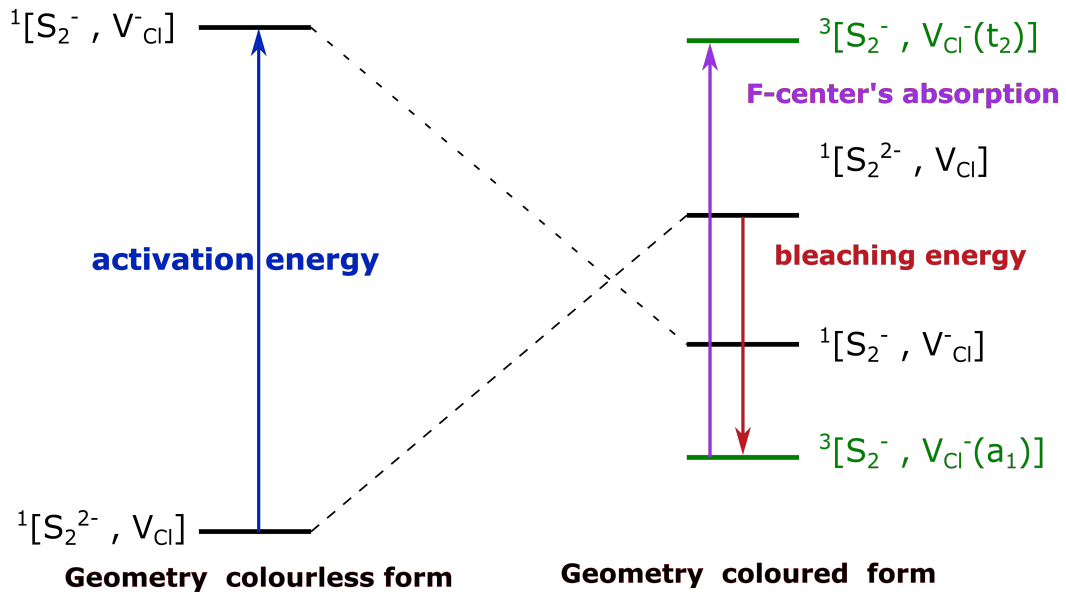

Figure IV.2: Jablonski diagram representing the electron transfers at stake in sodalite's photochromism. The F-center's absorption energy, activation energy and the bleaching energy are depicted by respectively a purple, a blue and a red arrows.

Being able to control the amounts of energy necessary for activation and bleaching, along with the colour taken by the material is paramount to design efficient material for diverse applications (UV sensors, smart windows, etc.). Hence, the main goal of this research project is to create a quantum chemistry protocol in order to model accurately the three steps of the working principle. Sodalite is the ideal base material to develop our computational model, with the amount of experimental data collected so far proving very useful. This project will hopefully bring more insights into the chemistry of these tenebrescent minerals and a small contribution to model development in computational chemistry.

Modelling the different charge transfers is *a priori* more complex than simulating the spectroscopic properties of localized defects, since it requires to consider two defects instead of one. Hence this chapter will not follow the chronology of the photochromism mechanism but start with the simulation of the F-center's absorption, after a brief introduction on the bulk properties of sodalite. Then will come a section devoted to the activation and bleaching processes.

IV.1. Bulk properties of sodalite

Relaxation of sodalite's geometry was performed in the cubic space group ($P\bar{4}3n$) with the initial Wickoff positions (taken from experimental data) and optimized ones presented in Table IV.1.

	site	x	y	z
Na	8e	0.176	0.176	0.176
		0.178	*0.178*	*0.178*
Cl	2a	0	0	0
Si	6c	0.25	0.5	0
Al	6d	0.25	0	0.5
O	24i	0.140	0.149	0.439
		0.140	*0.149*	*0.434*

Table IV.1: Experimental and *computed* Wyckoff positions of atoms in the bulk sodalite.

The experimental cell parameter is reported around 8.85-8.87 Å[3, 4] and the computational one is 8.83 Å, hence the error (< 0.5 %) falls in the expected error range for the PBE0 functional.[5]
It has been reported that the cell parameter increases a little (up to 0.8 %) when the material contains sulfur impurity. However, for a sake of computational time saving the cell parameters obtained for pristine sodalite will be kept for now on even when impurities are included.

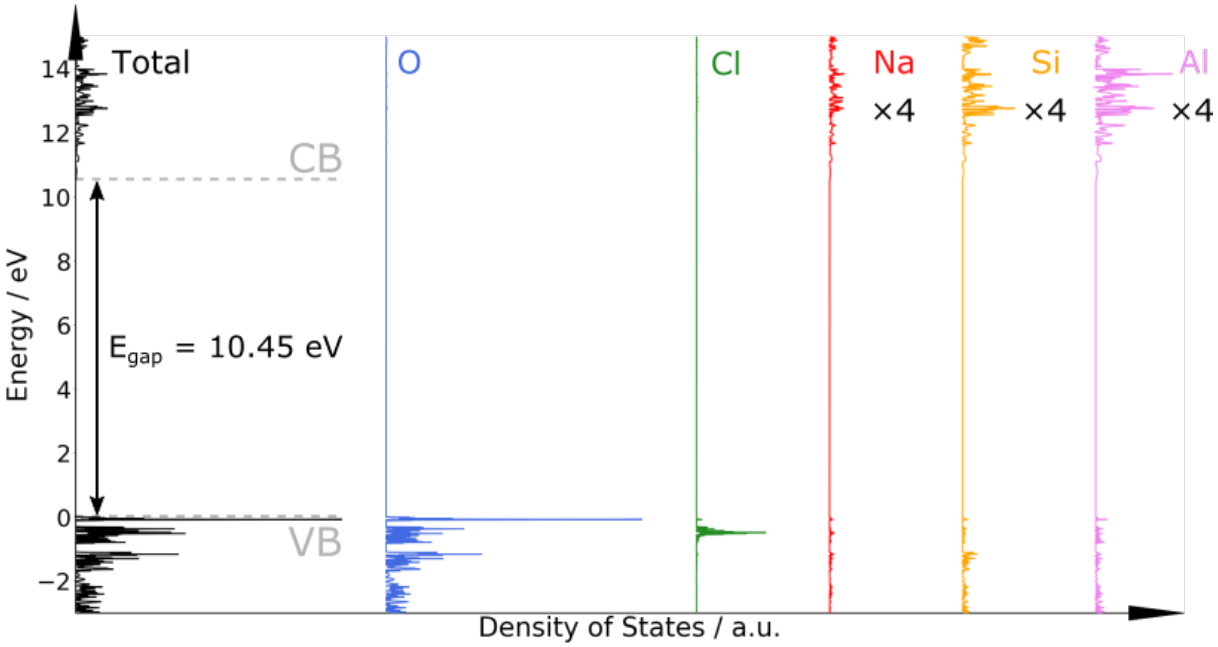

Figure IV.3: Pristine sodalite DOS (black) and PDOS on O (blue), Cl (green), Na (red), Si (yellow), and Al (pink) atoms.

Concerning the electronic properties of the bulk (cf. Figure IV.3), as previously reported[6, 7], the projection of the DOS indicates that the VB is located on the 2p orbitals of chloride and oxygen atoms while the conduction band is a made from Na, Si, and Al atomic orbitals. The band gap obtained computationally (10.45 eV) overestimates the one reported by our collaborators (around 8 eV) which is a known drawback of PBE0

functional.[5, 8]
Hence the PBC calculation provide good geometric and electronic description of sodalite material despite of a small overestimation of the band gap, and will be a good starting point for further calculations.

IV.2. Simulation of the F-center's absorption

In tenebrescent sodalite, the colouration is caused by F-center's absorption in the visible range (cf. Jablonksi diagram in Figure IV.2). This type of point defects is common in alkali earth minerals, perovskites, fluorides or other ionic oxides,[9–13] and thus has been studied both computationally and experimentally. Indeed, the presence of F-centers affects the physical and chemical properties of the materials, and in the best case leads to interesting applications especially in optics.[10, 11, 14]

At first sight, the F-center can be analyzed as a prototype of the trapped electron frequently presented in quantum physics textbooks. The first computational models were close to that philosophy, modelling the F-center as a trapped particle in a finite potential depending essentially on the Madelung potential of the material.[15, 16] But a deeper analysis reveals a larger complexity for this system, including interactions between the electron and the surrounding ions[17] or electron-phonon coupling. [18, 19]
Nowadays, two main methods are used to simulate F-centers' spectroscopic properties in solids. They can be divided into totally periodic approaches[20, 21] and molecular ones, each one with its own strengths and weaknesses.[22] In totally periodic approaches, the ground state level is obtained by solving the KS equations and the response function of the material to the perturbation is obtained through the GW approximation combined with the Bethe-Salpeter equation (BSE). Thanks to this methodology Rinke *et al.* for instance, have simulated the absorption properties of F-centers in MgO materials , with "unprecedented agreement with the experimental spectra".[20] If GW/BSE has been reported as efficient as TD-DFT to simulate excited states[23], it remains computationally expensive (runable on $\approx$ 100 atoms). However, recent ongoing developments lead us to believe that calculations on several hundred of atoms is within reach.[24]
In molecular approaches, the geometry of the ground state level is also obtained through PBC calculations. Then the calculations of the spectroscopic properties are performed on an extracted cluster at different level of theory (TD-DFT, post-HF). When dealing with spectroscopic properties of deep centers (energy level far from both VB and CB), molecular approaches have been reported to be efficient.[12, 25, 26] Moreover, when combined with (TD-)DFT level of theory they are also computationally relatively cheap to access the optical properties of the material and can be performed on several hundred of atoms.

This methodology was recently and successfully employed by Chuklina *et al.* to simulate the absorption spectra of F-center in lanthanum trifluoride.[12]

Since our systems contain several hundred of atoms, in this project the second type of approach was chosen. Thus, to investigate the spectroscopic properties of the F-center in sodalite, we used a protocol based on a combination of PBC calculations to determine geometries and vibrational frequencies of the system followed by a cluster approach to simulate excited state properties taking particular care of the embedding.
The results presented in this section have been mostly published in The Journal of Physical Chemistry C under the name: "*On the spectroscopic modelling of localized defects in Sodalites by TD-DFT*".[27]

IV.2.1. Methodology

IV.2.1.1. From periodic to cluster approach

Geometry optimizations by PBC calculations

It is common to consider that apparition of point defects do not lead to rearrangement of the crystalline matrix around (this is called the rigid lattice model[28]) but it is not correct for most defects.[12] The substitution of a chloride anion (Cl^-) by an electron in the structure was thus followed by a geometry optimization on a 2X2X2 supercell. This corresponds to 6.25% of the chloride sites modified. The introduced F-center is a neutral defect with respect to crystal lattice so that the supercell has a zero total charge.
As a matter of fact, creation of a chloride vacancy in the lattice leads to a rearrangement of the sodium tetrahedron surrounding it by an average increase of the Na-Na distance in the tetrahedron of 1 Å. Similarly the Na-Na distance around the electron increased by 0.4% compared to pristine material.

Traditionally, when substituting an element by an F-center, the basis set of the substituted element is attributed to the F-center.[12] However, there is no physical reason to do so and the chlorine's double-ζ basis set is quite big with 27 gaussian type orbitals. We decided to optimize a smaller basis set for the trapped electron. Quantum mechanics tell us that the wavefunctions of a particle in a box (trapped by an external potential) have a cosine shape.[29] Gaussian type orbitals seem then particularly adapted to describe the trapped electron. In order to describe the GS we need an *s*-type orbital, the wavefunction being nodeless and nearly isotropic. To get a description of the ES we added *p* orbitals since our ES must resemble the hydrogen's ones (cf. trapped particle in an isotropic finite potential[30]). Finally, we added a *d*-type orbital for polarization.

In the end, we decided to use three *sp* orbitals and 1 *d* orbital. The optimization of the α exponent coefficients of the radial part was conducted in an extracted Na_4 tetrahedron from the PBC calculation, in the middle of which we placed the electron (ghost atom) for which we want to optimize the basis set. The coefficients were optimized one by one following the variational principle. The criterion for the best coefficients would be the ones minimizing the energy of the system $[NaV_{Cl}]^{3+}$ in a gaussian calculation with PBE0 functional. The optimized α exponent coefficients of the radial part of 111G(d) basis set are given in table III.1.

As a matter of illustration, after PBC geometry optimization of the 2X2X2 supercell single point energy calculations on the extracted cluster $[Na_4,V_{Cl}^-]^{3+}$ were conducted using either the optimized 111G(d) basis set or the bigger chlorine's one for the trapped electron. Using the 111G(d) basis set provides a stabilization in energy by 1.79 eV compared to the initial chlorine basis set, and at a lower computational cost.

Choice of the cluster

The geometry of the structure being optimized in PBC, what interests us is modelling the absorption of the F-center responsible for the nice colouration of this tenebrescent mineral. A molecular approach (cf. section II.4) was followed in which a cluster was extracted from the geometry of the PBC calculation. The cluster is centered around the defect, that is around the trapped electron, and its transition energies and respective oscillator strengths are obtained thanks to TD-DFT calculations (without further relaxation).

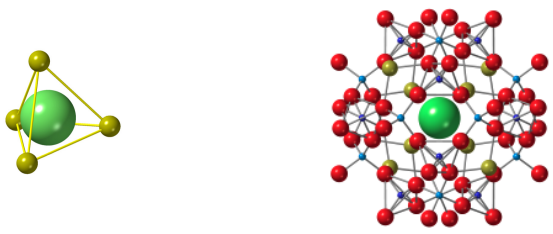

(a) Na_4 (b) Na_4 + β-cage

Figure IV.4: The two clusters surrounding the F-center, extracted from PBC geometries. Na, Cl, O, Si, and Al atoms are depicted in yellow, green, red, blue, and cyan respectively.

On account of the material's structure made of repeating β-cages each containing a sodium tetrahedron, we considered two types of clusters (that will be treated at QM level): the smallest one being the sodium tetrahedron surrounding the F-center (cf. Figure IV.4a);

the other one including as well the β-cage around the tetrahedron and the defect (cf. Figure IV.4b).

IV.2.1.2. Embedding methods

However, the use of a molecular approach comes with introduction of border effects. To deal with it and try to obtain results as close as possible to the ones one would obtain with calculations on the periodic defective solid, four approaches of embedding have been tested (only on the large cluster) and are represented in Figure IV.5

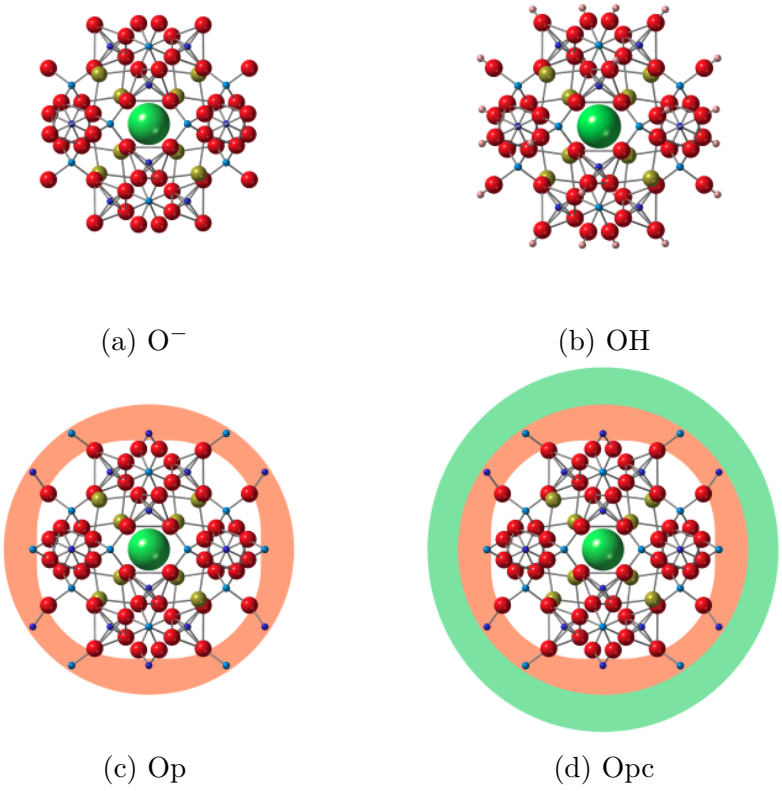

(a) O^- (b) OH

(c) Op (d) Opc

Figure IV.5: The four tested embedding of the β-cage considered for TD-DFT calculations, with Na, Cl, O, Si, Al and H atoms in yellow, green, red, blue, cyan and pink respectively. Atoms treated by pseudopotentials (pp) are placed in a purple annulus. Presence of point charges (pc) is schematically represented by a green annulus.

(a) **O^-**: no embedding, β-cage with oxygen pending bonds.

(b) **OH**: saturation of oxygen pending bonds with hydrogen, covering the β-cage with OH groups (MCM approach).

(c) **Op**: the terminating O atoms of the β-cage are surrounded by the next shell of cations described by pseudopotentials (pp) without the related basis set.

(d) **Opc**: the cluster and the cation's pseudopotential shell (d) are surrounded by an array of point charges (pc) in order to simulate the Madelung potential of the ionic sodalite crystal.

In the end we have five different systems (*i.e.* cluster + embedding): Na_4, O^-, OH, Op and Opc which allow a comparative study of several solid-state embeddings.

IV.2.1.3. Inclusion of vibronic coupling

In their work on compositional and structural control of tenebrescence in sodalite, Williams *et al.* present the main absorption band of the F-center, which is made of several small transitions.[1] These bands are attributed to vibronic coupling. Preliminary works[7] support this hypothesis by showing the influence of including the vibronic coupling in the simulation of the F-center's absorption spectra.

Starting on these first results, the idea was to include the vibronic coupling in our calculations by considering the vibrations of the tetrahedron and questioning the inclusion of β-cage's ones. In order to do so, the geometries of both the GS and the ES were needed. If for the first one it is straightforward, the geometry of T_2 excited state was obtained in PBC through a ΔSCF procedure. This was done by applying constraints consisting in removing all the *s* orbitals from the trapped electron basis set which entails a forced fill of the *p* ones (compatible with the T_2 representation) during the SCF procedure.
From these geometries the vibrational frequencies were calculated. Frequency calculations on 68 atoms (Na_4 + β-cage) is particularly tough and computationally demanding, especially for excited state normal modes analysis. That is why when including the vibration of the β-cage a smaller basis set was used for the trapped electron. It consists in removing the most diffuse *sp* orbital (*e.g.* 11G(d)). Indeed too small α exponent coefficients gives rise to a large overlap between the basis functions, and can lead to numerical instabilities.

The adiabatic electronic transition energy is approximated by the average value between the absorption and emission energies related to the transition at stake obtained through TD-DFT calculations on the system.

IV.2.2. Results and discussion

IV.2.2.1. Density of states

In the first instance, the addition of the F-center impurity in the periodic structure of pristine sodalite material leads to apparition of new states in the band gap (yellow in Figure IV.6). They correspond to the highest occupied orbital (a_1) and the first degenerated lowest unoccupied orbitals (t_2) of the trapped electron (cf. Character Table A.1 for Td point group of symmetry), and are separated by 3.77 eV. This first estimate of the F-center's energy of absorption obviously overestimates the experimental one by 1.4 eV and further modelling are of course required. The difference in energy between the HOMO of the trapped electron and the VB or CB is more than 10% of the band gap, making this defect a deep center.

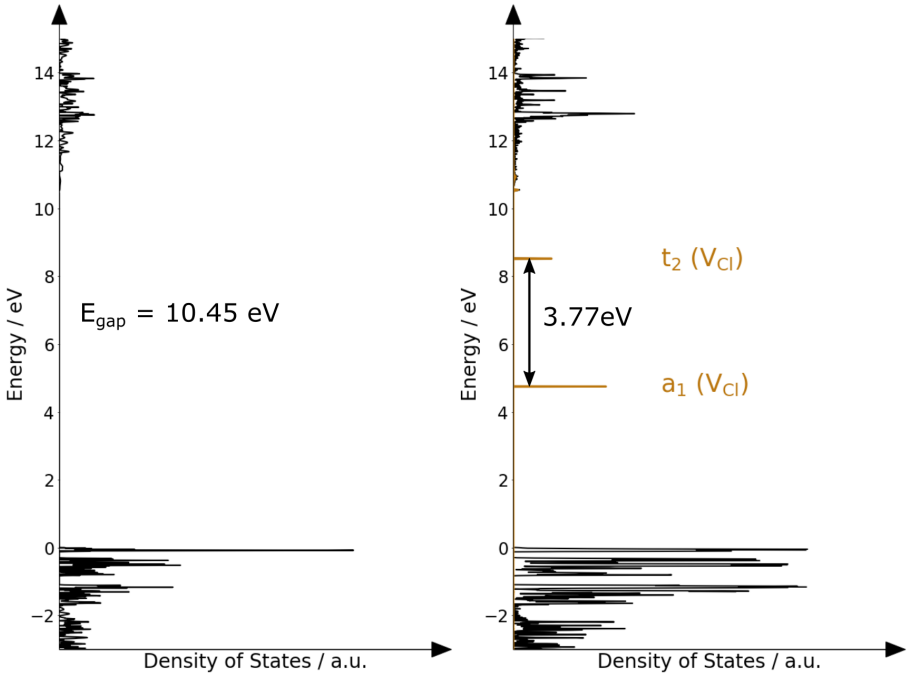

Figure IV.6: Density of States of pristine material compared with the one containing the F-center. New states appear in the band gap; they correspond to the HOMO (a_1) and the first degenerated LUMO (t_2) of the F-center.

IV.2.2.2. Spectroscopy

IV.2.2.2.a Influence of the embedding

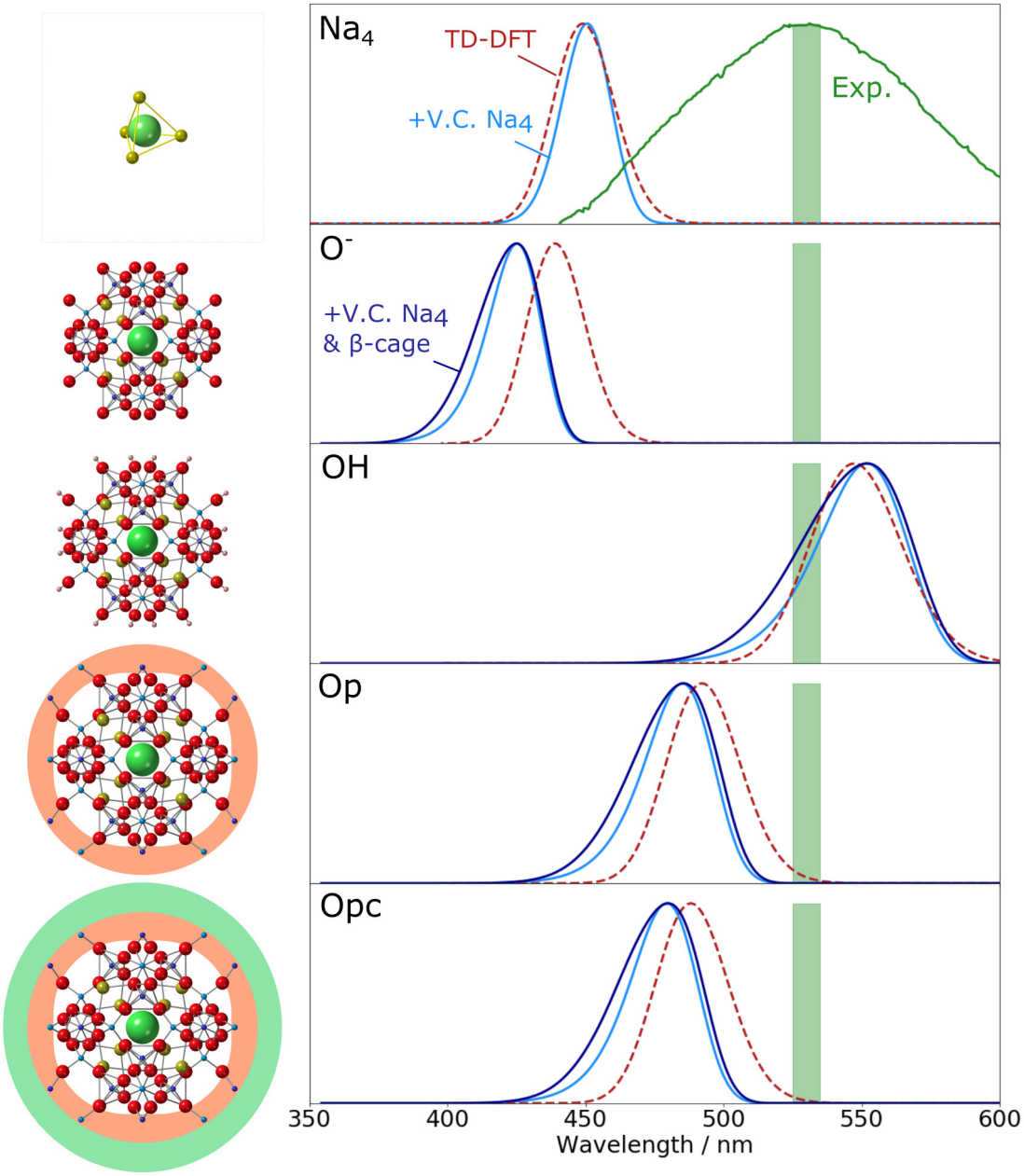

Figure IV.7: F-center's absorption simulated with the use of different calculations methods including or not vibronic coupling. On the outer parts, the molecular approaches considered (cluster + embedding) with Na, Cl, O, Si, Al and H atoms in yellow, green, red, blue, cyan and beige respectively. Atoms treated by pseudopotentials (pp) are placed in an orange annulus. Presence of point charges (pc) is schematically represented by a green annulus. On the graphics, the experimental data are fully represented on the uppermost rectangle and otherwise shown by the green bar standing for the maximum absorption wavelength. TD-DFT/PBE0 results convoluted by a gaussian are represented by a red dotted line (no vibronic coupling). The light blue curves are obtained by the addition of the vibronic coupling considering only the vibrations of the sodium tetrahedron. The dark blue curves are obtained by the addition of the vibronic coupling of both the sodium tetrahedron and the β-cage, but using a smaller basis set for the F-center (11G(d), most diffuse sp orbital removed)).

We conducted a comparative study on the five different systems (*i.e.* combination of cluster and embedding). TD-DFT/PBE0 vertical absorption peaks convoluted by a gaussian are represented by a red dotted line in Figure IV.7. By comparing them with the experimental data one can draw the conclusion that inclusion of a properly embedded β-cage in the quantum mechanical (QM) part is necessary. This can be explained by the significant delocalization of the trapped electron's orbitals onto the β-cage as seen in Figure IV.8.

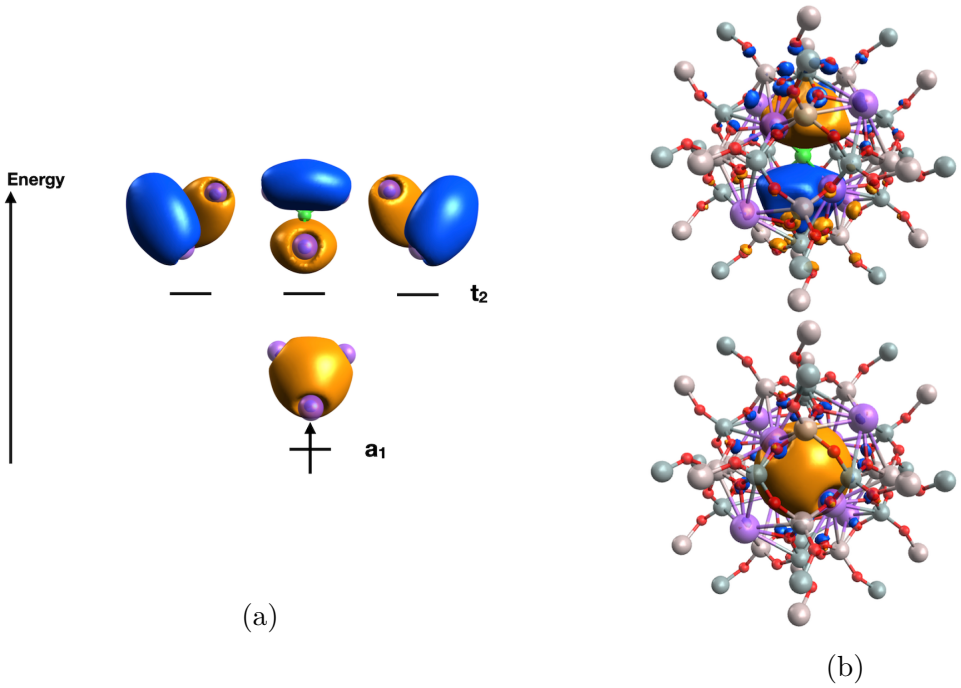

(a) (b)

Figure IV.8: (a) trapped electron's orbitals involved in the absorption arranged in energy and labelled in symmetry. (b) representation of the a_1 and one t_2 orbital of the trapped electron in the β-cage. Orbitals generated with isovalue 0.02 after TD-DFT/PBE0 calculation on Opc system.

As in the orbital description from PBC calculations PBE0 functional overestimates F-center's absorption energy, which corresponds to a blue-shift of the maximum absorption wavelength with respect to the experimental one, for all systems but OH. Distinction between the last three embeddings, OH (underestimation by 0.07 eV), Op (overestimation by 0.10 eV) and Opc (overestimation by 0.17 eV) is difficult. Even if the result obtained with OH system is closer to experiment, the underestimation of the absorption energy suggests an error compensation due to spurious effect on the cage boundaries. At this stage, more data have to get collected to conclude on the best embedding.

Fortunately, experimental data[1] have been recorded on so called artificial sodalites and will enable statistical approach to compare both the embedding methods and the functionals. These minerals are sodalites for which one or several atom types among Si, Al and Cl

have been substituted by Ge, Ga and Br or I respectively. For six of them the experimental maximum absorption wavelength has been measured: $Na_8(SiAlO_4)_6\mathbf{Br}_2$, $Na_8(SiAlO_4)_6\mathbf{I}_2$, $Na_8(Si\mathbf{Ga}O_4)_6Cl_2$, $Na_8(Si\mathbf{Ga}O_4)_6\mathbf{Br}_2$, $Na_8(\mathbf{Ge}AlO_4)_6Cl_2$, $Na_8(\mathbf{Ge}AlO_4)_6\mathbf{Br}_2$. For simplicity, they will respectively be named SiAl**Br**, SiAl**I**, Si**Ga**Cl, Si**GaBr**, **Ge**AlCl and **Ge**Al**Br**. The atom types in bold letters are the ones substituted in comparison with pristine sodalite.

For the six artificial sodalites and the pristine one the maximum absorption wavelength has been computed within TD-DFT framework (λ_{TDDFT}) using either OH embedding or Opc one (respectively blue and red points in Figure IV.9). The results presented are obtained with B3LYP functional for homogeneity reason with the following (cf. IV.2.2.2.c), but one gets qualitatively similar results with PBE0 so that the conclusion drawn in that section would not be different.

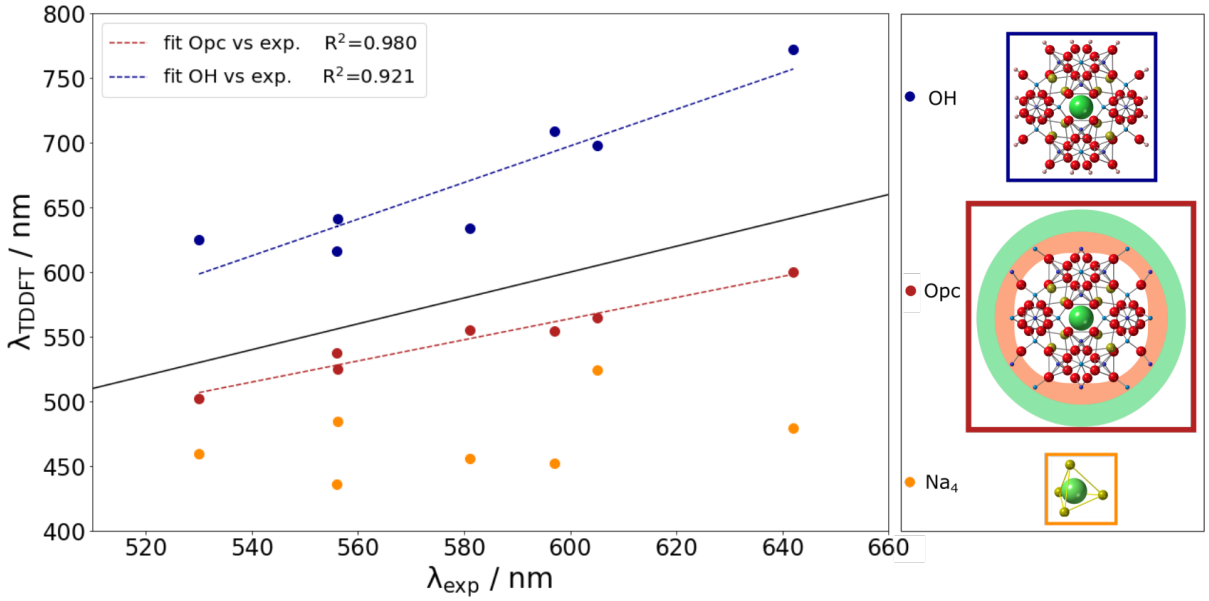

Figure IV.9: (left) TD-DFT absorption wavelength of F-centers in artificial sodalites using the OH embedding (blue points) or the one with pseudopotentials and point charges (red points) at the B3LYP level. For comparison the TD-DFT absorption wavelengths in Na_4 are reported in orange. The black line represents the match between experimental and computational data. (right) the respective systems (*i.e.* cluster + embeddings) used for the calculations.

As expected, the addition of the β-cage leads to a great improvement of the results compared with the ones obtained with the smallest cluster (*i.e.* Na_4, orange points in Figure IV.9). Again, with OH systems there is an underestimation of the absorption energy, and a larger dispersion of the points compared with Opc ones (cf. R^2=0.92 v.s. 0.98). The latter is then the best embedding model among all tested for the simulation of the F-center's absorption in sodalite type materials. Numerically, MAEs are 0.12 eV

for Opc and 0.28 eV for the H saturated cluster.

IV.2.2.2.b Influence of the vibronic coupling

Addition of vibronic coupling was done for all five different systems described in the previous subsection (cf. IV.2.2.2.a) with pristine sodalite only (AlSiCl). For all of them the adiabatic electronic transition energy (E_{adia}, cf. Figure IV.10) is approximated by the average value between the absorption and emission energies related to the transition at stake obtained through TD-DFT/PBE0 calculations on the system. It is the only parameter that actually distinguishes the different systems since both geometries ($\mathbf{R}^{GS}$ and $\mathbf{R}^{EES}$ in Figure IV.10) and Normal Vibration Modes (NVMs) are otherwise provided by PBC calculations. The different spectra are presented in Figure IV.7.

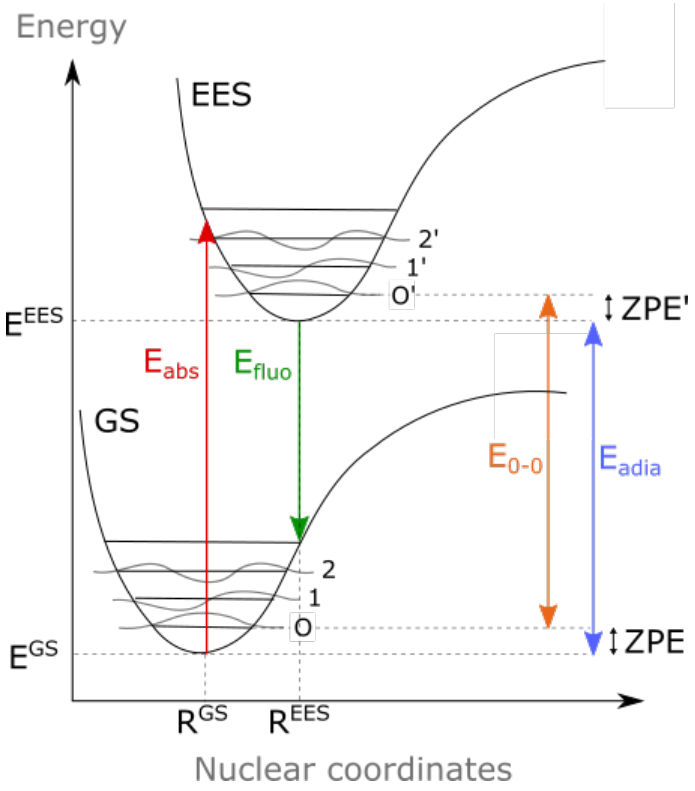

Figure IV.10: Energy diagram drawn from [31] representing the energy as a function of the nuclear coordinates $\mathbf{R}$ of the GS and one EES of a system. The three first vibrational states are indicated for each state, with the 0-0 energy (E_{0-0}) indicated by an orange arrow. The absorption and fluorescence phenomena are represented by a red and green arrow respectively. The real adiabatic energy indicated in blue ($E_{adia} = E^{EES}(\mathbf{R}^{EES}) - E^{GS}(\mathbf{R}^{GS})$) will be approximated in this work (cf. II.2.5) .

The light blue curves are obtained by considering only the vibrations of Na_4, while dark blue curves include also the vibrations of the β-cage. From these results one can see that the maximum absorption wavelength is globally blue-shifted by the addition of the vi-

bronic coupling whatever the strategy followed to include it, reducing by a small amount the agreement on energy with the experiment (0.05 eV on average). This blue shift can be partly ascribe to our approximation of the adiabatic energy. We will actually see in the following that changing the functional, hence the adiabatic energy, can change the nature of the shift with respect to TD-DFT calculations without vibronic coupling. However addition of vibronic coupling provides a realistic broadening of the curve, better improved when considering the β-cage.

The shape of the curve is the results of different transitions between the NVMs of GS and ES. The fact that the light blue and dark blue curves are centred on the same wavelength suggest that the most significant contribution to the vibronic coupling belongs to the vibrations of Na_4. Indeed, the calculation's output indicates that only the NVM corresponding to the "breathing" mode of Na_4 couples notably with the electronic transition, so that considering the β-cage provides other vibrational modes that contribute slightly to the broadening of the spectra without changing the position of its maximum. This mode corresponds to a symmetric elongation of all Na-Na bonds of the tetrahedron. The frequency of this mode is 173.2 cm^{-1} and 144.1 cm^{-1} at respectively the GS and the ES geometry for frequencies calculated only on Na_4. The description of the vibrational coupling with these soft modes could be improved by considering anharmonic effects.

Finally, the addition of the normal modes of the β-cage increases considerably the computational cost and does not improve the results dramatically. In the following, we will only consider sodium tetrahedron for frequency calculations.

IV.2.2.2.c Functional benchmark

Another important parameter of our calculation is the functional used for TD-DFT calculations. Since a mathematical expression for the universal functional has not been found, one has to choose between the numerous approximations to the exchange-correlation functional. For the simulation of F-center's absorption spectrum, sensitivity to the functional has been looked at by benchmarking 16 functionals one can gather in four groups:

- pure GGA: BP86, PW91, PBE, B97D;
- hybrid GGA: TPSSh, B3PW91, B3LYP, PBE0, BMK, M062-X;
- range-separated hybrid (RSH): CAM-B3LYP, ωB97X-D, LC-ωHPBE, HSE06;
- pure meta GGA: MN15-L, tHCTH.

TD-DFT calculations were conducted on the seven minerals (pristine sodalite + SiAl**Br**, SiAl**I**,Si**Ga**Cl, Si**GaBr**, **Ge**AlCl and **Ge**Al**Br**) using the Opc systems. The absorption,

emission and resulting adiabatic energies for all minerals can be found in Appendix Table A.6.
The mean signed error on absorption energy for all of the functionals can be found in Figure IV.11. The references are the experimental maximum absorption wavelengths from Williams' study.[1]. Discussion on the results of the benchmark while taking into account the vibronic coupling (on Na_4) can be found in Appendix C.

From a general point of view, pure GGA functionals and global hybrids functionals with a low exact exchange fraction (<30%) are the best to reproduce the spectroscopic properties of the F-center. This is in agreement with a similar trend observed for local transitions computed on organic molecules.[32] More specifically, B3LYP gets close to the experiment with an error of 0.12 eV on average, similar to BP86 and PBE (MAE = 0.13 eV).

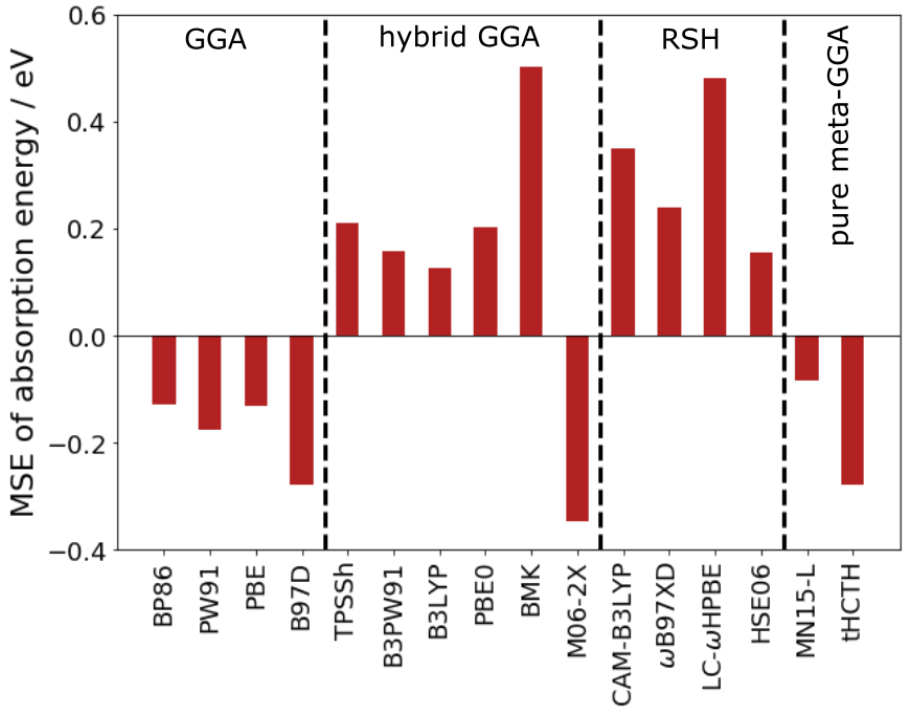

Figure IV.11: Mean signed error of F-center absorption energy in different sodalites compositions, as a function of different functionals.

As a matter of fact, it appears that for the best functionals such as B3LYP and PBE, the addition of the vibronic coupling changes the maximum absorption wavelength by less than 10 nm (cf. Appendix C). However, to include the vibronic coupling it is necessary to realize two geometry optimizations (for GS and ES) instead of one but also to realize frequency calculations. This multiplies by at least four the total CPU time compared to simple TD-DFT calculations, on the order of days (≈ 30h and ≈ 60h respectively for the frequency calculations on Na_4 at the GS or ES on the optimized geometries). Moreover,

the FWHM of the final curve can actually be extrapolated from experimental data. Hence, in the following B3LYP functional will be used to simulate absorption properties of F-center in sodalite and the results will be convoluted by a gaussian with a FWHM of 0.3 eV.

IV.2.2.3. Simulation of the colour

Since one of the main characteristics of the F-center is to give a colour to a, generally, colourless mineral, the final colour simulation of the trapped electron as a function of the mineral chemical formula can give an idea of the range of colours accessible by tuning the sodalite composition.

Figure IV.12: Simulated (at the TD-DFT/B3LYP level) and experimental colours in absorption for different sodalites without (a) or with (b) vibronic coupling

The simulated colours (at TD-DFT/B3LYP level of theory) are given in Figure IV.12 and compared with experimental ones.[1] The purple colour of the natural mineral (of formula $Na_8Si_6Al_6O_{24}Cl_2$ simplified by the notation SiAlCl) is well reproduced. All Si-based minerals are in the purple-pink range of colours, while the Ge-based minerals are generally more in the cyan-blue colour tone. Simulated aspects of the minerals without vibronic coupling agree qualitatively very well with the colour reported by Williams et al, even if the measures performed on powders give dark colours. The quantitative discrepancy,

could then be reduced by conducting the measures on monocrystals or including light dispersion effects induced by the powder in the simulation of the colour.

Figure IV.13 gives the simulated (without vibronic coupling) colours for never-reported artificial sodalites. Again, the Si-based minerals seem to be more in the pink-purple range, while the Ge-based sodalites are in a cyan tone. It is interesting to note that the other substitutions (Al vs Ga or Cl vs Br vs I) have a less marked effect on the final colour of the mineral.

Figure IV.13: Simulated colours in absorption for different artificial sodalites without vibronic coupling.

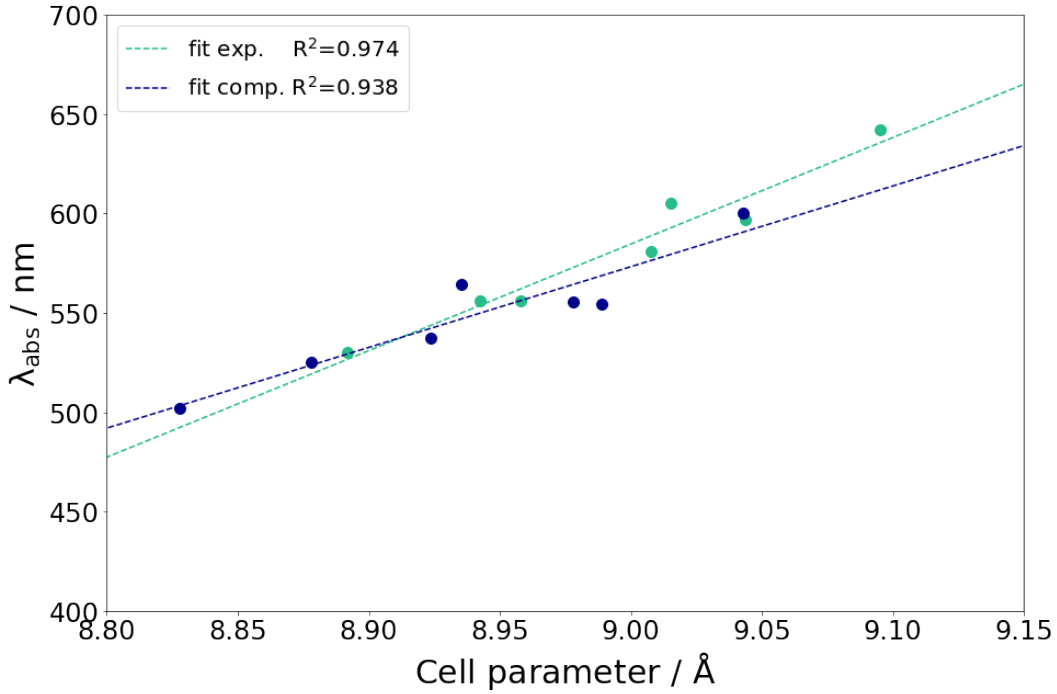

Figure IV.14: Plot of absorption wavelength against lattice parameter for the different sodalite compositions considering the experimental values (green) or the computed ones (purple).

To understand this observation, the absorption wavelength has been plotted as a function of the cell parameter, showing a possible correlation between these two parameters, as suggested by Williams *et al.* (cf. Figure IV.14).[1] The larger the cell parameter, the

larger the absorption wavelength (and the more the colour appears blue). Among the substitutions investigated (Si by Ge, Al by Ga, and Cl by Br or I), the largest change of ionic radius is for the Si (54 pm) substituted by Ge (67 pm), with 24% of ionic radius increase (against 13% for Al/Ga and 22% for Cl/I). Thus, the blue colour experimentally observed for Ge-based materials is due to the cell parameter increase induced by the large Ge^{4+} ion.

IV.2.2.4. Effect of the tetrahedron composition

This study results from the experimental observation of the sensibility to the incorporation of potassium (K) or rubidium (Rb) as sodium substituents.[33] Here we are interested in the impact of potassium substitutions on F-center's absorption.

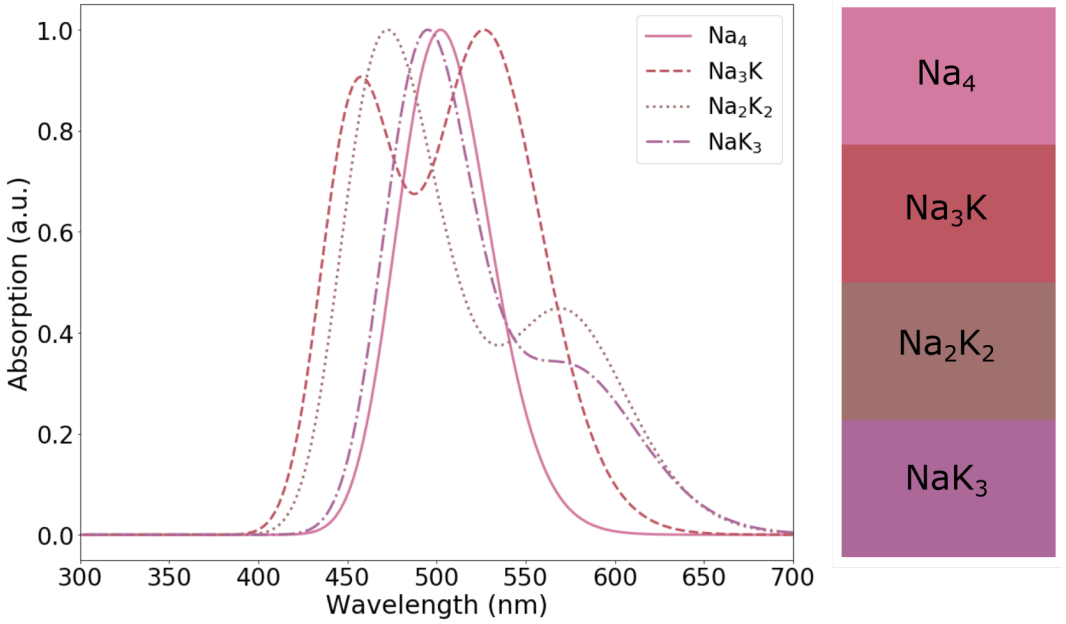

Figure IV.15: (left) F-center's absorption simulation in a structure with one (red dashed line), two (brown dotted line) or three (purple dash-dotted line) sodium atoms substituted by the corresponding number of potassium atoms, compared with the non-modified structure (Na_4 in pink and plain line). TD-DFT/B3LYP absorption energies are convoluted by a gaussian with FWHM of 0.3 eV. (right) simulated colours for the corresponding structures.

2X2X2 supercells containing 6.25% F-center in chloride contents (*i.e.* one Cl^- among the 16 is replaced by a trapped electron) are optimized with a potassium doping of 1.6 % (*i.e.* 1 atom in the supercell), 3.2% (*i.e.* 2 atoms in the supercell) or 4.8% (*i.e.* 3 atoms in the supercell) in sodium contents. It has been showed that the substituents are thermodynamically more stable if placed close to V_{Cl}.[33] Indeed, K^+ cations are bigger than Na^+ and there is more space next to the vacancy.

F-center's absorption simulations were thus conducted on structures with the tetrahedron surrounding V_{Cl}^{-} having the following compositions: Na_3K, Na_2K_2 and NaK_3 (cf. Figure IV.15). The corresponding simulated colours are given in the right part of Figure IV.15.

We can see the effect of the introduction of anisotropy around the trapped electrons producing more bands in absorption compared with the unmodified Na_4 structure. This is explained by the removing of degeneracy of t_2 orbitals (due to symmetry breaking) leading to three possible distinct transitions from a_1 orbital. We can expect that the inclusion of K would lead to a broadening of the curve more than a shift in the transition energy.

IV.2.2.5. Effect of the tetrahedron structure

After γ-ray irradiation, it has been experimentally observed a modification of the absorption properties of the mineral (cf. Figure IV.16). Our collaborators observed a broadening of the curve attributed to two new transitions. These transitions appear by subtracting the spectra obtained after γ-ray irradiation (red curve in Figure IV.16) by the one obtained after UV irradiation (blue curve in Figure IV.16). The resulting curve (dotted line in Figure IV.16) shows two peaks corresponding to either a red (by 0.35 eV) or a blue (by 0.37 eV) shift of F-center's absorption. This could be explained by a structural rearrangement around the trapped particle, induced by the radiation. Indeed, under lower energy radiations (X-rays irradiation), damages of sodalite were already reported. They consist in partial decomposition of the material with the apparition at the surface of NaCl compound leaving $Na_{8-x}(AlSiO_4)_6Cl_{2-x}$ still possessing the sodalite structure.[34]

Hence, the hypothesis tested to explain the change in the absorption properties was a modification of the sodium tetrahedron surrounding the trapped electron allowed by the high level of energy the mineral was exposed to. We considered two cases:

- creation of a sodium vacancy: $Na_4 \rightarrow Na_3$ (offset by the substitution of one Al^{3+} by one Si^{4+} in the calculations)
- apparition of interstitial sodium: $Na_4 \rightarrow Na_5$ (offset by the substitution of one Si^{4+} by one Al^{3+} in the calculations)

For each one, the geometries were optimized through PBC calculations and the absorption's energy obtained with TD-DFT/B3LYP level of theory using Opc systems. In Figure IV.17 the respective results convoluted by a gaussian are compared to the one obtained with the unmodified structure. We can observe a blue-shift (by 0.55 eV) after the addition of a sodium atom and a red-shift (by 0.17 eV) when removing one. The modification of

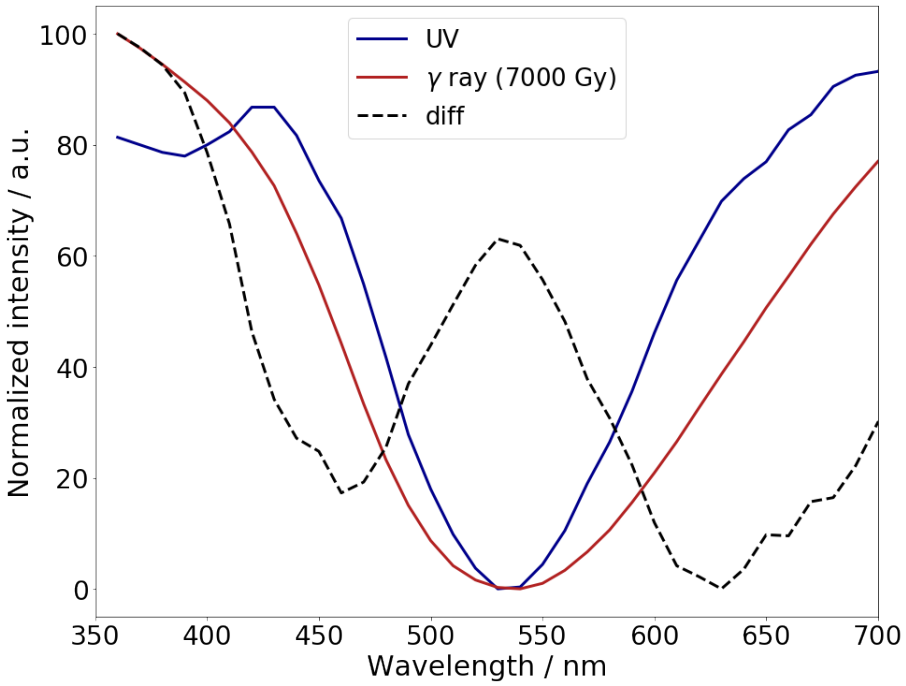

Figure IV.16: Experimental sodalite absorption spectra after UV (blue) or γ-ray (red) irradiation. The dotted line is obtained by subtracting the red curve by the blue one/

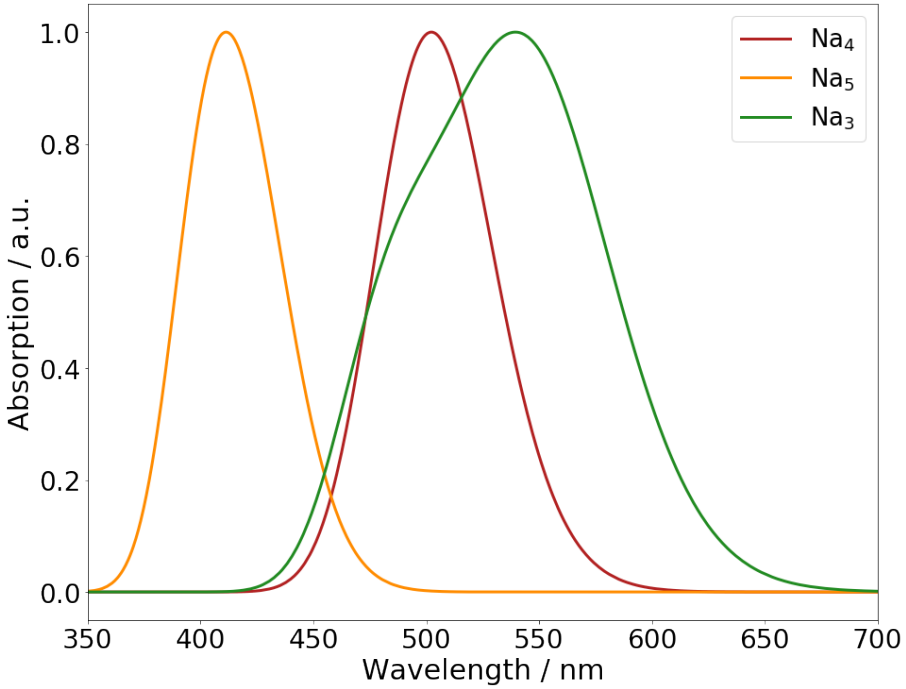

Figure IV.17: F-center's absorption simulation in a structure with one sodium atom removed (Na_3 in green) or one sodium atom added (Na_5 in orange) compared with the non-modified structure (Na_4 in red). TD-DFT/B3LYP absorption energies are convoluted by a gaussian with FWHM of 0.3 eV.

the absorption spectra is in a qualitative agreement with the experimental observations and provides partial explanation of the modification of the mineral's absorption proper-

ties. The quantitative differences between theory and experiments can originate from the method (*e.g.* no search of other minima) or the intrinsic simplification of the reality in our simulation. Indeed, along with the local modification of the polyhedron can happen other structural distortions.
For future applications, control of this structural modification could be obtained through the development of chemical processes.

To conclude on this section, it appears that the simulation of F-center's absorption in sodalite through a molecular approach leads to results in close agreement with experiment. To reach them, it is necessary to include the β-cage in the QM part of the cluster and surround it with an embedding made of pseudopotentials and point charges. The choice of the functional is also crucial to retrieve a good qualitative agreement, and we drew the conclusion that hybrid GGA with a low HF fraction (*e.g.* B3LYP, PBE0) seems to be a reasonable choice to describe these systems. Inclusion of the vibronic coupling is possible and qualitatively improves the shape of the simulated curves but at a high computational cost, suggesting to by-pass this step by using a FWHM of 0.3 eV when convoluting the results with a gaussian. Finally, this methodology enables to simulate the effects of composition or distortion on the absorption and to predict the colour taken by the material under UV irradiation.

IV.3. Modelling the charge transfer process at stake in tenebrescence

Tenebrescent minerals are fascinating due to their reversible colouration caused by the presence of F-centers in their structure. In the previous section we have presented a model enabling us to simulate the spectroscopic properties of this colour center in an aluminosilicate framework. The reversibility of the photochromism reveals that the trapped electrons can be formed and "destroyed" in turns. Modelling the corresponding processes of formation and annihilation at stake is the subject of this section.
In order to do so, we now have to consider two defects in the structure at the same time:

- V_{Cl}, the chloride vacancy that will receive the electron,
- S_2^{2-} the sulfur impurity that plays the role of the activator.

The mineral sodalite can reversibly go from the colourless form to the coloured one, through a charge transfer between S_2^{2-} and V_{Cl}. The two states involved in this transfer are $^1[S_2^{2-}, V_{Cl}]$ and $^3[S_2^{-}, V_{Cl}^{-}]$ and correspond to the energy minima for the geometries of respectively the colourless form and the colored one. The energy required to go from the

colourless to the coloured form is the activation energy, the backwards process requires an energy referred to as bleaching energy.
The computational methodology will have to be adapted. Indeed, the method used for simulating the absorption of F-center can not just be transferred to the simulation of the charge transfer. It is indeed a challenging case for TD-DFT (cf. section II.3), especially with the final inversion of the two states (cf. Jablonski diagram Figure IV.2). Once a methodology set up,it will be possible to study the effects of the composition and structure on both the activation and bleaching energies.

IV.3.1. Methodology

IV.3.1.1. From periodic to cluster approach

Geometry optimization

The introduction of S_2^{2-} impurity in sodalite structure leads to the formation of a chloride vacancy for electroneutrality reasons. In term of geometry optimization, there will be two nearby chloride anions substituted in the 2X2X2 supercell. One can imagine different possibilities to place these two defects relatively to one another in the supercell.

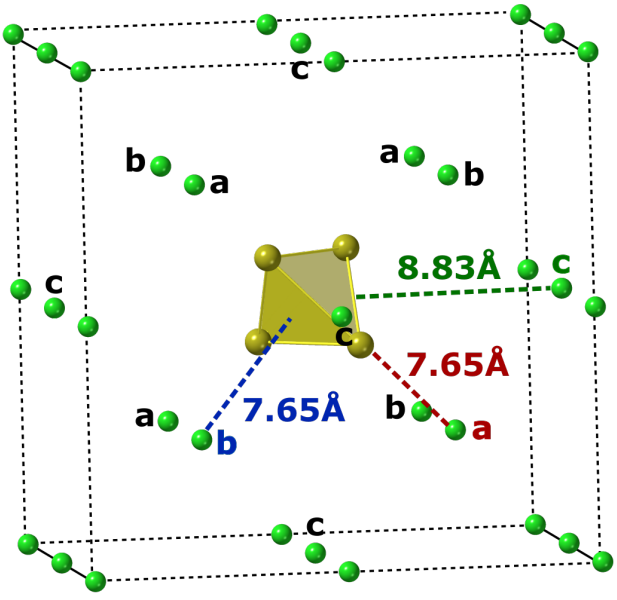

Figure IV.18: Position of Cl^- (green points) around the vacancy (central yellow tetrahedron). Three non-equivalent positions corresponding to the letters a, b, and c were tested for S_2^{-2} doping. The distances from these positions to the center of the vacancy are given in the picture.

To facilitate understanding, the vacancy, V_{Cl}, will replace the chloride anion in the middle of the supercell and the sulfur impurity will substitute one Cl^- in a nearby β-cage (cf. Figure IV.18). In terms of symmetry, there are three possibilities:

(a) inside a tetrahedron pointed by the central tetrahedron,

(b) inside a tetrahedron leading to one of the central tetrahedron's faces,

(c) inside a tetrahedron leading to one of the central tetrahedron's edges.

A previous study[7] indicates that the most stable geometry corresponds to S_2^{2-} at the closest position to which the vacancy points. Hence, following these results position labelled (a) (cf. Figure IV.18) will be considered for geometry optimizations.
It is interesting to report here the fact that the n(S)/n(Cl) = 0.13 ratio obtained with the 2X2X2 supercell corresponds to a material that will show strong photochromism (close to the optimal ratio of 0.06, cf. Figure IV.19). [35]

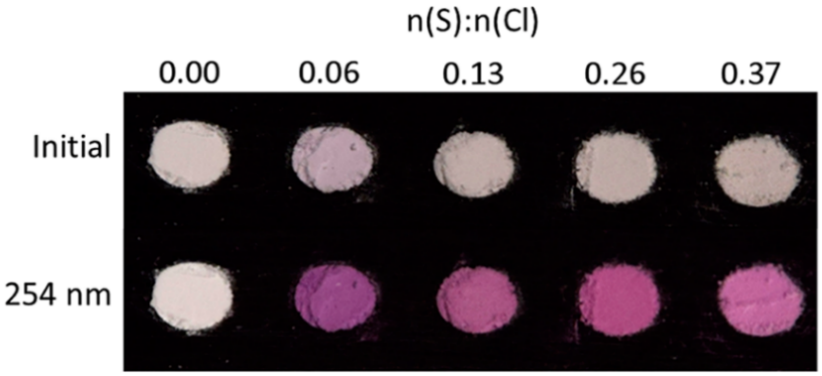

Figure IV.19: Intensity of color change for $Na_8(AlSiO_4)_6(Cl,S)_2$ after 254 nm irradiation for different n(S)/n(Cl) ratios. Photo taken from [35].

Choice of the cluster

Similarly to what has been done for the simulation of the F-center's absorption, a molecular approach will be followed for modelling the charge transfer transition. The calculations will be performed on clusters extracted from the PBC geometries. Again, on account of the material structure made of repeating β-cages each containing a sodium tetrahedron, we considered two types of clusters (treated at the QM level): the smallest one being two sodium tetrahedra surrounding the defects (cf. Figure IV.20a); the other one including as well the β-cages around the tetrahedra and the two defects (cf. Figure IV.20b).

(a) Na_8 (b) O^-

Figure IV.20: The two clusters extracted from PBC geometries surrounding the two defects. Na, Cl, O, Si, and Al atoms are depicted in yellow, green, red, blue, and cyan respectively.

IV.3.1.2. Embedding methods

The sensibility to the environment will also be investigated for the simulation of the charge transfer transition where it is expected to be even more important. This time we will consider three approaches of embedding on the large cluster, which are represented in Figure IV.21.

(a) **O^-**: no embedding, β-cage with oxygen pending bonds.

(b) **OH**: saturation of oxygen pending bonds with hydrogen, covering the β-cage with OH groups.

(c) **Opc**: the terminating O atoms of the β-cage are surrounded by the next shell of cations described by pseudopotentials (pp) without the related basis set and an array of point charges (pc) in order to simulate the Madelung potential of the ionic sodalite crystal.

In the end we have four different systems, Na_8, O^-, OH and Opc, which allow a comparative study of several solid-state embeddings for the simulation of charge transfer.

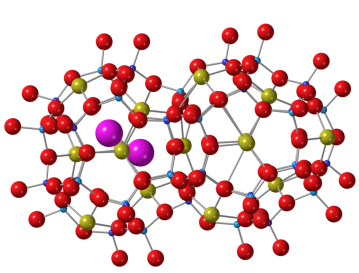

(a) O^-

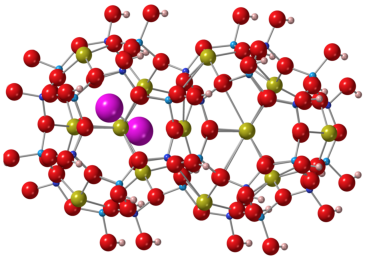

(b) OH

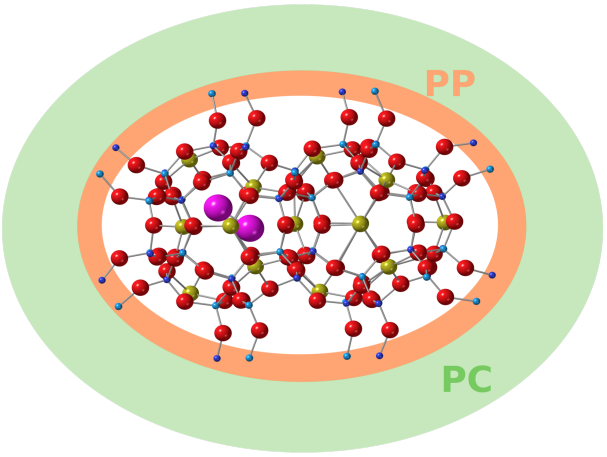

(c) Opc

Figure IV.21: The three tested embedding of the β-cage considered for modelling charge transfer transition. Na, Cl, O, Si, Al and H atoms are depicted in yellow, green, red, blue, cyan and pink respectively. Atoms treated by pseudopotentials (pp) are placed in an orange annulus. Presence of point charges (pc) is schematically represented by a green annulus.

IV.3.1.3. Level of theory

The simulation of F-center's absorption was done by TD-DFT calculations. In the case of charge transfer transition simulation we will have to adapt the method since it is a pathological case of TD-DFT (cf. section II.3). The solutions considered will be either the use of post Hartree-Fock methods: CIS(D), SAC-CI, CASPT2, CC2*, CCSD* and CCSDR(3)*; or keeping TD-DFT level of theory but going for range-separated hybrid functionals: CAM-B3LYP, ωB97X-D, LC-ωHPBE (cf. section II.3.2).
Moreover, when considering transitions involving triplet states, TDA[36, 37] will be used in place of TD-DFT, as suggested by Sears *et. al* when using long-range corrected functionals.[38]

*calculations performed by D. Jacquemin, Université de Nantes

IV.3.2. Results an discussion

IV.3.2.1. Geometries

One of the first accessible results after geometry optimization is the structural changes induced by the introduction of defects. Actually only the sodium tetrahedra were deformed while the cages remained almost unaffected. As a reference the Na-Na distance in the tetrahedra was 4.44 Å in the bulk.

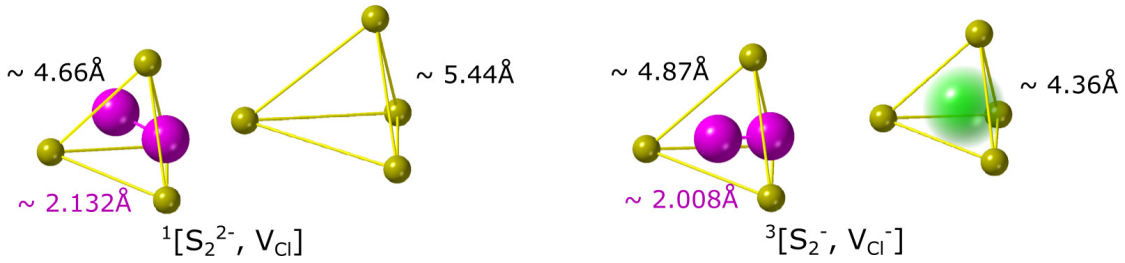

Figure IV.22: Optimized geometries of the tetrahedra surrounding the defects in the (a) colourless and (b) coloured forms. The Na, and S atoms are represented respectively by yellow and pink spheres, the trapped electron is symbolized by the bright green one. For each tetrahedron, the average edge length is written next to the structure. The distances in pink correspond to S-S bond length.

In the colourless form (cf. Figure IV.22a) we first observe a volume increase of the sodium tetrahedron surrounding the vacancy that is explained by a lack of a negative charge in the center of the vacancy giving rise to only repulsion between the four Na atoms. On average the Na-Na distance in the tetrahedron around the vacancy is 5.44 Å. Furthermore, there is a distortion of the sodium tetrahedron towards the S_2^{2-} anion because of the high attractive electrostatic interaction between this anion and the closest Na cation. Because of this distortion, it was decided to optimize a new basis set in the form 111G(d) to describe the trapped electron in this tetrahedron (cf. Table III.1). The sodium tetrahedron that contains the S_2^{2-} ion is also larger, with a 4.61 Å edge on average, because of the larger size of S_2^{2-} compared to Cl^-.

The geometry of the coloured form was obtained through a ΔSCF procedure imposing a triplet spin state (thus imposing occupation of the a_1 orbital of the vacancy). The criterion of convergence for the SCF cycles was lowered to 10^{-6} Hartree (cf. section III.1.2). In this geometry (cf. Figure IV.22b), the withdrawal of an electron from S_2^{2-} $\pi*$ orbital to fill the vacancy induced an increase of the tetrahedron around S_2^- and a decrease of the one surrounding the electron due to electrostatic effect, with the respective average

Na-Na distances of 4.87 Å and 4.36 Å (smaller than in the bulk for the last one).

The S-S distances are respectively 2.132 Å and 2.008 Å for the colourless and coloured forms, which is in very good agreement with experimental measurements.[39] The decrease of the bond length is explained by partial emptying of the antibonding molecular orbital $\pi*$ to populate the nearby vacancy.

IV.3.2.2. Density of States

The density of states of the colourless form with the corresponding basis set for the vacancy is represented in Figure IV.23. The HOMO is the π^* orbital on S_2^{2-} and the LUMO is the a_1 orbital located on V_{Cl}. From this electronic structure, it appears that the first expected transition, from the HOMO to the LUMO, is a charge transfer transition explaining the F-center formation upon light exposure. The transition energy obtained from this DOS is 3.9 eV (320 nm). Experimentally, the excitation spectrum to generate the F-center is a large band centered on 300 nm (4.1 eV)[2] (cf. section V.2), hence the HOMO-LUMO difference in energy provides a good estimation of the activation energy.

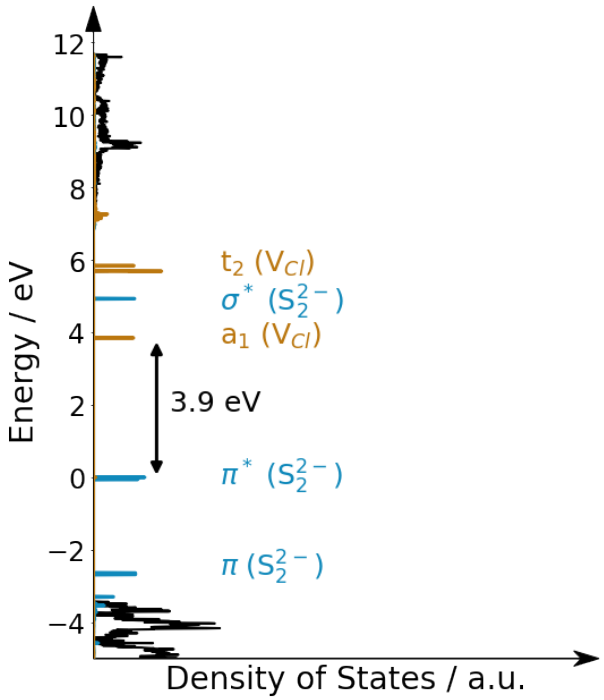

Figure IV.23: DOS of the 2X2X2 supercell containing S_2^{2-} (cyan) and V_{Cl} defects (black) and projected DOS on the S_2^{2-} (cyan) and V_{Cl} (yellow) orbitals, at the geometry of the colourless form.

IV.3.2.3. Spectroscopy

IV.3.2.3.a Influence of the level of theory

The activation energy, required to transfer the electron from S_2^{2-} to V_{Cl}, and the bleaching one required for the backwards transfer, were calculated on the minimal cluster (Na_8) using different methods. The results are presented in Figure IV.24 for the activation energy and Figure IV.25 for bleaching one along with the experimental energies.

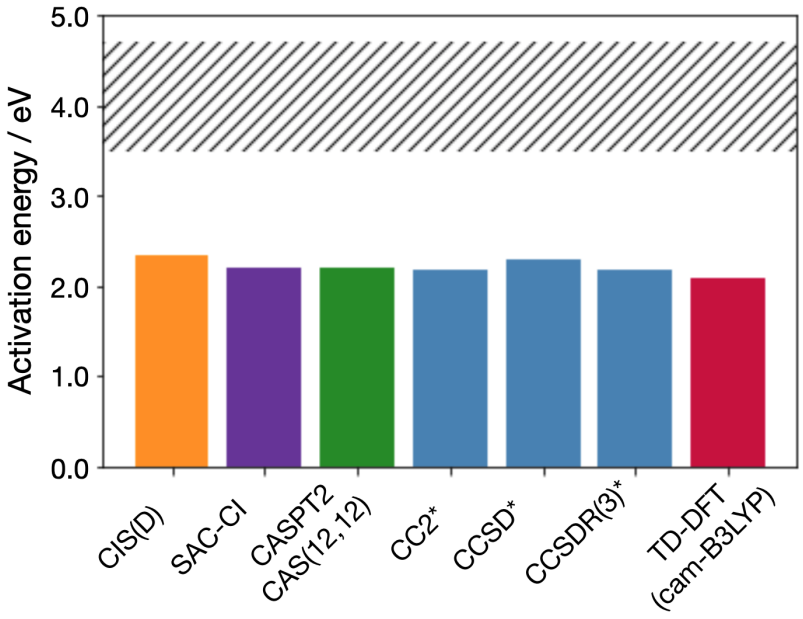

Figure IV.24: Activation energies calculated on Na_8 system according to different level of theory. The experimental expected range of values is depicted by the hatched rectangle.

Interestingly whatever the level of theory, the activation energy on Na_8 is around 2.2 eV far from the expected experimental range (3.5-4.7 eV). The fact that the energy obtained with TD-DFT is similar to the one obtained with CCSDR(3) suggests that the first method is adapted for investigating this transition.

Concerning the bleaching energy, let's recall that it is expected to be negative (cf. Jablonski diagram IV.2), and actually measured at -0.48 eV on a synthetic sodalite.[33] Whatever the level of theory we clearly have an inversion of the electronic states (*i.e.* negative energies), but the relative energies vary notably, from -2.7 eV (CIS(D)) to -0.5 eV (TDA/CAM-B3LYP), highlighting the fact that it is a challenging system. Surprisingly, TD-DFT provides results close to the experiment but higher in energy by 1.3 eV compared to CCSDR(3). This suggests that the good agreement with experiment is obtained by an error compensation.

*calculations performed by D. Jacquemin, Université de Nantes

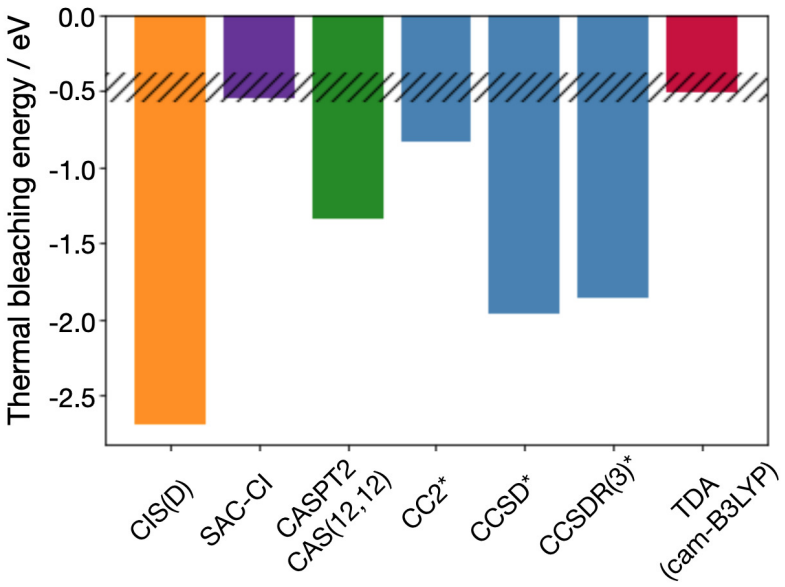

Figure IV.25: Bleaching energies calculated on Na_8 system according to different level of theory. The experimental expected range of values is depicted by the hatched rectangle.

The discrepancy between post-HF methods considered to be a reliable reference (*e.g.* CCSDR(3)) and experiment suggests that our model for the system (i.e. only the Na_8 cluster) is not adapted to simulate the bleaching phenomenon. The most obvious way to improve our model is to increase the cluster's size as we did for the F-center study. However, increase in the system size by taking into account the β-cages (O^-, 162 atoms), comes with a more important increase of the number of basis functions: greater than 2500. This does not allow reliable post Hartree-Fock calculations. Among the levels of theory accessible for such system, we chose TD-DFT, that was already used for the simulation of F-center's absorption, keeping in mind the fact that the error for thermal bleaching energies can be as important as the one observed on Na_8 system.

IV.3.2.3.b Influence of the embedding

Activation and bleaching energies were computed with TD-DFT/CAM-B3LYP level of theory (within TDA for bleaching energies) on the four different systems presented in section IV.3.1.1. The errors with respect to experiment are presented in Figure IV.26 as a function of the system. The experimental reference values are 4.1 eV and -0.48 eV respectively for the activation and bleaching energies, measured on synthetic sodalite[33].

First of all, as for the simulation of F-center's absorption, the addition of the β-cage (O^- compared to Na_8) improves the description of the activation energy by 1.1 eV but

*calculations performed by D. Jacquemin, Université de Nantes

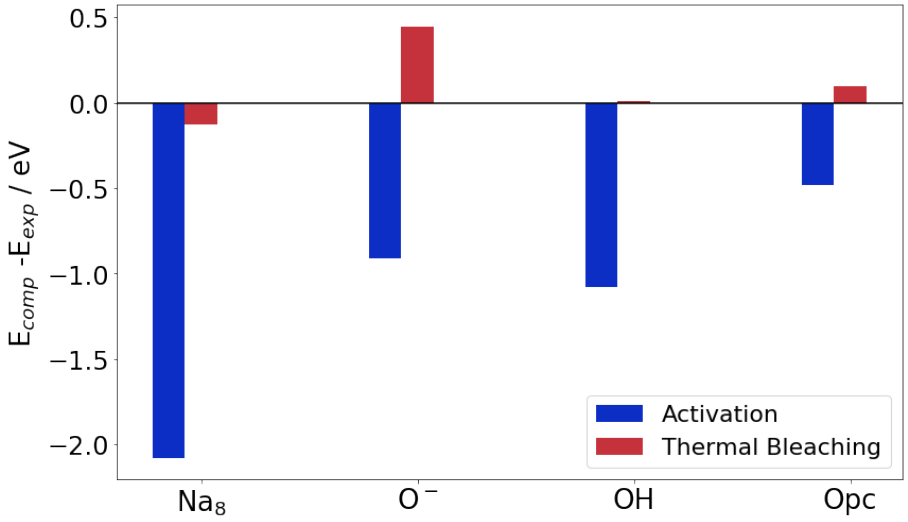

Figure IV.26: Errors (eV) with respect to experiment for activation and bleaching energies as a function of the system (*i.e.* cluster+embedding).

provides a positive bleaching energy. OH provides the smallest error on bleaching energy (0.01 eV) but underestimates the activation energy by more than 1.0 eV. Finally, Opc provides the smallest error on activation energy compared to the expected experimental value (underestimation by 0.48 eV), and a negative bleaching energy of -0.39 eV (*e.g.* overestimation of 0.09 eV with respect to the experimental value). According to the discussion on the level of theory in the previous section, the criteria to select the best embedding for our model, would be a good quantitative agreement with the experiment for the activation energy, and at least a good qualitative one for bleaching energy. Opc approach appears as the best solution here.
It is interesting to note that long-range effects, added through pseudopotentials and point charges embedding, have a great influence. Charge transfer transitions are indeed more sensitive to the environment than localized absorption processes.

IV.3.2.3.c Influence of the functional

Three RSH functionals were compared for the calculations of the activation and bleaching energies: CAM-B3LYP, ωB97X-D and LC-ωHPBE on Opc system. The different results can be seen in Figure IV.27

LC-ωHPBE functional can be eliminated since it does not allow a good qualitative description of the phenomenon, providing a positive bleaching energy. Both CAM-B3LYP and ωB97X-D give acceptable results. With CAM-B3LYP, the activation energy is underestimated by 0.48 eV and the bleaching energy is overestimated by 0.09 eV. The use of ωB97X-D provides an activation energy in perfect agreement with the 4.1 eV experi-

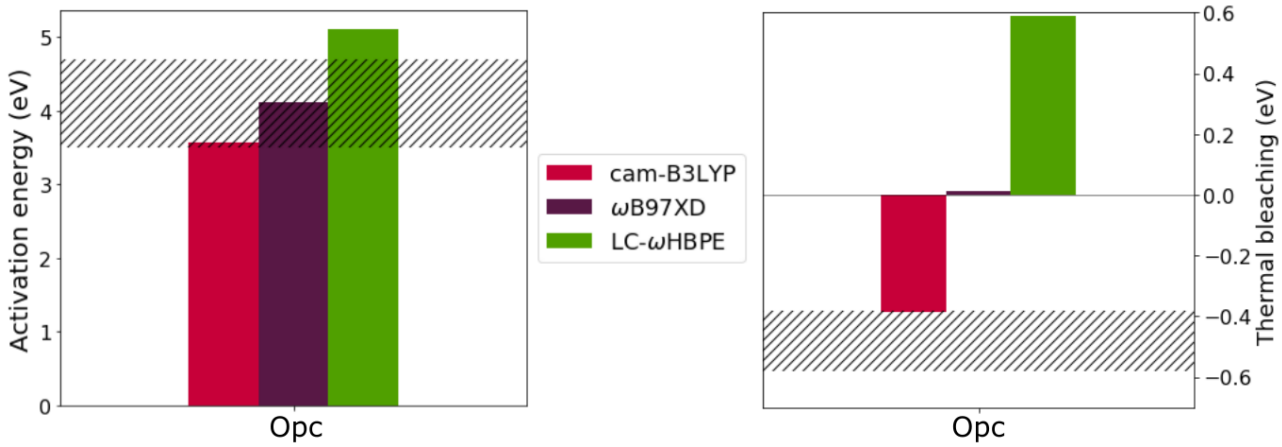

Figure IV.27: Activation energies (left) and bleaching energies (right) calculated at the TD-DFT (with TDA for thermal beaching) level of theory with three different RSH functionals. The experimental values are represented by the hatched rectangles, centered respectively on 4.1 and -0.3 eV for the activation and bleaching processes.

mentally measured, but overestimates the bleaching energy by ≈ 0.49 eV, falling close to 0.

The evaluation of the activation and bleaching energies were actually conducted on all four systems (*i.e.* Na_8, O^-, OH and Opc, cf. Figures A.3 and A.4), and it appears that CAM-B3LYP is the only one of the three tested functionals to provide a negative bleaching energy, whatever the system used for the calculation. This observation along with the fact that the bleaching energy obtained on Opc with ωB97X-D functional is closer to 0 than to the experimental value, tilts the balance in favour of CAM-B3LYP that should provide a good qualitative description of the phenomenon even if we change the system studied (*e.g.* composition, structure...).

In the end, simulation of the charge transfer process in sodalite will be done with a molecular approach, Opc, at the TD-DFT/CAM-B3LYP level of theory. Now that we have a methodology to computationally access the activation and bleaching energies of sodalite type minerals, we will see that it is possible to tune them by playing either on the composition of the material, or on the nature of the activator.

IV.3.2.4. Influence of the composition of the β-cage

The study of influence of the composition on the activation energy was conducted on the set made by the pristine sodalite and the 11 artificial ones (cf. section IV.2.2.2.a).

The geometry of the colourless form for all compositions was optimized, and a cluster was extracted and embedded to get Opc type systems. A basis set for the trapped electron in

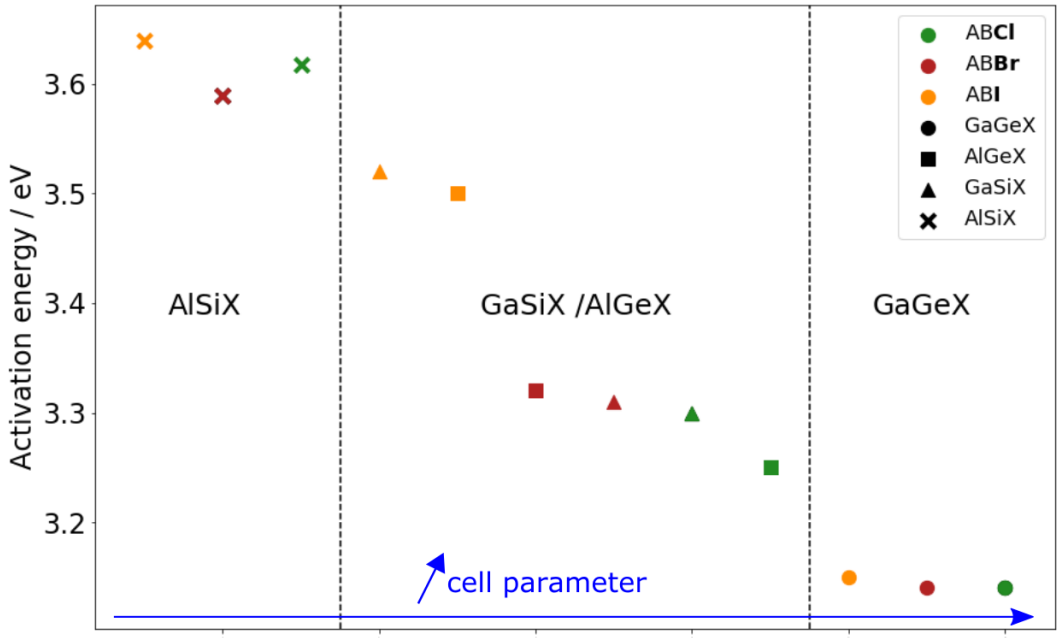

Figure IV.28: Activation energy of the 12 different compositions ABX of sodalite type minerals with A=Al,Ga, B=Si,Ge and X=Cl,Br,I calculated with TD-DFT/CAM-B3LYP level of theory.

the distorted vacancy was optimized for each composition (cf. Table III.1). The activation energies for the different systems calculated at the TD-DFT/CAM-B3LYP level of theory are reported in Figure IV.28.

As a first observation, GaGeX structures provide the lowest activation energies (3.14 eV on average) and AlSiX the highest ones (3.61 eV on average). GaSiX and AlGeX have an activation energy of 3.37 eV on average. The composition of the β-cage influences the cell parameter (a) of the structure (cf. Table A.4 in Appendix) and we observe the following behaviour:

$$\begin{aligned} &\bar{a}(GaGeX) > \bar{a}(GaSiX) > \bar{a}(AlGeX) > \bar{a}(AlSiX) \\ &\bar{E_a}(GaGeX) < \bar{E_a}(GaSiX) < \bar{E_a}(AlGeX) < \bar{E_a}(AlSiX) \end{aligned} \tag{IV.2}$$

with $\bar{a}$ and $\bar{E_a}$ the average cell parameter and activation energy for the different composition.

Moreover, for a same composition of the cages, the modification of the halogen atoms X=Cl^-, Br^-, I^- leads to a lesser extent to an increase of the activation energy by respectively 0.02 eV and 0.12 eV on average for a substitution by Br^- or I^-. The average increase in energy is related to the increase of the halogen anions ionic radius (r(Cl^-) $\approx$ 167 pm, r(Br^-) $\approx$ 182 pm, r(I^-) $\approx$ 216 pm). The bigger the ionic radius, the bigger the volume of the tetrahedron.

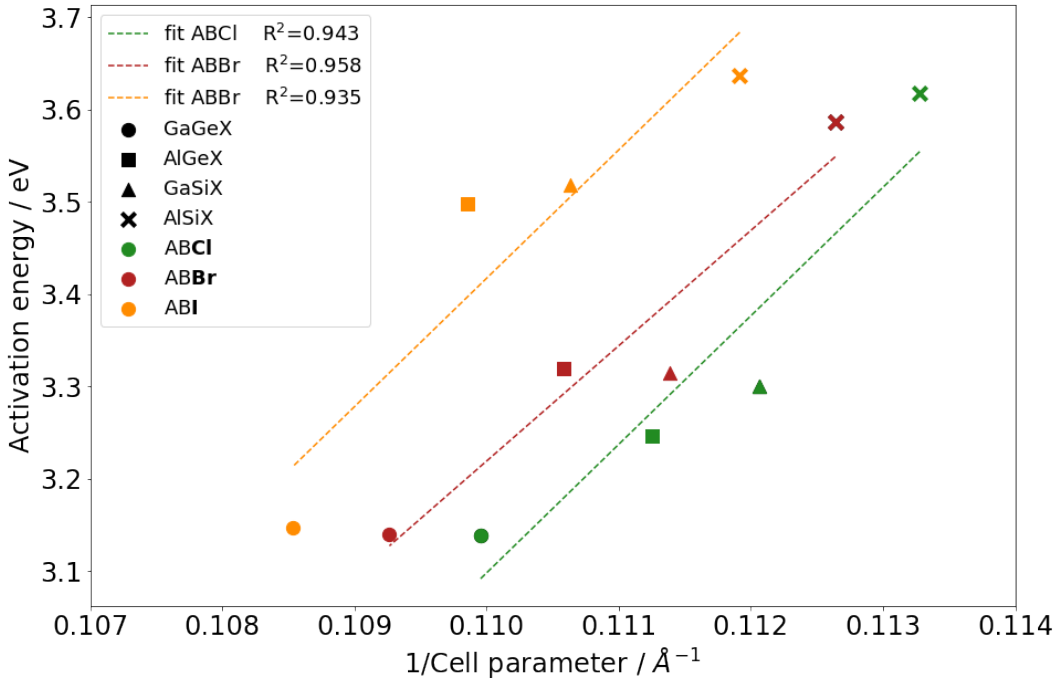

Figure IV.29: Inverse relationship between the cell parameter and the activation energy as a function of the composition.

To explain the observed behaviours, the activation energy, which is the energy required for the charge transfer, can be approximated by the formula (cf. Equation II.73):

$$E_{\text{activation}} \approx E_{CT} = IP^D - EA^A - \frac{1}{R} \tag{IV.3}$$

with IP^D the ionisation potential of the donor (here S_2^{2-}), EA^A the electronic affinity of the acceptor (here V_{Cl}) and R the distance between the two. In that extent, increasing the cell parameter, increases R which reduces in turn $E_{\text{activation}}$. Actually, an inverse relationship could be drawn between the cell parameter and the activation energy, as represented in Figure IV.29.

The study of the influence of the composition was also conducted for the bleaching energy using the same set of materials. The basis set for the trapped electron corresponds to the one optimized for simulation of F-center's absorption. In Figure IV.30, we report the transition energies from $^1[S_2^{2-}, V_{Cl}]$ towards the triplet state $^3[S_2^-, V_{Cl}^-]$, and the the singlet state $^1[S_2^-, V_{Cl}^-]$.

The first observation is that our model reproduces the inversion of states at the origin of the coloured form metastability (*i.e.* negative transition energies towards the triplet states) for all 12 compositions. Moreover, that stability would not be observed without

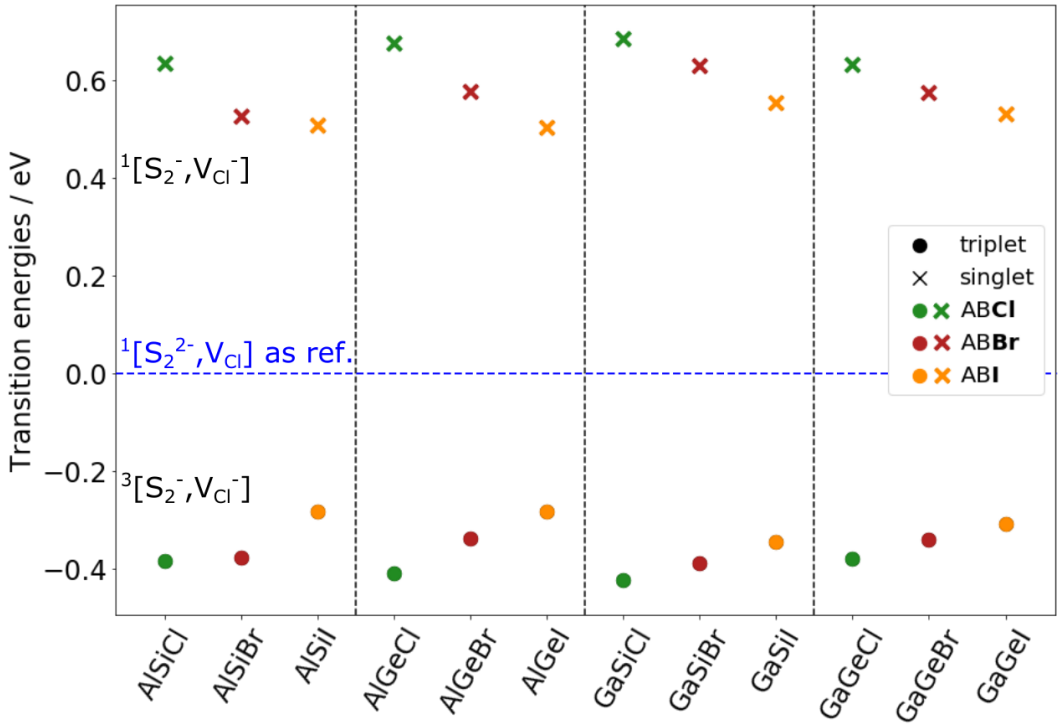

Figure IV.30: Average transition energies from $^1[S_2^{2-}, V_{Cl}]$ towards the triplet and singlet states of $[S_2^-, V_{Cl}^-]$ electronic configuration for the pristine sodalite and the 11 artificial ones.

the spin relaxation towards the triplet state, since $E(^1[S_2^-, V_{Cl}^-]) > E(^1[S_2^{2-}, V_{Cl}])$ contrary to what was presented at the beginning on Jablonski diagram (cf. Figure IV.2).

Interestingly, the range of accessible bleaching energies through compositional change of the structure is not as big as the range of activation energies (from -0.43 to -0.28 eV hence a difference of 0.14 eV, and from 3.14 to 3.64 eV hence a difference of 0.50 eV respectively) and is actually close to the typical error reported for TD-DFT calculations (few tenths of eV).[40] By considering that this error is systematic for such similar systems (*e.g.* artificial sodalites), the conclusion of this study is the possibility to slightly tune the bleaching energy essentially by modifying the halogen atom. Indeed, whatever A A=Al,Ga) and B (B=Si,Ge) in ABX's composition (X=Cl,Br,I) we have:

$$E_{bleaching}(AB\mathbf{I}) < E_{bleaching}(AB\mathbf{Br}) < E_{bleaching}(AB\mathbf{Cl})$$

the smaller the tetrahedron volume, the higher the stabilisation of the trapped electron.

Hence, the overall composition of the β-cage does not play quantitatively on the bleaching energy. However, it appears that the activation energy can be reduced by increasing the cell parameter (*i.e.* composition of the β-cage) or reducing the tetrahedron's volume (*i.e.* playing on the ionic radius of the halogen anion), even if no clear mathematical

relationship could be found. This observation deserves greater investigations, but shows promising perspectives in terms of tuning.

IV.3.2.5. Influence of the composition of the sodium tetrahedron

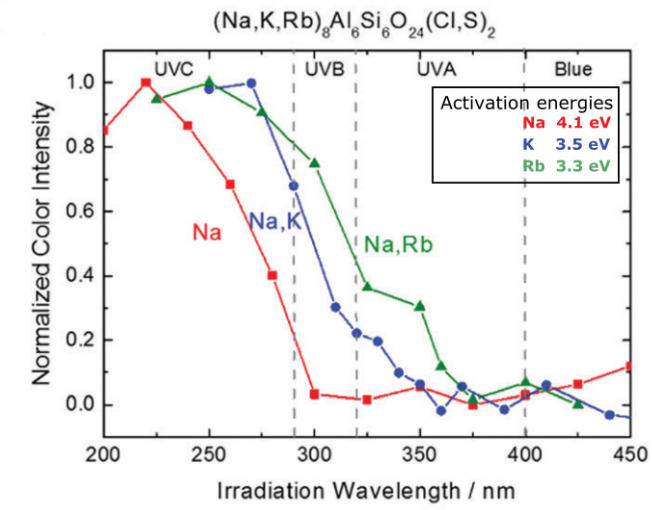

(a)

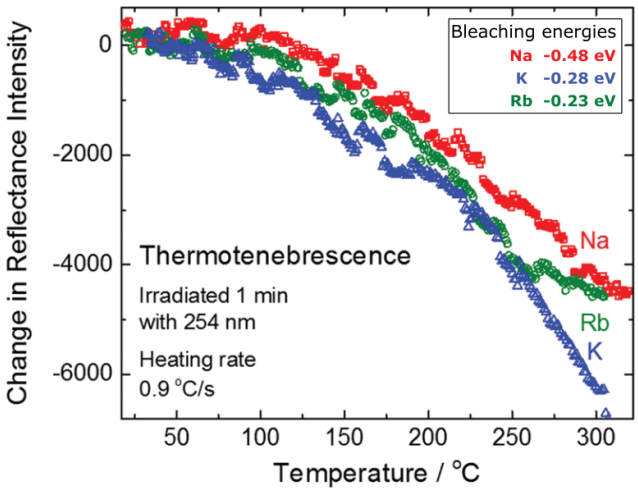

(b)

Figure IV.31: (a) Tenebrescence excitation spectra of $(Na,M)_8(AlSiO_4)_6(Cl,S)_2$ (M = none, K and Rb). Figure taken from [33]. (b) Thermotenebrescence curves for $((Na,M)_8(AlSiO_4)_6(Cl,S)_2$ (M = non, K or Rb) after full coloration. Red squares, blue triangles and green circles are for pristine, K- and Rb-doped hackmanites, respectively. Figure taken from [33].

Experimentally, it was observed both a diminution of the required activation energy and a diminution of the bleaching energy by doping the material with potassium (K) or Rubidium (Rb) (cf. Figures IV.31a and IV.31b).

As for the F-center's absorption simulation, we studied the impact of the modification of the sodium tetrahedron on the activation and bleaching energies. The modification consists in substituting one (Na_3K), two (Na_2K_2) or three (NaK_3) sodium atoms surrounding the vacancy by the same amount of potassium atoms (cf. IV.2.2.4).

The activation energies obtained were computed on Opc systems at TD-DFT/CAM-B3LYP level of theory. As a general result, increasing the concentration of K^+ leads to a diminution of the activation energy from 3.6 eV (Na_4) to 3.1 eV (NaK_3). This is similar to the experimentally reported decrease of energy from 4.1 eV to 3.5 eV after K doping, as shown in Figure IV.31.[33]

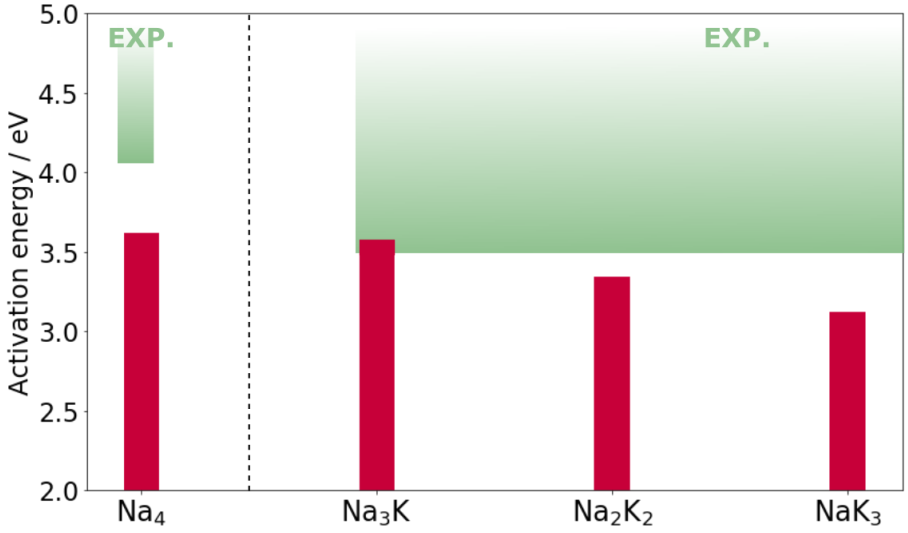

Figure IV.32: Activation energies as a function of the sodium tetrahedron composition. The experimental activation energies are 4.1 and 3.5 eV respectively for the non-doped and K-doped materials.

The bleaching energies of the different systems have been computed at TD-DFT level of theory (within TDA), with the three RSH functionals introduced before (cf. section IV.3.1.3), on Opc sytems. This comparative study of the functionals illustrates again the better agreement of CAM-B3LYP with the experiment, the K-doped coloured form being experimentally stable (cf. Figure IV.33). Indeed, experimentally, the bleaching energy is reported around 0.23 eV for $\approx$ 10% of doping.[33] The model reproduces the decrease in bleaching energy observed by doping.

Interestingly, the previously reported decrease in activation energy through potassium doping of the composition comes with a decrease in bleaching energy. To design photochromic materials, one will have to find the balance between stability of the coloured form and required activation energy.

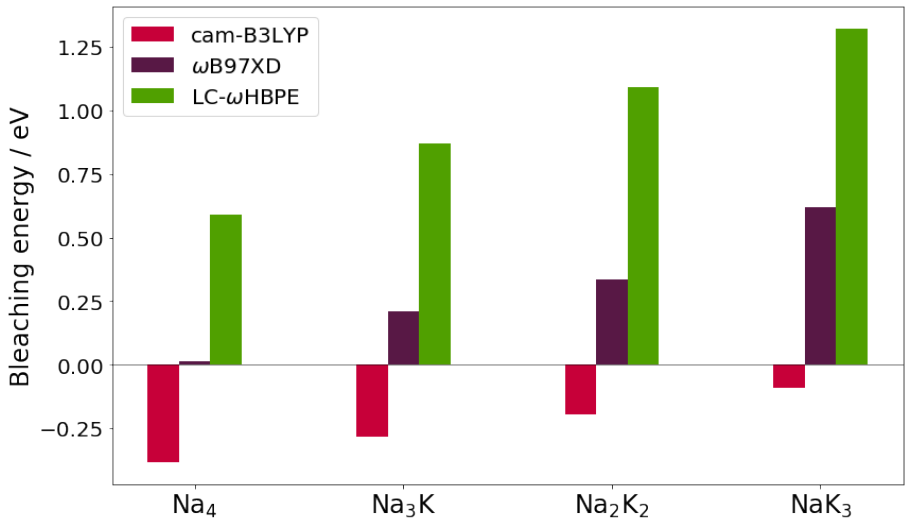

Figure IV.33: Bleaching energies as a function of both the sodium tetrahedron composition and the functional.

IV.3.2.6. Influence of the activator

Sulfur XPS measurements on natural sodalite minerals on the S2p binding energies (cf. top curves in Figure IV.34) indicate the presence of several sulfur impurities that differ by their oxidation state (from -II to +VI).
The lower the oxidation state, the lower the measured binding energy. Assuming that the same trend can be transferred to valence shifts of the polyatomic impurities, the transfer of an electron from an impurity to a nearby vacancy (photochromism activation) requires less energy for sulfur impurities with low oxidation state.

After UV irradiation, the XPS measurement on the coloured material (cf. bottom curves in Figure IV.34) indicates a decrease of the peak corresponding to the lowest binding energies and -II/-I sulfur oxidation states (*e.g.* S_2^{2-} impurity) and an increase of the peak corresponding to -I/2 oxidation state (*e.g.* S_2^{-} impurity) compared to the white material (cf. [33] for more details on the peaks' assignment). This is in agreement with the mechanism of photochromism in sodalite summarized in Equation IV.1.

However, the presence of other sulfur impurities in the material (cf. Figure IV.34) leads on to the question what would be the activation energy for photochromism related to each of them. In what extent is it possible to play on photochromism activation energy by modifying the nature of the impurity? To answer this we optimized 2X2X2 supercells containing 6.25% chloride anions substituted by different sulfur impurities: SO_4^{2-} (S(+VI)), SO_3^{2-} (S(+IV)) and S^{2-} (S(-II)). In parallel to this, we addressed the role of the nature of the impurity by looking at other chalcogen elements, Se and Te, with two

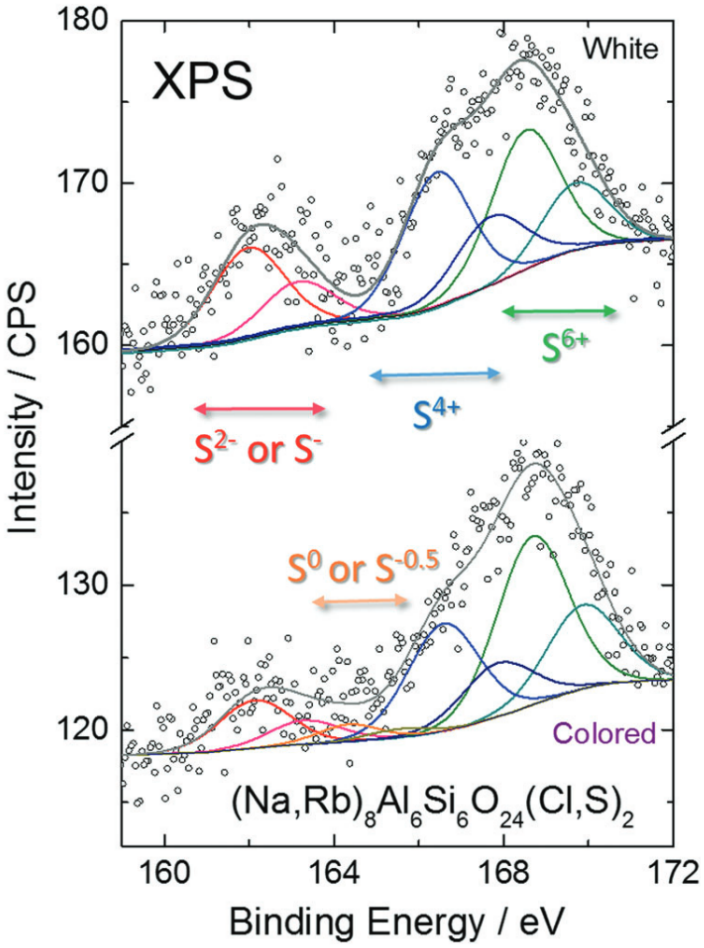

Figure IV.34: XPS S2p spectrum for a white (before UV irradiation) and coloured (after UV irradiation) $(Na,Rb)_8(AlSiO_4)_6(Cl,S)_2$ material. Picture taken from [33]

oxidation states for each: Se_2^{2-}, Se^{2-}, Te_2^{2-} and Te^{2-}. The activation energies calculated at the TD-DFT/CAM-B3LYP level of theory for all six investigated activators are reported in Figure IV.35, along with the one of S_2^{2-}.

The activation energy is related to the oxidation state as suggested in the previous paragraph with:

$$E_{activation}(SO_4^{2-}) > E_{activation}(SO_3^{2-}) > E_{activation}(S_2^{2-})$$

However, the fact that the activation energy of any chalcogen dianion (X^{2-}, X=S,Se,Te) is greater than its respective dichalcogenur's (X_2^{2-}) activation energy suggests that the oxidation state is not the only parameter one can play on. The other difference between X^{2-} and X_2^{2-} is their size. The dichalcogenur being bigger than the substituted chloride anion, it is reasonable to think that the X_2^{2-} will experience steric hindrance. Indeed, as reported before S_2^{2-} computed bond length is 2.13 Å in the cage while it is larger when optimized in vacuum: 2.25 Å. The effect is even more important for bigger elements (Se

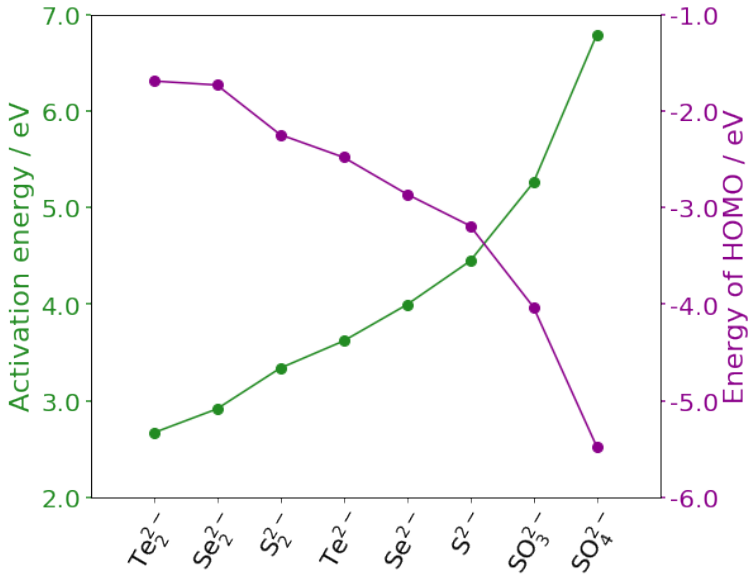

Figure IV.35: Activation energy calculated at TD-DFT/CAM-B3LYP level of theory on Opc systems with different activators (green). Energy of the HOMO ($\pi*$) of each activator (purple).

and Te). This constraint on the geometry of the dianions impacts in turn the level of energy of the molecular orbitals, with an increase in energy of the HOMO ($\pi*$) and so a proportional decrease of the activation energy. This is in agreement with the formula:

$$E_{\text{activation}} \approx E_{CT} = IP^D - EA^A - \frac{1}{R} \approx \epsilon_{\text{HOMO}} - \epsilon_{\text{LUMO}} - \frac{1}{R} \qquad \text{(IV.4)}$$

when ϵ_{HOMO} increases, $E_{\text{activation}}$ increases. The agreement is further shown in Figure IV.36. Hence, to get an idea of the activation energy for any activator, one can look at the energy of the HOMO of the impurity in the β-cage through a single point calculation (cf. purple curve in Figure IV.35), and compare it with a reference for which the activation energy has been calculated.

If it is possible to tune the activation energy by playing on the nature of the activator this should also impact the bleaching process, hence the stability of the coloured form. Not much work have been conducted on that aspect for the moment. Calculations have been conducted for S^{2-} and SO_4^{2-} activators. In the case of SO_4^{2-}, the transitions obtained ($^1[SO_4^{2-}, V_{Cl}] \rightarrow {}^3[SO_4^-, V_{Cl}^-]$) for the corresponding coloured form are all positive (> 0.7 eV) suggesting no stability of the trapped electron. Interestingly, in the case of S^{2-}, the bleaching energy obtained computationally is -0.2 eV, meaning that this time an increase in activation energy (cf. Figure IV.35) comes with a decrease in bleaching energy.

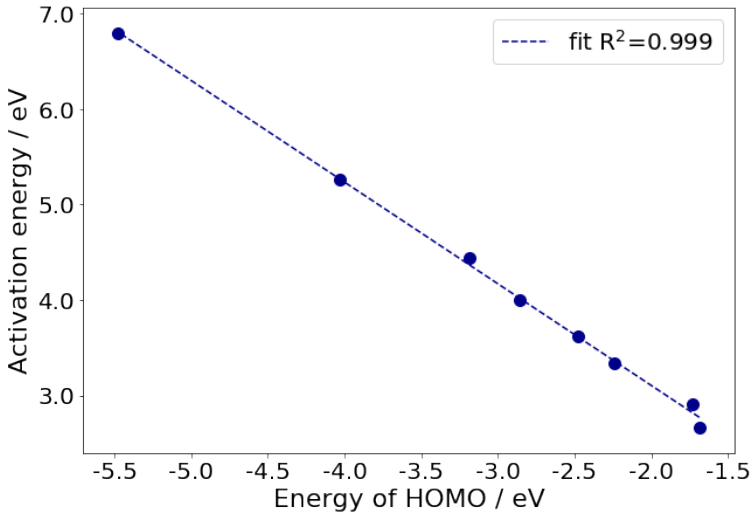

Figure IV.36: Activation energy (eV) as a function of the energy of the HOMO (eV) localized on the activator. Both energies are obtained at the TD-DFT/CAM-B3LYP level of theory.

IV.4. Conclusion

In this chapter we have presented and discussed the methodologies chosen for simulating the F-center's absorption and accessing both activation and bleaching energies. By systematic comparison with available experimental data, methodologies have emerged as satisfactory and reliable. They are based on PBC calculations for the optimisation of the geometries followed by a molecular approach consisting in extracting a cluster made of one (F-center's simulation) or two (charge transfer processes) β-cages, embedded in pseudopotentials and point charges.
In the case of F-center's absorption simulation, the inclusion of vibronic coupling is possible and improve the shape of the simulated curves but at a low benefits-costs ratio.

The methodologies were then apply to artificial materials or doped ones to investigate the possibilities of tuning reachable with this type of systems. The composition of both the β-cage and the tetrahedron play on F-center's absorption, activation energy and bleaching energy. Besides, if one wants only to tune the activation and bleaching energies without modifying the colour taken by the material it is possible by changing the nature of the activator species.
In any case careful considerations must be given to the stability of the coloured form. Indeed, studies presented here showed that decreasing the activation energy by modifying the activator or the volume of the tetrahedra surrounding the defects, often comes with a destabilisation of the coloured form (*i.e.* reduction of the bleaching energy).

References Chapter IV.

[1] E. R. Williams, A. Simmonds, J. A. Armstrong, and M. T. Weller *Journal of Materials Chemistry*, vol. 20, no. 48, pp. 10883–10887, **2010**.

[2] I. Norrbo, P. Gluchowski, I. Hyppanen, T. Laihinen, P. Laukkanen, J. Makela, F. Mamedov, H. S. Santos, J. Sinkkonen, M. Tuomisto, A. Viinikanoja, and M. Lastusaari *ACS Applied Materials & Interfaces*, vol. 8, no. 18, pp. 11592–11602, **2016**.

[3] J. A. Armstrong and M. T. Weller *Chemical Communications*, no. 10, pp. 1094–1096, **2006**.

[4] I. Hassan, S. M. Antao, and J. B. Parise *American Mineralogist*, vol. 89, no. 2-3, pp. 359–364, **2004**.

[5] T. Le Bahers, M. Rerat, and P. Sautet *The Journal of Physical Chemistry C*, vol. 118, no. 12, pp. 5997–6008, **2014**.

[6] K. T. Thomson and R. M. Wentzcovitch *The Journal of Chemical Physics*, vol. 108, no. 20, pp. 8584–8588, **1998**.

[7] A. Curutchet and T. Le Bahers *Inorganic Chemistry*, vol. 56, no. 1, pp. 414–423, **2017**.

[8] F. Labat, P. Baranek, C. Domain, C. Minot, and C. Adamo *The Journal of Chemical Physics*, vol. 126, no. 15, p. 154703, **2007**.

[9] M. Sokolov, R. I. Eglitis, S. Piskunov, and Y. F. Zhukovskii *International Journal of Modern Physics B*, vol. 31, no. 31, p. 1750251, **2017**.

[10] E. Kotomin, V. Kuzovkov, A. Popov, and R. Vila *Nuclear Instruments and Methods in Physics Research Section B: Beam Interactions with Materials and Atoms*, vol. 374, pp. 107–110, **2016**. Basic Research on Ionic-Covalent Materials.

[11] R. Eglitis, A. I. Popov, J. Purans, and R. Jia *Low Temperature Physics*, vol. 46, no. 12, p. 1206–1212, **2020**.

[12] N. Chuklina, S. Piskunov, N. Popov, A. Mysovsky, and A. Popov *Nuclear Instruments and Methods in Physics Research Section B: Beam Interactions with Materials and Atoms*, vol. 474, p. 57–62, **2020**.

[13] T. Biswas and M. Jain *Physical Review B*, vol. 99, no. 14, **2019**.

[14] D. A. Drabold and S. K. Estreicher, *Theory of defects in semiconductors.* **2007**.

[15] T. Inui and Y. Uemura *Progress of Theoretical Physics*, vol. 5, no. 2, p. 252–265, **1950**.

[16] J. A. Krumhansl and N. Schwartz *Physical Review*, vol. 89, no. 5, p. 1154–1155, **1953**.

[17] P. Tiwald, F. Karsai, R. Laskowski, S. Gräfe, P. Blaha, J. Burgdörfer, and L. Wirtz *Physical Review B*, vol. 92, no. 14, p. 144107, **2015**.

[18] Y. Toyozawa and M. Inoue *Journal of the Physical Society of Japan*, vol. 21, no. 9, pp. 1663–1679, **1966**.

[19] T. Koyama and T. Suemoto *Reports on Progress in Physics*, vol. 74, no. 7, p. 076502, **2011**.

[20] P. Rinke, A. Schleife, E. Kioupakis, A. Janotti, C. Rödl, F. Bechstedt, M. Scheffler, and C. G. Van De Walle *Physical Review Letters*, vol. 108, no. 12, **2012**.

[21] B. M. Klein, W. E. Pickett, L. L. Boyer, and R. Zeller *Physical Review B*, vol. 35, no. 11, p. 5802–5815, **1987**.

[22] C. Freysoldt, B. Grabowski, T. Hickel, J. Neugebauer, G. Kresse, A. Janotti, and C. G. Van de Walle *Reviews of Modern Physics*, vol. 86, no. 1, p. 253, **2014**.

[23] L. E. Ramos, J. Paier, G. Kresse, and F. Bechstedt *Physical Review B*, vol. 78, no. 19, **2008**.

[24] X. Blase, I. Duchemin, D. Jacquemin, and P.-F. Loos *The Journal of Physical Chemistry Letters*, vol. 11, no. 17, pp. 7371–7382, **2020**.

[25] R. Évarestov *Journal of Structural Chemistry*, vol. 24, no. 4, pp. 540–555, **1984**.

[26] R. Shendrik, N. Popov, and A. Myasnikova *IEEE Transactions on Nuclear Science*, vol. 67, no. 6, pp. 946–951, **2020**.

[27] P. Colinet, A. Gheeraert, A. Curutchet, and T. Le Bahers *The Journal of Physical Chemistry C*, vol. 124, no. 16, pp. 8949–8957, **2020**.

[28] Y. F. Zhukovskii, E. A. Kotomin, R. A. Evarestov, and D. E. Ellis *International Journal of Quantum Chemistry*, vol. 107, no. 14, pp. 2956–2985, **2007**.

[29] C. Cohen-Tannoudji, B. Diu, and F. Laloë, *Mécanique Quantique.* Centre de Publications Universitaire, Téhéran, **1986**.

[30] T. J. Konno *Journal of Chemical Education*, vol. 78, no. 5, p. 674, **2001**.

[31] D. Jacquemin, A. Planchat, C. Adamo, and B. Mennucci *Journal of Chemical Theory and Computation*, vol. 8, no. 7, pp. 2359–2372, **2012**.

[32] D. Jacquemin, V. Wathelet, E. A. Perpete, and C. Adamo *Journal of Chemical Theory and Computation*, vol. 5, no. 9, pp. 2420–2435, **2009**.

[33] I. Norrbo, A. Curutchet, A. Kuusisto, J. Mäkelä, P. Laukkanen, P. Paturi, T. Laihinen, J. Sinkkonen, E. Wetterskog, F. Mamedov, T. Le Bahers, and M. Lastusaari *Materials Horizons*, vol. 5, no. 3, pp. 569–576, **2018**.

[34] S. Vuori, P. Colinet, I. Norrbo, R. Steininger, T. Saarinen, H. Palonen, P. Paturi, L. C. V. Rodrigues, J. Göttlicher, T. Le Bahers, and M. Lastusaari *Advanced Optical Materials*, p. 2100762, **2021**.

[35] I. Norrbo, P. Gluchowski, P. Paturi, J. Sinkkonen, and M. Lastusaari *Inorganic Chemistry*, vol. 54, no. 16, pp. 7717–7724, **2015**.

[36] M. J. Peach, M. J. Williamson, and D. J. Tozer *Journal of Chemical Theory and Computation*, vol. 7, no. 11, pp. 3578–3585, **2011**.

[37] M. J. Peach, N. Warner, and D. J. Tozer *Molecular Physics*, vol. 111, no. 9-11, pp. 1271–1274, **2013**.

[38] J. S. Sears, T. Koerzdoerfer, C.-R. Zhang, and J.-L. Brédas *The Journal of Chemical Physics*, vol. 135, no. 15, p. 151103, **2011**.

[39] R. J. Clark and D. G. Cobbold *Inorganic Chemistry*, vol. 17, no. 11, pp. 3169–3174, **1978**.

[40] E. K. Gross and N. T. Maitra, "Introduction to TDDFT," in *Fundamentals of Time-Dependent Density Functional Theory*, pp. 53–99, Springer, **2012**.

CHAPTER V

Complete characterization of naturally photochromic minerals

What we observe is not nature itself, but nature exposed to our method of questioning.

Werner Heisenberg

In the previous chapter the interest was on choosing computational methodologies to study all essential characteristics of photochromism in the sodalite mineral. These methodologies have proven consistency with experimental data and were then applied onto never synthesized materials. This sheds light on the great possibilities regarding the control of photochromic parameters (*e.g.* colour, activation energy...) in sodalite materials.

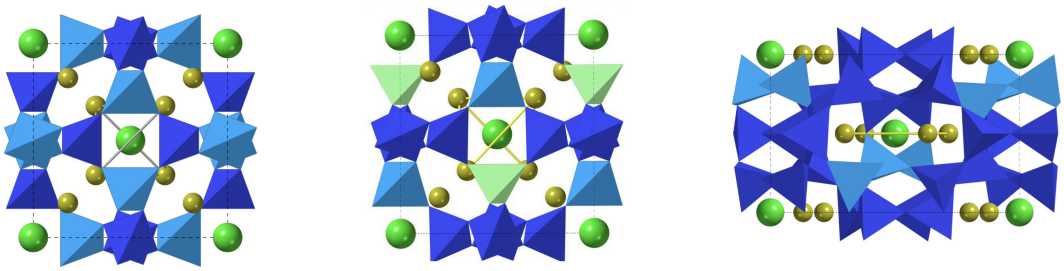

(a) (b) (c)

Figure V.1: Three minerals' structure enhancing the characteristic β-cages made of silicate SiO_4^{4-} (blue), aluminate AlO_4^{5-} (cyan) and beryllate BeO_4^{6-} (mint green) corner-shared tetrahedra. Four sodium atoms (yellow) form a tetrahedron (sodalite (a) and tugtupite (b)) or a square (scapolite (c)) in which lays a chloride atom (bright green).

Actually, this variability in terms of photochromic properties is also, in a lesser extent, present in Nature. Indeed, along with sodalite exist other naturally-reversible photochromes that belong to the aluminosilcate family: tugtupite ($Na_8Al_2Be_2Si_8O_{24}Cl_2$) and scapolite ($[Na,Ca]_4Al_3Si_9O_{24}Cl_2$).

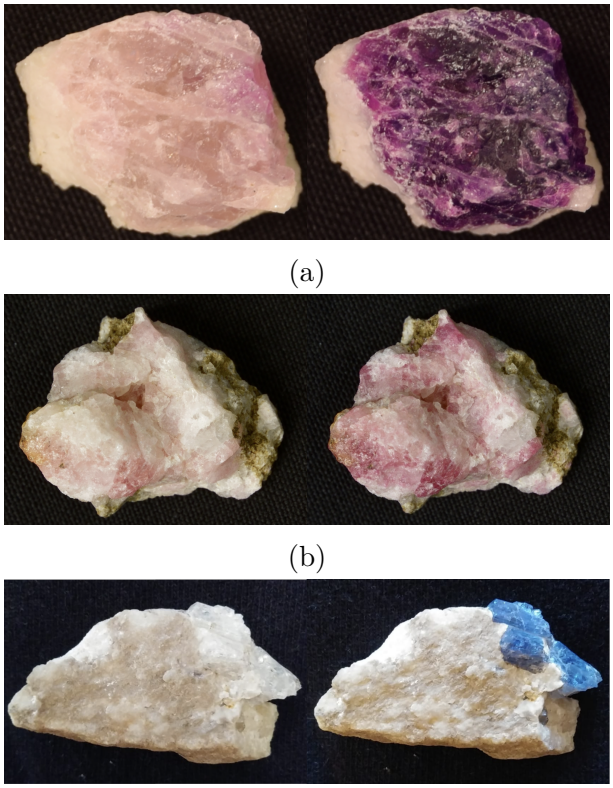

(a) (b) (c)

Figure V.2: Photos of white materials (left) and colour change experienced after UV irradiation (right), in (a) sodalite, (b) tugtupite and (c) marialite

Contrary to sodalite, tugtupite and scapolite have almost not been considered for their photochromic properties up to now. In terms of crystal structure, they possess the characteristic aluminosilicate cage (the β-cage) containing a sodium polyhedron (a tetrahedron for tugtupite, a square for scapolite) with a chlorine ion standing in its center (cf. Figure V.1). Due to composition and crystal structure similarities between the three minerals considered, it has been assumed that the photochromic mechanism is the same for all of them, summarized in the equation:

$$S_2^{2-} + V_{Cl} \underset{\text{bleaching energy}}{\overset{\text{activation energy}}{\rightleftharpoons}} S_2^{-} + V_{Cl}^{-} \tag{V.1}$$

However, analysis of the oxidation states of sulfur in these minerals typically reveals a large variety of sulfur-based species (as discussed for natural sodalite in IV.3.2.6) and we cannot rule out the possibility that the F-center can be generated from another sulfur

impurity than S_2^{2-}. This will be investigated all along the chapter by considering other sulfur impurities in addition to S_2^{2-}: sulfite (SO_3^{2-}) and sulfide (S^{2-}) anions.

While belonging to the same family, these three minerals actually experience different properties in term of colouration (cf. Figure V.2), activation energy and bleaching energy. This can be attributed to the change in composition and/or three dimensional arrangements of their constitutive atoms. The aim of this chapter is to provide the complete characterization of these three natural minerals and bring a physico-chemical interpretation of the origin of their different behaviours based on quantum chemical calculations. To do so, we will use the methodologies introduced in the previous chapter, along with experimental characterizations (provided by our collaborators from Turku University). This study is also an opportunity to test the robustness of the quantum chemical protocol on similar systems to the one it was developed on.

Before introducing the reader with the main results of this investigation, a first section (V.1) will provide information about the structure and composition of the different studied materials in order to highlight their common features and structural differences. Some information about the models used for the calculations can be found in the same section. Then the chapter will have a structure based on the chronology of photochromism mechanism. Indeed, a section will focus on the activation process (V.2), followed by the study of the F-center's absorption properties (V.3) and eventually we will come to the bleaching analysis (V.4).

The results presented in this chapter have been submitted for publication under the name: "*Why does the structure of natural photochromic minerals make them so efficient?*".

V.1. A combined experimental and computational study

This chapter presents the results of a hand in hand experimental and computational study. It is necessary to know the models used and their limitations as well as the materials studied, otherwise comparisons or validations can not be drawn.
Experimentally, the first step consists in acquiring the materials (which is not straightforward) and then to check their structure and composition. It is important to note that some analysis are destructive and so limited in number. It is the case for the bleaching analysis that requires the materials to be crushed into powders.

The overall methodology presented in the previous chapter for modelling the photochromism of sodalite mineral will be used in this chapter. That is PBC calculations for geometry optimizations (bulk or supercells containing defect(s)) followed by a molecular approach consisting in TD-DFT calculations on embedded clusters (*i.e.* clusters embedded in pseudopotentials and point charges).

V.1.1. Origin and structural analysis of the minerals

The three minerals come from different parts of the world: tugtupite is from Greenland, while sodalite and scapolite are both from Afghanistan. XRD and elemental analysis (cf. Appendix Figure A.5 and Table A.9) confirm their respective crystallographic structure. These analyses do not reflect possible local structural variabilities.
The scapolite corresponds to a mineral family whose composition is between two crystallographic systems called marialite ($Na_4(Al_3Si_9O_{24})Cl$) and meionite ($Ca_4(Al_6Si_6O_{24})(CO_3)$). The sample investigated here has 75% of marialite and 25% for meionite character based on the Na/Ca ratio.

Only sodalite and scapolite have a measurable quantity of sulfur (around 0.2 at% for both) while the tugtupite has no detectable S impurites by XPS indicating that the S content is below 0.1 at% corresponding to the limit of detection of the XPS. Yet, all three minerals show the characteristic orange photoluminescence (370 nm excitation, cf. Figure V.3) characteristic of the S_2^- ion in the material as a signature of both the presence of sulfur-based impurities and the appropriate oxidation state of sulfur.[1–3]

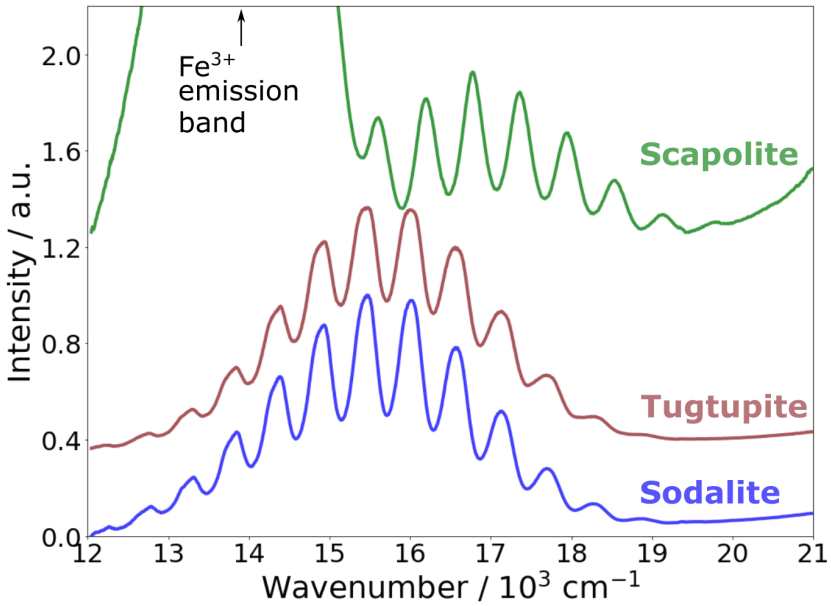

Figure V.3: Vibrational fine structure in the photoluminescence emission spectra of S_2^- in scapolite (green), tugtupite (brown) and sodalite (blue) recorded at 77 K.

V.1.2. Geometry optimizations in PBC

V.1.2.1. Sodalite

The methodology is obviously unchanged concerning sodalite material compared to the one presented in the previous chapter, so that detailed results on this mineral can be found in chapter IV.

V.1.2.2. Tugtupite

Regarding tugtupite mineral, the only difference with sodalite lies in the composition of the β-cage with the substitution of some aluminium atoms by beryllium or silicon ones. This entails a drop of symmetry in comparision with sodalite; tugtupite belonging to the tetragonal space group $I\bar{4}$. The overall methodology remains unchanged compared to sodalite. The optimized cell parameters for tugtupite are $a = b = 8.583$Å and $c = 8.831$Å close to the experimental ones ($a = 8.864$Å, $c = 8.873$Å [4]). The volume of the β-cage is then a bit smaller than for sodalite: ≈ 477 Å^3 (tugtupite) against ≈ 503 Å^3 (sodalite).

Concerning the introduction of the defects in the structure, a 2X2X2 supercell containing as many atoms as for sodalite (368 atoms) has been optimized. Moreover, the relative position of the two defects is similar to the one used during the study on sodalite.

V.1.2.3. Scapolite

For simplicity, scapolite was modelled with a 100% marialite character. However, the marialite ($Na_4Al_3Si_9O_{24}Cl_2$) structure by itself is a solid solution. Aluminum and silicon atoms are occupying two types of tetrahedral sites. Using the notation proposed by Sokolova *et al.*,[5] these sites are named T_1 and T_2. While the T_1 site is only occupied by Si atoms, the T_2 sites is a Al/Si solid solution having the Al/Si ratio of 3/5.

In this work, in order to have a bulk structure of pristine scapolite, we considered a supercell two times bigger than the primitive cell of the scapolite (*i.e.* $\approx$ 12x12x7.5 Å^3, 82 atoms), and all possible conformations of Al/Si in the T_2 site corresponding to the 3/5 ratio were built, leading to 7 different conformations (cf. Figure V.4). We optimized all of them and observed that their energy does not deviate more than 0.08 eV from the most stable to the least stable. We eventually chose the most symmetric one ($a = b = 11.906$Å, $c = 7.538$Å) in the sake of saving computational time. Details about results of the optimizations are given in Appendix Table A.8.

The optimized geometry shows the characteristic square of sodium surrounding the chloride anion, and the elongated β-cage (cf. left part of Figure V.4) which volume is $\approx$ 300 Å^3, much smaller than tugtupite and sodalite.

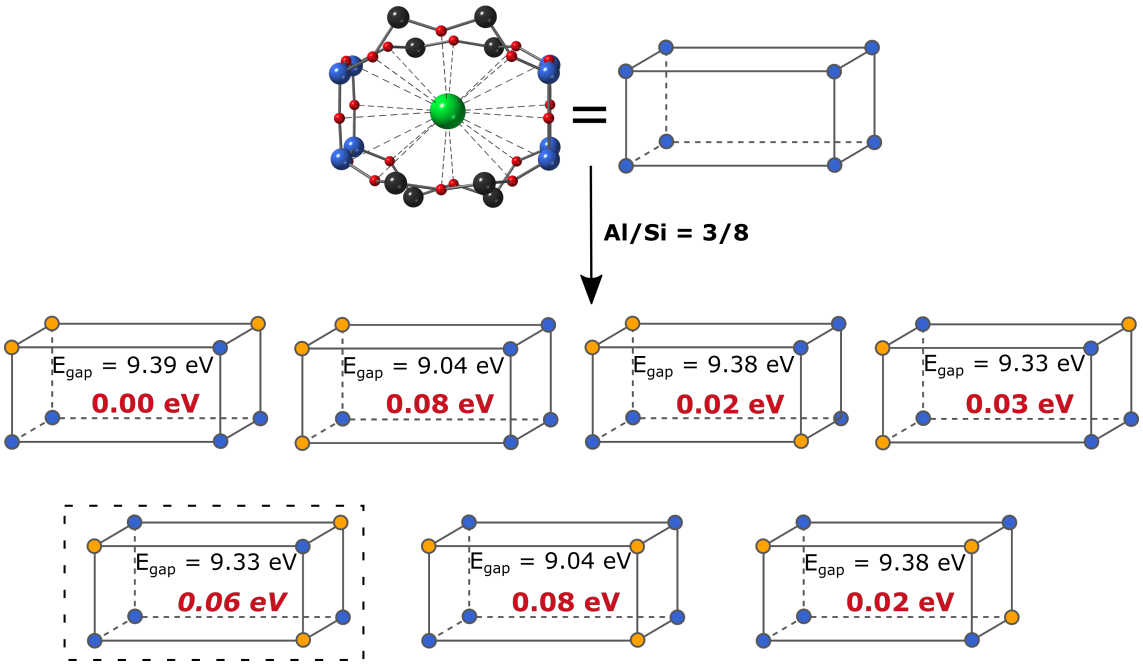

Figure V.4: Different conformations investigated for marialite solid solution. In the β-cage on the left, silicon atoms in T_1 or T_2 sites are respectively depicted by grey or blue spheres; oxygen and chlorine atoms by red and green spheres. T_2 sites are then represented as a rectangle made by 8 silicon atoms that can be substituted by aluminium ones (yellow) leading to 7 possible combinations with the 3/5 Al/Si ratio. The (indirect) band gap are given for each combination along with the relative energy (green) with respect to the most stable combination. The combination used in the following is highlighted by a dashed type box.

Concerning the introduction of the defects in the structure, a 1X2X2 supercell containing 328 atoms has been optimized. Due to the symmetry of scapolite, the relative positions of the two defects are equivalent whatever the two nearby β-cages chosen.

V.1.2.4. Structural modification around the defect

When a sulfur impurity substitutes a chloride anion in the structure we observe a modification of the Na_4 polyhedron structure. This is visible by the modification of the average Na-Na distance (cf. Table V.1). The bigger the impurity, the higher the structural change.

	Sodalite	Tugtupite	Scapolite
Cl^- (Ref.)	4.44	4.40	4.10
S_2^{2-}	4.66	4.58	3.96
S^{2-}	4.30	4.27	3.43
SO_3^{2-}	4.76	4.34*	4.07

Table V.1: Average Na-Na distance in the tetrahedra (Å) around defects for the three materials. The reference values (around Cl^-) are given for further comparison. *The tetrahedron is deformed so that the average Na-Na value is not representative of the available volume.

V.1.2.5. Densities of states

The electronic properties of the bulks are similar due to the very close structure and composition of the three materials (cf. Figure V.5). The band gap decreases from sodalite to tugtupite by 0.15 eV and from tugtupite to scapolite by 1.02 eV, but the three materials remain large band gap insulators.

Based on XPS analysis, we considered several sulfur-based dianions as activators: S_2^{2-}, S^{2-} and SO_3^{2-}. The DOS for the three materials containing different pairs of defects (S_2^{2-}, V_{Cl}), (S^{2-}, V_{Cl}), and (SO_3^{2-}, V_{Cl}) are given respectively in Figure V.6, Figure V.7 and Figure V.8. Whatever, the material and the sulfur impurity considered, new states appear in the band gap. The HOMO is a $\pi*$ or p orbital on the impurity and the LUMO is always the a_1 (a_{1g} for scapolite) orbital located on V_{Cl}. From these electronic structures, it appears that the first expected transition, from the HOMO to the LUMO, is always a charge transfer transition in agreement with the F-center formation upon light exposure. For all three minerals the optimized basis sets for the trapped electron are given in Table III.1.

When considering sodalite material, the transition energies obtained from the DOS for S_2^{2-}, S_2^- and SO_3^{2-} activators are in good qualitative agreement with the conclusions drawn in section IV.3.2.6, about the influence of the nature of the activator on the activation energy:

$$E_{activation}(SO_3^{2-}) > E_{activation}(S^{2-}) > E_{activation}(S_2^{2-}) \quad (V.2)$$

The behaviour is similar when considering tugtupite, with transition energies requiring less energy than in sodalite on average. Scapolite on the other hand is more unique with an inversion between S_2^{2-} and S^{2-} (*i.e.* $E_{activation}(S^{2-}) < E_{activation}(S_2^{2-})$). This can be explained by less constraints on the sulfur impurity in scapolite structure compared to the other ones, because of the Na_4 square shape allowing the dianion to place itself almost

perpendicularly to the plane of the square.[2]

This study on the electronic properties of the different materials with different defects provide us with a first idea of the differences existing for the activation process in the three minerals. That we will study more thoroughly in the following.

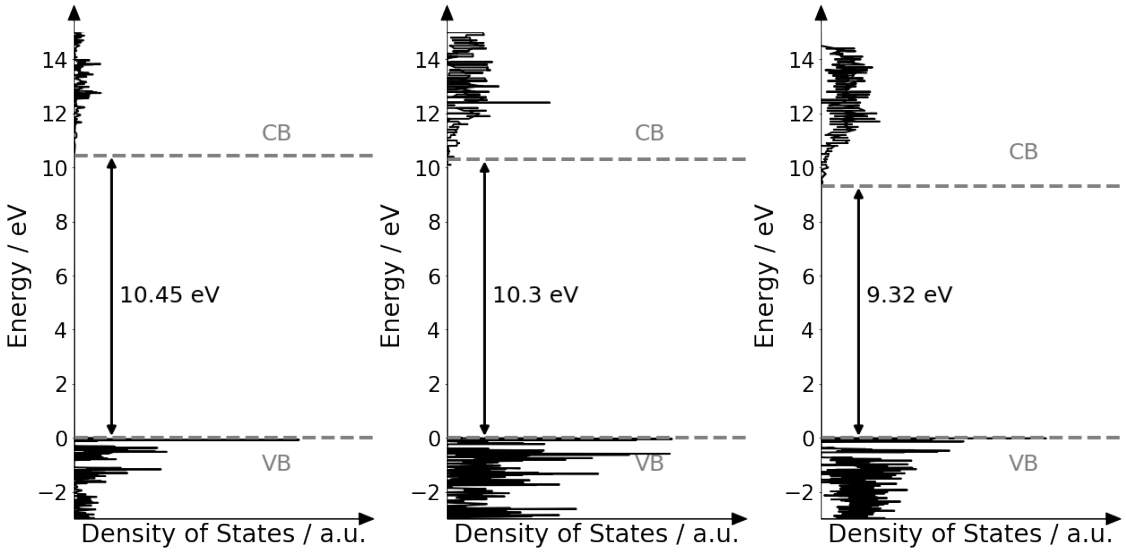

(a) Sodalite (b) Tugtupite (c) Scapolite

Figure V.5: Density of states of the bulk materials.

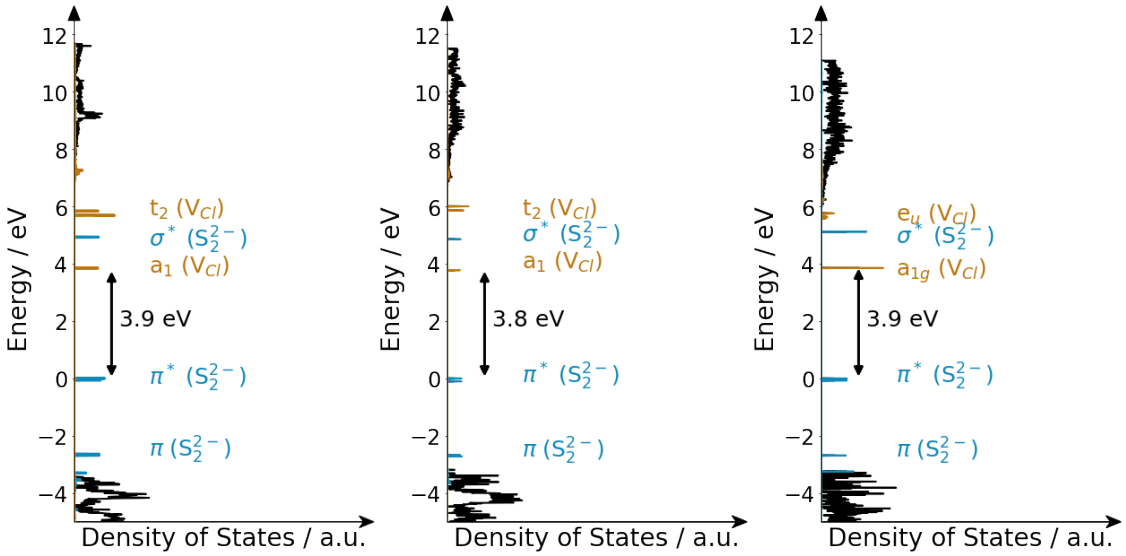

(a) Sodalite (b) Tugtupite (c) Scapolite

Figure V.6: DOS of the supercell containing S_2^{2-} and V_{Cl} defects (black) and projected DOS on the S_2^{2-} (cyan) and V_{Cl} (yellow) orbitals, at the geometry of the colourless form.

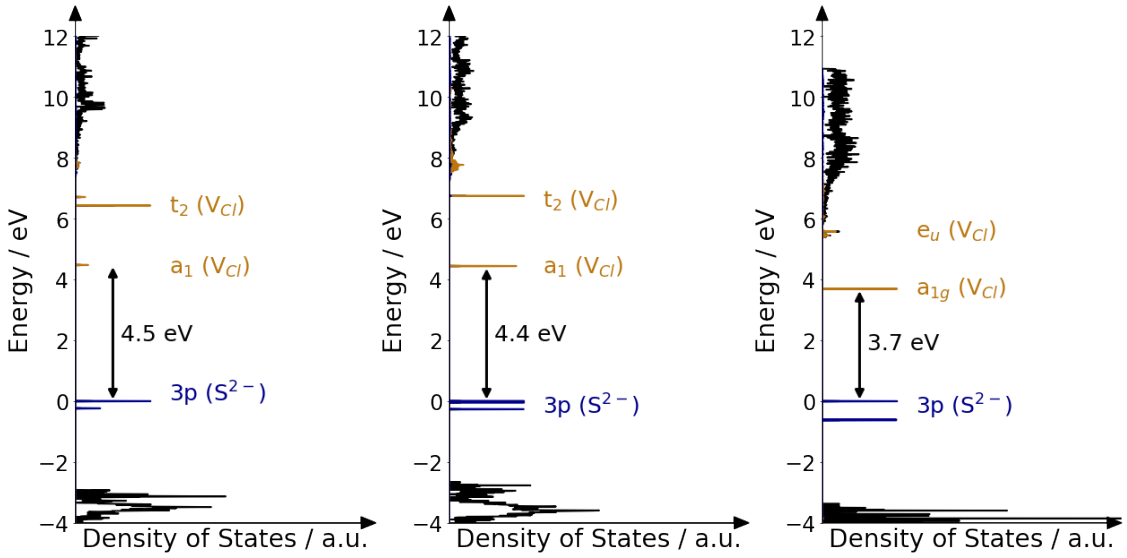

(a) Sodalite (b) Tugtupite (c) Scapolite

Figure V.7: DOS of the supercell containing S^{2-} and V_{Cl} defects (black) and projected DOS on the S^{2-} (dark blue) and V_{Cl} (yellow) orbitals, at the geometry of the colourless form.

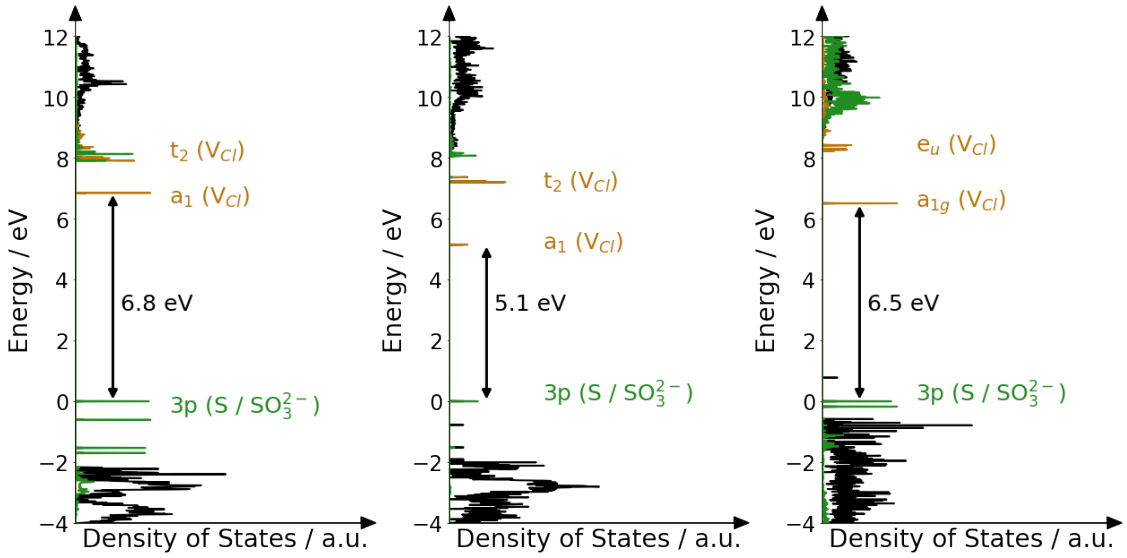

(a) Sodalite (b) Tugtupite (c) Scapolite

Figure V.8: DOS of the supercell containing SO_3^{2-} and V_{Cl} defects (black) and projected DOS on the S (from SO_3^{2-} in green) and V_{Cl} (yellow) orbitals, at the geometry of the colourless form.

V.2. Investigation of the activation of photochromism

The experimental excitation spectra associated with the colouration of the material is reported in Figure V.9 along with the TD-DFT computed charge transfer transition energies for the formation of the trapped electron. The orbitals involved in the transitions are also shown inside the corresponding clusters used for the calculations. In Figure V.9 one can see that the clusters are made of two β-cages ($\approx$ 160 atoms for sodalite and tugtupite, $\approx$ 130 atoms for scapolite) surrounded by a shell of cations that will be treated by pseudopotentials. As previously, this is further embedded by a cloud of point charges.

For the three materials, the experimental spectrum is characterized by a broad band ranging from 375 nm ($\approx$ 3.3 eV) to 250 nm ($\approx$ 5.0 eV). The existence of shoulders (scapolite and sodalite) indicates that several activators are probably responsible for the colouration. This is confirmed by computed activation energies when several sulfur-based activators are considered (SO_3^{2-}, S^{2-}, S_2^{2-}). Interestingly, while the S_2^{2-} activator is generally considered to be the one responsible for the photochromism in artificial sodalites, in natural aluminosilicates the activation energies computed with S^{2-} seem to be in better agreement with experiment. Computed activation energies for S_2^{2-} (at lower energy) or SO_3^{2-} (at higher energy) are also included in the range of experimental excitation, but more so in the shoulder parts. However, we have to recall that our computational model *a priori* underestimates the activation energy (cf. section IV.3.2.3.c), so that S_2^{2-} anion remains in play.

This observation suggests again the possibility to tune the activation energy as already discussed in Chapter IV. In other words, in natural minerals several sulfur-based impurities can activate the photochromism, while in artificial ones for which the synthesis conditions are well defined, it may be possible to select the oxidation state of sulfur impurities and consequently the activation energy of the photochromism. Computed oscillator strengths associated to the photo-induced electron transfer are notably weak (between 10^{-4} and 10^{-2}), in agreement with the experimental observation that a longtime exposition under UV light is necessary to saturate the colour (several minutes, depending on the sample). Also, it must be noted that the inherent compositional inhomogeneity of natural minerals results in multiple slightly different local structures around the sulfur-containing activators. This may cause some shifts and asymmetric broadening in all observed optical spectra.

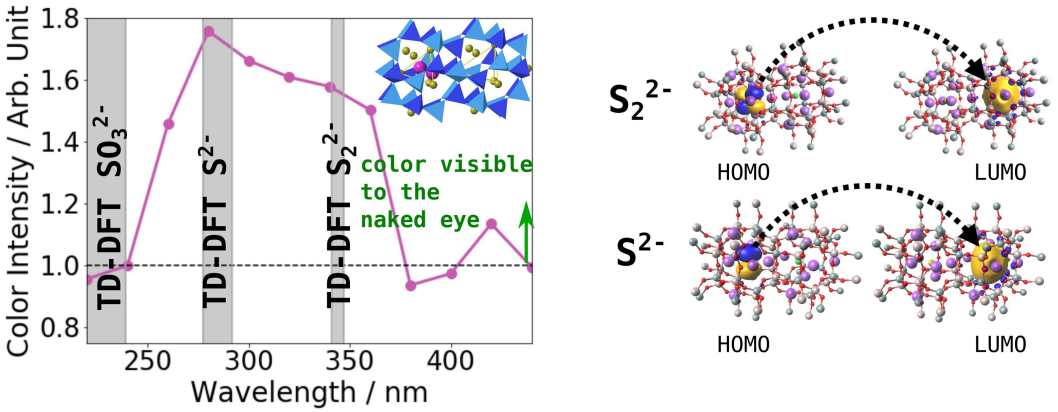

(a) Sodalite

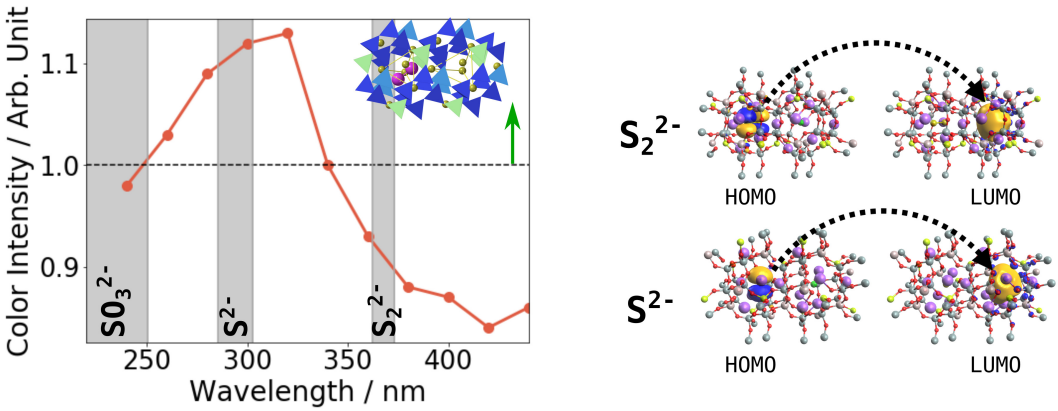

(b) Tugtupite

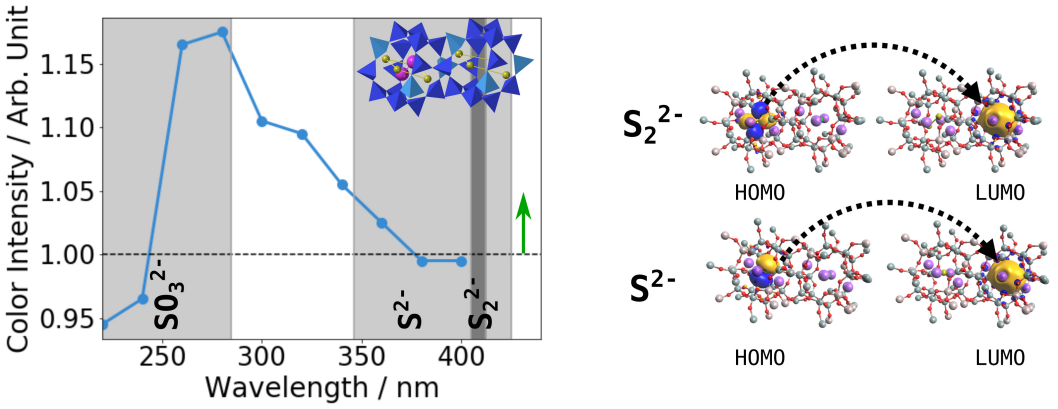

(c) Scapolite

Figure V.9: (left) Colouration excitation spectra of (a) sodalite, (b) tugtupite and (c) scapolite. The colour intensity is given in arbitrary units with the part above the dotted line indicating when the colour becomes visible to the naked eye. Vertical grey areas show the calculated excitation energy range by TD-DFT. The cluster used for the computation is represented on the top-right corner of each graph. (right) Representation of the extracted clusters along with the HOMO (π^* or $3p$) and LUMO (a_1 or a_{1g}) orbitals involved in the transition for the activation of photochromism (isovalue 0.02 a.u.). The black dotted arrow depicts the electron transfer.

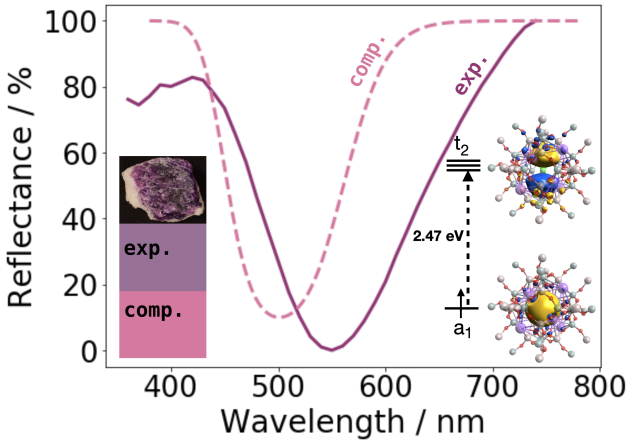

(a) Sodalite

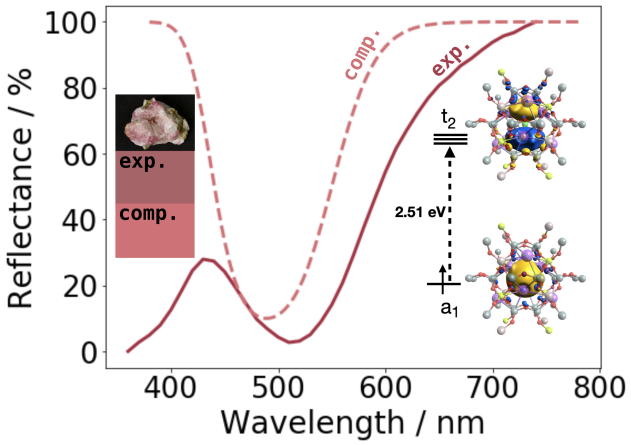

(b) Tugtupite

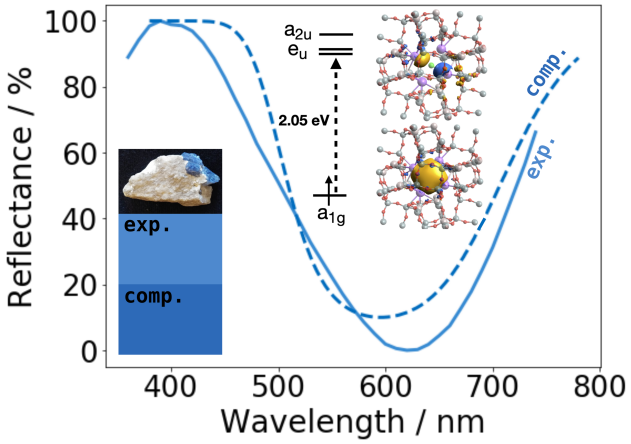

(c) Scapolite

Figure V.10: Experimental (solid line) and simulated from TD-DFT (dotted line) reflectance spectra of (a) sodalite, (b) tugtupite and (c) scapolite. On the left part, experimental and simulated colours are given under a picture of the material. On the right part of each graph lies the representation of the orbitals involved in the absorption of the F-center (isovalue 0.02 a.u.). Orbital labels are associated to the point group of the Na_4 polyhedron (T_d for sodalite and tugtupite, D_{4h} for scapolite cf. Tables A.1 and A.2).

V.3. Tuning the colour through composition and geometry

The most obvious difference between the three minerals considered in this work is the final colour of the coloured form (cf. Figure V.2). These colours originate from the absorption spectrum of the trapped electron, presented in Figure V.10 in the form of reflectance spectra. The reflectance curves show broad minima centered at 550 nm (sodalite), 510 nm (tugtupite) and 620 nm (scapolite). The nature of the colour center is confirmed by TD-DFT calculations as an electron trapped in a chlorine vacancy with computed transitions at 500 nm (sodalite), 490 nm (tugtupite) and 615 nm (scapolite). The shape and positions of the simulated reflectance spectrum agree with the experiment ultimately leading to a simulated colour close to the observed one (cf. insert of each subfigure in Figure V.10).

The orbitals of the trapped electron (cf. Figure V.10) are delocalized beyond the Na_4 polyhedron explaining why a modification of the β-cage composition affects the transition energy of the F-center (when comparing sodalite and tugtupite). This is in agreement with the previous study on artificial sodalites, showing the relationship between F-center's absorption and the cell parameter of the material (cf. IV.2.2.2).

The very different absorption spectrum of the scapolite (both experimentally and computationally) compared to the two other minerals highlights also the large sensitivity of the F-center transitions with respect to the nature of the Na_4 polyhedron (a square for scapolite and a tetrahedron for the two other minerals). This is actually quite similar to the observations made in the case of the deformed Na_3 polyhedron of sodium obtained after γ-ray irradiation, with a broadening of the absorption curve (cf. section IV.2.2.5).

V.4. Investigation of the photochromism stability

V.4.1. First observations

Once the F-center has been formed, questions of its relative stability (from a thermodynamic point of view) and its life-time (from a kinetic point of view) arise. As a first and simple observation, we note that at room temperature and under indoor light, the minerals return to a colourless form (in other words "bleach") with different kinetics, generally faster for scapolite than sodalite and in a much longer time for tugtupite. This is a first clue toward very different electronic state energy profiles for the three minerals.

To quantify the activation energy associated to the bleaching, our collaborators set-up a

thermotenebrescence experiment similar to the thermoluminescence experiments used to probe defect states in solids (cf. III.2.3). The colour intensity of the F-center is recorded upon a gradual temperature increase (3°C/s) allowing to extract the thermal bleaching activation energies: -0.30 eV, -0.99 eV and -0.03 eV for sodalite, tugtupite and scapolite respectively confirming the first rough observation.

V.4.2. Potential energy surfaces analysis: S_2^{2-} activator

To get an insight into the reason behind the metastability of the F-center at the atomic scale, we optimized the geometries of the colourless form (*i.e.* the minimum of the potential energy surface (PES) of the $^1[S_2^{2-}, V_{Cl}]$ state corresponding to the electron on S_2^{2-}) and of the coloured form (*i.e.* the minimum of the PES of the $^3[S_2^-, V_{Cl}^-]$ state corresponding to the electron in Cl vacancy) at the DFT level using PBC. The $^3[S_2^-, V_{Cl}^-]$ state was obtained by a ΔSCF procedure.
Looking at the structural changes between the coloured and colourless, the shape and size of the β-cages are similar between the two forms, corresponding to the observation of Weller *et al.*[6] The main change occurs on the Na_4 polyhedron's shape and the dianion's bond length and orientation (cf. left part of Figure V.11) with a contraction of Na_4 around the F-center (because the trapped electron attracts the surrounding Na^+ ion) and a decrease in S-S bond length in agreement with the depopulation of the π^* antibonding orbital. A scan of the PESs associated with the $^1[S_2^{2-}, V_{Cl}]$ and $^3[S_2^-, V_{Cl}^-]$ states was computed (cf. right part of Figure V.11) as a function of the sodium tetrahedra and S_2^{2-} deformations by DFT single points PBC calculations. These scans indicate that the two PESs are mainly affected by the sodium polyhedron relaxation rather than the S-S contraction for the sodalite and tugtupite while both motions contribute to the states' inversion for the scapolite. Indeed, the sulfur anion experiences a greater re-orientation in the course of the scan in scapolite as illustrated in left part of Figure V.11.

The colour bleaching energy of these minerals can be extracted from the PES either as the vertical energy difference between the two states at the geometry of the coloured form (*i.e.* the minimum energy of the $^3[S_2^-, V_{Cl}^-]$ state), depicted by the pink arrow in Figure V.11 or as the energy difference between the minimum energy of the $^3[S_2^-, V_{Cl}^-]$ state and the energy of the conical intersection, depicted by the black arrow in Figure V.11. The vertical energy can also be computed by TD-DFT on a cluster extracted from the periodic system, as we did in the previous chapter. All values are given in the Table V.2. Whatever the computational approach chosen, the trend obtained from theory is the same as the one obtained experimentally. The F-center is the most stable in tugtupite followed by sodalite and finally scapolite.

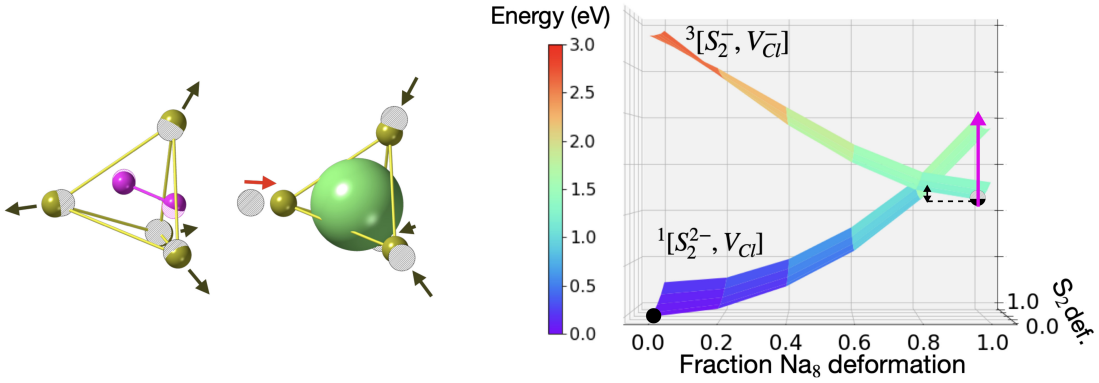

(a) Sodalite

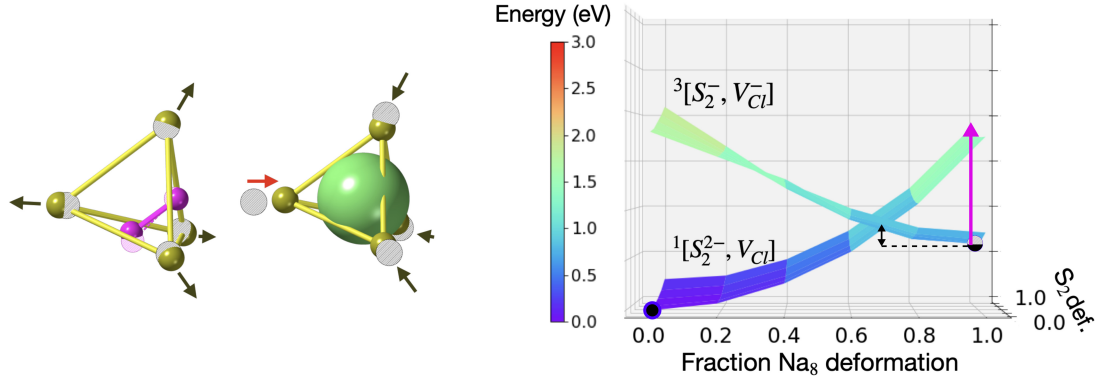

(b) Tugtupite

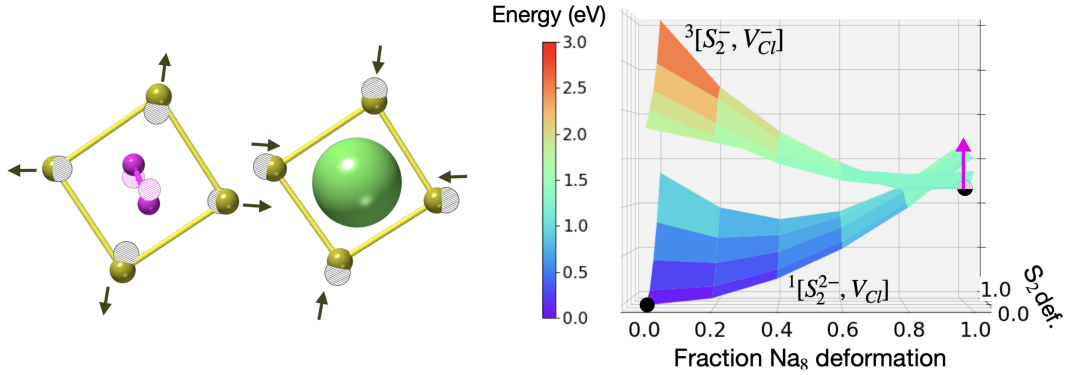

(c) Scapolite

Figure V.11: Deformation of the two Na_4 polyhedra from the geometry of the colourless form (hatched atoms) to the geometry of the coloured form. Dark arrows indicate the direction of deformation. Na are represented in yellow (or black when hatched), sulfur in pink and the trapped electron is depicted by a light green sphere. Potential energy surfaces of the two states $^1[S_2^{2-},V_{Cl}]$ and $^3[S_2^-,V_{Cl}^-]$ with respect to the energy of $^1[S_2^{2-},V_{Cl}]$ at the geometry of the colourless form (0% deformation), as a function of the geometry deformation of S_2 and 2xNa_4. Stable geometries for the $^1[S_2^{2-},V_{Cl}]$ and $^3[S_2^-,V_{Cl}^-]$ states are presented by black points.

		Sodalite	Tugtupite	Scapolite
Exp.		-0.30	-0.99	-0.03
comp. S_2^{2-}	ΔSCF (vertical)	-0.88	-1.22	-0.44
	ΔSCF (conical)	-0.12	-0.22	-0.01
	TD-DFT (vertical)	-0.38	-0.40	-0.26
comp. S^{2-}	ΔSCF (vertical)	-0.96	-0.96	-0.67
	ΔSCF (conical)	-0.23	-0.14	-0.09
	TD-DFT (vertical)	-0.19	-0.18	-0.14

Table V.2: Experimental (from thermotenebrescence analysis) and computed (by ΔSCF on a periodic model or by TD-DFT from a cluster approach) bleaching energies in eV for the three minerals and the main two investigated activators S_2^{2-} and S^{2-}.

V.4.3. Potential energy surfaces analysis: S^{2-} activator

A similar study was conducted with S^{2-} as the activator. We optimized the geometries of the colourless form (*i.e.* the minimum of the potential energy surface, PES, of the $^1[S^{2-}, V_{Cl}]$ state corresponding to the electron on S^{2-}) and of the coloured form (*i.e.* the minimum of the PES of the $^3[S^-, V_{Cl}^-]$ state corresponding to the electron in Cl vacancy) at the DFT level using PBC. This time, we only considered the Na_4 polyhedron's deformation (cf. left part of Figure V.12). A scan of the PESs associated with the $^1[S^{2-}, V_{Cl}]$ and $^3[S^-, V_{Cl}^-]$ states was computed (cf. right part of Figure V.12) as a function of the sodium tetrahedra deformations by DFT in PBC. We observe again the inversion of the two states responsible for the photochromism phenomenon. Once again, the bleaching energy (calculated as the vertical energy difference between the two states at the geometry of the coloured form) is smaller for scapolite, in agreement with the experimental observation. However, the energies obtained for tugtupite and sodalite are identical, if not higher for sodalite (ΔSCF(conical)), which does not represent the reality (cf. Table V.2). This suggests that S_2^{2-} is most probably the main actor in the photochromism of these natural minerals. This is actually logical, the activator requiring less energy to transfer its electron among all present species will be the one favoured.

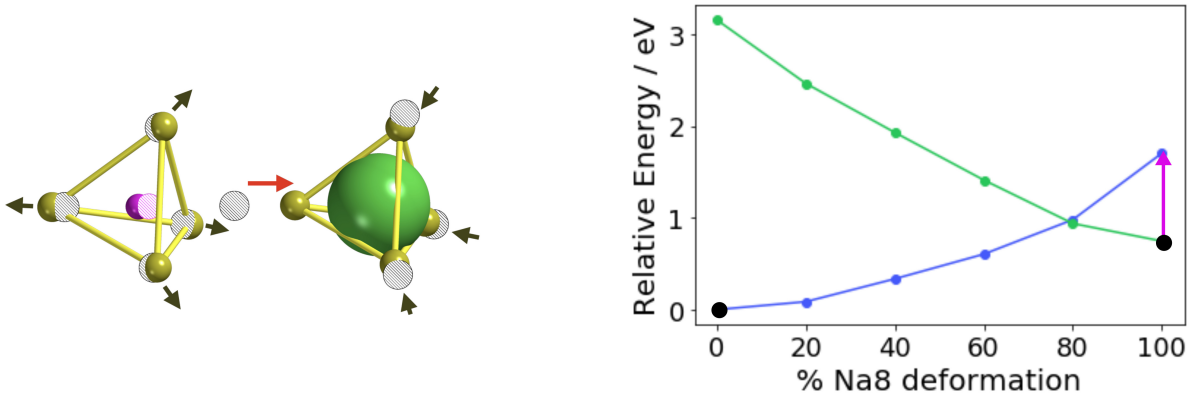

(a) Sodalite

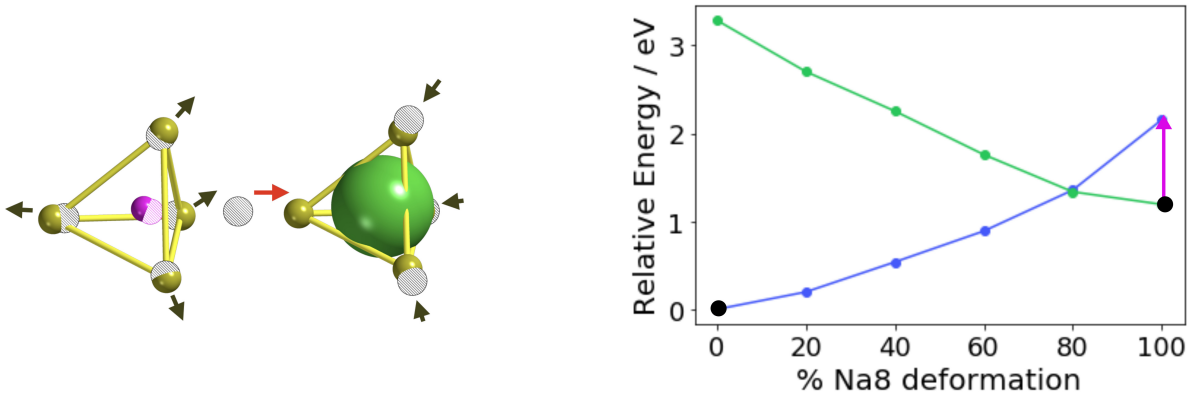

(b) Tugtupite

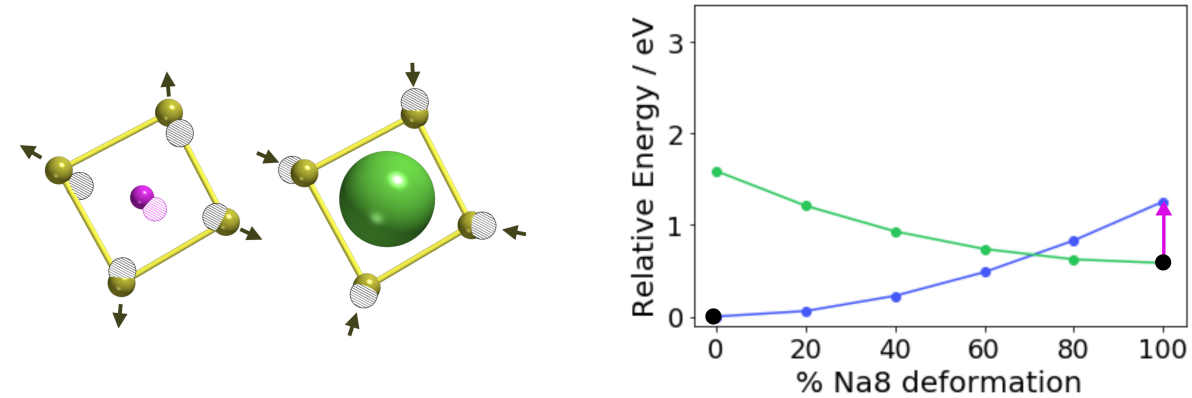

(c) Scapolite

Figure V.12: (left) Deformation of the two Na_4 polyhedra from the geometry of the colourless form (hatched atoms) to the geometry of the coloured form. Dark arrows indicate the direction of deformation. Na are represented in yellow (or black when hatched), sulfur in pink and the trapped electron is depicted by a light green sphere. (right) Potential energy surfaces the two states $^1[S^{2-},V_{Cl}]$ and $^3[S^-,V_{Cl}^-]$ with respect to the energy of $^1[S^{2-},V_{Cl}]$ at the geometry of the colourless form (0% deformation), as a function of the geometry deformation of 2xNa_4. Stable geometries for the $^1[S^{2-},V_{Cl}]$ and $^3[S^-,V_{Cl}^-]$ states are presented by black points. The pink arrow represents the transition at ΔSCF level of theory.

V.4.4. Origin of the metastability: "breathing" of the sodium polyhedron

Finally, quantum calculations actually bring the understanding of the origin of this stable and reversible photochromism. The structure of the aluminosilicate made of a β-cage surrounding a sodium polyhedron offers enough free space to allow a reversible "breathing" of the sodium polyhedron ultimately leading to an inversion of two electronic states involved in the photochromic mechanism. As a matter of illustration, sodalite and tugtupite experience a very large stabilization of the F-center (cf. Table V.2), much more than the scapolite. This is accomplished by a considerable motion of a specific sodium atom (presented by the red arrow in Figures V.11 and V.12), the one surrounding the F-center but pointing toward the activator (S_2^{2-} or S^{2-} ion). If we consider S_2^{2-} activator, this atom moves by more than 1 Å to stabilize the F-center in sodalite and tugtupite. In scapolite, this motion is only 0.6 Å because the two Na_4 squares surrounding the activator and V_{Cl} defects are far from each other. This explains the difference of stability of tugtupite and sodalite coloured form compared with scapolite's one.

	Sodalite	Tugtupite	Scapolite
S_2^{2-}	1.33	1.07	0.60
S^{2-}	1.89	1.93	0.90

Table V.3: Motion of the sodium atom surrounding the F-center but pointing toward the activator depending on both the activator and the mineral.

In the end, the greater stability of tugtupite's coloured form compared to sodalite's one could be explained through structural considerations. The smaller volume of tugtupite's β-cage would better stabilize the trapped electron. For the moment no rigorous explanation can be provided to the reader but calculations are ongoing.

V.5. Conclusion

As a first and general result the study presented in this chapter highlight again the possibility to tune the different parameters of photochromism in these minerals through composition (*e.g.* sodalite v.s. tugtupite) or structure (*e.g.* sodalite v.s. scapolite). Indeed, while belonging to the same family, sodalite, tugtupite and scapolite show different colouration and stability of their coloured form. In that sense, and adding to it the results of the previous chapter, it appears that these inorganic photochromes show an attractiveness comparable to the organic ones reported for the high adaptation of their absorption properties through synthesis.

Moreover, organic photochromic systems whose mechanisms are based on molecular reorganization, are not adapted to experience the photochromism in the densely packed solids as there is not enough free volume to allow such molecular motion. In that sense, the photochromic minerals presented in this work are particularly unique and open perspectives to develop solid-sate photochromic systems. This study indeed sheds light on the origin of the stability of the coloured form in naturally-occuring photochromes. It is the possible "breathing" of the sodium polyhedron in the β-cage that allows the inversion of states responsible for the photochromism.

References Chapter V.

[1] P. Colinet, A. Gheeraert, A. Curutchet, and T. Le Bahers *The Journal of Physical Chemistry C*, vol. 124, no. 16, pp. 8949–8957, **2020**.

[2] F. Blumentritt, C. Latouche, Y. Morizet, M.-T. Caldes, S. Jobic, and E. Fritsch *The Journal of Physical Chemistry Letters*, vol. 11, no. 12, pp. 4591–4596, **2020**.

[3] A. Sidike, A. Sawuti, X.-M. Wang, H.-J. Zhu, S. Kobayashi, I. Kusachi, and N. Yamashita *Physics and Chemistry of Minerals*, vol. 34, no. 7, p. 477–484, **2007**.

[4] S. M. Antao, I. Hassan, and J. B. Parise *American Mineralogist*, vol. 89, no. 4, pp. 492–497, **2004**.

[5] E. Sokolova and F. C. Hawthorne *The Canadian Mineralogist*, vol. 46, no. 6, pp. 1527–1554, **2008**.

[6] J. A. Armstrong and M. T. Weller *Chemical Communications*, no. 10, pp. 1094–1096, **2006**.

CHAPTER VI

Other luminescence properties of sodalite

I am among those who think that science has great beauty.

Marie Curie.

We have previously investigated the photochromic properties of sodalite mineral, but it is not the only unusual optical phenomenon that occurs when considering this material. In this chapter, the focus will move to other spectroscopic aspects of this mineral. It is indeed interesting to note that sodalite type minerals have more to show than tenebrescence in terms of spectroscopic properties.

(a) (b)

Figure VI.1: (a) Fluorescence of a tenebrescent sodalite mineral after UV irradiation (365 nm). (b) Persistent luminescence at 490 nm of a sodalite mineral after UV irradiation (275 nm).[1]

Known for a long time[2, 3], and mentioned in the previous chapters, is the fluorescence property of tenebrescent sodalites under UV excitation (365nm). This typical orange fluorescence is characteristic of the disulfur (S_2^-) emission (cf. Figure VI.1a). The first section (VI.1) will focus on modelling the emission of the S_2^- anion. Similarly to the study on the F-center's absorption, the influence of several parameters will be investigated among which the embedding or the functional. Most of the results of this section have been published in ref. [4].
In a second part (VI.2), the reader will find a study on the persistent luminescence (PeL) property. That is the natural "glow-in-the-dark" phenomenom you can observe on many self-lit emergency exit signs. It happens after UV exposition of the material and give this teal glow one can see in Figure VI.1b. Interestingly, this phenomenon has been reported to be in competition with photochromism (PC) in sodalite, and some explanation of this observation will be provided here. Most of the results of that section have also been published in ref. [1].

VI.1. Modelling the emission spectra of dichalcogenures anions in sodalite

VI.1.1. Methodology

The characteristic orange fluorescence of S_2^- in hackmanite has been reported several times and experimental data are then accessible.[2, 5, 6] The emission is due to an electronic transition from a π^* to a π orbital and corresponds to a $^2\Pi_u \rightarrow {}^2\Pi_g$ transition (cf. Figure VI.2).

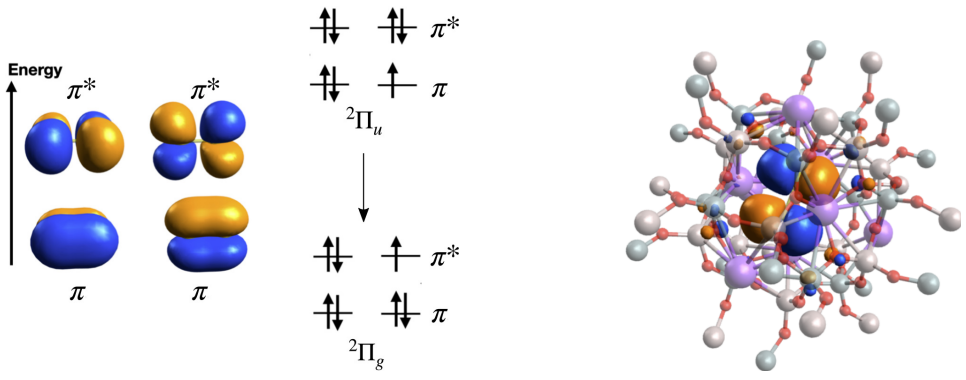

(a) (b)

Figure VI.2: (a) HOMO (π) and LUMO (π^*) isosurfaces (isovalue 0.02 au) of the S_2^- anion along with electronic occupation of the π and π^* orbitals of S_2^- for the two electronic states at stake in fluorescence. (b) representation of one π^* orbital inside the β-cage.

We applied the model developed for simulating the F-center's absorption (cf. section IV.2) on the simulation of the emission properties of this anion. An identical supercell was considered (2X2X2, 368 atoms), this for the same reasons of balance between accuracy and computational cost, with one Cl^- substituted by one S_2^-.
Similarly to the F-center's study, several systems (*i.e.* cluster + embedding) were considered for the TD-DFT calculations using the supercell geometries computed in PBC.

- $\mathbf{S_2^-}$: isolated anion,
- $\mathbf{Na_4}$: S_2^- anion in the Na_4 tetrahedron,
- **OH**: addition of the β-cage with its oxygen pending bonds saturated with hydrogen, covering the cage with OH groups,
- **Opc**: the terminating O atoms of the β-cage are surrounded by the next shell of cations described by pseudopotentials (pp) without the related basis set, and an array of point charges (pc) in order to simulate the Madelung potential of the ionic sodalite crystal.

This time, the smallest system consists in the isolated anion S_2^-. The representation of the different clusters and their embedding can be found on the left part of Figure VI.4.
The reported emission spectra of S_2^- in sodalite shows a vibrational fine structure (cf. green curve, top rectangle of Figure VI.4). Hence, to reproduce the spectroscopic properties of this colour center, we considered the inclusion of the vibronic coupling in the simulated spectra.

Compared to the F-center, the emission is due to an electronic transition from a π^* to a π orbital and corresponds to a $^2\Pi_u \rightarrow {}^2\Pi_g$ transition (cf. Figure VI.2). Hence the excited-state geometry can not be obtained by constraining the occupation of p orbitals as it was done for the F-center's absorption study (cf. section IV.2.1.3). By analysing the energy of the GS and the first EESs of S_2^- as a function of the S-S bond length, it appears that the geometry at equilibrium of $^4\Sigma_u$ state is close to the one of $^2\Pi_u$ (cf. Figure VI.3). Hence, the geometry of the $^2\Pi_u$ excited state in PBC was simulated with the one of the $^4\Sigma_u$ state, obtained through a ΔSCF procedure by imposing a quartet spin multiplicity.

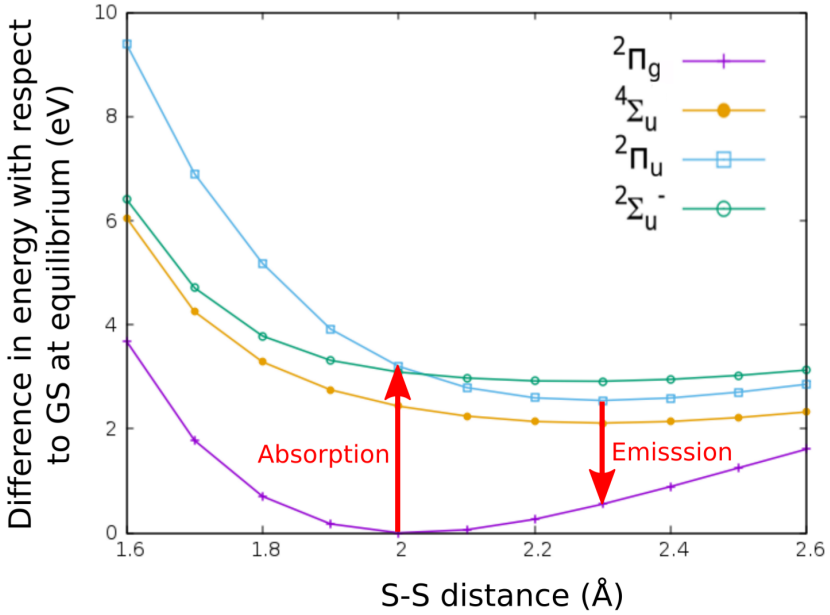

Figure VI.3: Reaction coordinate diagram of S_2^- energy levels in vacuum computed at the TD-DFT/PBE0 level. The experimentally observed fluorescence corresponds to the transition tagged "emission".

VI.1.2. Results and discussion

VI.1.2.1. Influence of the embedding

The simulated spectra obtained by convoluting the TD-DFT/PBE0 results by a gaussian are reported in Figure VI.4 (dotted red lines) along with the experimental data (green) for the different systems: S_2^- isolated, S_2^- in Na_4, and both the OH and Opc approaches. For comparison, the first rectangle also provides the simulated emission of the anion optimized in gas phase.

Once the β-cage belongs to the QM part, the effects at a longer-range (*i.e.* addition of peudopotentials and point charges) do not impact the simulated emission. In comparison with the F-center's absorption, this can be explained by the lower delocalization of the orbital at stakes onto the β-cage (cf. Figure VI.2). Hence, long-range embedding (Opc) appears necessary only for coloured centers for which the orbitals involved in the transition of interest are delocalized onto the β-cage, otherwise the OH approach should be sufficient enough. A quick analysis of the delocalization of the defect orbitals seems to be a good indicator for choosing the most relevant embedding.

The transition obtained on S_2^- is slightly more red-shifted (644 nm) than on the anion in gas phase (673 nm). The difference comes from the shorter S-S bond length at the excited state computed in the β-cage (2.317 Å) compared to the one computed in the gas phase

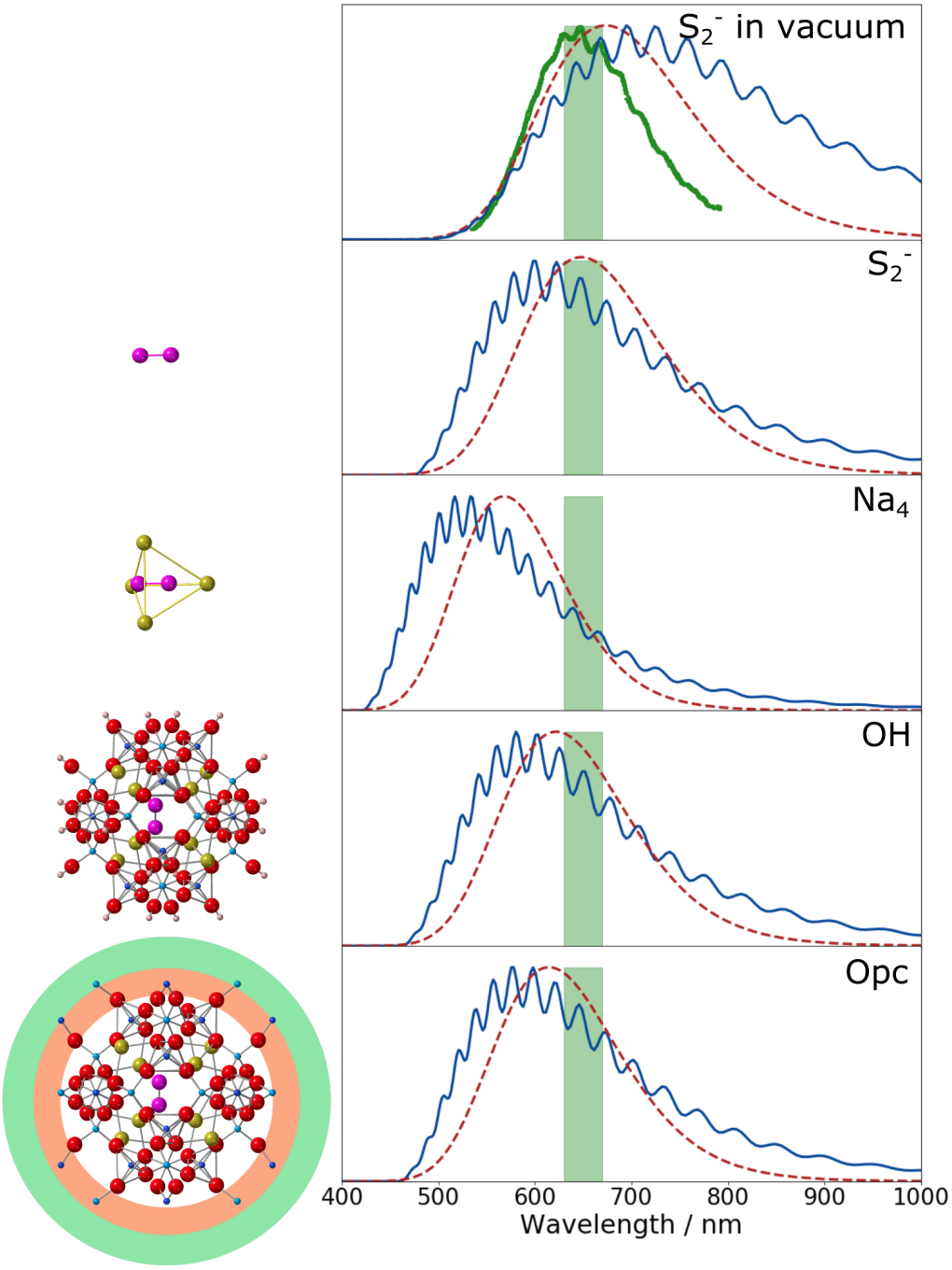

Figure VI.4: Disulfure anion's emission simulated with the use of different embedding methods. On the outer parts, the systems considered with Na, Cl, O, Si, Al, S and H atoms in yellow, green, red, blue, cyan, pink and beige respectively. Atoms treated by pseudopotentials (pp) are placed in an orange annulus. Presence of point charges (pc) is schematically represented by a green annulus. On the graphics, the experimental data are fully represented on the uppermost rectangle and otherwise shown by the green bar standing for the maximum absorption wavelength. TD-DFT/PBE0 results convoluted by a gaussian are represented by a red dotted line (no vibronic coupling). The dark blue curves are obtained by the addition of the vibronic coupling considering only the vibrations of disulfure anion.

(2.336 Å). This illustrates the effect of the confinement on the spectroscopic properties of the anion.

VI.1.2.2. Influence of the vibronic coupling

During the excited-state ($^4\Sigma_u$) relaxation, the S_2^- anion experiences a motion (rotation) inside the Na_4 tetrahedron. Due to this rotation, the transition cannot be considered to be in the Franck-Condon regime. To overcome this problem, only the vibrations of S_2^- were included for vibronic coupling, that is the vibronic coupling study on S_2^- systems only considers the normal mode of the anion at 620.3 cm^{-1} at the GS, computed in PBC.

On the simulated spectra for the different systems (S_2^-, Na_4, OH and Opc cf. Figure VI.4) one can see that it is sufficient to qualitatively reproduce the shape of the experimental emission curve, with the experimental vibrational energy reported around 600 cm^{-1}.[5] The vibronic coupling blue-shifts the transition by 0.14 eV on average with PBE0 functional.
The computational time (CPU time) required for the frequency calculation of S_2^- in sodalite structure is only 5h for the GS and a bit less than two days when considering the ES, which makes the inclusion of vibronic coupling low-priced in that case, compared to the F-center.

VI.1.2.3. Functional benchmark

The simulation of the emission spectra were conducted with PBE0 functional for the different systems. However, as for the F-center it is possible to perform a benchmark of different functionals. Although OH already provides good qualitative results, the functional benchmark was conducted on the most sophisticated embedded systems (Opc) similarly to what was done for F-center study. The same set of 16 functionals was used:

- pure GGA: BP86, PW91, PBE, B97D;
- hybrid GGA: TPSSh, B3PW91, B3LYP, PBE0, BMK, M062-X;
- range-separated hybrid (RSH): CAM-B3LYP, ωB97X-D, LC-ωHPBE, HSE06;
- pure meta GGA: MN15-L, tHCTH.

This time, the influence of the functional was not evaluated on artificial sodalites but on several dichalcogen anions: S_2^-, Se_2^- and Te_2^- for which we also have the experimental spectra and fundamental vibrational energies (Se_2^-: 335 cm^{-1}, Te_2^-: 228 cm^{-1}).[5] When considering the substitution of a chloride anion by Te_2^-, a sodium atom in the surrounding tetrahedron was removed to cope with the steric hindrance.[5] Similarly to S_2^- the

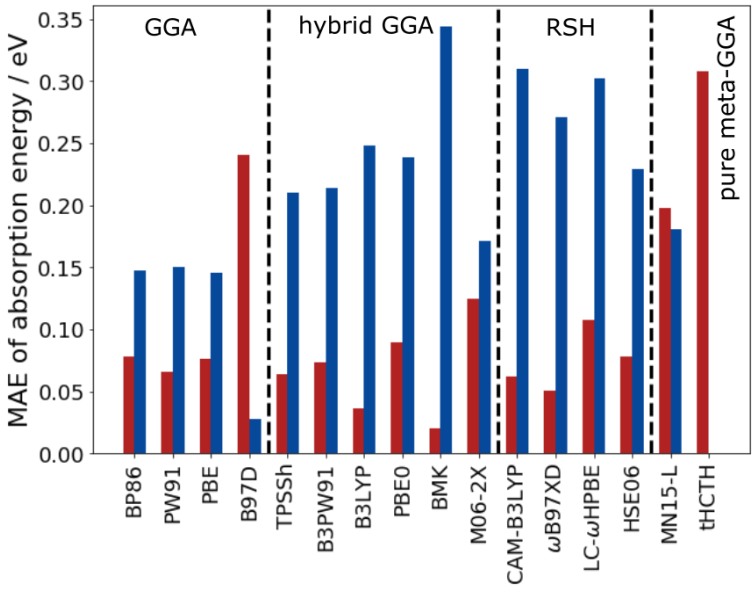

Figure VI.5: Mean averaged error of dichalcogen anion emission energy, without (red) or with (blue) considering the vibronic coupling for different functionals.

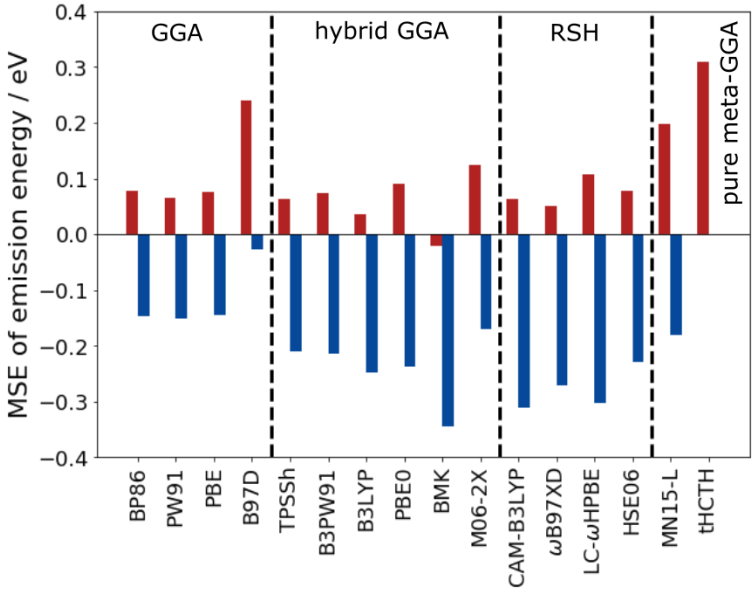

Figure VI.6: Mean signed error of dichalcogen anion emission energy, without (red) or with (blue) considering the vibronic coupling for different functionals.

computationally obtained fundamental vibrational energies are in close agreement with the experiment, being respectively 341 cm^{-1} and 228 cm^{-1} for Se_2^- and Te_2^-.
Due to their bigger mass, intersystem crossings between different spin states are assumed for the Se_2^- and Te_2^- ions leading to phosphorescence emission, while only fluorescence is observed for S_2^-. The energies of phosphorescence emission are obtained thanks to a ΔSCF procedure on the geometry of the excited state, between the first doublet and first quadruplet states. The MAEs and MSEs presented in Figures VI.5 and VI.6 correspond

to the average of the errors obtained for the three dichalcogen anions. All detailed results can be found in Tables A.10 and A.11.

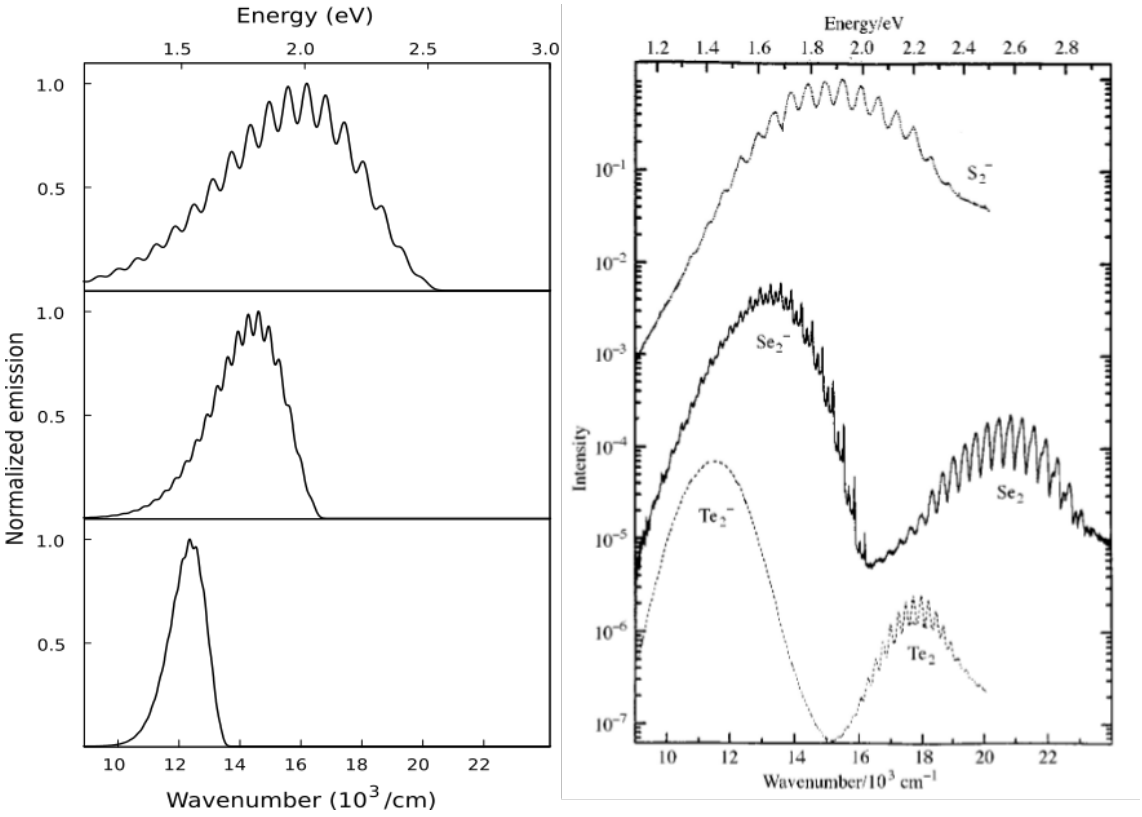

Figure VI.7: Simulated (TD-B97D + vibronic coupling) and experimental emission spectra of X_2^- ions (X=S, Se and Te) trapped in sodalite.[5] Reproduced by permission from the Royal Society of Chemistry.

Almost all functionals overestimate vertical transition energies and underestimate vibronically resolved emission energies. The influence of functionals is notably different compared to the F-centers' absorption spectra. For dichalcogens, if the vibronic coupling is not considered, the emission energy is generally correctly reproduced by all functionals except for some individual cases (i.e., B97D and meta-GGA). On average, the inclusion of vibronic coupling red-shifts the transitions by a large amount, leading to a weaker agreement with the experiment. The worst functionals without vibronic coupling become the best when the phenomena are included in the simulation, by error compensation. For example, the MAE obtained with B97D when considering the vibronic coupling is 0.03 eV, against 0.25 eV without vibronic coupling. While detrimental quantitatively, the inclusion of vibronic coupling gives a shape of the emission band very close to that found experimentally. In that extent we simulated the emission spectra of the three dichalcogen ions in sodalite structure with B97D functional and taking into account the vibronic coupling. The results of these simulations are in good agreement with experiment as shown in Figure VI.7.

VI.2. Persistent luminescence in sodalite minerals

Persistent luminescence is the continuous released of absorbed energy as visible light for an appreciable time after the excitation source has been removed. It usually lasts minutes to hours. This phenomenon is actually known for over a thousand years, even if comprehension of the mechanisms at stake is more recent.[7, 8]

The possible applications for materials showing persistent luminescence are luminous paints, self-lit clock alarms and exit signs[8] but there were also reports of applications in bio-imaging.[9] Nowadays, synthetized materials can reach up to 100h of glowing, but are mainly composed of heavy metals or expensive rare earths (lanthanides).[10] The PeL phenomenon has actually been observed on some natural sodalite and described as prolonged afterglow of teal light, after excitation in the UV range (cf. Figure VI.1b).[11] If in natural materials it lasts only a few minutes,[1] in synthetic ones, it can lasts several hours and up to 100h when prepared in some conditions.[10] In that extent, sodalite type materials are particularly interesting for both their cost and environmental-friendly composition.

VI.2.1. Experimental resolution of the mechanism

The mechanism of persistent luminescence in sodalite has been solved by Mika Lastusaari and co-workers.[11]. Through an elegant procedure, they showed that the phenomenon is due to ppm level of titanium impurity and the presence of oxygen vacancies. More precisely, the luminescence center has been identified as being the titanium cation Ti^{3+} (preferentially occupying Al^{3+} sites). It is involved in both the absorption and the emission processes.

The mechanism is summarised in Figure VI.8 (b). Under UV irradiation (required energy reported around 3.9 eV [1]), the valence electron from the titanium impurity will get excited and send to the conduction band (CB) of the material before getting trapped in an oxygen vacancy (V_O):

$$Ti^{3+} + V_O \xrightarrow{h\nu} [Ti^{4+} + V_O{}^{-}]^* \rightarrow Ti^{4+} + V_O{}^{-} \tag{VI.1}$$

The trapped charge carriers can then be slowly released into the conduction band thanks to available thermal energy (k_BT). Finally, de-excitation process associated to the back return of the electron to the titanium impurity produces the glowing phenomenon:

$$[Ti^{4+} + V_O{}^{-}]^* \xrightarrow{h\nu'} Ti^{3+} + V_O \tag{VI.2}$$

In the end, the phenomenon is a thermally stimulated luminescence.[12]

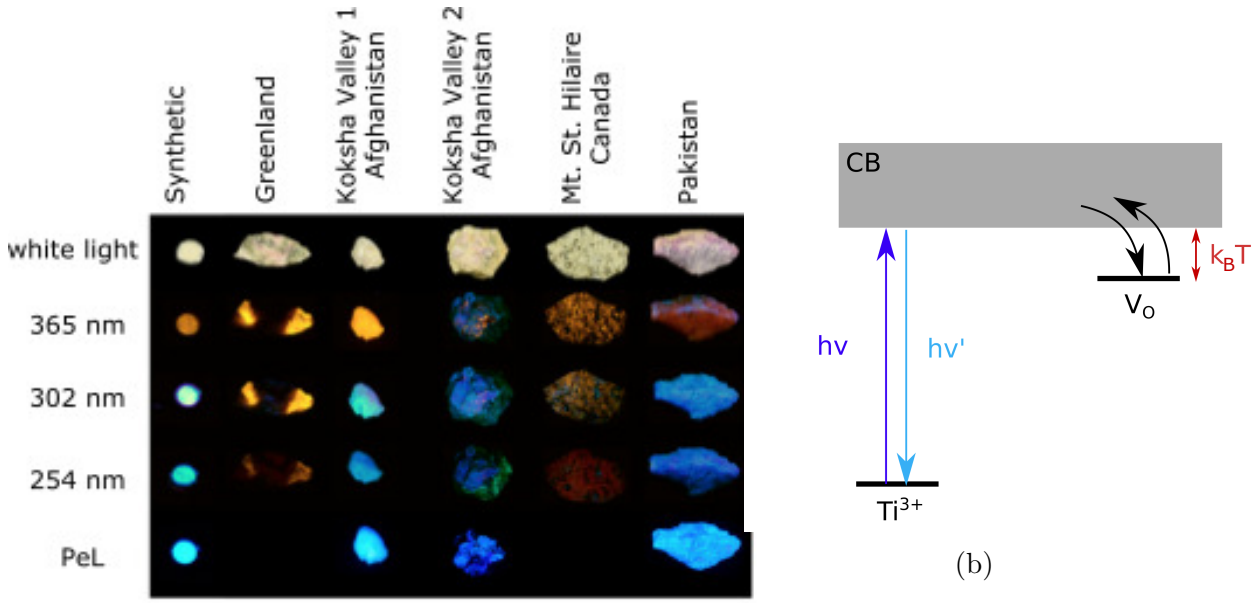

(a) (b)

Figure VI.8: (a) Photos of the samples used in this study: under white light, 365, 302, and 254 nm and their persistent luminescence. (b) Mechanism of persistent luminescence in sodalite mineral. Under UV irradiation an electron is send from the Ti impurity to the CB (blue arrow). The electron is then trapped into an oxygen vacancy and further released to the CB thanks to available thermal energy (k_BT). Finally, the visible glow corresponds to the de-excitation process due to the back-return of the electron from the CB to titanium impurity.

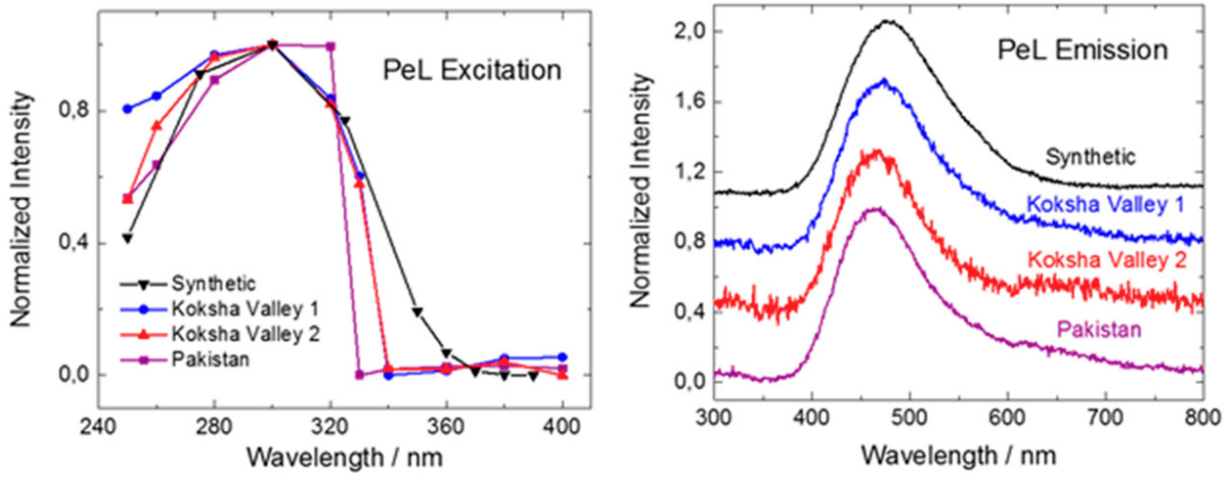

(a) (b)

Figure VI.9: (a) PeL excitation spectra and (b) PeL emission spectra of the material showing persistent luminescence in Figure VI.8a.

Interestingly, not all natural sodalite minerals, even those containing Ti show PeL (cf.

Figure VI.8). A statistical analysis (principal componant analysis followed by a variance analysis) reveals correlation between the joint concentration of pairs of ions and the intensity of PeL. To be more explicit, it has been observed in a set of natural samples that the higher are the ratio [K]/[S] and [Ti]/[Fe], the stronger will be the phenomenon. With [A], the concentration of A in the material. The composition of the natural samples used in this study can be found in Appendix G.1.[1]

In order to provide complementary explanations, we conducted simulations involving the different defects: Ti, Fe, S and K. Mössbauer measurements on natural sodalites indicate that Fe^{3+} is the most dominant oxidation state of iron, but the presence of Fe^{2+} can not be ruled out completely so that we will consider both oxidation states.[1] Ti being involved in both absorption and emission, their can be competition at different steps of the mechanism. Experimental excitation and emission spectra of the minerals showing PeL are provided in Figure VI.9.

VI.2.2. Methodology for quantum calculations

In terms of simulation, the methodology was very similar to the one exposed so far.

K and S impurities:

Concerning sulfur and potassium, it is actually identical to what was presented in section IV.3. That is we optimized at the PBC level, the geometry of a 2X2X2 supercell containing the sulfur impurity, S_2^{2-}, and the vacancy, V_{Cl} both substituting a chloride anion. Moreover, Na^+ cations were replaced by K^+ leading to $Na_{4-x}K_x(SiAlO_4)_6(Cl,S)_2$ compositions, with the potassium atoms substituting the sodium surrounding the vacancy for stability reason. Then, a cluster containing two β-cages with the defects was extracted and embedded by pseudopotentials and point charges (Opc) to perform TD-DFT/CAM-B3LYP calculations. The embedded cluster is shown on the right part of Figure VI.15.

Ti and Fe impurities:

Concerning, titanium and iron impurities, they were placed in tetrahedral site, substituting an aluminium or a silicon atom. Whenever, the overall neutrality of the material was altered, Fe^{2+} substituting Al^{3+}, it was offset by the substitution of one Al^{3+} by one Si^{4+} ($Si^{\bullet}_{Al}$) and 2X2X2 supercell were optimized at the PBC level.
For the Fe^{3+} and Fe^{2+} ions, several spin states were considered. ΔSCF calculations revealed that the highest spin state was always the most stable one. Kröger-Vink notation along with the GS spin multiplicity for the systems containing an impurity are given here:

- $Ti^{3+} \leftrightarrow Ti^{\times}_{Al}$ with $2S+1=2$,
- $Ti^{4+} \leftrightarrow Ti^{\times}_{Si}$ with $2S+1=1$,
- $Fe^{3+} \leftrightarrow Fe^{\times}_{Al}$ with $2S+1=6$,
- $Fe^{2+} \leftrightarrow Fe'_{Al},Si^{\bullet}_{Al}$ with $2S+1=5$.

Electronic configurations of *d* orbitals at GS are represented in Figure VI.10 for the four metal ion in tetrahedral environment.

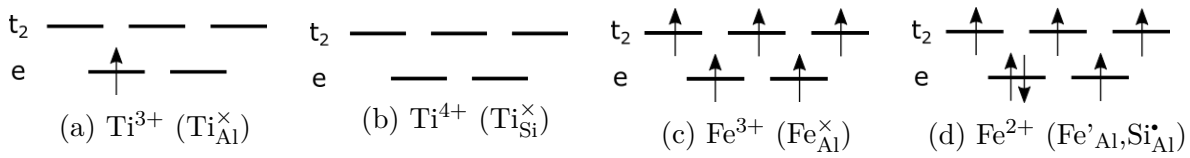

(a) Ti^{3+} ($Ti^{\times}_{Al}$) (b) Ti^{4+} ($Ti^{\times}_{Si}$) (c) Fe^{3+} ($Fe^{\times}_{Al}$) (d) Fe^{2+} ($Fe'_{Al},Si^{\bullet}_{Al}$)

Figure VI.10: *d* orbitals occupation at the highest spin state for the four metal ion in tetrahedral environment.

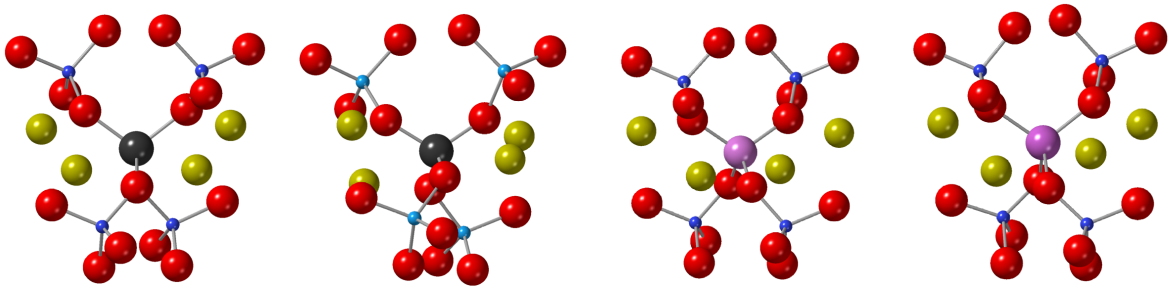

(a) Ti^{3+} ($Ti^{\times}_{Al}$) (b) Ti^{4+} ($Ti^{\times}_{Si}$) (c) Fe^{3+} ($Fe^{\times}_{Al}$) (d) Fe^{2+} ($Fe'_{Al},Si^{\bullet}_{Al}$)

Figure VI.11: Clusters centered around the different defects: Ti^{3+}, Ti^{4+}, Fe^{3+} and Fe^{2+}. The Kroger Vink notation is given in parenthesis to indicate the substituted site. Titanium, iron, oxygen, silicon, aluminum and sodium atoms are depicted respectively by black, pink, red, dark blue, cyan and yellow spheres.

We investigated two types of transitions: localized *d-d* ones and charge transfer ones (from the impurity to the CB or from the VB to the impurity). Based on previous works (*e.g.* dichalcogen anions), we know that cluster's size and embedding will have *a priori* a limited effect on the computed energy transitions for localized *d-d* transitions. However the charge-transfer transitions are much more affected by the choice of the cluster and of the embedding. In the end, clusters made of 25 atoms including at least the two first spheres of coordination, were surrounded by a shell of pseudopotentials and a cloud of point charges reproducing the Madelung potential. The clusters are represented in Figure VI.11. The reader can find complementary information concerning the size of the cluster

and its impact on the transition energies calculated in Appendix G.2.

TD-DFT/CAM-B3LYP calculations using 6-31G(d) basis set were conducted on the different clusters. To evaluate the energy diagram of Fe^{2+} and Fe^{3+} ions, ΔSCF approaches were actually used to estimate the difference in energy between the lowest energy level of each spin multiplicity. The other energy differences were obtained at the TD-DFT level of theory.

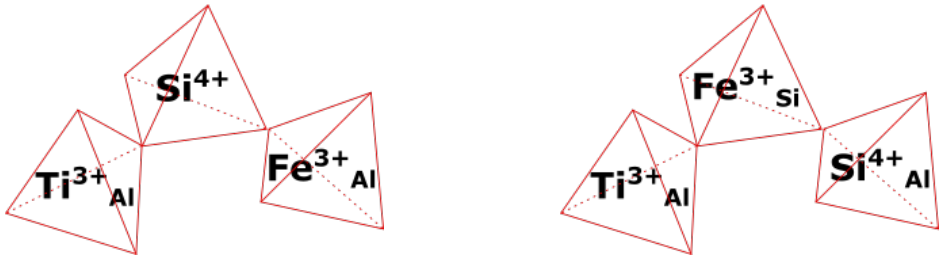

(a) (Fe^{3+},Ti^{3+}) $(Fe^{\times}_{Al},Ti^{\times}_{Al})$ (b) (Fe^{3+},Ti^{3+}) $(Fe^{\times}_{Al},Ti'_{Si},Si^{\bullet}_{Al})$

Figure VI.12: Two relative positions of the defects investigated for intervalence transitions in 2X2X2 supercell of PBC calculations.

We also considered CT transitions between iron and titanium impurities. In that case, energies for intervalence transitions between two impurities were obtained at the ΔSCF/CAM-B3LYP level in PBC. The relative positions of the two defects in the systems considered are represented in Figure VI.12. They were either in neighboured tetrahedra or separated by one tetrahedron. When in neighboured tetrahedra, the overall neutrality of the material was altered, Fe^{3+} substituting Si^{4+}, it was offset by the substitution of one Al^{3+} by one Si^{4+} ($Si^{\bullet}_{Al}$).

VI.2.3. Results of the simulations

VI.2.3.1. Validation of the mechanism

First of all, energy levels from quantum calculations for Ti^{3+} ($Ti^{\times}_{Al}$) and Ti^{4+} ($Ti^{\times}_{Si}$) in sodalite are represented in Figure VI.13a. The calculated data indicate that an electron can be excited from Ti^{3+} to the CB with an energy of 3.7 eV (335 nm), which agrees very well with the PeL excitation threshold energy (≈ 3.9 eV/320 nm, cf. Figure VI.9a). Moreover, this complies with the common understanding that PeL is initiated with electron transfer from the absorbing ion to the conduction band.
The results also confirm that Ti^{4+} is not the absorbing ion since its only transition (the CT transition $O^{2-} \rightarrow Ti^{4+}$) requires more than 5 eV.[11]

Furthermore, the teal emission observed does not correspond to *d*-*d* transition of Ti^{3+} that is computed in the near IR around 1.2 eV, but more probably to the back charge transfer from the conduction band to Ti^{3+}. Hence, our calculations are in agreement with the hypothesis that Ti^{3+} is involved both in the absorption and emission parts of PeL.

VI.2.3.2. Interplay between iron and titanium ions

The experimental observations report a decrease of PeL whenever the amount of iron impurity increases in the material's composition. The results of our calculations are presented in Figure VI.13a. There would be competition with PeL if the *d*-*d* transitions associated to Fe^{3+} and Fe^{2+} are in the same range of energy as the absorption and emission processes of PeL: [3.7;5.2] eV (240-340 nm) and [2.4;2.9] eV (425-525 nm) respectively (cf. Figure VI.9).

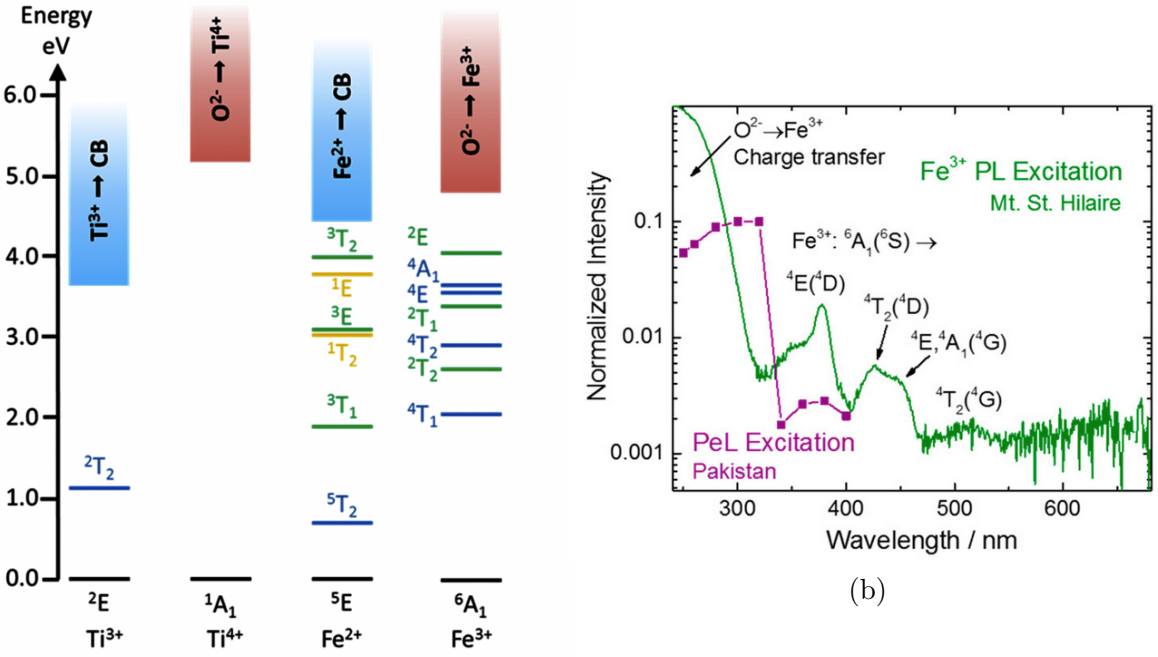

(a) (b)

Figure VI.13: (a) Quantum chemically calculated energy states of Fe^{3+}, Fe^{2+}, and Ti^{3+} in the Al^{3+} site as well as Ti^{4+} in the Si^{4+} site. Symmetry labels are attributed based on Tanabe-Sugano diagrams (d^5 for Fe^{3+} and d^6 for Fe^{2+}) (b) Photoluminescence excitation spectrum of the Mt. St. Hilaire sample showing PeL (green curve) and the Pakistan sample that does not show PeL (purple curve). This shows the competition for energy between PeL excitation and $O^{2-} \rightarrow Fe^{3+}$ charge transfer transition.

Concerning Fe^{3+}, the transitions to higher states involved change in spin multiplicity and

would then be weak, so that the $O^{2-} \rightarrow Fe^{3+}$ charge transfer transition is the most probable cause of competition. In fact, this charge transfer has been experimentally observed and is reported to be intense.[1] This is shown in Figure VI.13b, with the photoluminescence excitation spectra of a material showing PeL (purple curve) compared to the one of a material that does not show PeL and that contains iron (green curve). In the second case, there is a wide band attributed to $O^{2-} \rightarrow Fe^{3+}$ charge transfer transition. This shows the competition for energy between PeL excitation and $O^{2-} \rightarrow Fe^{3+}$ charge transfer transition.

If we look at the transitions involving Fe^{2+} ion in Figure VI.13, there is only one spin allowed transition ($^5E \rightarrow {}^5T_2$) which is in the IR region, but the $Fe^{2+} \rightarrow$ CB charge transition could compete for the excitation photons with PeL.

Finally to get a more complete picture of the effect of the energy states of iron species, we also considered the possibility of intervalence transitions between the two defects: from Ti^{3+} to Fe^{3+} or from Fe^{2+} to Ti^{4+} ((Fe^{3+},Ti^{3+}) $\leftrightarrow$ (Fe^{2+},Ti^{4+})) (cf. Figure VI.12). Intervalence transitions associated with these defects are expected around 2.2-3.0 eV by DFT calculations, thus far from the PeL excitation wavelength. However, there could be a quenching effect of the PeL emission.

In conclusion, the main competition paths induced by iron ions for the $Ti^{3+} \rightarrow$ CB transition (responsible of the PeL) are the $O^{2-} \rightarrow Fe^{3+}$ and in a lesser extent the $Fe^{2+} \rightarrow$ CB charge transfer transitions. The possibility for Fe^{3+} to capture the trapped electron (yielding Fe^{2+}) cannot be discarded.

VI.2.3.3. Competition between PeL and PC

The other goal of this computational study was to explain the role of potassium and sulfur on the intensity of the observed PeL. The higher the ratio [K]/[S], the higher the PeL. The quenching effect of S_2^{2-} can be explained by the fact that it is the element that absorbs radiation during the tenebrescence process. Indeed, the activation energy of PC is around 4.1 eV, and thus overlaps with the energy required for the absorption of PeL mechanism. This is at the origin of the competition between PC and PeL in natural sodalite as illustrated by pictures of two natural materials showing either a strong PC and a weak PeL (cf. Figure VI.14a) or a weak PC and a strong PeL (cf. Figure VI.14b).

To understand the role of potassium, one has to recall the study presented in section IV.3.2.5 on the influence of the substitution of Na^+ by K^+ on the activation energy of photochromism. As a general results, we showed that an increase in potassium concentration led to a decrease in the activation energy. This is presented in Figure VI.15 which

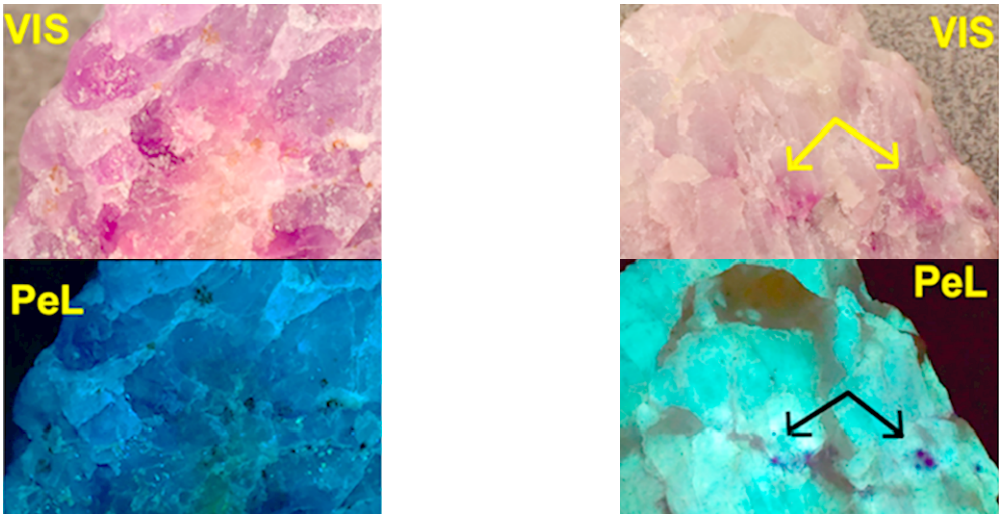

(a) (b)

Figure VI.14: Photos of materials showing either (a) strong PC and weak PeL or (b) weak PC and strong PeL.The black arrows, on (b) indicate spots were the PeL is weak and similar yellow arrows indicate a strong PC.

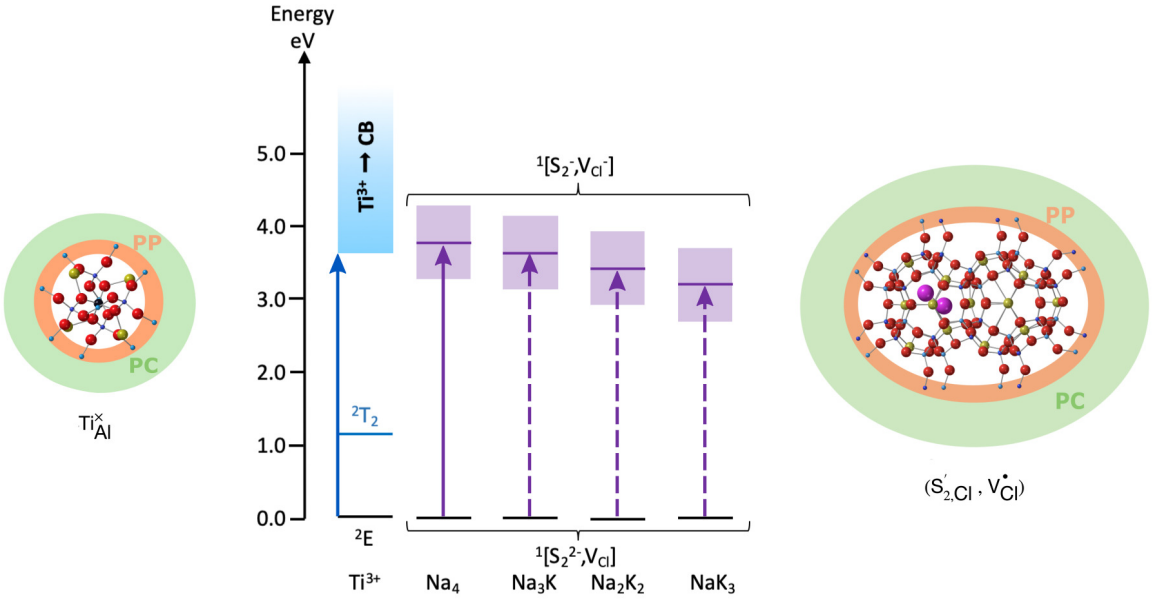

Figure VI.15: Competition for the excitation photons between PeL and PC. Quantum chemically calculated energy states of Ti^{3+} (in the Al^{3+} site) as well as $[S_2^{2-},V_{Cl}]$ pair in different $Na_{4-x}K_x$ stoichiometries in sodalite (horizontal dark purple line is the computed energy, the purple box depicts an 1 eV FWHM around the transition). On the outer parts, the systems considered with Na, Cl, O, Si, Al, S and Ti atoms in yellow, green, red, blue, cyan, pink and black respectively. Atoms treated by pseudopotentials (pp) are placed in an orange annulus and the presence of point charges (pc) is represented by a green annulus.

shows the calculated energy states of Ti^{3+} ($Ti^{\times}_{Al}$) as well as those involved in the creation of the colour center ($S'_{2,Cl}$,$V^{\bullet}_{Cl}$) when different numbers of sodium atoms have been replaced with potassium. It is clear that if there are no potassium atoms present, then there is a high overlap between the absorption band of Ti^{3+} and the band associated with the F-center creation. Thus, the photochromic process will decrease PeL efficiently and one can safely assume that the more sulfur there is the less PeL will be present. However, when potassium is incorporated in the structure, the overlap decreases with increasing potassium concentration. Therefore, the competition between PC and PeL will become weaker.

VI.3. Conclusion

In this chapter the models developed and exposed in chapter IV were involved in the explanation of other luminescent properties of sodalite minerals: S_2^- characteristic orange emission and the persistent luminescence.

In the first part, the computational model has been refined and extended. Knowledge on the nature of the orbitals involved in the transition of interest will help in choosing the most relevant embedding. Again, inclusion of the vibronic coupling helps to reproduce the shape of the spectra, but we showed that it shifts the transitions, generally reducing the agreement with experiment.
Finally, the choice of the functional is crucial to retrieve a good qualitative agreement, and the conclusion is that the nature of the point defect has a large effect on the most appropriate functional to describe its spectroscopic properties. However, GGA and global hybrids with a low HF fraction seems to be a reasonable choice to describe these systems if no experimental data are available.

In the second part, the simulation of the spectroscopic properties of different type of defects in sodalite following a cluster approach provide good qualitative results, supplementing the experimental investigations. To be more specific, localized transitions as well as CT transitions could be conducted at the same level of theory (TD-DFT/CAM-B3LYP) which provided explanations on the competition between PC and PeL and on the potential quenching of iron cations in the different processes. The possibility to have materials showing both PeL and PC has been demonstrated, which could prove useful to develop multifunctional optical markers.

References Chapter VI.

[1] C. Agamah, S. Vuori, P. Colinet, I. Norrbo, J. M. de Carvalho, L. K. Okada Nakamura, J. Lindblom, L. van Goethem, A. Emmermann, T. Saarinen, T. Laihinen, E. Laakkonen, J. Lindén, J. Konu, H. Vrielinck, D. Van der Heggen, P. F. Smet, T. Le Bahers, and M. Lastusaari *Chemistry of Materials*, vol. 32, no. 20, pp. 8895–8905, **2020**.

[2] R. D. Kirk *American Mineralogist: Journal of Earth and Planetary Materials*, vol. 40, no. 1-2, pp. 22–31, **1955**.

[3] M. Gaft, R. Reisfeld, and G. Panczer, *Modern luminescence spectroscopy of minerals and materials*. Springer, **2015**.

[4] P. Colinet, A. Gheeraert, A. Curutchet, and T. Le Bahers *The Journal of Physical Chemistry C*, vol. 124, no. 16, pp. 8949–8957, **2020**.

[5] D. Reinen and G.-G. Lindner *Chemical Society Reviews*, vol. 28, no. 2, p. 75–84, **1999**.

[6] A. Sidike, I. Kusachi, S. Kobayashi, K. Atobe, and N. Yamashita *Physics and Chemistry of Minerals*, vol. 35, no. 3, pp. 137–145, **2008**.

[7] K. Van Den Eeckhout, P. F. Smet, and D. Poelman *Materials*, vol. 3, no. 4, p. 2536–2566, **2010**.

[8] J. Xu and S. Tanabe *Journal of Luminescence*, vol. 205, p. 581–620, **2019**.

[9] T. Maldiney, A. Bessière, J. Seguin, E. Teston, S. K. Sharma, B. Viana, A. J. Bos, P. Dorenbos, M. Bessodes, D. Gourier, D. Scherman, and C. Richard *Nature Materials*, vol. 13, no. 4, pp. 418–426, **2014**.

[10] I. Norrbo, J. M. Carvalho, P. Laukkanen, J. Mäkelä, F. Mamedov, M. Peurla, H. Helminen, S. Pihlasalo, H. Härmä, J. Sinkkonen, and M. Lastusaari *Advanced Functional Materials*, vol. 27, no. 17, p. 1606547, **2017**.

[11] I. Norrbo, P. Gluchowski, I. Hyppanen, T. Laihinen, P. Laukkanen, J. Makela, F. Mamedov, H. S. Santos, J. Sinkkonen, M. Tuomisto, A. Viinikanoja, and M. Lastusaari *ACS Applied Materials & Interfaces*, vol. 8, no. 18, pp. 11592–11602, **2016**.

[12] I. Norrbo, P. Gluchowski, P. Paturi, J. Sinkkonen, and M. Lastusaari *Inorganic Chemistry*, vol. 54, no. 16, pp. 7717–7724, **2015**.

CHAPTER VII

Conclusion and perspectives

Tantas cosas he aprendido de ustedes, los hombres. He aprendido que todo el mundo quiere vivir en la cima de la montaña, sin saber que la verdadera felicidad está en la forma de subir la escarpada.

Gabriel García Márquez.

The work presented in this thesis aimed at providing a quantum chemistry computational protocol in order to understand the photochromism of naturally tenebrescent minerals. In that extent, the methodology developed on sodalite and used throughout the research project, allowed a thorough investigation of the different aspects of tenebrescence: activation, colouration (F-center's absorption) and bleaching.

This protocol, which has been detailed in Chapter IV, consists first in PBC optimization of the geometry of pristine material. It is followed by the introduction of one or two defects in the structure's supercell, made of ≈ 350 atoms, which is optimized in PBC. Unless vibronic coupling is considered, it would be the last step of PBC calculations. Otherwise, PBC frequency calculations on the atoms of interest in the supercell are performed.
Next comes a molecular approach which consists in extracting a cluster centered on the impurities. The extracted cluster is embedded in a shell of pseudopotentials and further surrounded by an array of point charges. The point charges aim at simulating the Madelung potential of the ionic sodalite crystal. On the embedding aspect of the

methodology, it eventually appears sufficient enough to saturate the dangling bond of the extracted cluster with hydrogen in the case in which the orbitals at stake in the studied transitions are not delocalized onto the β-cage. That was demonstrated for the simulation of S_2^- emission.
To access the transition energies, TD-DFT is then performed whatever the type of transition considered: localized or charge transfer transitions. In the case of CT transitions a functional benchmarking on different long-range corrected hybrid functionals selected CAM-B3LYP as the best to model both activation and bleaching processes in sodalite materials. When simulating the absorption of the F-center for different sodalites, B3LYP functional was the one with the smallest error compared to experiment. However, it is interesting to note that the nature of the point defect has a huge effect on the most appropriate functional to describe its spectroscopic properties. This was shown when considering different types of defects when simulating other luminescence properties of sodalite minerals (cf. Chapter VI). If a general conclusion must be drawn, GGA and global hybrids with a low HF fraction seem to be a reasonable choice to describe these systems if no experimental data are available.
If the protocol has proven its reliability, it lacks some computational reference values. It would be interesting to perform reliable post-HF (*e.g.* excited state coupled cluster methods) on bigger systems than Na_8 to provide a quantitative validation of the results.

The protocol was applied onto artificial sodalites (cf. Chapter IV), and other naturally-occuring tenebrescent minerals: scapolite and tugtupite (cf. Chapter V). This demonstrates the photochromic parameters variability, which is of particular interest for the development of new photochromic materials. In the last few years, the facility to tune the composition of these minerals has actually been reported experimentally and computationally. However these works were done mainly to investigate the effect of composition on the final colour of the F-center. We understand from the the work presented here that all the characteristics associated with the photochromism of the aluminosilicate minerals can be controlled:

- The activation energy by selecting the oxidation state of the sulfur activator, by using another alkaline ion instead of Na^+, or by playing on the composition of the β-cage ;
- The F-center colour by selecting the appropriate Na_4 polyhedron (sodalite, tugtupite vs scapolite), by using another alkaline ion instead of Na^+, or by selecting the composition of the β-cage;
- The bleaching energy and the kinetic of the phenomenon by modifying the flexibility of the Na_4 polyhedra first by selecting the structure (sodalite, tugtupite vs scapolite)

then by tuning the β-cage volume upon chemical modifications.

In the study on natural minerals we also investigated the origin of photochromism in these minerals. Indeed, the aluminosilicate minerals investigated here present unusually stable and reversible photochromism for inorganic materials. We proved that this phenomenon is due to an easy geometrical relaxation when going from the electronic state of the colourless form to the electronic state of the coloured form. This is not possible without the combination of the stable aluminosilicate β-cage and the space for movement within its voids.

The new information obtained in the present work shines light on the origin of the photochromism in these minerals and on all the possibilities to tune the characteristic properties of this effect. There is thus no doubt that a new family of inorganic photochromic materials with controllable properties is within reach.

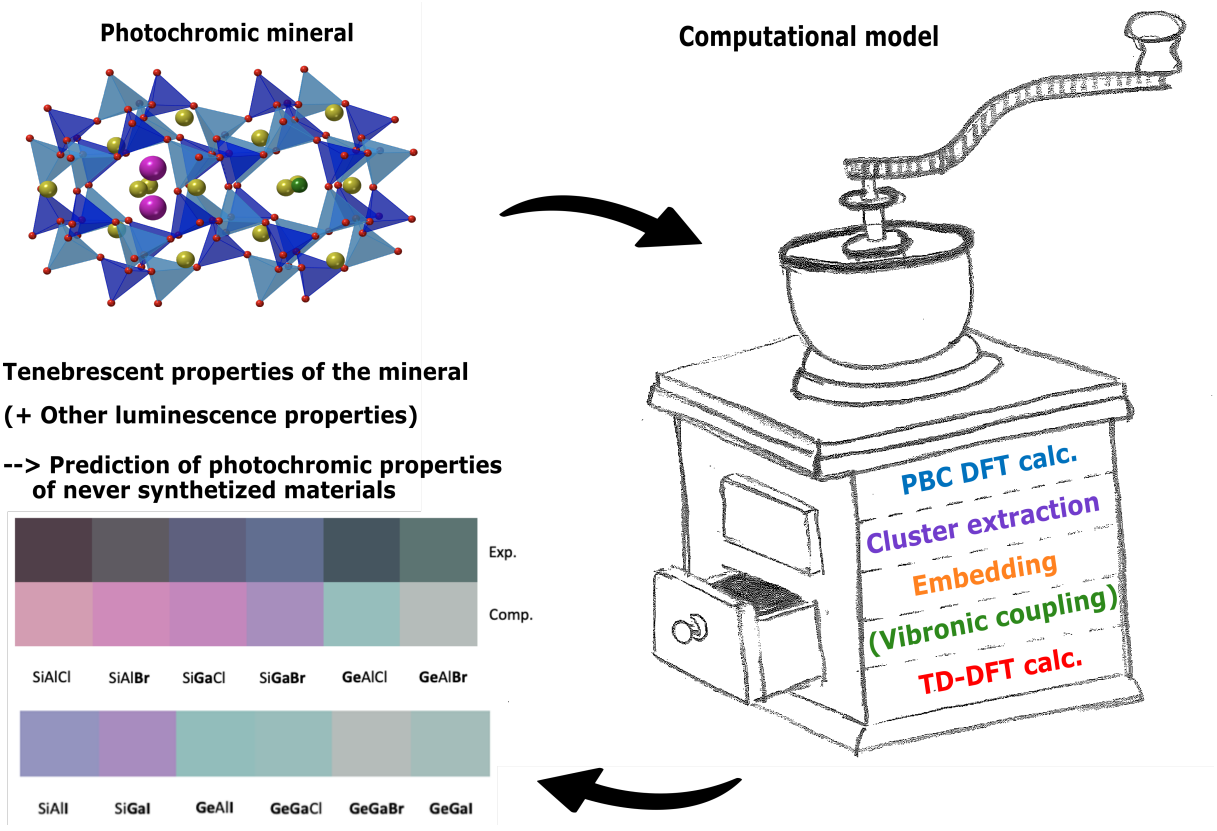

Figure VII.1: Schematic representation of the computational model used for the *in silico* study of tenebrescent materials.

This thesis, "Tenebrescent minerals by *in silico* modelling", is actually part of the ANR Tenemod project that goes beyond tenebrescence, with interest in modelling the polychromism of different materials. Polychromic materials present different colours depending on the conditions of observation. This phenomenon differs from photochromism in the sense that the change of colour is not related to a modification of the material's property under light irradiation but to its intrinsic anisotropy combine with light's properties. Indeed, according to the nature of the electromagnetic irradiation (*e.g.* spectral density, polarization), the interaction will obviously not be the same.

Examples of natural polychromic minerals are alexandrite ($BeAl_2O_4$,Cr^{3+}) and cordierite ($Al_3Mg_2AlSi_5O_{18}$;Fe^{3+},Fe^{2+}). Due to the similarities between these two oxides and the tenebrescent minerals studied, we believe that the methodology developed so far can be applied to simulate the spectroscopic properties of alexandrite and cordierite. Hence we optimized the geometry of the minerals in PBC and eventually performed TD-DFT calculations on extracted cluster embedded in an Opc form to access the transition energies. The main idea of this last work is of course to test again our computational protocol, demonstrating its reliability on other spectroscopic properties, but also to bring some knew knowledge by investigating at the atomic scale the different processes at stake in the aforementioned materials. If the phenomenon is known, the explanation of these nice properties is still discussed, especially in the case of cordierite. In the following paragraphs we will briefly introduce some of the preliminary results.

Nature of light can change the perception we will have of a material, a white page under natural light will appear white, but yellowish if we switch for an artificial light. In a more impressive manner, this is what happens for alexandrite. Under sunlight, the mineral is green, but if you change the light source and irradiate the material with incandescent light, it turns redish-pink. Picture of alexandrite under the different light sources can be found on Figure VII.2. First of all, the absorption in the visible range is attributed to *d-d* transitions of a chromium impurity (Cr^{3+}) substituting Al^{3+}. We computationally tested the chromium hypothesis, that is we optimized a supercell containing the defect before performing TD-DFT/M06-2X calculations on a cluster centered around Cr^{3+} impurity (55 atoms). The transmission spectrum obtained is qualitatively in agreement (positions of the peak) with the experimental one, [1] but there is room for improvement concerning the intensity of the peaks. However, this confirms the nature of the colour center. There are two peaks, one corresponding to an absorption in the blue ($\approx$ 440 nm), the other one to an absorption in the yellow region ($\approx$ 600 nm). The difference of colour is then explained by the difference of spectral density for the two light sources (cf. pink and green curves on Figure VII.2). In the case of incandescent light, the spectral density increasing

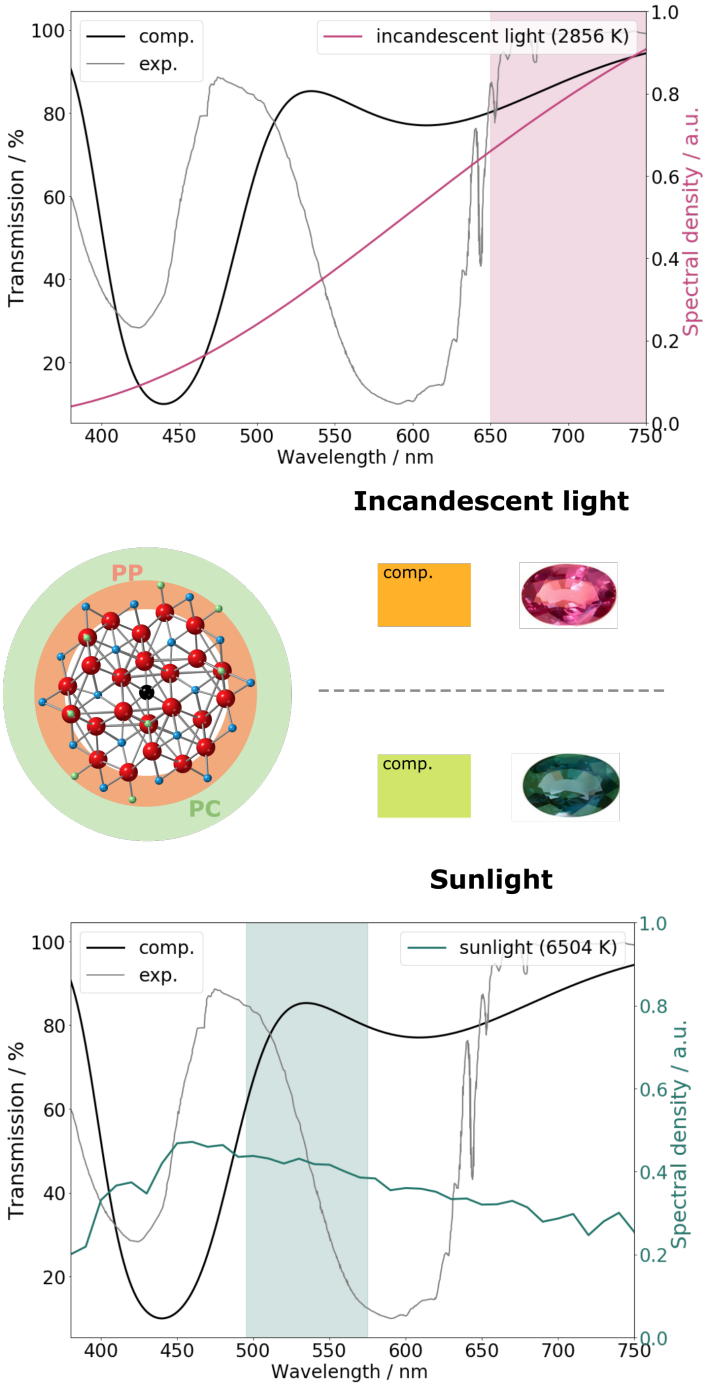

Figure VII.2: Simulation of the transmission spectrum of alexandrite at the TD-DFT/MO6-2X level of theory with 6-311G(d) basis set (black lines). Experimental data (grey lines) comes from [1]. Spectra density of the different sources of light are represented and associated with a rectangle representing the main range of wavelengths for alexandrite's absorption under the irradiation considered. In the middle part, the system considered with O, Al, Be and Cr atoms in red, cyan, green and black respectively. Atoms treated by pseudopotentials (pp) are placed in an orange annulus and the presence of point charges (pc) is represented by a green annulus. Simulated colours are given next to pictures of the minerals according to the different sources of light considered.

progressively until 550 nm, light will mainly be transmitted in the range 650-750 nm and the colour will be redish/pink. However, when the material is irradiated with sunlight, the spectral density is slightly decreasing from 450 to 750 nm, and light will mainly be transmitted in the range 500-570 nm; the material will appear green.

Another cause of polychromism comes from the anisotropy of the material. According to the direction you look at the crystal, the colour will be different. This type of polychromism is referred to as pleochroism. The phenomenon can also be observed by using light polarized along the directions characteristic of the material (cf. polarised-light microscopy).
Cordierite is a famous example of pleochroic mineral, appearing blue when looking at it in one direction and white in the other ones. In the case of cordierite, the origin of the absorption in the visible range is often attributed to intervalence transitions between ferric (Fe^{3+}) and ferrous (Fe^{2+}) ions distributed in the structure.[2]
We optimized a supercell containing the two impurities with Fe^{2+} substituting a magnesium cation in an octahedral site and Fe^{3+} in a tetrahedral site in place of an aluminium cation ($Fe^{\times}_{Mg}$, $Fe^{\times}_{Al}$).[2] In the end, TD-DFT/PBE0 calculations were performed on a cluster made of $\approx$ 50 atoms embedded in pseudopotentials and points charges (cf. Figure VII.3). The simulated spectra along the three directions are in good qualitative agreement with the experiment [2], with a wide band, when irradiating with light polarized along the a-axis, corresponding to the charge transfer transition between the ferrous and ferric cations. This band is not present when using other polarization of light, as observed experimentally. The simulated colours reproduce qualitatively the change of colour when looking at the mineral in the different directions, from blue to beige.

This study on simulation of polychromism in minerals is currently ongoing and needs some refinement. However, the overall protocol seems suitable for studying such phenomena and will hopefully enables us to bring interesting results to the scientific community.

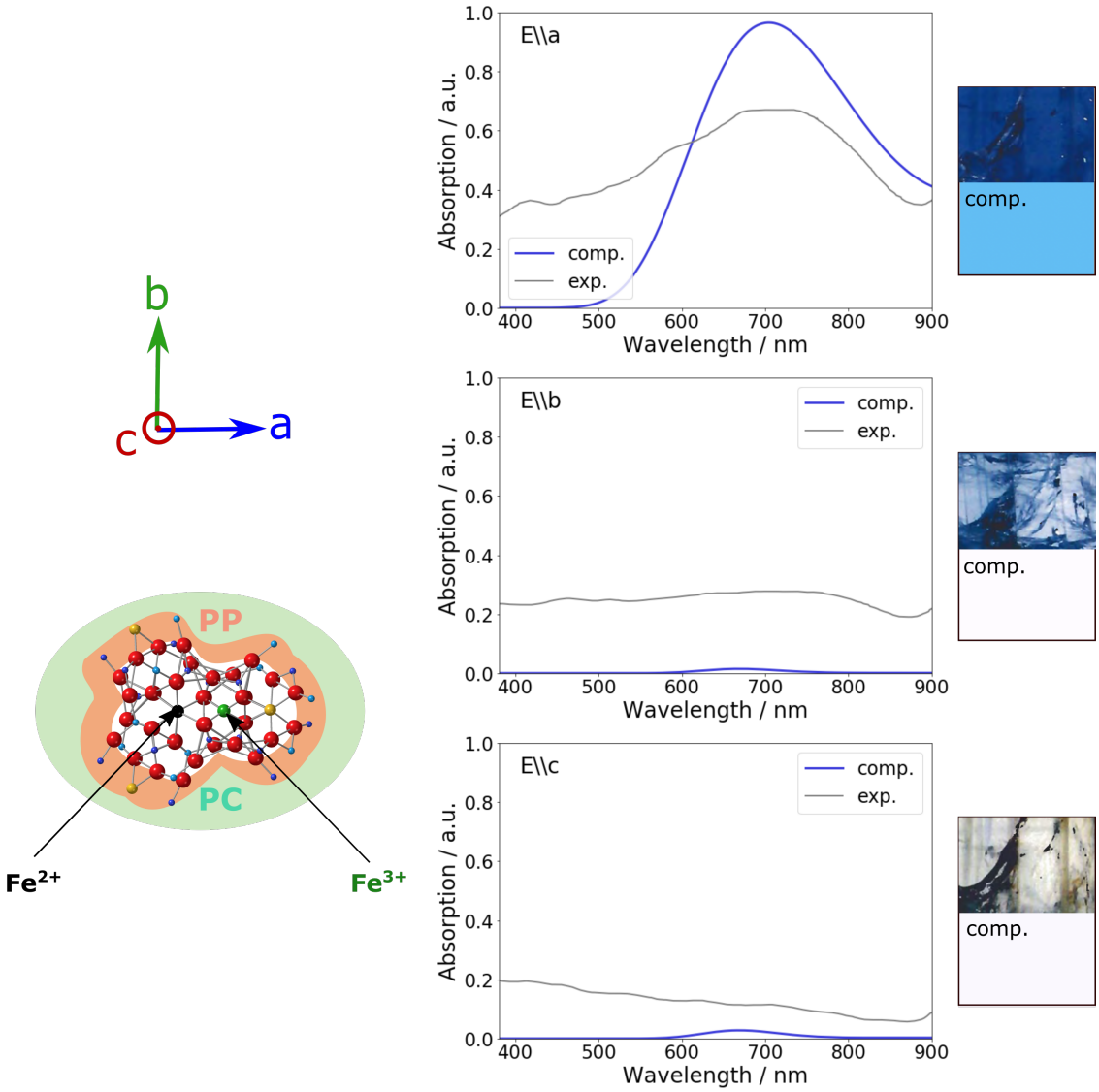

Figure VII.3: Simulation of the absorption spectra of cordierite along the three directions at the TD-DFT/PBE0 level of theory with 6-311G(d) basis set (blue lines). Experimental data (grey lines) comes from [2]. On the left, the system considered with O, Al, Si and Mg atoms in red, cyan, blue and yellow and respectively. The Fe^{2+} and Fe^{3+} are respectively represented by black and grey spheres. Atoms treated by pseudopotentials (pp) are placed in an orange annulus and the presence of point charges (pc) is represented by a green annulus. Simulated colours are given next to pictures of the minerals according to the direction of viewing. Photos are taken from [3].

References

[1] M. Fibrich, J. Šulc, D. Vyhlidal, H. Jelinkova, and M. Čech *Laser Physics*, vol. 27, no. 11, p. 115801, **2017**.

[2] G. Faye, P. Manning, and E. Nickel *American Mineralogist: Journal of Earth and Planetary Materials*, vol. 53, no. 7-8, pp. 1174–1201, **1968**.

[3] E. Fritsch and G. R. Rossman *Gems & Gemology*, vol. 24, no. 1, pp. 3–15, **1988**.

Appendix

A. Character tables for T_d or D_{4h} point groups

The trapped electron in a tetrahedron of sodium (sodalite, tugtupite) or in a square of sodium (scapolite) belongs either to T_d or D_{4h} point group of symmetry. Tables of characters for these two point groups are given below.

	E	**8C$_3$**	**3C$_2$**	**6S$_4$**	**6σd**	**linear, rotations**	**quadratic**
A$_1$	1	1	1	1	1		$x^2+y^2+z^2$
A$_2$	1	1	1	-1	-1		
E	2	-1	2	0	0		$(2z^2-x^2-y^2, x^2-y^2)$
T$_1$	3	0	-1	1	-1	(R_x, R_y, R_z)	
T$_2$	3	0	-1	-1	1	(x, y, z)	(xy, xz, yz)

Table A.1: Character table for T_d point group of symmetry.

	E	**2C$_4$**	**C$_2$**	**2C$_2$'**	**2C$_2$"**	**i**	**2S$_4$**	**σ_h**	**2σ_v**	**2σ_d**	**linear, rotations**	**quadratic**
A$_{1g}$	1	1	1	1	1	1	1	1	1	1		$x^2+y^2+z^2$
A$_{2g}$	1	1	1	-1	-1	1	1	1	-1	-1	R_z	
B$_{1g}$	1	-1	1	1	-1	1	-1	1	1	-1		x^2-y^2
B$_{2g}$	1	-1	1	-1	1	1	-1	1	-1	1		xy
E$_g$	2	0	-2	0	0	+2	0	-2	0	0	(R_x, R_y)	(xz, yz)
A$_{1u}$	1	1	1	1	1	-1	-1	-1	-1	-1		
A$_{2u}$	1	1	1	-1	-1	-1	-1	-1	1	1	z	
B$_{1u}$	1	-1	1	1	-1	-1	1	-1	-1	1		
B$_{2u}$	1	-1	1	-1	1	-1	1	-1	1	-1		
E$_u$	2	0	-2	0	0	-2	0	2	0	0	(x,y)	

Table A.2: Character table for D_{4h} point group of symmetry.

B. More data on artificial sodalites

Complementary information on the artificial sodalites studies.

Numerical details of the relation between structural and spectroscopic properties of F-centers in different sodalite structures:

	$\lambda_{exp.}$ (nm)	$a_{exp.}$ (Å)	$\lambda_{comp.}$ (nm)	$a_{comp.}$ (Å)
SiAlCl	530.03	8.89	502.21	8.83
Si**Ga**Cl	556.04	8.94	537.55	8.92
SiAl**Br**	556.22	8.96	525.11	8.88
Si**GaBr**	581.11	9.00	555.39	8.98
SiAl**I**	605.08	9.02	564.46	8.94
GeAlCl	597.09	9.04	554.66	8.99
GeAl**Br**	642.04	9.10	600.38	9.04

Table A.3: Cell parameter (Å) from experimental data (exp.) and periodic boundary conditions calculation (comp.) using CRYSTAL 17 code and PBE0 functional; maximum absorption wavelength (nm) from experimental data (exp.) and molecular cluster model calculations using Gaussian 16 and B3LYP functional.

Activation energies and cell parameters of different sodalite structures:

	Activation energy (eV)	a (Å)
SiAlCl	3.569	8.828
SiAl**Br**	3.587	8.878
Si**Ga**Cl	3.300	8.923
SiAl**I**	3.637	8.935
Si**GaBr**	3.315	8.978
GeAlCl	3.247	8.989
Si**GaI**	3.518	9.039
GeAl**Br**	3.319	9.043
GeGaCl	3.138	9.095
GeAl**I**	3.498	9.103
GeGaBr	3.134	9.152
GeGaI	3.147	9.214

Table A.4: Computational activation energies and cell parameters for the different sodalite.

C. Functional benchmark and vibronic coupling

Complementary information on the addition of vibronic coupling for the simulation of the absorption spectra of F-centers in different sodalite structures.

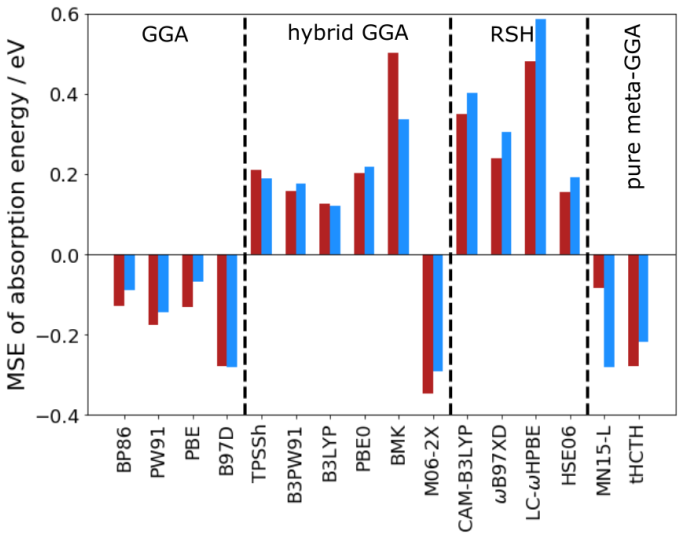

Figure A.1: Mean signed error of F-center absorption energy, in different sodalites structures, without (red) or with (light blue) considering the vibronic coupling for different functionals.

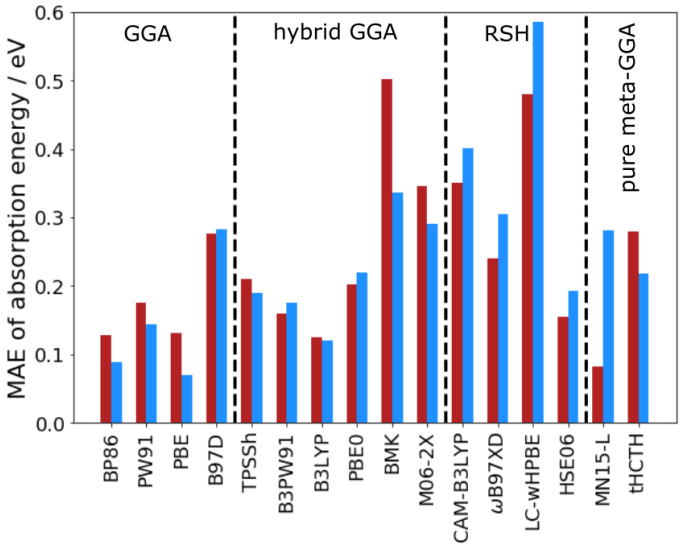

Figure A.2: Mean averaged error of F-center absorption energy, in different sodalites structures, without (red) or with (light blue) considering the vibronic coupling for different functionals.

By including vibronic coupling, the results from the pure GGA PBE and BP86 are improved since vibronic coupling blue-shifts the transitions, thus partly compensating the

underestimation of transition energy of GGA functionals (cf. Figure A.1).
The difference between vertical absorption and vibrationally resolved transitions is not constant when changing from one functional to the other. The origin of this variability is not straightforward. Indeed, the difference between vertical absorption and vibrationally resolved transitions is both material and functional dependent. It is first functional dependent for the estimation of the adiabatic energy. Secondly, the shifts presented on Figures A.2 and A.1 are averaged over different materials. However, for each material the ZPE of the GS and the one of the ES, or else the quantum number (n') of the vibrational state giving the most intense vibronic transition will change (cf Table A.5). All these parameters have different impacts on the final simulated maximum absorption wavelengths, which are combined in a complex way. The absorption wavelengths without or with vibronic coupling for the different sodalite structures depending on the functional can be found in Table A.7.

	$\bar{\nu}_{\text{vib,GS}}$	$\bar{\nu}_{\text{vib,ES}}$	ZPE_{GS}	ZPE_{ES}	ΔZPE	n'_{max}
SiAlCl	175	156	1104	1170	66	9
SiAl**Br**	165	155	1062	1110	48	10
SiAl**I**	153	148	748	1384	636	12
Si**Ga**Cl	181	168	1108	1213	105	10
Si**GaBr**	177	158	1096	1195	100	11
GeAlCl	179	168	1116	1148	33	13
GeAl**Br**	170	170	1107	1282	176	14

Table A.5: Frequency of the breathing mode of the Na_4 tetrahedron computed in PBC for the ground and excited state (cm^{-1}). Zero-Point Energy computed at the ground and excited state from frequencies computed at the PBE0 level in PBC (in cm^{-1}). Quantum number of the vibrational state giving the most intense vibronic transition.

This analysis of the difference between vertical absorption and vibrationally resolved transitions lacks some quantitative (*i.e.* more materials) and qualitative (*e.g.* E_{0-0}) experimental data and undoubtedly suffers from the definition of the adiabatic energy used for the calculations. More generally, it would be interesting to perform higher level of theory calculations such as couple cluster calculations to get reference values for this model development.

	BP86			PW91			PBE		
	λ_{abs}	λ_{emi}	E_{adia}	λ_{abs}	λ_{emi}	E_{adia}	λ_{abs}	λ_{emi}	E_{adia}
SiAlCl	548.42	674.55	2.05	558.8	707.95	1.99	547.54	582.37	2.20
SiAl**Br**	567.55	685.86	2.00	576.99	716.41	1.94	575.67	692.32	1.97
Si**Ga**Cl	629.46	841.35	1.72	644.75	871.35	1.67	627.82	838.42	1.73

Si**GaBr**	648.16	839.97	1.69	663.64	866.24	1.65	645.56	834.94	1.70
GeAlCl	641.09	853.00	1.69	650.33	873.15	1.66	639.61	843.08	1.70
GeAl**Br**	685.75	982.30	1.54	701.82	1035.14	1.48	681.71	986.17	1.54
SiAl**I**	614.69	733.75	1.85	642.02	785.30	1.75	621.90	750.58	1.82
		B97D			TPSSh			B3PW91	
	λ_{abs}	λ_{emi}	E_{adia}	λ_{abs}	λ_{emi}	E_{adia}	λ_{abs}	λ_{emi}	E_{adia}
SiAlCl	574.18	720.30	1.94	447.18	573.99	2.38	500.54	591.36	2.29
SiAl**Br**	602.10	730.75	1.88	496.82	583.98	2.31	521.30	606.80	2.21
Si**Ga**Cl	689.17	946.09	1.55	526.41	676.76	2.09	528.21	672.00	2.10
Si**GaBr**				538.62	678.06	2.07	544.70	677.37	2.05
GeAlCl	699.86	946.82	1.54	549.87	705.87	2.01	547.93	697.54	2.02
GeAl**Br**	771.14	1127.44	1.35	588.89	806.76	1.82	584.63	788.61	1.85
SiAl**I**	652.74	801.59	1.72	528.24	622.04	2.17	552.89	643.30	2.08
		B3LYP			PBE0			BMK	
	λ_{abs}	λ_{emi}	E_{adia}	λ_{abs}	λ_{emi}	E_{adia}	λ_{abs}	λ_{emi}	E_{adia}
SiAlCl	502.21	610.95	2.25	493.90	565.20	2.35	487.64	523.25	2.46
SiAl**Br**	525.11	623.95	2.17	514.53	597.40	2.24	459.89	955.20	2.00
Si**Ga**Cl	537.55	701.78	2.04	516.22	649.47	2.16	416.77	646.23	2.45
Si**GaBr**	555.39	709.94	1.99	532.06	657.52	2.11	496.44	660.68	2.19
GeAlCl	554.66	719.97	1.98	534.88	673.01	2.08	459.75	674.16	2.27
GeAl**Br**	600.38	836.96	1.77	570.29	760.33	1.90	486.79	724.19	2.13
SiAl**I**	564.46	672.88	2.02	546.66	634.22	2.11	485.31	861.85	2.00
		M06-2X			CAM-B3LYP			wB97-XD	
	λ_{abs}	λ_{emi}	E_{adia}	λ_{abs}	λ_{emi}	E_{adia}	λ_{abs}	λ_{emi}	E_{adia}
SiAlCl	653.78			473.50	549.60	2.44	488.83	580.59	2.34
SiAl**Br**	669.77	819.41	1.68	493.04	568.91	2.35	522.32	597.49	2.23
Si**Ga**Cl	641.16	795.38	1.75	478.02	583.27	2.36	499.31	612.08	2.25
Si**GaBr**	672.82	868.68	1.64	495.00	595.89	2.29	518.95	625.25	2.19
GeAlCl	713.64	977.69	1.50	496.98	609.85	2.26	517.36	634.86	2.17
GeAl**Br**	764.78	1196.49	1.33	526.53	678.74	2.09	546.81	694.03	2.03
SiAl**I**	738.82	928.46	1.51	523.96	603.28	2.21	556.17	617.01	2.12
		HSE06			MN15-L			tHCTH	
	λ_{abs}	λ_{emi}	E_{adia}	λ_{abs}	λ_{emi}	E_{adia}	λ_{abs}	λ_{emi}	E_{adia}
SiAlCl	501.30	598.63	2.27	553.21	682.18	2.03	571.92	734.31	1.93
SiAl**Br**	523.08	613.31	2.20	582.35	696.57	1.95	583.92	741.32	1.90
Si**Ga**Cl	530.80	681.98	2.08	574.72	788.09	1.87	703.11	984.68	1.51
Si**GaBr**	547.16	685.65	2.04	586.89	782.08	1.85	720.94	971.30	1.50

GeAlCl	547.7	701.86	2.02	628.91	855.87	1.71	705.21	981.71	1.51
GeAl**Br**	578.93	803.47	1.84	686.88	1006.96	1.52	765.45	803.47	1.58
SiAl**I**	557.04	655.82	2.06	623.01	777.98	1.95	659.48	826.70	1.69

	LC-wHPBE		
	λ_{abs}	λ_{emi}	E_{adia}
SiAlCl	457.86	514.44	2.56
SiAl**Br**	475.13	531.74	2.47
Si**Ga**Cl	453.26	524.90	2.55
Si**GaBr**	468.20	538.60	2.48
GeAlCl	469.25	546.36	2.46
GeAl**Br**	490.45	582.76	2.33
SiAl**I**	499.07	557.31	2.35

Table A.6: Vertical absorption and emission wavelengths (nm) along with adiabatic energy (eV) for different sodalite structures depending on the functional. TD-DFT calculations performed on Opc systems.

	BP86		PW91		PBE		
	λ_{TDDFT}	λ_{VC}	λ_{TDDFT}	λ_{VC}	λ_{TDDFT}	λ_{VC}	λ_{exp}
SiAlCl	548.42	551.16	558.8	567.31	547.54	517.06	530.03
SiAl**Br**	567.55	561.94	576.99	576.02	575.67	568.02	556.22
Si**Ga**Cl	629.46	637.08	644.75	654.08	627.82	635.98	556.04
Si**GaBr**	648.16	640.41	663.64	656.41	645.56	638.19	581.11
GeAlCl	641.09	628.37	650.33	638.19	639.61	624.11	597.09
GeAl**Br**	685.75	677.08	701.82	697.63	681.71	675.84	642.04
SiAl**I**	614.69	553.64	642.02	578.92	621.90	561.25	605.08
	B97D		TPSSh		B3PW91		
	λ_{TDDFT}	λ_{VC}	λ_{TDDFT}	λ_{VC}	λ_{TDDFT}	λ_{VC}	λ_{exp}
SiAlCl	574.18	587.95	447.18	486.71	500.54	504.93	530.03
SiAl**Br**	602.10	593.69	496.82	491.50	521.30	512.02	556.22
Si**Ga**Cl	689.17	697.49	526.41	535.12	528.21	534.34	556.04
Si**GaBr**	708.55	697.24	538.62	537.46	544.70	540.62	581.11
GeAlCl	699.86	680.71	549.87	542.22	547.93	539.04	597.09
GeAl**Br**	771.14	751.66	588.89	585.37	584.63	578.92	642.04
SiAl**I**	652.74	588.18	528.24	485.01	552.89	502.23	605.08
	B3LYP		PBE0		BMK		
	λ_{TDDFT}	λ_{VC}	λ_{TDDFT}	λ_{VC}	λ_{TDDFT}	λ_{VC}	λ_{exp}
SiAlCl	502.21	512.89	493.90	492.29	487.64	472.64	530.03

SiAl**Br**	525.11	519.99	514.53	505.34	459.89	561.09	556.22
Si**Ga**Cl	537.55	548.69	516.22	520.67	416.77	464.20	556.04
Si**GaBr**	555.39	556.16	532.06	527.88	496.44	510.60	581.11
GeAlCl	554.66	548.69	534.88	525.45	459.75	486.30	597.09
GeAl**Br**	600.38	599.69	570.29	564.32	486.79	511.31	642.04
SiAl**I**	564.46	569.06	546.66	495.85	485.31	520.72	605.08
		M06-2X		CAM-B3LYP		wB97-XD	
	λ_{TDDFT}	λ_{VC}	λ_{TDDFT}	λ_{VC}	λ_{TDDFT}	λ_{VC}	λ_{exp}
SiAlCl	653.78		473.50	475.55	488.83	495.45	530.03
SiAl**Br**	669.77	655.24	493.04	484.38	522.32	508.48	556.22
Si**Ga**Cl	641.16	629.45	478.02	479.95	499.31	500.19	556.04
Si**GaBr**	672.82	661.13	495.00	489.53	518.95	510.60	581.11
GeAlCl	713.64	694.85	496.98	486.94	517.36	504.99	597.09
GeAl**Br**	764.78	762.57	526.53	519.25	546.81	533.56	642.04
SiAl**I**	738.82	655.24	523.96	477.46	556.17	494.80	605.08
		HSE06		MN15-L		tHCTH	
	λ_{TDDFT}	λ_{VC}	λ_{TDDFT}	λ_{VC}	λ_{TDDFT}	λ_{VC}	λ_{exp}
SiAlCl	501.30	501.55	553.21	563.81	571.92	582.59	530.03
SiAl**Br**	523.08	514.75	582.35	560.21	583.92	588.00	556.22
Si**Ga**Cl	530.80	539.04	574.72	593.87	703.11	714.86	556.04
Si**GaBr**	547.16	544.63	586.89	592.92	720.94	713.47	581.11
GeAlCl	547.7	539.91	628.91	623.05	705.21	692.38	597.09
GeAl**Br**	578.93	579.93	686.88	683.24	765.45	660.07	642.04
SiAl**I**	557.04	507.08	623.01	569.06	659.48	597.00	605.08
		LC-wHPBE					
	λ_{TDDFT}	λ_{VC}	λ_{exp}				
SiAlCl	457.86	454.76	530.03				
SiAl**Br**	475.13	462.45	556.22				
Si**Ga**Cl	453.26	447.26	556.04				
Si**GaBr**	468.20	456.70	581.11				
GeAlCl	469.25	452.77	597.09				
GeAl**Br**	490.45	472.55	642.04				
SiAl**I**	499.07	452.77	605.08				

Table A.7: Absorption wavelengths (nm) without (λ_{TDDFT}) or with (λ_{VC}) vibronic coupling for different sodalite structures depending on the functional. TD-DFT calculations performed on Opc systems. The maximum absorption respective experimental wavelengths are given in the last column (λ_{exp}).

D. Modelling the charge transfer transition: influence of the functional and the embedding

The evaluation of the activation and bleaching energies conducted on all four systems (*i.e.* Na_8, O^-, OH and Opc, cf. section IV.3.2.3.c). CAM-B3LYP is the only one of the three tested functionals to provide a negative bleaching energy, whatever the cluster used for the calculation.

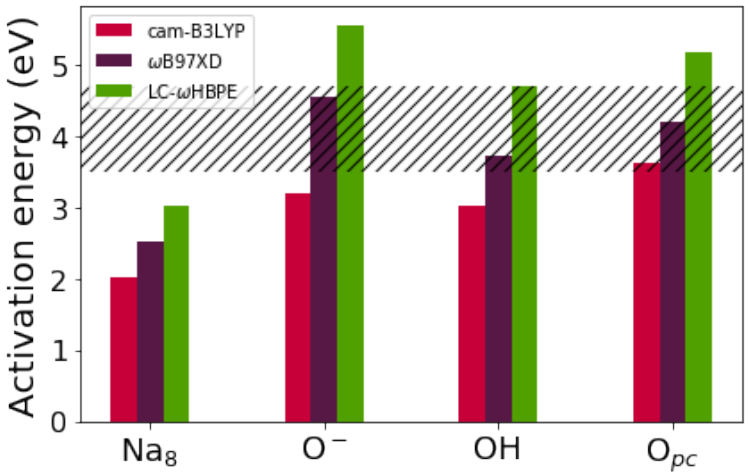

Figure A.3: Activation energies calculated at the TD-DFT/TDA level of theory with three different RSH functionals on four different type of systems: Na_8, O^-, OH and Opc. The experimental values are represented by the hatched rectangles, centered on -0.3 eV.

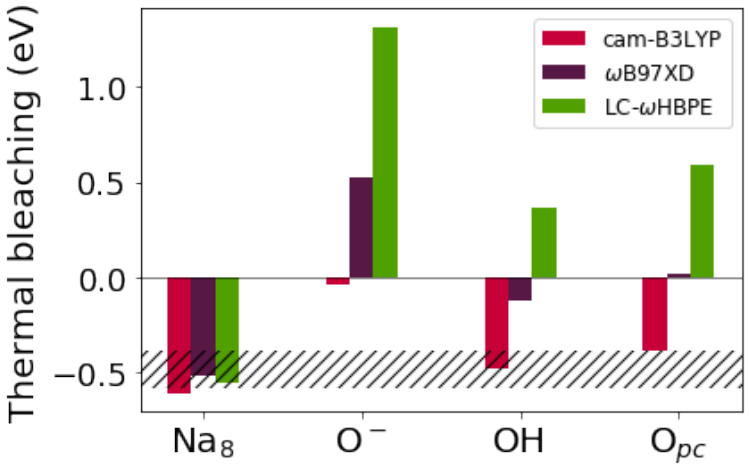

Figure A.4: Thermal bleaching energies calculated at the TD-DFT/TDA level of theory with three different RSH functionals on four different type of systems: Na_8, O^-, OH and Opc. The experimental values are represented by the hatched rectangles, centered on -0.48 eV.

E. Naturally photochromic minerals - supporting information

structure #	relative energy (eV)	a=b	c	% err a	% err c	angle °
1	0.000	11.921	7.556	1.156	0.217	0.074
2	0.079	11.917	7.541	1.182	0.409	0.078
3	0.023	11.924	7.539	1.129	0.439	0.099
4	0.034	11.907	7.576	1.269	-0.054	0.047
5	0.059	11.906	7.538	1.275	0.446	0.037
6	0.079	11.918	7.541	1.177	0.410	0.042
7	0.023	11.924	7.543	1.129	0.383	0.095

Table A.8: Cell parameters and %errors with respect to experiment[1] for the 7 combinations investigated in the optimization of marialite structure.

Element	Scapolite	Ideal scapolite	Tugtupite	Ideal tugtupite	Sodalite	Ideal sodalite
Na	5.3	5.3	10.3	17.4	17.3	17.5
Ca	2.2	5.3	0.7	0.0	0.0	0.0
Al	9.6	7.9	5.0	4.3	8.8	13.1
Be	0.0	0.0	4.0	4.3	0.0	0.0
Si	18.4	15.8	18.2	17.4	10.4	13.1
O	63.5	63.2	59.8	52.2	61.1	52.5
Cl	0.8	2.6	2.0	4.3	1.1	3.5
S	0.2	0.0	0.0	0.0	1.3	0.2

Table A.9: Elemental compositions (atomic %) obtained with XPS measurements. Compositions for "ideal" stoichiometries $Na_2Ca_2Al_3Si_6O_{24}Cl$, $Na_4AlBeSi_4O_{12}Cl$ and $Na_8Al_6Si_6O_{24}Cl_{1.6}S_{0.4}$ are given for comparison.

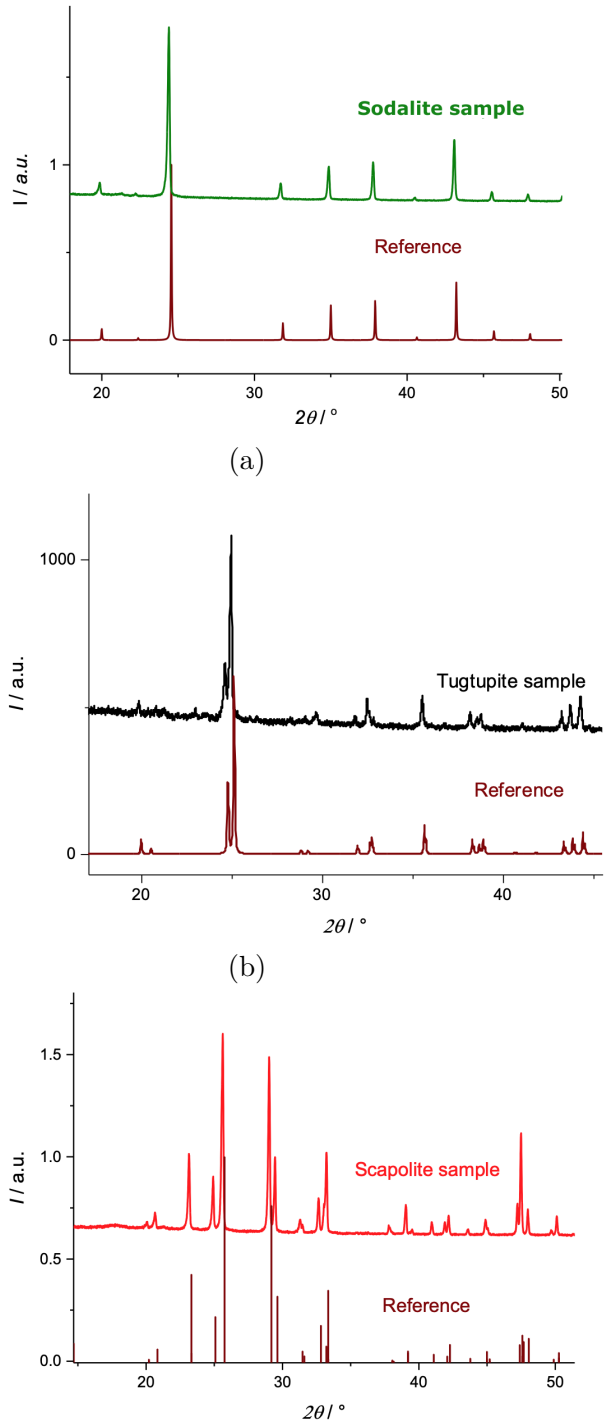

Figure A.5: X-ray powder diffraction patterns together with the reference patterns for (a) sodalite, (b) tugtupite and (c) scapolite.

F. Dichalcogenures functional benchmark

	BP86			PW91			PBE		
	λ_{abs}	λ_{emi}	E_{adia}	λ_{abs}	λ_{emi}	E_{adia}	λ_{abs}	λ_{emi}	E_{adia}
S_2^-	419.10	543.73	2.62	417.92	543.40	2.28	417.95	546.16	2.62
Se_2^-	477.70	1053.01	1.88	479.19	988.61	1.92	478.70	1010.64	1.91
Te_2^-	561.02	907.80	1.79	562.76	936.71	1.76	563.76	929.67	1.76
	B97D			TPSSh			B3PW91		
	λ_{abs}	λ_{emi}	E_{adia}	λ_{abs}	λ_{emi}	E_{adia}	λ_{abs}	λ_{emi}	E_{adia}
S_2^-	411.87	634.28	2.48	400.78	599.09	2.58	392.61	602.21	2.61
Se_2^-	506.31	1085.41	1.79	459.29	919.87	2.02	459.32	927.10	2.02
Te_2^-	599.69	999.38	1.65	537.22	855.19	1.88	538.90	859.41	1.87
	B3LYP			PBE0			BMK		
	λ_{abs}	λ_{emi}	E_{adia}	λ_{abs}	λ_{emi}	E_{adia}	λ_{abs}	λ_{emi}	E_{adia}
S_2^-	399.49	598.58	2.59	383.77	616.62	2.62	392.03	625.10	2.57
Se_2^-	447.42	899.03	2.07	456.88	928.77	2.02	419.61	820.08	2.23
Te_2^-	523.50	826.54	1.93	516.02	858.87	1.92	488.84	763.78	2.08
	M06-2X			CAM-B3LYP			wB97-XD		
	λ_{abs}	λ_{emi}	E_{adia}	λ_{abs}	λ_{emi}	E_{adia}	λ_{abs}	λ_{emi}	E_{adia}
S_2^-	404.01	645.39	2.49	371.1	673.98	2.59	386.10	660.30	2.54
Se_2^-	464.42	913.42	2.01	430.39	858.04	2.16	452.16	867.11	2.08
Te_2^-	536.06	881.56	1.86	500.60	781.22	2.03	499.77	775.88	2.04
	HSE06			MN15-L			tHCTH		
	λ_{abs}	λ_{emi}	E_{adia}	λ_{abs}	λ_{emi}	E_{adia}	λ_{abs}	λ_{emi}	E_{adia}
S_2^-	386.54	615.63	2.61	358.10	666.43	2.66	404.84	695.24	2.42
Se_2^-	456.36	920.89	2.03	469.13	959.13	1.97	504.58	1110.22	1.78
Te_2^-	533.22	847.23	1.89	558.19	945.07	1.76	602.11	1005.30	1.64
	LC-wHPBE								
	λ_{abs}	λ_{emi}	E_{adia}						
S_2^-	359.87	786.59	2.51						
Se_2^-	439.12	818.88	2.17						
Te_2^-	491.21	753.83	2.08						

Table A.10: Absorption and emission wavelengths (nm) along with adiabatic energy (eV) for the three dichalcogen anions (S_2^-, Se_2^-, Te_2^-) depending on the functional. The values were obtained through TD-DFT calculations for S_2^- fluorescence, and through ΔSCF calculations for Se_2^- and Te_2^- phosphorescence.

	BP86		PW91		PBE		
	λ_{TDDFT}	λ_{VC}	λ_{TDDFT}	λ_{VC}	λ_{TDDFT}	λ_{VC}	λ_{exp}
S_2^-	543.73	571.32	543.40	571.32	546.16	573.44	626
Se_2^-	1053.01	742.96	988.61	727.93	1010.64	733.10	751
Te_2^-	907.80	744.88	936.71	755.81	929.67	753.97	869
	B97D		TPSSh		B3PW91		
	λ_{TDDFT}	λ_{VC}	λ_{TDDFT}	λ_{VC}	λ_{TDDFT}	λ_{VC}	λ_{exp}
S_2^-	634.28	609.65	599.09	582.08	602.21	575.57	626
Se_2^-	1085.41	785.57	919.87	686.59	927.10	688.42	751
Te_2^-	999.38	809.27	855.19	705.74	859.41	708.98	869
	B3LYP		PBE0		BMK		
	λ_{TDDFT}	λ_{VC}	λ_{TDDFT}	λ_{VC}	λ_{TDDFT}	λ_{VC}	λ_{exp}
S_2^-	598.58	579.90	616.62	571.40	625.10	584.28	626
Se_2^-	899.03	667.63	928.77	686.28	820.08	615.09	751
Te_2^-	826.54	683.87	858.87	688.44	763.78	633.40	869
	M06-2X		CAM-B3LYP		wB97-XD		
	λ_{TDDFT}	λ_{VC}	λ_{TDDFT}	λ_{VC}	λ_{TDDFT}	λ_{VC}	λ_{exp}
S_2^-	645.39	607.25	673.98	579.90	660.30	593.26	626
Se_2^-	913.42	690.26	858.04	637.38	867.11	663.62	751
Te_2^-	881.56	713.90	781.22	649.37	775.88	646.65	869
	HSE06		MN15-L		tHCTH		
	λ_{TDDFT}	λ_{VC}	λ_{TDDFT}	λ_{VC}	λ_{TDDFT}	λ_{VC}	λ_{exp}
S_2^-	615.63	573.44	666.43	560.94	695.24	629.52	626
Se_2^-	920.89	683.55	959.13	708.27	1110.22	789.99	751
Te_2^-	847.23	699.35	945.07	753.97	1005.30	813.53	869
	LC-wHPBE						
	λ_{TDDFT}	λ_{VC}	λ_{exp}				
S_2^-	786.59	602.51	626				
Se_2^-	818.88	635.55	751				
Te_2^-	753.83	632.10	869				

Table A.11: Emission wavelengths (nm) without (λ_{TDDFT}) or with (λ_{VC}) vibronic coupling for the three dichalcogen anions (S_2^-, Se_2^-, Te_2^-) depending on the functional. The maximum emission respective experimental wavelengths are given in the last column (λ_{exp}).

G. Persistent luminescence study: supporting information

G.1. Composition of the samples studied

Element	Nominal	Synthetic	Greenland wt %	Koksha Valley 1 wt %	Koksha Valley 2 wt %	Mt. St. Hilaire wt %	Pakistan wt %
Na	31.64	33.1	20.0	21.0	18.5	17.7	24.2
Al	30.95	26.8	29.5	29.3	30.6	28.1	29.3
Si	28.98	28.0	31.6	30.5	33.3	33.0	28.4
Cl	7.88	11.1	17.7	17.5	16.9	19.1	14.7
S	0.55	0.00	0.80	0.30	0.30	0.13	0.24
Mg	-	-	-	-	-	-	0.90
K	-	1.0	-	0.84	0.0	0.16	0.83
Ca	-	-	0.06	0.31	0.15	0.04	0.69
Ti	-	0.0	0.05	0.04	0.0	0.0	0.06
V	-	-	-	-	0.16	-	-
Mn	-	-	-	-	0.02	0.13	-
Fe	-	-	0.11	0.05	0.03	1.13	0.08
Ni	-	-	-	-	0.02	0.01	-
Cu	-	-	-	-	-	0.01	-
Zn	-	-	0.09	-	-	0.03	0.03
Ga	-	-	0.08	0.03	0.02	0.02	0.05
Ge	-	-	-	-	0.03	0.01	-
Br	-	-	0.05	0.04	0.1	0.16	0.20
Sr	-	-	-	-	0.0	-	-
Zr	-	-	-	-	-	0.02	-
Pd	-	-	-	-	-	-	0.24
Cs	-	-	-	-	-	0.10	-
La	-	-	0.08	0.05	-	-	0.11
Nd	-	-	-	-	-	0.14	-
Tl	-	-	-	-	-	0.02	-

Table A.12: Overall elemental compositions (in weight%) of the studied samples based on XRF analyses. The nominal composition for a typical tenebrescent sodalite $Na_8(AlSiO_4)_6Cl_{1.6}S_{0.1}$ is given as well.

G.2. Choice of cluster and embedding

For Fe and Ti defects, we investigated both the effect of the size of the cluster and the embedding of the cluster. Three sizes were considered (i) a small cluster including only the bonded oxygen atoms (13 atoms, cf. Figure A.6a), (ii) a medium size cluster including the first shell of silica/alumina tetrahedrons around the defect (37 atoms, cf. Figure A.6b) and (iii) the two first shells of silica/alumina tetrahedrons around the defect (103 atoms, cf. Figure A.6d). All these clusters were saturated with H atoms. A saturation made of a shell of pseudo-potentials and point charges (≈46000 point charges) for the simulation of the Madelung potential was also considered for the medium size cluster (cf.

Figure A.6c). This last type of embedding has proven its reliability to simulate point defect spectroscopic properties in sodalite in a previous work.[2]. Figure A.6 presents the structure of all these clusters for the Ti^{3+} defect. They are similar for the other three defects.

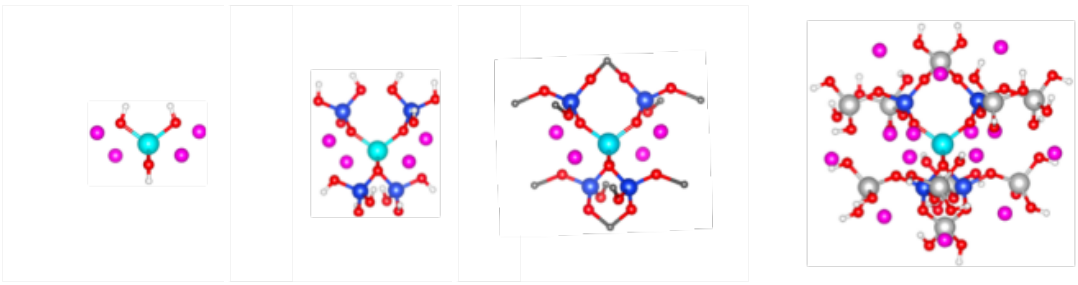

(a) (b) (c) (d)

Figure A.6: Investigated cluster's sizes to simulate the spectroscopic properties of Ti^{3+} defect by TD-DFT calculations. The Ti, Al, Si, O, Na and H atoms are in cyan, grey, blue, red, pink and white colours respectively. The small dark grey atoms are the positions of the pseudopotentials.

Only the first spin state was computed for each spin for Fe based defects. There are two types of transitions in these systems, the *d-d* localized transitions and the charge transfer transitions. In Figure A.7, for the *d-d* transitions, both the size of the cluster and the embedding have a limited effect on the computed energy transitions. The main difficulty comes from the spin contamination that can be very large for the largest cluster preventing to assign some transitions. The charge-transfer transitions are much more affected by the choice of the cluster and of the embedding. Based on previous works dedicated to the simulation of spectroscopic properties of localized defects, we decided to focus more on the embedding than on the size of the cluster. For that reason, results given in the main text are obtained for the medium size cluster surrounded by a shell of pseudopotentials for the closest cations and a cloud of point charges reproducing the Madelung potential. All the clusters are presented on Figure A.6. For the Fe^{3+} and Fe^{2+} ions, several spin states were considered for the DFT and TD-DFT calculation performed on the cluster. The highest spin state was always found to be the most stable one, as for periodic calculation. The energy diagrams of these ions were obtained by using a ΔSCF approach to estimate the difference in energy between the lowest energy level of each spin multiplicity and the higher energy levels of each spin multiplicity were placed by using TD-DFT calculations (cf. Figure A.7).

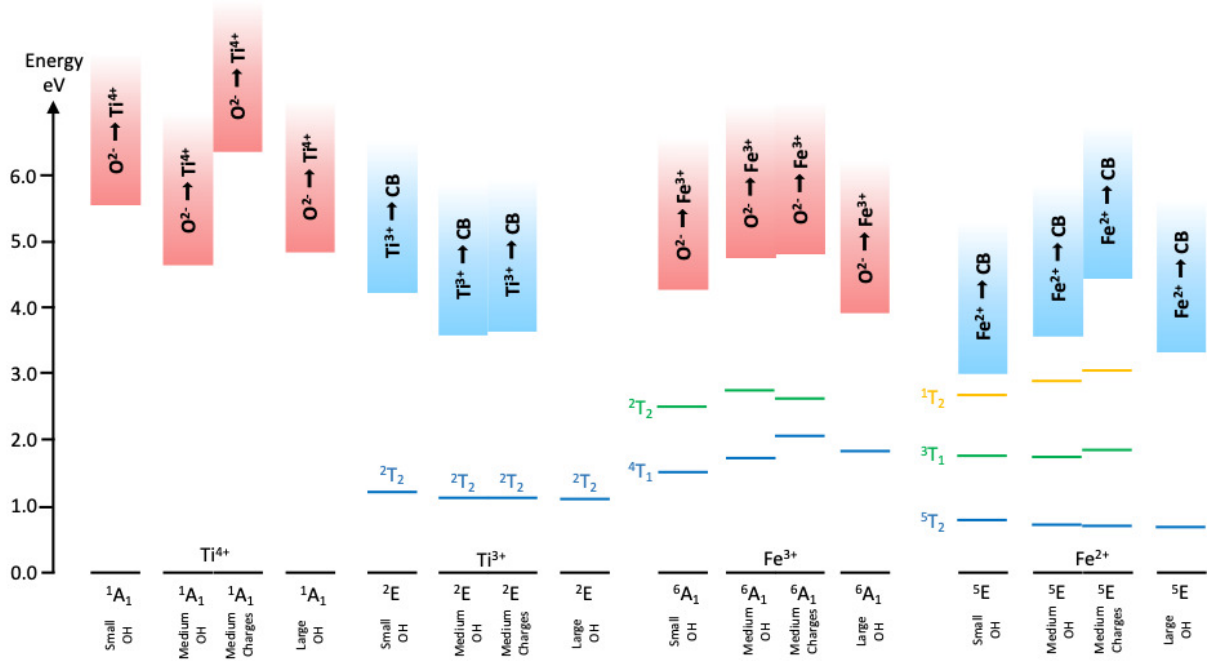

Figure A.7: Computed energy levels for all Ti^{4+}, Ti^{3+}, Fe^{3+} and Fe^{2+} defects for three sizes of cluster and two types of embedding.

H. XANES study

H.1. Observations and results

A collaborative study with Turku University was led on the ability of sodalite minerals for reversible photochromism upon X-ray exposure. Details of the study can be found in ref [3]. As a general result, we showed that the X-ray-induced colour center is similar to that induced by UV radiation and that the main colouration mechanism involves the transfer of an electron from S_2^{2-} to the chloride vacancy as for UV radiation.

During the course of the study, experimental XANES spectra of sodalite compounds were obtained by our collaborators (cf. Figure A.8a). The more the samples were irradiated, the more the 2465 eV peak increases and the 2472 eV peak decreases. In order to help in the assignment of peaks and clarify the results we carried out quantum chemical calculations to simulate the XANES spectra of the S_2^{2-} and S_2^{-} species (cf. Figure A.8b). This allowed us to show that the modification of the peaks' intensity in the experimental spectra were due to an increase of S_2^{-} concentration associated with a decrease of S_2^{2-}'s one. This is in agreement with the mechanism of photochromism in sodalite.

Due to the qualitative agreement between experimental and computational data for S_2^{-} and S_2^{2-} impurities, we decided to simulate the XANES spectra of other sulfur impurities

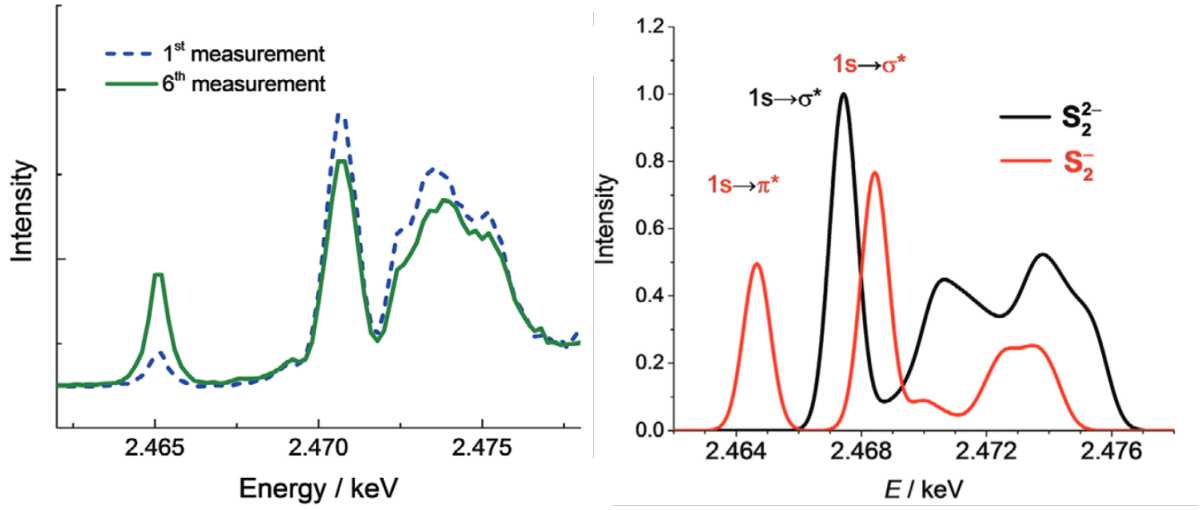

(a) (b)

Figure A.8: (a) Experimental XANES spectra for sodalite sample $(Na,Li)_8(SiAlO_4)_6(Cl,S)_2$ with background subtracted after several X-ray irradiations (1 or 6). (b) Computed sulfur K-edge XANES spectrum of S_2^{2-} (black) and S_2^- (red) on Opc systems (*i.e.* impurity in the β-cage embedded in pseudopotentials and point charges). The spectra were shifted by 36 eV for agreement with experiment. Peaks assigned to different transitions (cf. Figure A.9).

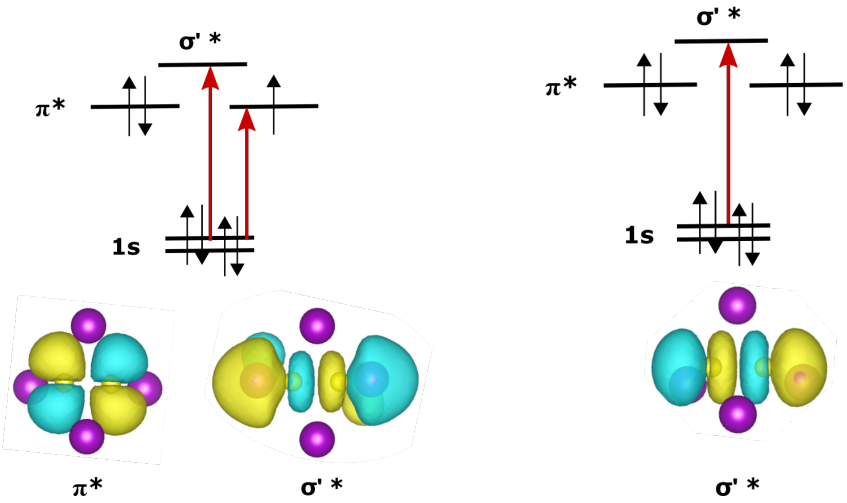

(a) (b)

Figure A.9: Transitions and associated orbitals for S_2^- (a) and S_2^{2-} (b).

in sodalite with the same level of theory. The simulated spectra are given in Figure A.10, and can help in future experimental analysis.

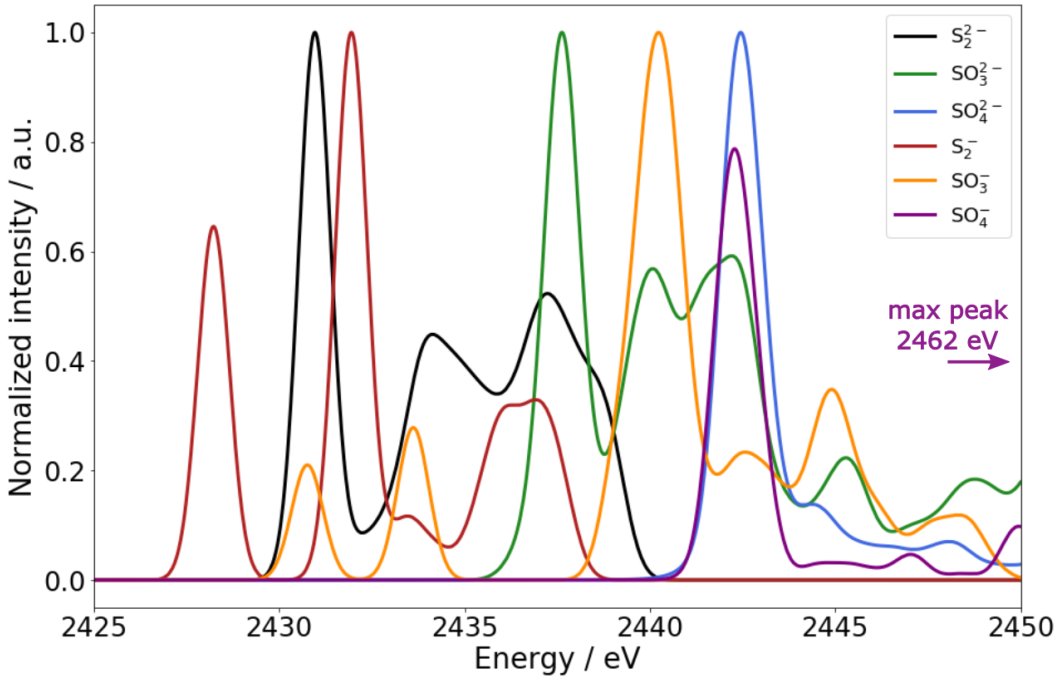

Figure A.10: Computed sulfur K-edge XANES spectrum for different sulfur impurities in sodalite. Calculations were performed on Opc structures (*i.e.* impurity in the β-cage embedded in pseudopotentials and point charges).

H.2. Computational details

X-ray Absorption Near Edge Spectroscopy calculations were performed using a Time-Dependent Density Functional Theory formalism implemented in Orca[4, 5] with B3LYP/Def2-SVP[6] level of theory. Relativistic corrections were considered thanks to the zero-order regular approximation (ZORA) and RIJCOSX approximation was used in order to speed up the calculations. Energy convergence criterion for the SCF cycles was fixed at 10^{-8} Ha per unit cell. The excitation window was restricted to the 1s core orbital of the sulfur species of interest (cf. Figure A.9), along with the virtual orbitals having an energy higher than the first virtual orbital of the sulfur species, and more than 240 transitions were computed.

References Appendix.

[1] E. Sokolova and F. C. Hawthorne *The Canadian Mineralogist*, vol. 46, no. 6, pp. 1527–1554, **2008**.

[2] P. Colinet, A. Gheeraert, A. Curutchet, and T. Le Bahers *The Journal of Physical Chemistry C*, vol. 124, no. 16, pp. 8949–8957, **2020**.

[3] S. Vuori, P. Colinet, I. Norrbo, R. Steininger, T. Saarinen, H. Palonen, P. Paturi, L. C. Rodrigues, J. Göttlicher, T. Le Bahers, and M. Lastusaari *Advanced Optical Materials*, p. 2100762, **2021**.

[4] F. Neese *Wiley Interdisciplinary Reviews: Computational Molecular Science*, vol. 2, no. 1, pp. 73–78, **2012**.

[5] F. Neese *Wiley Interdisciplinary Reviews: Computational Molecular Science*, vol. 8, no. 1, pp. 4–9, **2018**.

[6] F. Weigend and R. Ahlrichs *Physical Chemistry Chemical Physics*, vol. 7, no. 18, p. 3297, **2005**.

Abstract:
Naturally tenebrescent (reversibly photochromic) materials have been known from geologists since the 1970's but were investigated seriously only recently. The adaptability of these materials, along with their high stability and good reversibility of the photochromism make them of great interest. The aluminosilicate sodalite ($Na_8Al_6Si_6O_{24}Cl_2$) is one of them, with the assessed mechanism being a reversible photoinduced electron transfer from an impurity to a chloride vacancy, leading to the formation of a trapped electron in a crystal box. This trapped electron, called F-center, has quantified levels and absorbs in the visible light. The aim of this work is to develop a methodology based on quantum chemistry to confirm and get more insights on the mechanism at stake.
We first designed a simulation protocol to investigate the spectroscopic properties of point defects in sodalite minerals, using Time Dependent Density Functional Theory (TD-DFT). We highlighted the influence of the close environment and the vibronic coupling in these spectra, but also very interestingly the influence of the nature of the defect on the choice of some parameters in the methodology, such as the functional. The methodology was then successfully applied on other aluminosilicate materials, and other type of defects leading to a deeper understanding of these minerals.
Then, by adapting the methodology, the photoinduced charge was investigated to understand both the mechanism of the F-center formation and the process of bleaching. These last calculations, performed both at the TD-DFT and post-HF levels, provide paramount information for future development of, among others, specific wavelength sensors.

Résumé :
Les matériaux naturels ténébrescents (photochromisme réversible), sont connus des géologues depuis les années 1970 mais ont été étudiés plus attentivement seulement récemment. Leur grande adaptabilité, ainsi que leur stabilité et la bonne réversibilité du photochromisme leur confèrent un grand intérêt. La sodalite ($Na_8Al_6Si_6O_{24}Cl_2$) en est un exemple, et le mécanisme supposé consiste en un transfert photo-induit réversible d'un électron depuis une impureté vers une lacune de chlore, menant à la formation d'un électron piégé dans une boîte cristalline. Cet électron piégé, appelé F-center, a des niveaux quantifiés d'énergie et absorbe dans le domaine du visible. L'objectif de ce travail est de développer une méthode basée sur les outils de la chimie quantique afin de confirmer et d'étudier plus profondément le mécanisme en jeu.
Dans un premier temps, nous avons développé un protocole pour simuler les spectres d'absorption ou de fluorescence de défauts ponctuels au sein du matériau sodalite, en utilisant la théorie de la fonctionnelle de la densité dépendante du temps (TD-DFT). Cela a permis de mettre en évidence l'influence de l'environnement proche et du couplage vibronique dans ces spectres, mais aussi, de manière très intéressante, l'influence de la nature du défaut sur le choix de certains paramètres tels que la fonctionnelle. Le protocole a ensuite été appliqué avec succès à l'étude d'autres aluminosilicates, ou d'autres types de défauts, amenant à une compréhension plus complète de ces matériaux.
Dans un second temps, en adaptant la méthode, le transfert de charge photo-induit a été simulé pour comprendre à la fois le mécanisme de formation du F-center et le processus de blanchiment. Ces derniers calculs, utilisant la TD-DFT ou des méthodes post Hartree-Fock, ont apporté des éléments de compréhension importants pouvant mener au développement de nouveaux systèmes photochromiques artificiels.